Magnetization dynamics of nanostructures in strongly out-of-equilibrium regimes

Igor Ngouagnia Yemeli

To cite this version:

Igor Ngouagnia Yemeli. Magnetization dynamics of nanostructures in strongly out-of-equilibrium regimes. Materials Science [cond-mat.mtrl-sci]. Université Paris-Saclay, 2022. English. NNT : 2022UPASP145 . tel-03945919

HAL Id: tel-03945919
https://theses.hal.science/tel-03945919

Submitted on 26 Feb 2024

université
PARIS-SACLAY

Magnetization dynamics of nanostructures in strongly out-of-equilibrium regimes

Dynamique de l'aimantation de nanostructures dans des régimes fortement hors-équilibre

Thèse de doctorat de l'université Paris-Saclay

École doctorale n° 564, Physique en Île-de-France (EDPIF)
Spécialité de doctorat : Physique
Graduate School : Physique Référent : Faculté des sciences d'Orsay

Thèse préparée dans l'unité de de recherche **SPEC** (Université Paris-Saclay, CEA, CNRS), sous la direction de **Grégoire de Loubens**, directeur de recherche

Thèse soutenue à Paris-Saclay, le 08/12/2022, par

Igor Boris Ngouagnia Yemeli

Composition du Jury

Membres du jury avec voix délibérative

Joo-Von Kim Directeur de recherche, CNRS, Centre de Nanosciences et de Nanotechnologies	Président
Ursula Ebels Directrice de recherche, CEA, Spintec	Rapporteur & Examinatrice
Laura Thévenard Directrice de recherche, CNRS, Institut des Nanosciences de Paris	Rapporteur & Examinatrice
Philipp Pirro Junior professor, Technische Universität Kaiserslautern	Examinateur
Nicolas Vukadinovic Ingénieur, Dassault Aviation	Examinateur
Abdelmadjid Anane	Invité

THESE DE DOCTORAT

NNT : 2022UPASP145

Acknowledgements

La thèse est un long et difficile parcours qui, comme la dynamique de l'aimantation qui peut devenir turbulente dans certains régimes, peut être parsemé d'obstacles. Il est impossible de les surmonter tout seul. Je veux donc tout d'abord remercier tous ceux qui m'ont aidé tout au long du chemin parcouru. Je commence par mon directeur de thèse Grégoire, à la fois pour ses qualités humaines et son encadrement scientifique. Il m'a transmis les bases d'une recherche de qualité que sont la curiosité, la méthodologie et la rigueur scientifique. J'ai particulièrement apprécié son attention durant les différentes périodes de restriction liées à la pandémie du Covid 19 qui a grandement contribué à maintenir allumée la flamme de ma motivation.

Je veux ensuite remercier les personnes avec qui j'ai collaboré. Je pense ici à Vladimir Nalétov qui au total aura passé quelques mois au sein du labo durant ma thèse. Il a précédemment contribué à la fabrication du dispositif expérimental sur lequel j'ai travaillé et a donc été d'une grande aide en ce qui concerne l'utilisation technique et la compréhension du dispositif. Ensuite, je souhaite remercier toute l'équipe de l'UMR CNRS-Thales, Diane Gouéré, Hugo Merbouche sous la supervision d'Abdelmadjid Anane qui ont fabriqué les échantillons sur lesquels j'ai travaillé durant ma thèse. Je veux également remercier Hervé Hurdequint que j'ai cotoyé au laboratoire et qui est un véritable puits de connaissance en ce qui concerne la résonance ferromagnétique de couches minces, et avec qui j'ai eu de longs échanges scientifiques. Je remercie aussi Olivier Klein de SPINTEC à Grenoble pour son aide dans quelques simulations micromagnétiques ainsi que Nicolas Vukadinovic qui a quelques fois trouvé du temps en marge de son travail à Dassaut aviation pour des échanges sur les résultats obtenus. Ayant une très grande culture scientifique concernant la dynamique d'ondes de spin en général, il a également été de très bons conseils pour des références bibliographiques pertinentes pour nos résultats. Je remercie mes parrain académique et tuteur scientifique Aumaitre Sébastien et Kim Joo-Von pour l'intérêt qu'ils ont toujours porté à mes travaux et le suivi de mes travaux de thèse à travers notamment leur participation à la réunion annuelle de mon comité de suivi.

Je remercie chaleureusement l'ensemble des membres du jury qui ont bien voulu accepter d'examiner ce travail de thèse : Ursula Ebels (Spintec), Laura Thévenard (INSP), Nicolas Vukadinovic (Dassaut aviation), Joo-Von Kim (C2N) et Abdelmadjid Anane (UMR CRNS-Thales).

Je remercie bien sûr l'ensemble des chercheurs du Laboratoire de Nanomagnétisme et Oxydes (LNO) du Service de Physique de l'Etat Condensé (SPEC) du CEA Saclay qui m'ont acceuilli depuis mon stage de recherche et où j'aurai donc passé un bout de temps. Je veux citer en particulier Michel, Aurélie, Jean-Yves, Jean-Baptiste, Gwen, Myriam, Claude, Anne, Dana... Je tiens à remercier spécialement les techniciens du groupe Gregory Cannies et Gérald Le-Goff pour leurs rares mais précieuses interventions sur le dispositif expérimental qui m'ont parfois éviter de perdre quelques jours d'expériences. Un merci spécial à Corinne pour son aide précieuse dans les démarches administratives qui ne sont pas la chose la plus simple au CEA. À l'heure où j'écris ces lignes il m'est encore impossible de liquider tout seul une mission sur l'espace sigma sans son aide.

Je remercie chaleuresement l'ensemble des thésards et postdoc que j'ai croisés durant mon séjour au SPEC. Je pense aux thésards qui ont déjà fini à savoir Chloé, Julien, Christophe, Anas, Paul; à ceux qui ont commencé une année après moi, Wanissa, Denitsa, Zixin, Binh, Omar, et aux plus récents Sanjay et Mahé. Je leurs souhaite bonne chance pour la suite. Une pensée particulière à Maïkane avec qui j'ai partagé le même bureau et dont la période de thèse aura été quasiment identique à la mienne, à Emma qui a été avec nous dans le bureau durant une année environ et à Artem qui nous a rejoints il y a quelques mois. Un merci spécial à Titiksha qui, entre son premier postdoc à cheval entre Thales et le LNO et le second au LNO a été présente durant toute ma thèse. Ayant souvent eu à travailler sur le même dispositif expérimental, je la remercie pour toutes les discussions scientifiques ou pas, et ses précieux conseils en particulier durant la rédaction. Une grosse pensée à Elmer qui a fini son postdoc il y a plus d'un an maintenant. Avec lui, Jean Yves et Aurélie nous avons été des membres réguliers du rendez-vous "foot" du vendredi après le boulot où j'aurai passé de magnifiques moments de détente concluant parfois des semaines éreintantes. La relève semble assurée sur ce plan avec Sanjay, Mahé et Binh.

Ayant enseigné au Cameroun avant ma thèse durant trois années et ici pendant ma thèse, j'ai une pensée spéciale pour tous les enseignants qui m'ont marqué tout au long de mes études. Je pense particulièrement à Mmes Adjeba, Mbosso, Mrs Kengfack, Keuabou, Lenta, Kapche, Ndjaka, Kofane (bao)... qui ont grandement contribué à développer mon esprit de curiosité et m'ont donné chacun à sa façon le goût d'apprendre et surtout de transmettre.

Je remercie tous mes amis pour leurs encouragements tout au long de ces trois années. L'équilibre entre le travail et les moments partagés ensemble m'ont procuré l'épanouissement indispensable à la réalisation d'un tel projet.

Aussi bien en français qu'en anglais je n'ai pas trouvé de mots assez forts pour dire merci à ma famille, mon papa, ma maman et mes frères et sœurs pour leur soutien et leur amour inconditionnel. Je ne serais pas là sans eux. Enfin, merci à Audrey, pour sa patience, sa présence, son soutien et tout ce qu'elle sait déjà.

Contents

Introduction

“Le début ne laisse pas présager la fin.”

Hérodote

0.1 General background

In addition to its electric charge and mass, the electron has an intrinsic angular momentum called spin which is associated with a magnetic moment. Spintronics or spin electronics exploits this additional degree of freedom to encode information, rather than charge as in conventional electronics. It has led to numerous technological benefits such as the development of magnetic sensors and memories. In an ordered magnetic material, there is an exchange interaction between the spins which leads to a spin alignment. An initial local disturbance of the magnetic order can propagate as a wave. Such a wave was first predicted by F. Bloch in 1929 [1] and was then called spin wave (SW) since it is due to the collective excitations of the electron spin system in ferromagnetic metals and insulators [2]. As these spin waves consist of a collective precession of the magnetic moments, they can transport angular momentum. The quanta of spin waves are magnons and their field of study is called magnonics [3, 4]. Spin waves have attracted significant interest since the beginning of the 21st century, both for their interesting underlying fundamental physics and potential technological applications. With typical frequencies in the GHz range and wavelengths in the micron and submicron range, they are of great interest for applications in microlectronics, information and telecommunication technologies, and radars [5]. Because of their singular properties, they can be used for information transmission and processing. They can indeed carry the information without moving charges, allowing a Joule-heat-free transfer, one of the main limitations of current conventional CMOS-based electronic circuits. Moreover, perhaps more than any other kind of wave (for example electromagnetic or acoustic), spin waves display a diversity of tunable dispersion characteristics with anisotropic and non-reciprocal properties, which can be tuned via the choice of the magnetic material, the shape of the sample, and the orientation and amplitude of the applied magnetic field [6]. Among the wide range of envisaged applications of spin waves, we can mention non-Boolean logic, neuromorphic and reservoir computing [7], quantum magnonics [8] and THz applications [5].

The strongly nonlinear properties of spin waves, directly inherited from the equation of magnetization dynamics, also lead to many interesting physical phenomena. Among others, they manifest themselves by the appearance of bistable dynamics [9, 10], solitons [11], spin wave instabilities [12], synchronization phenomena [13], dynamical reversal of topological textures such as vortices [14, 15], auto-oscillations and chaos [16, 17]. The type of nonlinear dynamics depends on one hand on the ground state and the associated spin wave spectrum of the sample, which are determined by its magnetic properties, its geometry and the applied field, and on the other hand on the excitation used to drive the system out-of-equilibrium.

0.2 Context and motivations

Magnetic materials are the seat of magnetic losses characterized by a magnetic damping. The lowest magnetic damping of yttrium iron garnet or YIG ($Y_3Fe_5O_{12}$) [18] which is an insulating ferrimagnet, makes it the ideal material to study spin waves. This magnetic damping sets the spin wave relaxation time, hence propagation length, as well as nonlinear thresholds. The recent development of ultra-thin layers of YIG maintaining high dynamical quality, grown in particular by pulsed laser deposition [19] (Figure 1 A) and liquid phase epitaxy [20] opens opportunities to control these nonlinear effects. Firstly, they can be nanopatterned by standard nanofabrication techniques. The nanopatterning induces a quantization of the excitation spectrum [21] (Figure 1 B), which limits the nonlinear interactions between modes, and allows one to reach strongly nonlinear regimes of ferromagnetic resonance (FMR) [22] (Figure 1 C). Secondly, it is possible to adjust by doping their physical properties [23], in particular their effective anisotropy, responsible for the nonlinear dependence of the precession frequency [24], which results in the typical foldover of the resonance line observed in Figure 1 C. Thirdly, their very small thickness allows one to drive their magnetization out of equilibrium not only by microwave fields, as in FMR, but also by spin currents at their interface with a metal with strong spin-orbit coupling.

In 2010, it was indeed shown the evidence of a transfer of angular momentum between a YIG layer and an adjacent platinum film [31]. This transfer allows a direct conversion of an electrical current in the platinum film to a spin wave in YIG and vice versa via spin Hall effect and inverse spin Hall effect. Subsequent experimental works showed that it is possible to control the relaxation of spin wave modes in YIG by means of an electrical current injected in an adjacent platinum layer thanks to spin transfer torque [32]. When this torque, of spin-orbit origin, compensates the natural damping in the electrically insulating YIG layer, its magnetization enters an auto-oscillation regime [25] (Figure 1 D), similarly to fully metallic spin torque oscillators [33, 34]. It was also demonstrated that the propagation length of SWs excited by a standard microwave antenna could be controlled to a large extent using this spin-orbit torque (SOT) in YIG/Pt waveguides [26] (Figure 1 E).

However, undesired nonlinear effects strongly affect the magnetization dynamics in these YIG/Pt hybrid devices. As a matter of fact, the sudden drops observed beyond certain excitation thresholds in the amplitude of the

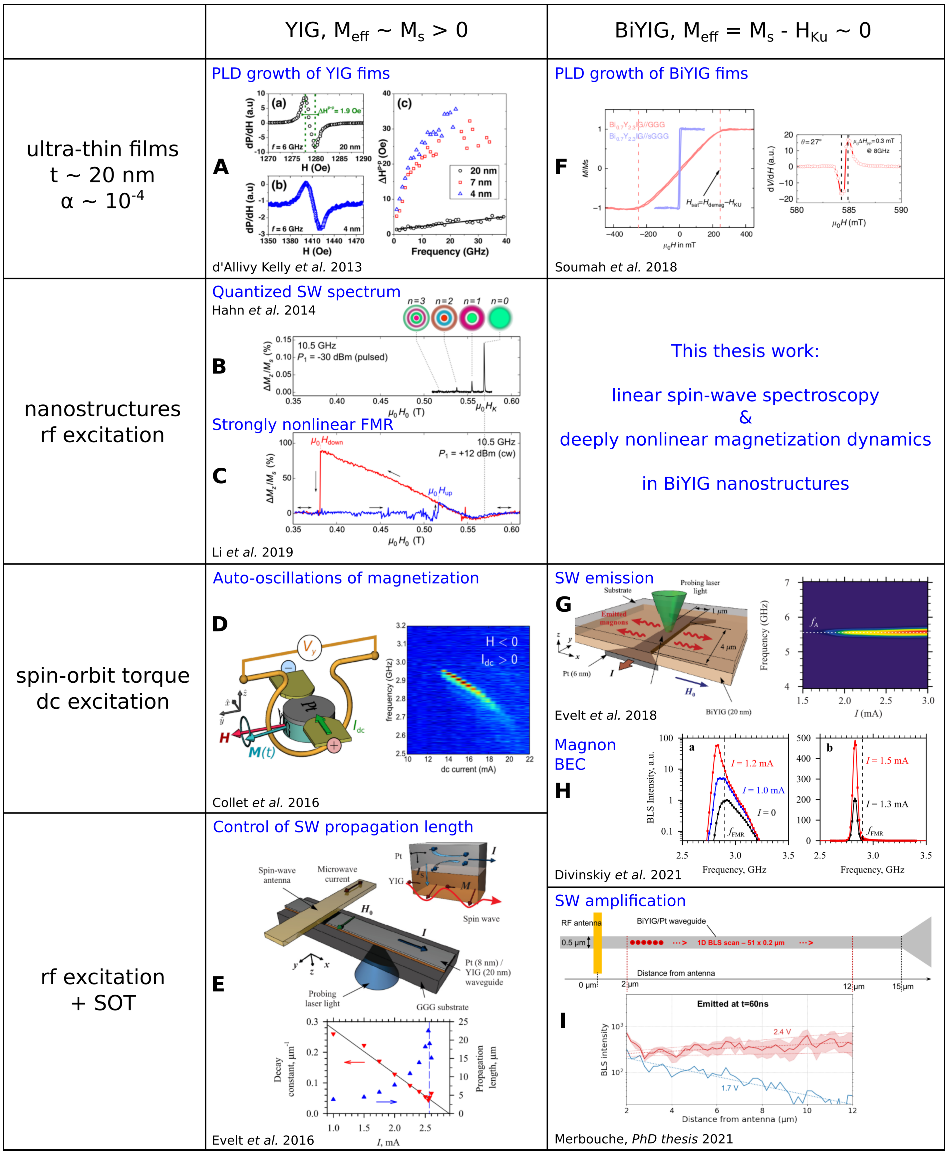

Figure 1: Context of this thesis work. Illustrations of panels A to I are respectively taken from [19, 22, 25, 26, 27, 28, 29, 30].

auto-oscillating mode (Figure 1 D) and of the SW propagation length (Figure 1 E) are due to nonlinear interactions with other SW modes [35]. The underlying physical mechanism is very similar to the Suhl threshold [12] observed in standard FMR experiments on bulk YIG samples in the 1950s [36], where SW instabilities redistributing the energy among different modes occur beyond a certain excitation amplitude set by the damping. These nonlinear couplings between SW modes are known to be stronger if the magnetization precession is elliptical, due to the generation of harmonics of the fundamental FMR frequency [2], and in large samples, due to the large number of available SW modes. It was recently shown that using out-of-plane magnetized YIG nanodisks, where the magnetization precession is purely circular and the fundamental mode is lying at the bottom of the discrete SW spectrum, these nonlinear saturation effects can be postponed and very large angles of coherent precession can be excited by FMR [22] (Figure 1 C) [1]. It was also recently demonstrated that the associated nonlinear damping could be controlled by tuning the effective demagnetization field, therefore the nonlinear frequency shift, to nearly zero in metallic spin-orbit torque devices, leading to circular precession for in-plane magnetized devices and greatly enhanced characteristics of the pure spin current driven dynamics [37].

In this context, the growth of ultra-thin films of Bismuth doped YIG (BiYIG) with tunable perpendicular magnetic anisotropy (PMA) while preserving a damping value in the $10^{-4} - 10^{-3}$ by the group of Abdelmadjid Anane at Unité Mixte de Physique CNRS/Thales in 2018 [27] (Figure 1 F) has opened interesting perspectives. This thesis work is part of a concerted effort between the partners of the ANR project Maestro "Magnon excitation in the strong out-of-equilibrium regime", whose aim is to investigate and control the nonlinear regimes of magnetization dynamics in devices based on thin BiYIG films with nearly vanishing effective magnetization, i.e., a uniaxial anisotropy almost compensating their shape anisotropy. Different means to excite the magnetization dynamics have been investigated in this project :

i) standard harmonic (rf) excitation, where selection rules impose the frequency and spatial symmetry of the primarily excited SWs [38].

ii) static (dc) spin-orbit torque (SOT) excitation, which enhances/suppresses all SW modes (no selection rule) [39].

iii) the combination of the former two, i.e., stimulated amplification by dc SOT of rf excited SWs [30].

Shortly after the growth of these compensated BiYIG thin films, improved characteristics of spin wave emission by SOT were indeed demonstrated by microfocused Brillouin light scattering (BLS) [28], as shown in Figure 1 G.

---

[1] It eventually decays into SW instabilities at very large amplitude.

Here, the auto-oscillation frequency remains constant and their amplitude keeps growing with the dc current injected in Pt, in contrast to the previous case of YIG, where the red shift of frequency was accompanied by a disappearance of the auto-oscillation signal (Figure 1 D). These first very positive results motivated further work related to dc SOT excitation (ii) and a magnon Bose Einstein condensate driven by pure spin currents was eventually observed on a very similar system a few years later [29] (Figure 1 H).

The combination of rf excitation of SWs and dc SOT to control their relaxation time (iii) was part of the PhD work of Hugo Merbouche under the supervision of Abdelmadjid Anane at CNRS/Thales, in parallel to the thesis presented in the current manuscript. Figure 1 I highlights the principal result obtained in 2021, namely, the SOT enables *amplification* of propagating SWs in a BiYIG/Pt hybrid waveguide.

The investigation of deeply nonlinear regimes of magnetization dynamics in BiYIG nanostructures driven by a harmonic microwave field (i), i.e., by conventional FMR, is the main purpose of the current thesis. Its initial motivation was to combine both nanostructuration, leading to quantization of the SW mode spectrum, and compensation of magnetization enabled by Bi doping, leading to vanishing nonlinear frequency shift, to obtain highly coherent, single mode rf driven magnetization dynamics by increasing the excitation amplitude at constant frequency, and to study the influence of magnetic parameters and finite size effects on the deeply nonlinear dynamics. Moreover, it is important to evaluate the impact of nanostructuration on the magnetic properties of the garnet film (in particular damping and magnetic anisotropies, which are famous to be sensitive on defects [40], ion irradiation [41] and interfaces with other materials [20, 28]), therefore another objective of this thesis is to perform a detailed FMR spectroscopy study of SW modes in BiYIG nanostructures.

0.3 Outline of the manuscript

I will start by presenting some reminders on micromagnetism and the theoretical basis of magnetization dynamics in chapters **1** and **2**. In particular, at the end of chapter **2**, I will focus on different aspects of nonlinear magnetization dynamics.

In chapter **3** I will present the experimental technique used during this thesis : the magnetic resonance force microscopy (MRFM). I will explain the foundation of the mechanical detection principle on which it is based. I will specify the characteristics of some key elements of the setup. I will also give a detailed presentation of the sample, which consists of BiYIG disks with diameters ranging from 200 nm to 1000 nm.

In the following 2 chapters, I will present all the experimental results in the perpendicular configuration of the applied static field. In chapter **4**, I will present the SW spectroscopy of the nanodisks in the linear regime. In particular, thanks to the comparison of experimental results to micromagnetic simulations, it will be demonstrated that the nanopatterning affects the magnetic properties at the periphery of the disks.

In chapter **5** I will present the results of the nonlinear regime when the amplitude of the rf pumping field is increased. In particular, we will uncover a regime of auto-oscillation instabilities, which takes place in the largest nanodisks beyond a relatively low threshold. Based on experimental results and micromagnetic simulations, we will analyse and classify the different regimes of nonlinear dynamics that can occur in BiYIG nanodisks.

In chapter **6** I will briefly present the results obtained for an in-plane applied field by highlighting the main differences with the perpendicular configuration such as the change of the sign of the nonlinear frequency shift and the breaking of the cylindrical symmetry. In particular, we will see that it is possible to reach very large amplitude of coherent magnetization precession in the smallest disks.

I will conclude by summarizing the main results of this work and presenting some perspectives.

Chapter 1

Magnetic ground state

"Magnetism is one of the six fundamental forces of the universe, with the other five being gravity, duct tape, whining, remote control, and the force that pulls dogs toward the groins of strangers."

Dave Barry

Contents

In this chapter, we introduce micromagnetism by reminding the main magnetic interactions involved. Then we apply it to the simple case of an infinite thin film magnetized by a magnetic field making a certain angle with its normal in order to find its equilibrium state. We take advantage of this to define the effective magnetization M_{eff} in the case of a film with a uniaxial perpendicular magnetic anisotropy (PMA).

1.1 Magnetic moment

The magnetism of matter comes from the magnetic moment of the constituent elements, in particular the electrons. This magnetic moment is due to the movement of electrons and has two components. An orbital angular momentum from the movement of the electron in the electron cloud and an intrinsic angular momentum or spin due to the rotation of the electron on itself. The existence of different types of interactions between the magnetic moments is at the origin of different magnetic properties of materials. One will thus has dia-, para-, ferro-, ferri- or antiferromagnetic materials. Among all the interactions, the exchange interaction, which is a short-range interaction of quantum origin, coming from the electronic orbitals overlap, plays a major role. It is indeed responsible for the alignment of the magnetic moments in a ferromagnet. To study the dynamics of magnetic moments in a ferromagnet, we define the density of magnetic moments per unit volume or magnetization :

$$\boldsymbol{M} = \frac{\sum_V \boldsymbol{m}(\boldsymbol{r'})}{V} \tag{1.1}$$

where $\sum_V \boldsymbol{m}(\boldsymbol{r'})$ is the magnetic moment of a volume V [2], $\boldsymbol{m}(\boldsymbol{r'})$ being the local magnetic moment in $\boldsymbol{r'} \in V$. For the sizes of the magnetic structures we will study (typically a few hundred nm), the magnetization $\boldsymbol{M}(\boldsymbol{r})$ is a continuous function. Micromagnetism is the part of physics that focuses on predicting the behavior of magnetization at sub-micrometer length scales.

1.2 Magnetic interactions

A ferromagnetic material is characterized by a certain magnetic order below a Curie temperature T_c. At a constant temperature lower than T_c, the magnetization is therefore constant and equal to $M_s \neq 0$. The goal of micromagnetism is then to determine the spatial distribution of the magnetization within the material. This distribution is obviously the one that minimizes the total energy $\in_t$ of the system, which corresponds to the sum of all the magnetic interactions. If E is the local energy density, then the two quantities are related by :

$$\in_t = \int_V E(\boldsymbol{r}) d\boldsymbol{r}. \tag{1.2}$$

This local energy density is at the origin of a total magnetic field felt by a magnetic moment at the point $\boldsymbol{r}$; it is called the *effective field* and is given by :

$$\boldsymbol{H}_{eff}(\boldsymbol{r}) = -\frac{1}{\mu_0}\frac{\partial E(\boldsymbol{r})}{\partial \boldsymbol{M}} \tag{1.3}$$

where $\mu_0 = 4\pi.10^{-7}$ kg m A^{-2} s^{-2} is the vacuum permeability. It contains all the energy contributions of the system.

Let us now consider a ferromagnet of magnetization $\boldsymbol{M}$ and express the different magnetic energy densities.

1.2.1 Zeeman

It comes from the application of an external field $\boldsymbol{H}$. The corresponding energy density is written :

$$E_z = -\mu_0 \boldsymbol{M}.\boldsymbol{H} \tag{1.4}$$

So, the Zeeman interaction tends to align $\boldsymbol{M}$ with $\boldsymbol{H}$.

1.2.2 Exchange

It is a short range local interaction between magnetic moments that tends to align them. We can therefore think that any non-uniformity will increase the exchange energy. It is given by :

$$E_{ex} = \frac{A}{M_s^2}(\nabla.\boldsymbol{M})^2 \tag{1.5}$$

where ∇ is the vector nabla[1] and A is a constant called exchange constant and depends on the material. It is related to the exchange length λ_{ex} by the formula :

$$\lambda_{ex} = \frac{1}{M_s}\sqrt{\frac{2A}{\mu_0}}. \tag{1.6}$$

This exchange length is typically of the order of few nanometers [42].

1.2.3 Dipolar

It is the energy associated with the long range dipolar interaction between the individual magnetic moments. It depends on the relative positions of the moments in interaction. So it is an anisotropic interaction. It is given by :

$$E_d = -\frac{\mu_0}{2}\boldsymbol{M}.\boldsymbol{H}_d \tag{1.7}$$

Where $\boldsymbol{H}_d$ is the demagnetizing field of the studied material. For an ellipsoidal sample, it can be shown that it is uniform and depends on the shape of the sample through the demagnetizing factors N_x, N_y, N_z [43]. E_d can then be written as :

$$E_d = \frac{\mu_0}{2}(N_x M_x^2 + N_y M_y^2 + N_z M_z^2) \tag{1.8}$$

in the case of uniform magnetization, with

$$N_x + N_y + N_z = 1. \tag{1.9}$$

For an ellipsoid of revolution of dimensions L_x, L_y and L_z and symmetry axis z ($L_x = L_y$), $N_x = N_y = N_\perp = \frac{1-N_z}{2}$;

- if $L_z < L_{x,y}$, $N_z > N_\perp$ and it is called an oblate (flattened) ellipsoid.

---

[1] The vector nabla is defined as $\nabla.\mathbf{V} = \frac{\partial V_x}{\partial x} + \frac{\partial V_y}{\partial y} + \frac{\partial V_z}{\partial z}$ in a cartesian coordinate system (x, y, z).

- if $L_z > L_{x,y}$, $N_z < N_\perp$ and it is called a prolate (elongated) ellipsoid.

In the absence of an applied magnetic field, this energy is responsible for the formation of magnetic domains in ferromagnetic materials.

1.2.4 Anisotropies

There is an interaction between the spin angular momentum $\boldsymbol{S}$ of the electrons responsible for magnetism and their orbital angular momentum $\boldsymbol{L}$: this is called spin-orbit coupling. In a crystal, this interaction will favor the alignment of the magnetization with the main axes of the crystal lattice. We then speak of magnetocrystalline anisotropy. There are several, the most common being uniaxial anisotropy and cubic anisotropy. The energy density corresponding to the uniaxial anisotropy is written:

$$E_u = K_1 sin^2\theta + K_2 sin^4\theta + ... \tag{1.10}$$

where K_1 and K_2 are the uniaxial anisotropy constants of the first and second order respectively, and θ is the angle between the magnetization and the anisotropy axis. The anisotropy axis is an easy axis if $K_1 > 0$ and a hard axis if $K_1 < 0$. In the latter case, there is an easy plane, the plane perpendicular to the anisotropy axis.

For the case of thin films, the anisotropic shape of the film gives rise to a demagnetization energy term that favors in-plane magnetization. It is given by equation (1.8) in which we use the thin film parameters $N_x = N_y = 0$ and $N_z = 1$. And taking the maximum energy, corresponding to the magnetization along z, $M_z = M_s$ and this term also called shape anisotropy is written :

$$K_{shape} = \frac{\mu_0 M_s^2}{2} \tag{1.11}$$

For our study we will need out-of-plane magnetic anisotropy in the thin films. To do this, it is then necessary to compensate this shape anisotropy. For the case of YIG thin films, $K_{shape} \approx 12$ kJ.m^{-3} and it is then a very important contribution to the magnetic energy for YIG thin films. To induce perpendicular magnetic anisotropy (PMA) in such films, an additional anisotropy term is required. This can be achieved by ionic doping, for example Bismuth or Thulium doping, which produces a growth induced anisotropy K_{growth} [23, 44]. Interfacial PMA can also be achieved in ultra-thin multilayer structures such as CoFeB/MgO [45] or Co/Ni [46].

In our case we will use Bismuth doping. Since YIG has a cubic structure, it also has a cubic magnetocrystalline anisotropy. But in our BiYIG sample, we will have PMA about 20 times larger than the cubic anisotropy [44]. For this reason we will neglect the cubic anisotropy.

NB : All the formula are given in the SI units system. M_s is in A/m, $\mu_0 M_s$ in T, A in J/m, the anisotropy constants K_i, i=1,2... in J/m^3.

1.3 Equilibrium state

Ultimately, the equilibrium configuration of a ferromagnetic material will be given by the balance between all energy contributions; in other words, the equilibrium magnetic distribution is the one which minimizes the total energy of the system. Let us consider the simple case of an infinite thin film and the cartesian coordinate system (x,y,z) such that the film is in the (x,y) plane. The applied static field $\boldsymbol{H}$ makes an angle θ_0 with the z axis, normal to the film. Let's assume that the film has the z axis as its uniaxial anisotropy axis with the anisotropy constant K_u. Let us denote by (M_x, M_y, M_z) the coordinates of the magnetization $\boldsymbol{M}$ of the film, with a modulus M_s. Following the application of the magnetic field, $\boldsymbol{M}$ is oriented so as to form an angle θ with the z axis and its projection in the (x,y) plane makes an angle φ with the x axis (see Figure 1.1). Let's assume that $\boldsymbol{H}$ is in the (y,z) plane. It will be the same for $\boldsymbol{M}$, so we will have $\varphi = \frac{\pi}{2}$.

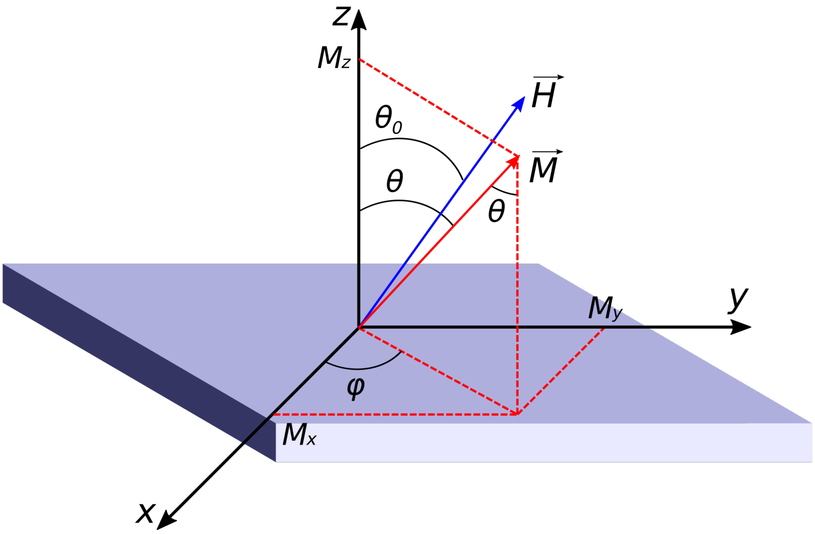

Figure 1.1: Magnetized thin film.

The coordinates of $\boldsymbol{M}$ are :

$$\begin{cases} M_x = M_s \sin\theta \cos\varphi = 0 \\ M_y = M_s \sin\theta \sin\varphi = M_s \sin\theta \\ M_z = M_s \cos\theta \end{cases} \tag{1.12}$$

The equilibrium angle θ_{eq} of the magnetization is the one which minimizes the total magnetic energy density E_t of the system. E_t is given by :

$$E_t = -\mu_0 M_s H \cos(\theta - \theta_0) + K_{shape} \cos^2\theta + K_u \sin^2\theta. \tag{1.13}$$

We check that the demagnetization energy favors the in-plane magnetization while the uniaxial anisotropy favors the alignement with the z axis. By replacing $\sin^2\theta$ with $1 - \cos^2\theta$, the equation becomes :

$$E_t = -\mu_0 M_s H \cos(\theta - \theta_0) + (\frac{\mu_0 M_s^2}{2} - K_u) \cos^2\theta + K_u \tag{1.14}$$

which can be written :

$$E_t = -\mu_0 M_s H \cos(\theta - \theta_0) + \frac{\mu_0 M_s}{2}(M_s - \frac{2K_u}{\mu_0 M_s}) \cos^2\theta + K_u. \tag{1.15}$$

It becomes :

$$E_t = -\mu_0 M_s H \cos(\theta - \theta_0) + \frac{\mu_0 M_s M_{eff}}{2} \cos^2\theta + K_u \tag{1.16}$$

where we define the *effective magnetization* M_{eff} of the thin film :

$$M_{eff} = M_s - H_u \tag{1.17}$$

and $H_u = \frac{2K_u}{\mu_0 M_s}$ is the uniaxial anisotropy field associated with the PMA[2]. θ_{eq} satisfies the equation :

$$\frac{\partial E_t}{\partial \theta}(\theta_{eq}) = 0 \tag{1.18}$$

i.e :

$$H \sin(\theta_{eq} - \theta_0) = M_{eff} \sin\theta_{eq} \cos\theta_{eq} \tag{1.19}$$

For simple cases, the equilibrium state is trivial.

- Case $M_{eff} > 0$

---

[2] We will also call it the PMA field.

1. For an applied field perpendicular to the thin film : $\theta_0 = 0 \Longrightarrow \sin\theta_{eq}(H - M_{eff}\cos\theta_{eq}) = 0 \Longrightarrow \theta_{eq} = 0$ or $\cos\theta_{eq} = \frac{H}{M_{eff}}$
    - (a) if $H < M_{eff}$, $\theta_{eq} = \arccos\frac{H}{M_{eff}}$: the magnetization lies between the film plane and the normal to the film.
    - (b) if $H > M_{eff}$, $\theta_{eq} = 0 = \theta_0$: the magnetization aligns with H.
2. For an in-plane applied field : $\theta_0 = \frac{\pi}{2}, \theta_{eq} = \frac{\pi}{2}\ \forall\ H$. The magnetization aligns with H.

- Case $M_{eff} = 0$

  $\theta_{eq} = \theta_0$. The magnetization aligns with H.

- Case $M_{eff} < 0$

1. For an applied field perpendicular to the thin film : $\theta_0 = 0$, $\theta_{eq} = 0\ \forall\ H$. The magnetization aligns with H.
2. For an in-plane applied field : $\theta_0 = \frac{\pi}{2}$
    - (a) if $H < -M_{eff}$, $\theta_{eq} = \arcsin\left(\frac{-H}{M_{eff}}\right)$: the magnetization lies between the film plane and the normal to the film.
    - (b) if $H > -M_{eff}$, $\theta_{eq} = \frac{\pi}{2}$: the magnetization aligns with H.

In the absence of an applied field or in the case of a weak field, the magnetization may not be saturated. To minimize the total energy, the material can divide itself into magnetic domains, regions of uniform magnetization separated by domain walls. In particular conditions or in the case of confined structures, even more complex configurations can be formed. We can mention among others vortices, skyrmions and spiral helical structures [47] which involve other types of magnetic interaction such as the Dzyaloshinskii-Moriya interaction known as the antisymmetric exchange. Due to the complex profile of these textures, it is necessary to perform advanced analytical methods or micromagnetic simulations in order to execute a complete analysis.

1.4 Conclusion

We have recalled and described the expressions of the main magnetic interactions that we will use later. We have studied the simple case of an infinite thin film with uniaxial anisotropy. We find that the total energy in this case no longer depends only on the magnetization but on an effective magnetization M_{eff} which also takes into account the uniaxial anisotropy. We found that the equilibrium state of such a film depends on the sign of M_{eff}. For example, for $M_{eff} < 0$, the magnetization is perpendicular to the film for a small perpendicular applied field. Thus, by playing on M_{eff} sign, it is possible to make the equilibrium state of a thin film out of the plane. We will see that M_{eff} will turn out to be crucial in the analysis of the experimental results.

Chapter 2

Magnetization dynamics

"No one can whistle a symphony. It takes a whole orchestra to play it."

H.E. Luccock

Contents

After the previous chapter, in which the static equilibrium state of a ferromagnet was determined, we are now interested in the motion of the magnetization in case of deviations around this equilibrium state. We show that for small deviations, it is a precessional motion, whose frequency is given by the well-known Kittel formula. We describe the ferromagnetic relaxation and study the dynamics of the magnetization under the effect of a small microwave field. Then we introduce the eigen modes of the magnetization dynamics in a normally magnetized thin disk, using the general theory of linear spin wave spectrum. Then we present some nonlinear effects that appear when one increases the microwave field intensity, with a focus on the well known foldover effect. Finally we present a bibliographic review of some nonlinear effects and phenomena found in the study of magnetization dynamics.

2.1 Larmor precession

As a magnetic moment in a magnetic field, in the presence of the effective field $\boldsymbol{H}_{eff}$, the magnetization $\boldsymbol{M}$ experiences a torque -$\gamma\mu_0\boldsymbol{M}$ x $\boldsymbol{H}_{eff}$. In the case of a small deviation of the magnetization and in the absence of damping, the magnetization will describe a precession motion due to this conservative torque. The magnetization dynamics is therefore described by the well known Landau-Lifshitz equation [48] :

$$\frac{\partial \boldsymbol{M}}{\partial t} = -\gamma\mu_0 \boldsymbol{M} \times \boldsymbol{H}_{eff} \tag{2.1}$$

where γ (> 0) is the opposite of the gyromagnetic ratio in the considered material, generally close to that of the free electron; $\gamma_{e^-} = \frac{e}{m}$ (< 0). The equation (1.3) combined with the expressions of the different energy contributions shows that the effective field depends in a very complicated way on the magnetization. So equation (2.1) is nonlinear. Let's consider the simplest case where the magnetization $\boldsymbol{M}$ is due to a single magnetic moment placed in a magnetic field $\boldsymbol{H}$. In this case, the only contribution to the effective field is the Zeeman interaction and $\boldsymbol{H}_{eff} = \boldsymbol{H}$. Within the limit of small oscillations, $\boldsymbol{M}$ can then be decomposed into a static part $\boldsymbol{M}_{eq}$ aligned with $\boldsymbol{H}$ and a very small dynamic part $\boldsymbol{m}$(t) :

$$\boldsymbol{M} = \boldsymbol{M}_{eq} + \boldsymbol{m}(t) \tag{2.2}$$

The equation (2.1) becomes :

$$\frac{\partial \boldsymbol{M}}{\partial t} = -\gamma\mu_0 \boldsymbol{M} \times \boldsymbol{H} \tag{2.3}$$

and noting that $\frac{\partial \boldsymbol{M}_{eq}}{\partial t} = \boldsymbol{0}$ and $\boldsymbol{M}_{eq} \times \boldsymbol{H} = \boldsymbol{0}$, we find :

$$\frac{\partial \boldsymbol{m}}{\partial t} = -\gamma\mu_0 \boldsymbol{m} \times \boldsymbol{H} \tag{2.4}$$

The solutions are exponential functions of the form $\boldsymbol{m} = \boldsymbol{m}_0 e^{i\omega t}$ where :

$$\omega = \omega_H = \gamma\mu_0 H \tag{2.5}$$

is called the Larmor frequency. Therefore, the magnetization $\boldsymbol{M}$ will precess with this frequency around the direction of the applied static field. The value of the gyromagnetic ratio of the free electron $\gamma/2\pi = 28$ GHz/T yields precession frequencies in the GHz range for usual fields in the Tesla range.

2.2 Ferromagnetic resonance

In a ferromagnetic material, we no longer have only the Zeeman interaction as in the previous case, but the whole set of interactions described in Chapter 1. Therefore, $\boldsymbol{M}$ will no longer precess at the Larmor frequency ω_H. In order to solve the new dynamics induced by taking into account all the interactions, let us decompose the effective field and the magnetization into two components, one static $\boldsymbol{H}_{eff}^{eq}$, $\boldsymbol{M}^{eq}$ and the other dynamic $\boldsymbol{h}_{eff}(t)$, $\boldsymbol{m}$(t) :

$$\begin{aligned} \boldsymbol{H}_{eff}(t) &= \boldsymbol{H}_{eff}^{eq} + \boldsymbol{h}_{eff}(t) \\ \boldsymbol{M}(t) &= \boldsymbol{M}^{eq} + \boldsymbol{m}(t) \end{aligned} \tag{2.6}$$

The Landau-Lifshitz equation becomes:

$$\frac{\partial \boldsymbol{M}}{\partial t} = -\gamma\mu_0 [\boldsymbol{M}^{eq} + \boldsymbol{m}(t)] \times [\boldsymbol{H}_{eff}^{eq} + \boldsymbol{h}_{eff}(t)] \tag{2.7}$$

If $|\boldsymbol{m}(t)|$ and $|\boldsymbol{h}_{eff}(t)|$ are much smaller than $|\boldsymbol{M}^{eq}|$ ($\approx M_s$) and $|\boldsymbol{H}_{eff}^{eq}|$ respectively and since $\boldsymbol{H}_{eff}^{eq} \parallel \boldsymbol{M}^{eq}$, the equation is then written at the first order :

$$\frac{\partial \boldsymbol{m}}{\partial t} = -\gamma\mu_0 [\boldsymbol{m}(t) \times H_{eff}^{eq}.\boldsymbol{u} + M_s.\boldsymbol{u} \times \boldsymbol{h}_{eff}(t)] \tag{2.8}$$

where $\boldsymbol{u}$ is the unit vector such as $\boldsymbol{M} \approx M_s.\boldsymbol{u}$

In general, for a sample of any shape, the demagnetizing field is not uniform and the analytical analysis is complicated (cf section 2.4). But if the sample is an ellipsoid whose principal axis are parallel to x, y and z axis, placed in a magnetic field $\boldsymbol{H}$, for a uniform magnetization distribution, the demagnetizing field is uniform and can be written :

$$\boldsymbol{H}_d = -\overline{N}.\boldsymbol{M} \tag{2.9}$$

where the demagnetizing tensor can be expressed as :

$$\overline{N} = \begin{bmatrix} N_x & 0 & 0 \\ 0 & N_y & 0 \\ 0 & 0 & N_z \end{bmatrix} \tag{2.10}$$

Let's assume that the sample has the z axis as the uniaxial anisotropy axis with the anisotropy constant K_u. $\boldsymbol{m}$ will describe a precession around the static field axis. So we can look for solutions under the form $\boldsymbol{m}(\mathrm{t}) = \boldsymbol{m}_0(t)e^{i\omega t}$ where $\boldsymbol{m}_0$ and ω are unknowns. Let us consider the two cases of the static field applied along the z axis or in the xy plane.

2.2.1 Static field along the anisotropy axis z

Here, $\boldsymbol{m}$ describes a precession in the xy plane, around the z axis. In the simplest case of *uniform* precession, the exchange field is zero and the effective field will consist only of the static field, the dipolar field and the uniaxial anisotropy field $\boldsymbol{H}_u$:

$$\boldsymbol{H}_{eff}(t) = \boldsymbol{H} + \boldsymbol{H}_d + \boldsymbol{H}_u \tag{2.11}$$

which leads to :

$$\boldsymbol{H}_{eff}(t) = \begin{pmatrix} -N_x m_x \\ -N_y m_y \\ H - N_z M_s + H_u \end{pmatrix} \tag{2.12}$$

Combining this result with the first relation of the equation (2.6), we can write :

$$\boldsymbol{H}^{eq}_{eff} = \begin{pmatrix} 0 \\ 0 \\ H - N_z M_s + H_u \end{pmatrix} \tag{2.13}$$

and

$$\boldsymbol{h}_{eff}(t) = \begin{pmatrix} -N_x m_x \\ -N_y m_y \\ 0 \end{pmatrix} \tag{2.14}$$

Replacing the different expressions in equation (2.8), we obtain :

$$\begin{aligned} i\omega m_x + \gamma\mu_0[H - (N_z - N_y)M_s + H_u]m_y = 0 \\ -\gamma\mu_0[H - (N_z - N_x)M_s + H_u] + i\omega m_y = 0 \end{aligned} \tag{2.15}$$

Let's take $\boldsymbol{m}_0 = \begin{pmatrix} m_x^0 \\ m_y^0 \end{pmatrix}$. This system can be rewritten :

$$\begin{pmatrix} i\omega & \omega_y \\ -\omega_x & i\omega \end{pmatrix} \begin{pmatrix} m_x^0 \\ m_y^0 \end{pmatrix} = \begin{pmatrix} 0 \\ 0 \end{pmatrix} \tag{2.16}$$

where $\omega_{x,y} = \gamma\mu_0[H - (N_z - N_{x,y})M_s + H_u]$. For an ellipsoid of revolution, $N_x = N_y = N_\perp$ and $\omega_x = \omega_y = \gamma\mu_0[H - (N_z - N_\perp)M_s + H_u]$. The condition of existence of solutions writes :

$$\omega^2 = \omega_x\omega_y = \gamma^2\mu_0^2[H - (N_z - N_\perp)M_s + H_u]^2. \tag{2.17}$$

Equation (2.17) is a particular case of the more general Kittel formula [49] which gives the resonance frequency of the main mode of a ferromagnet also known as the Kittel mode or the FMR mode. It clearly depends on the shape of the sample through demagnetizing factors. In this case of an ellipsoid of revolution, the frequency can be written :

$$\omega = \gamma\mu_0(H - H_K) \tag{2.18}$$

where $H_K = (N_z - N_\perp)M_s - H_u$ is a characteristic field of the ellipsoid on which the position of the Kittel mode will depend. Note that this resonance frequency is defined $\forall\ H$ when $H_K < 0$ i.e for $H > 0$ and for $H > H_K$ when $H_K > 0$.

For a thin film, $N_\perp = 0$, $N_z = 1$ and the equation becomes :

$$\omega^\perp = \gamma\mu_0(H - M_{eff}) \tag{2.19}$$

where $M_{eff} = M_s - H_u$ is the effective magnetization of the thin film defined in section 1.3, with $H_u = \frac{2K_u}{\mu_0 M_s}$. Another simple example is the case of the sphere where $N_x = N_y = N_z = 1/3$, leading to $\omega = \gamma\mu_0(H + H_u)$.

2.2.2 Static field applied in-plane

Let's assume that the field is applied along the x axis now and is strong enough to saturate the magnetization. Here, $\boldsymbol{m}$ describes a precession in the yz plane, around the x axis. For a uniform precession we consider only the static field, the dipolar field and the uniaxial anisotropy field. Now, the effective field is :

$$\boldsymbol{H}_{eff}(t) = \begin{pmatrix} H - N_x M_s \\ -N_y m_y \\ -N_z m_z + \frac{H_u}{M_s} m_z \end{pmatrix} \tag{2.20}$$

which gives :

$$\boldsymbol{H}_{eff}^{eq} = \begin{pmatrix} H - N_x M_s \\ 0 \\ 0 \end{pmatrix} \tag{2.21}$$

and

$$\boldsymbol{h}_{eff}(t) = \begin{pmatrix} 0 \\ -N_y m_y \\ -N_z m_z + \frac{H_u}{M_s} m_z \end{pmatrix} \tag{2.22}$$

Writing $\boldsymbol{m}_0$ as previously with the coordinates m_y^0 and m_z^0 in this case, we get an equation similar to (2.16) with $\omega_y = \gamma\mu_0[H - (N_y - N_x)M_s]$ and $\omega_z = \gamma\mu_0[H + (N_z - N_x)M_s - H_u]$. For an ellipsoid of revolution, $N_x = N_y = N_\perp$ and the condition of existence of solutions writes :

$$\omega^2 = \omega_y\omega_z = \gamma^2\mu_0^2 H[H + (N_z - N_\perp)M_s - H_u]. \tag{2.23}$$

In this case we find:

$$\omega = \gamma\mu_0\sqrt{H(H + H_K)}. \tag{2.24}$$

Note that this resonance frequency is defined $\forall\ H$ when $H_K > 0$ i.e for $H > 0$ and for $H > -H_K$ when $H_K < 0$. For a thin film, $N_\perp = 0$, $N_z = 1$ and the equation becomes :

$$\omega^{||} = \gamma\mu_0\sqrt{H(H + M_{eff})} \tag{2.25}$$

Thus, as shown in Figure 2.1, the direction of application of the static field and the sign of M_{eff} (adjustable in YIG films for example thanks to Bismuth doping) allow to modify the dispersion relation of the FMR. These elements will also play a key role in the nonlinear regime.

NB: In equations (2.19) and (2.25), the measurement of the graph of the resonance frequency vs field only allows the extraction of M_{eff} and γ. To extract H_u and M_s independently, the measurement of magnetization M_s is required (for example by SQUID magnetometry).

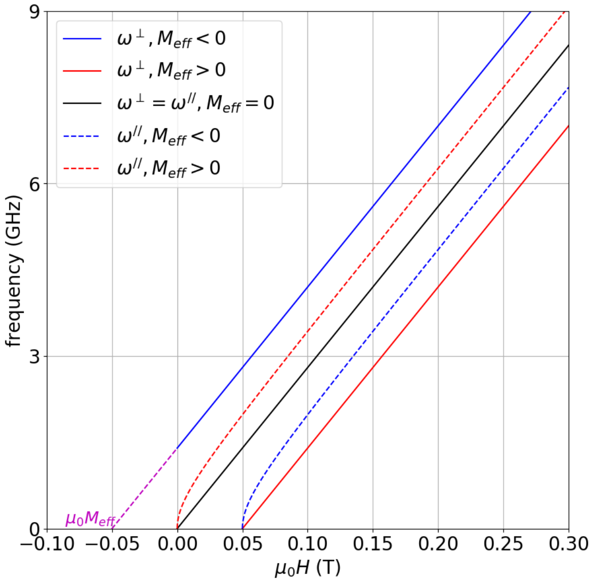

Figure 2.1: Representation of the resonance frequency vs field variations of a thin film in the two configurations of the in-plane and perpendicular static field for the two signs of M_{eff}. They correspond to equations (2.19) and (2.25). The parameters used are $\gamma/2\pi = 28$ GHz/T and $\mu_0 M_{eff} = +50$ and -50 mT.

2.3 Ferromagnetic relaxation and FMR excitation

Like any real physical system, this precession of the magnetization is damped and it will return to its equilibrium state, along the effective field. This damping comes from the coupling of the spin magnetic system to the degrees of freedom carrying angular momentum in solids : phonons and conduction electrons in the case of a metal. It results in a flow of energy to the external environment.

2.3.1 LLG equation

These relaxation processes can be expressed phenomenologically as a damping torque in the Landau-Lifshitz equation, analogous to a viscous friction term [50]. It becomes the Landau-Lifshitz-Gilbert (LLG) equation :

$$\frac{\partial \boldsymbol{M}}{\partial t} = -\gamma \mu_0 \boldsymbol{M} \times \boldsymbol{H}_{eff} + \frac{\alpha}{M_s} \boldsymbol{M} \times \frac{\partial \boldsymbol{M}}{\partial t} \tag{2.26}$$

where α is a dimensionless positive parameter, the Gilbert damping constant, which describes the relaxation. It depends on the material and its value typically ranges between 10^{-2} in metallic thin films (Ni, Fe, Co, Py) to about 10^{-4} in YIG films. The magnetization returns to its equilibrium state by spiraling around the effective field in a characteristic time of the order of $(\alpha\gamma H_{eff})^{-1}$, which is also the characteristic time of energy dissipation.

2.3.2 FMR excitation by a small microwave field

Let us consider a ferromagnetic system of magnetization $\boldsymbol{M}$. To study the dynamics of the magnetization, we apply a microwave field $\boldsymbol{h}$ at a frequency ω. The response of the system to the field $\boldsymbol{h}$ is described by the magnetic susceptibility χ. It is the coefficient between the complex amplitudes of the transverse magnetization $\overline{M_t}$ and the microwave field $\overline{h}$; $\overline{M_t} = \chi\overline{h}$. It is given by [2]:

$$\chi(\omega) = \frac{\gamma M_s}{(\omega_0 - \omega) - i\alpha\omega} \tag{2.27}$$

where ω_0 is the eigenfrequency of the system given by the relation (2.17). The modulus of $\chi(\omega)$ is maximal at $\omega = \omega_0$, i.e. at resonance; χ then becomes pure imaginary and $M_t = \chi^{''}(\omega_0)h$. This transverse component is accompanied

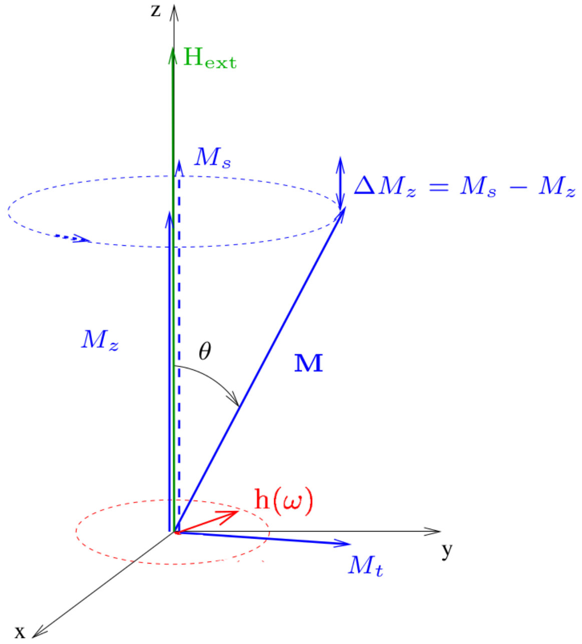

Figure 2.2: Schematic representation of the excitation of a magnetic resonance. A small microwave field h of frequency ω opens a precession angle θ of the magnetization around the static field H_{ext}, inducing a decrease of the longitudinal component M_z of the magnetization. The angle of equilibrium reached in steady state is determined by the competition between the driving torque due to the microwave field and the damping torque, which tends to bring $\boldsymbol{M}$ along the effective field, assumed here parallel to the static field.

by the opening of a precession angle θ of the magnetization with respect to the effective field (see Figure 2.2) which is determined by the balance of the driving torque created by the field $\boldsymbol{h}$ and the damping torque, in opposition to the motion. If M_z is the longitudinal component of the magnetization, i.e. its projection along the effective field, then the longitudinal decrease of the magnetization at resonance is :

$$\Delta M_z = M_s - M_z = M_s(1 - \cos\theta) \tag{2.28}$$

So for small precession angles, ΔM_z of order θ^2 is much smaller than the transverse component of order θ ($M_t = M_s \sin\theta$). The power absorbed by the magnetic system is the integral over the volume V_s of the sample of the scalar product of the time derivative of the transverse component by the microwave field. It is the overlap integral, which corresponds to the work done by the field per unit time :

$$P_{abs} = \int_{V_s} \frac{\partial \boldsymbol{M}_t(t)}{\partial t} . \boldsymbol{h} dV = \omega \chi^{''} h^2 \tag{2.29}$$

where $\chi^{''}$ is the imaginary part of the magnetic susceptibility:

$$\chi^{''}(\omega) = \frac{\alpha\gamma M_s \omega}{(\omega_0 - \omega)^2 + (\alpha\omega)^2}. \tag{2.30}$$

At a precession angle θ, the phase lag φ of the magnetization in the xy plane can be derived from the equation $\gamma\mu_0 h \sin\varphi = \alpha\omega \sin\theta$[1] which results directly from the equilibrium condition between the viscous friction and the driving torque of the microwave field.

2.3.3 FMR linewidth

This imaginary part of the magnetic susceptibility is a lorentzian centered on the resonance frequency ω_0, of linewidth $\alpha\omega_0$. So the magnetization precession has a finite lifetime. This limited lifetime, at the origin of the broadening of the ferromagnetic resonance, can be measured using a FMR setup. In experiments, we can sweep the magnetic field or the excitation frequency. At resonance, $\omega = \omega_0$ in equation (2.30), the imaginary part of the magnetic susceptibility is maximum (Figure 2.3), and thus the absorbed power. It can be shown that the linewidth which is the full width at half maximum (FWHM) is [2]:

$$\mu_0 \Delta H = \frac{2\alpha\omega}{\gamma} \tag{2.31}$$

---

[1] See equation (2.51) in section 2.5.1 for the derivation.

$$\Delta\omega = 2\alpha\left(\frac{\partial\omega}{\partial H}\right)\frac{\omega}{\gamma\mu_0} \tag{2.32}$$

which gives $\Delta\omega = 2\alpha\omega$ when $\omega \propto H$. With this relation, the Gilbert damping parameter α can therefore be deduced from FMR measurements. This is the main way to deduce the Gilbert damping of ferromagnetic films.

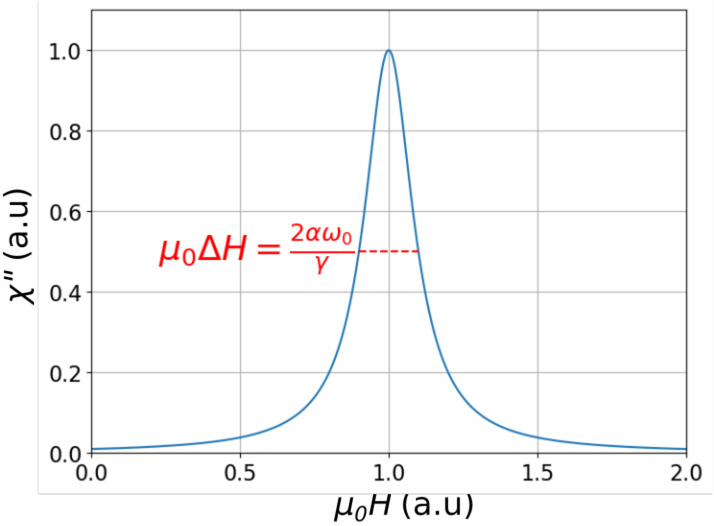

Figure 2.3: Illustration of the Lorentzian dependence of the imaginary part of the magnetic susceptibility on the resonance, when the magnetic field is swept at a fixed frequency $f_0 = \omega_0/2\pi$. The expression of the intrinsic linewidth is shown.

It is impossible in practice to have a film with perfectly uniform properties. This spread of magnetic properties combined with the unavoidable presence of inhomogeneities within the ferromagnetic film are at the origin of a linewidth broadening. These effects result in a non-zero intercept of the linear variation of ΔH as a function of ω : $\Delta H \neq 0$ at $\omega = 0$. The corresponding value is denoted ΔH_0 and called inhomogeneous broadening, which yields :

$$\mu_0\Delta H = \mu_0\Delta H_0 + \frac{2\alpha\omega}{\gamma}. \tag{2.33}$$

In YIG, ΔH_0 is relatively frequency invariant, allowing to extract the damping constant α from simple linear fit of the linewidth as a function of the frequency. However, in Bi-doped YIG films, such as the one used in this thesis, the spread of magnetic anisotropy introduces a field-dependent inhomogeneous broadening, making it harder to directly extract the damping constant from FMR experiments [27].

2.4 General theory of linear spin wave spectrum

We have studied in section 2.2 the general case of an ellipsoidal sample, focusing on the limit case of a thin film. For such a sample, the demagnetizing field is uniform. But in a finite and non-ellipsoidal sample, the demagnetizing field becomes non-uniform. The determination of the FMR mode and the other spin wave modes then requires a more elaborate calculation. Here, we want to find the spin wave eigenmodes of a normally magnetized thin disk.

2.4.1 Theory basis

We use the general theory of linear spin wave excitations, formulated by Andrei Slavin and Vasyl Tyberkevich [38],[51]. I briefly present here the general idea of this theory, inspired by the summaries presented in the theses of Benjamin Pigeau [52] and Abbass Hamadeh [53].

Following the linearization of the Landau-Lifshitz equation of motion of magnetization (2.1), the effective field can be written now :

$$\boldsymbol{H}_{eff} = \boldsymbol{H}_{ext} - \widehat{\boldsymbol{G}} * \boldsymbol{M} \tag{2.34}$$

where the sign $*$ denotes the convolution product, $\widehat{\boldsymbol{G}}$ is a linear tensor self-adjoint operator which includes all the internal magnetic interactions (demagnetizing, exchange and anisotropies energies). In the equilibrium state, the effective field $\boldsymbol{H}_{eff}$ is parallel everywhere to the local magnetization direction $\boldsymbol{u}_M$. In order to find the dynamical equations for the small (linear) magnetization excitations, the following ansatz is used to describe the out-of-equilibrium component of the magnetization $\boldsymbol{m}$:

$$\boldsymbol{M}(r,t) = M_s\big(\boldsymbol{u}_M + \boldsymbol{m}(\boldsymbol{r},t)\big) + \mathcal{O}(\boldsymbol{m}^2). \tag{2.35}$$

One notes that $\boldsymbol{m}$ now depends on the position $\boldsymbol{r}$. Since we consider a ferromagnet, the norm of the magnetization vector is a constant of motion, hence $\boldsymbol{m}.\boldsymbol{u}_M = 0$. So $\boldsymbol{m}$ is the small component of the magnetization ($|\boldsymbol{m}| \ll 1$) oscillating in the plane transverse to the local vector $\boldsymbol{u}_M$. This is the key parameter to describe the spin wave eigenmodes.

Substituting $\boldsymbol{M}(r,t)$ in equation (2.1), and keeping only the linear terms, a linear equation describing the transverse magnetization precession at the Larmor frequency is obtained:

$$\frac{\partial \boldsymbol{m}}{\partial t} = \boldsymbol{u}_M \times \widehat{\boldsymbol{\Omega}} * \boldsymbol{m} \tag{2.36}$$

This is just the new formulation of the equation (2.8) in the case of a finite ferromagnet where the demagnetizing field is no more uniform. The self-adjoint operator $\widehat{\boldsymbol{\Omega}}$ corresponds to the Larmor frequency :

$$\widehat{\boldsymbol{\Omega}} = \gamma\mu_0(H_{eff}\widehat{\mathbf{I}} + M_s\widehat{\mathbf{G}}) \tag{2.37}$$

where $\widehat{\mathbf{I}}$ is the identity matrix and H_{eff} is the norm of the effective field.

Considering only linear excitations of the spin system, $\boldsymbol{m}$ is developed in the general eigen-basis representing the spin wave eigenmodes, labelled by ν:

$$\boldsymbol{m}(\boldsymbol{r},t) \approx \sum_{\nu} c_\nu(t)\boldsymbol{m}_\nu(\boldsymbol{r}) + c.c \tag{2.38}$$

where c.c stands for complex conjugates. $c_\nu(t)$ are the amplitudes of the eigenmodes and $\boldsymbol{m}_\nu(\boldsymbol{r})$ represents their spatial profile.

2.4.2 Spectroscopy informations

For a given mode, its position (the resonance field or frequency), its linewidth and its amplitude depend on its spatial profile according to the following relations.

- The eigenfrequencies are simply given by the formula :

  $$\omega_\nu = \frac{\langle \overline{\boldsymbol{m}}_\nu . \widehat{\boldsymbol{\Omega}} * \boldsymbol{m}_\nu \rangle}{\mathcal{N}_\nu} \tag{2.39}$$

  The importance of that relation is that the frequencies ω_ν calculated using equation (2.39) are variationally stable with respect to perturbations of the mode profile $\boldsymbol{m}_\nu$ [38]. Thus, injecting some trial vectors inside equation (2.39) allows one to get approximate values of ω_ν with high accuracy. $\mathcal{N}_\nu$ is a normalization factor.

- Assuming that there are no degenerate modes, the spin wave damping rate of a mode is given by [38]

$$\Gamma_\nu = \alpha\omega_\nu \frac{\langle \overline{\boldsymbol{m}}_\nu . \boldsymbol{m}_\nu \rangle}{\mathcal{N}_\nu} \tag{2.40}$$

where α is the Gilbert damping.

- The excitation efficiency h_ν of a mode is proportional to the overlap integral between the excitation field $\boldsymbol{h}$ and the mode profile and given by :

$$h_\nu = \frac{\langle \overline{\boldsymbol{m}}_\nu . \boldsymbol{h} \rangle}{\mathcal{N}_\nu} \tag{2.41}$$

The signal amplitude which we will measure in experiments is the spatial average of the decrease of longitudinal component of magnetization ΔM_l, given by [38]:

$$\langle \Delta \boldsymbol{M} . \boldsymbol{u}_l \rangle = \Delta M_l \approx M_s \sum_\nu \frac{\gamma^2 |h_\nu|^2}{(\omega - \omega_\nu)^2 + \Gamma_\nu^2} \tag{2.42}$$

where $\boldsymbol{u}_l$ is the unit vector along the direction of longitudinal magnetization. For example $\boldsymbol{u}_l = \boldsymbol{u}_z$ in the case where the longitudinal magnetization is along the z axis and $\Delta M_l = \Delta M_z$.

Thus, according to the equation (2.42), a spectroscopy experiment will give a spectrum with a succession of Lorentzian-shaped resonance peaks corresponding to the sample's eigenmodes. The width of the resonance lines are directly related to the relaxation rate of the modes. Their amplitude being given by the overlap integral in (2.41), it gives information on the profile of the modes.

2.4.3 Spin waves in confined geometry: case of a normally magnetized thin disk

We now apply this general theory to the particular case of a normally magnetized thin disk with a uniaxial anisotropy field H_u.

2.4.3.1 Internal field profile

Lest's consider a thin magnetic disk (thickness t, radius R), see Figure 2.4 b, saturated by a strong magnetic field applied along the normal $\boldsymbol{u}_z$ of the disk.

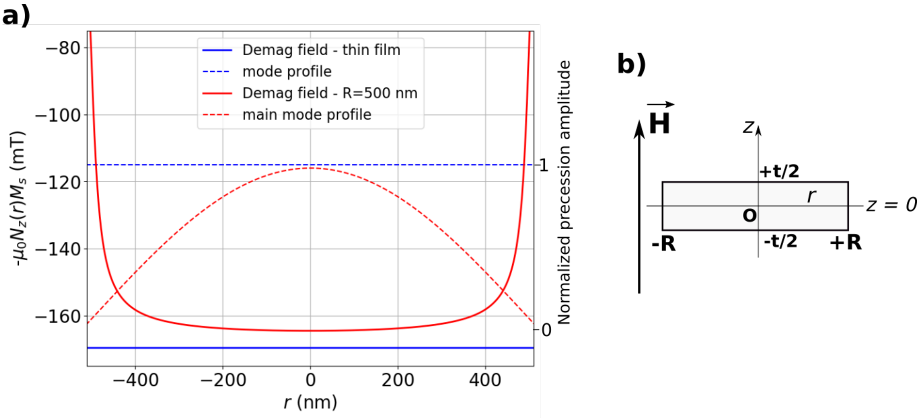

Figure 2.4: a) Calculated profiles of the demagnetizing field in a thin film (solid blue curve) and in a nanodisk (solid red curve) of radius $R = 500$ nm, thickness $t = 30$ nm; the magnetization is taken $M_s = 1.35\times10^5$ A/m. Draws of typical magnetization precession profiles are shown with the dashed curves. b) Cross-section of the nanodisk of thickness t and radius R.

Considering the finite size of the system, we expect a discrete spin-wave modes spectrum.

Figure 2.4 a shows the comparison between the demagnetizing field of a thin film (solid blue curve) and a 500 nm radius nanodisk (solid red curve). In contrast to the case of an ellipsoid of revolution (or a thin film), the demagnetizing field is non-uniform in the case of a nanodisk. The results are obtained with an analytical calculation for a disk of radius $R = 500$ nm, thickness $t = 30$ nm and magnetization $M_s = 1.35\times10^5$ A/m (this is the thickness and magnetization of the BiYIG nanodisks we will study).

Similar to the case of ellipsoid of revolution (equation (2.18)), the Kittel mode frequency of the disk can be approximately described by :

$$\omega^{\perp}_{disk} = \gamma\mu_0(H - H_K) \tag{2.43}$$

where in the characteristic field $H_K = (N_z^{eff} - N_{\perp}^{eff})M_s - H_u$, N_z^{eff} and $N_{\perp}^{eff}$ are now the diagonal elements of the effective demagnetization tensor of the uniformly magnetized disk [54], which depend in a complex way on the overlap between the profile of the non-uniform demagnetizing field and the profile of the Kittel mode (which is also not spatially uniform in the disk as we will see later). In addition to this complex demagnetizing field and the anisotropy field, for higher order modes, the exchange field should be taken into account in H_K. The dispersion relations of the BiYIG disks will be fitted using equation (2.43) to extract their characteristic field H_K and γ.

Now we explain the origin of the non-uniform demagnetizing field in the disk and how it leads to a spatially non-uniform precession profile. The disk is uniformly magnetized along the z axis by a strong magnetic field, see Figure 2.4 b, so that $M_z(\boldsymbol{r})=M_s$. The field profiles in Figure 2.4 a are calculated along the diameter of the disk, in the plane $z = 0$ shown in Figure 2.4 b, using the formula :

$$\mu_0 H_{demag}(\boldsymbol{r}) = -\mu_0 N_z(r, 0) M_s \tag{2.44}$$

where $N_z(r, 0)$ is the demagnetizing factor along the z axis in the plane $z = 0$ calculated at the radial position r. In the case of YIG, the applied static field must be added to have the total internal field, whereas in the case of BIYIG both the static field and the uniaxial anisotropy field H_u must be added. But since both are constants, their only effect is to shift the internal field without affecting its spatial profile. The shape of the internal field profile is therefore given by the demagnetizing field. This internal field profile in the nanodisk comes from finite size effects at the periphery. We have seen that this demagnetizing field is due to the dipolar interaction between the magnetic moments. The transition from thin film to nanodisk will therefore decrease the interaction felt by each magnetic moment. This decrease is taken into account by the variations of $N_z(r, z)$. This decrease is obviously much less important for a magnetic moment located at the centre of the disk than for a magnetic moment located at the edges of the disk. The latter loses almost half of its neighbouring moments. This explains why there is almost a factor of 2 between the demagnetizing field at the centre of the disk, -165 mT, and the demagnetizing field at the edge, -77 mT (see the solid red curve in Figure 2.4 a), as well as a strong field gradient at the periphery. In the central region, the demagnetizing field remains close to the value of the thin film -$\mu_0 M_s$ = -170 mT (for the thin film $N_z(r, 0)$ = cste = 1).

When the FMR is excited in the thin film or in an ellipsoïd, H_{demag} being uniform, the resonance condition is the same for all magnetic moments. They start to precess in a spatially coherent way : the precession amplitude is the same at all points in the thin film (see the dashed blue curve in Figure 2.4 a). However the situation is different in the disk. When the FMR is excited, due to the non-uniform profile of the demagnetizing field, the resonance relation is satisfied in the central region but not at the edges. As all the magnetization must precess at the same frequency, there will be a precession profile with a decreasing amplitude from the centre to the edges. So, the precession will be maximum at the centre and will decrease as one gets closer to the edges (see the dashed red curve in Figure 2.4 a). We can thus define a dipolar pinning which will account for the level of decrease of the precession amplitude of the magnetization at the periphery. For example, a maximum dipolar pinning will mean a zero precession amplitude at the edges of the nanostructure.

Furthermore, considering the finite size of the system, we expect a discrete spin-wave modes spectrum. Indeed, beyond the unique FMR mode for a thin film with no defects, nanopatterning lifts the degeneracy between the different spin wave modes, which can therefore be distinguished in a nanodisk. Their profiles are also directly related to the internal field profile.

2.4.3.2 Spin waves profiles

We present here some of these spin waves profiles. As the disk is considered to be thin, the magnetization is uniform along its thickness, and the 2D approximation holds. Therefore, two indices are sufficient to label the eigen modes : $\nu = (l, n)$. Due to the axial symmetry of the system, l should be related to the azimuthal symmetry of the spin wave modes, whereas n should be a radial index.

From symmetry arguments, it can be shown that the spin-wave mode profiles can be written as [38] :

$$\boldsymbol{m}_l = \frac{1}{2}(\boldsymbol{u}_x + \boldsymbol{u}_y)e^{-il\phi}\psi_l(\rho), \tag{2.45}$$

where (ρ, ϕ) are the cylindrical coordinates, and $\boldsymbol{u}_x$,$\boldsymbol{u}_y$ the orthogonal unit vectors in the plane of the disk.

The calculation of the radial functions $\psi_l(\rho)$ involves to solve integro-differential equations. An approximation consists of using a reasonable set of known mathematical trial functions. They should obey to some simple properties [53]. Here, the Bessel functions of the first kind $J_l(x)$ are well adapted, since they have the appropriate radial and azimuthal symmetry. Moreover, they reproduce well the strong pinning of the magnetization at the lateral boundaries due to the magneto-dipolar interaction [55]. We therefore use radial profiles of the form $\psi_l(\rho) = J_l(k_{l,n\rho})$. The eigenmodes wave numbers $k_{l,n\rho}$ are determined from the pinning conditions at the disk boundary. For very thin disks, this pinning is found to be almost complete [53], so that $k_{l,n} = \kappa_{l,n}/(R+t)$, where $\kappa_{l,n}$ is the n^{th} root of the Bessel function of the l^{th} order.

The spatial profiles of such functions are presented in Figure 2.5 with the rows corresponding to the azimutal index l and the columns to the radial index n. The phase (or direction) of the magnetization precession $\phi = \arg(\boldsymbol{m}_\nu)$ is displayed in color code using the hue, while the amplitude $|\boldsymbol{m}_\nu|^2$ is given by

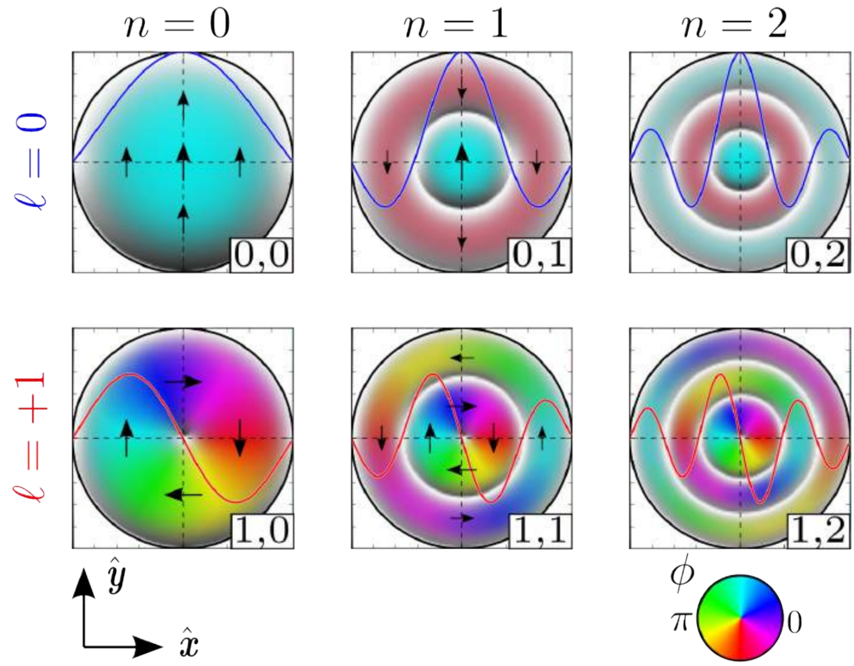

Figure 2.5: Color representation of the Bessel spatial patterns for different values of the azimuthal mode index l (by row) and radial mode index n (by column). The arrows are a snapshot of the transverse magnetization $\boldsymbol{m}_\nu$, labeled by the index $\nu = (l, n)$. All arrows are rotating synchronously in-plane at the spin-wave eigen-frequency. The hue indicates the phase $\phi = \arg(\boldsymbol{m}_\nu)$ (or direction) of $\boldsymbol{m}_\nu$, and the brightness the amplitude of $|\boldsymbol{m}_\nu|^2$. The nodal positions ($|\boldsymbol{m}_\nu| = 0$) are marked in white [38].

the brightness. One can identify the ($l = 0, n = 0$) mode as the "uniform" mode : the magnetization precesses in-phase uniformly in the disk, even if the precession amplitude is not uniform. The first azimutal mode ($l = +1, n = 0$) corresponds to a spin wave that is rotating around the disk in the same direction as the Larmor precession. The corresponding phase is in quadrature between two orthogonal positions and this mode has a node (position where the precession amplitude is zero) at the center of the disk (the nodal positions are marked in white). Then, increasing the index n results in an increase of the number of nodes in the radial direction.

2.4.4 Selection rules for a uniform excitation field

The spatial symmetry of the source is crucial to determine which spin wave eigen-modes can be excited [38]. From equation (2.41), it can be shown that a uniform microwave excitation field (this will often be the case in our experiments) can only excite ($l = 0, n$) spin waves modes with amplitudes proportional to $1/(n+1)^2$, because the overlap integrals with azimutal modes ($l \neq 0$) vanish. In order to excite azimutal spin wave modes with ($l = +1$), a field with an orthoradial symmetry can be used, as the one produced by an rf current flowing vertically through a conducting disk [38].

Figure 2.6 b presents the spin waves spectra of YIG nanodisks of different sizes measured in the lab [21]. These measurements were made with our experimental setup, the magnetic resonance force microscope (MRFM) which will be presented in the next chapter. Having used a uniform excitation field, the measured peaks represented the modes ($l = 0, n = 1$), ($l = 0, n = 2$) and ($l = 0, n = 3$) whose profiles were presented in the previous figure. Figure 2.6 a completes the Figure 2.4, showing now the evolution of the demagnetizing field profile with the disk size. An increase in H_{demag} is observed as the size decreases. In particular, at the centre of the disk, one shifts from -165 mT for the 500 nm disk radius to -145 mT for the 100 nm disk radius. The origin of this evolution is the same as that given previously between the thin film and the 500 nm radius disk, namely finite size effects. For large disks (D $>$ 500 nm), it is mainly this variation that explains the increase of the main mode resonance frequency as the disk size decreases as shown in Figure 2.6 b. For smaller disks, the exchange field is no longer negligible and must be taken into account.

NB: The mode ($l = 0, n = 0$) being the mode of largest amplitude and uniform phase[2], we will refer to it later by using independently and abusively the expressions "main mode", "uniform mode" or "FMR mode".

---

[2] In case of a uniform pumping field, as commonly used in FMR.

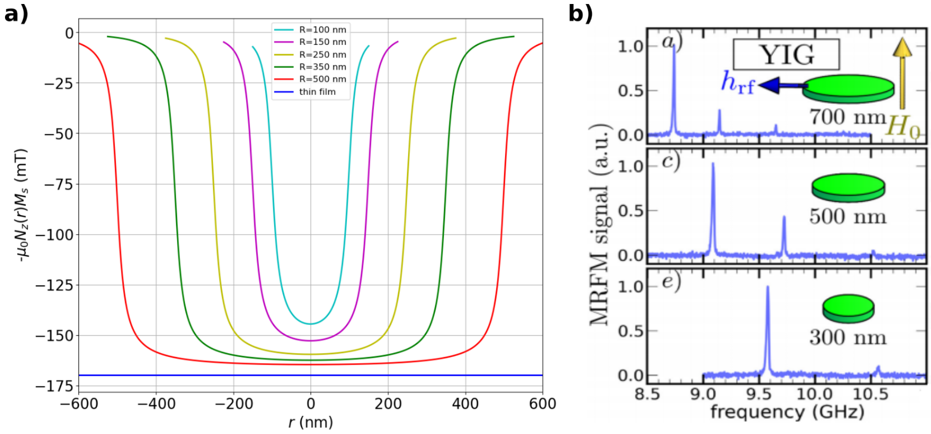

Figure 2.6: a) Internal field profile as a function of disk radius. b) MRFM spectra of YIG nanodisks at $H_0 = 0.499$ T as a function of disk diameter [21].

2.4.5 Influence of symmetry breaking

In the case of a small symmetry breaking from the perfect axial symmetry, which can be done either by a small tilt of the perpendicular applied field [56], [38] or a deviation from a perfect circular shape of the disk [38], the eigen-modes will become a superposition of $l = 0$ and $l \neq 0$ modes of the basis. Therefore, the selection rules are also affected and it is possible to excite modes with $l \neq 0$. However, it is still possible to use the same eigen-basis of equation (2.45) to decompose the new spin-wave modes.

2.5 Nonlinear regime

So far we have only studied cases where the excitation field is small enough for the dynamics equation to be linearized. However, a closer look at the LLG equation (2.26) shows that it is strongly nonlinear since the terms on the right-hand side of the equation contain both explicitly the magnetization $\boldsymbol{M}$ and implicitly through $\boldsymbol{H}_{eff}$ via exchange, demagnetizing interactions, etc... So it is expected that for very high excitations, nonlinear effects appear. We will present some of them. The most common one is the well-known resonance line foldover, which is also one of the most simple because it only concerns the uniform mode. We will then briefly present other effects involving several spin wave modes. These are subsidiary resonance and premature saturation of the main resonance, which are all explained by spin wave instabilities that we will describe.

2.5.1 Foldover effect of the resonance line

When the intensity of the excitation field is increased, the angle of precession increases and therefore the longitudinal component of the magnetization M_z decreases. This decrease leads to a variation of the demagnetizing field and therefore to a modification of the resonance frequency. In this case, the relation (2.17) which gives the resonance frequency of the uniform mode for small excitations when the dimunition of the longitudinal magnetization is negligible, is no longer valid. It is then necessary to replace M_s by M_z. In the simple case of absence of PMA, $H_u = 0$ and the equation becomes :

$$\omega = \gamma\mu_0[H - (N_z - N_\perp)M_z] \tag{2.46}$$

The eigen frequency of the system therefore depends on the amplitude ΔM_z. If $N_z > N_\perp$, as in the case of a thin film magnetized along the z axis ($N_z = 1$ and $N_\perp = 0$), when the excitation is increased, M_z decreases and the resonance frequency increases. If the FMR experiment is performed at a fixed frequency, there will be a decrease in the resonance field. This is the *foldover* of the resonance line, an effect predicted by Anderson and Suhl in 1955 [57] and observed by Weiss three years later [58].

Let's consider now the general case of a thin film with a uniaxial anisotroy constant K_u along the z axis, subjected to a static magnetic field $\boldsymbol{H}$ along its normal and to a circularly polarized rf field $\boldsymbol{h}$ of frequency ω, see Figure 2.7. In order to demonstrate this foldover with analytical calculations, in the following, we present the resolution of the nonlinear dynamics for a macrospin. As explained previously, the magnetization $\boldsymbol{M}$ precesses about the direction of $\boldsymbol{H}$.

Let's go back to the LLG equation (2.26). Using polar coordinates θ and φ, $\boldsymbol{M} = M_s(\sin\theta\cos\varphi,$
$\sin\theta\sin\varphi, \cos\theta)$ and the equation of motion can be written [59] :

$$\begin{aligned}\dot{\theta} &= -\frac{\gamma}{\mu_0 M_s \sin\theta}\frac{\partial E_t}{\partial\varphi} - \alpha\dot{\varphi}\sin\theta \\ \dot{\varphi} &= \frac{\gamma}{\mu_0 M_s \sin\theta}\frac{\partial E_t}{\partial\theta} + \frac{\alpha}{\sin\theta}\dot{\theta}\end{aligned} \tag{2.47}$$

where E_t is the thin film energy density. E_t is now given by :

$$E_t = -\mu_0 M_s H\cos\theta - \mu_0 h M_s \sin\theta\cos(\varphi - \omega t) + \left(K_u - \frac{\mu_0 M_s^2}{2}\right)\sin^2\theta \tag{2.48}$$

or :

$$E_t = -\mu_0 M_s H\cos\theta - \mu_0 h M_s \sin\theta\cos(\varphi-\omega t) - \frac{\mu_0 M_s M_{eff}}{2}\sin^2\theta \tag{2.49}$$

where M_{eff} is the effective magnetization defined in Chapter 1 and the second term is the component of the Zeeman interaction between $\boldsymbol{h}$ and the transverse magnetization $\boldsymbol{M}_t$, see Figure 2.7 :

The derivatives are given by :

$$\begin{aligned}\tfrac{\partial E_t}{\partial\theta} &= \mu_0 M_s H\sin\theta - \mu_0 h M_s\cos\theta\cos(\varphi-\omega t) - \mu_0 M_s M_{eff}\sin\theta\cos\theta\\ \tfrac{\partial E_t}{\partial\varphi} &= \mu_0 h M_s\sin\theta\sin(\varphi-\omega t)\end{aligned} \tag{2.50}$$

At steady state, the precession of $\boldsymbol{M}$ is circular, i.e θ = cste and $\varphi-\omega t$ = cste $\Longrightarrow \dot\theta = 0$ and $\dot\varphi = \omega$. These conditions, combined with the equations (2.47) yield the two relations :

$$\begin{aligned}&-\gamma h\sin(\varphi-\omega t) - \alpha\omega\sin\theta = 0\\ &\gamma H - \gamma h\tfrac{\cos\theta}{\sin\theta}\cos(\varphi-\omega t) - \gamma M_{eff}\cos\theta = \omega\end{aligned} \tag{2.51}$$

Extracting $\cos(\varphi-\omega t)$ and $\sin(\varphi-\omega t)$, we find :

$$\begin{aligned}\sin^2(\varphi-\omega t) &= \left(\tfrac{\alpha\omega}{\gamma}\right)\left(\tfrac{\sin\theta}{h}\right)^2\\ \cos^2(\varphi-\omega t) &= \left(\tfrac{\gamma(H-M_{eff}\cos\theta)-\omega}{\gamma\cos\theta}\right)^2\left(\tfrac{\sin\theta}{h}\right)^2\end{aligned} \tag{2.52}$$

Using $\cos^2(\varphi-\omega t)+\sin^2(\varphi-\omega t) = 1$, one finds :

$$\left(\frac{\sin\theta}{h}\right)^2\left[\left((H-M_{eff}\cos\theta)-\frac{\omega}{\gamma}\right)^2+\left(\frac{\alpha\omega}{\gamma}\right)^2\cos^2\theta\right]\frac{1}{\cos^2\theta} = 1 \tag{2.53}$$

which finally gives :

$$\sin^2\theta = \frac{h^2\cos^2\theta}{\left[\left((H-M_{eff}\cos\theta)-\frac{\omega}{\gamma}\right)^2+\left(\frac{\alpha\omega}{\gamma}\right)^2\cos^2\theta\right]} \tag{2.54}$$

which describes the foldover effect [60] : for some fields, we will have two possible values of the precession angle θ. A complete analytical treatment allows to solve (2.54) exactly as done in [61]. For simplicity of the mathematical treatment, we use as Gui et al. in [10] the well-known limited development valid for small angles :

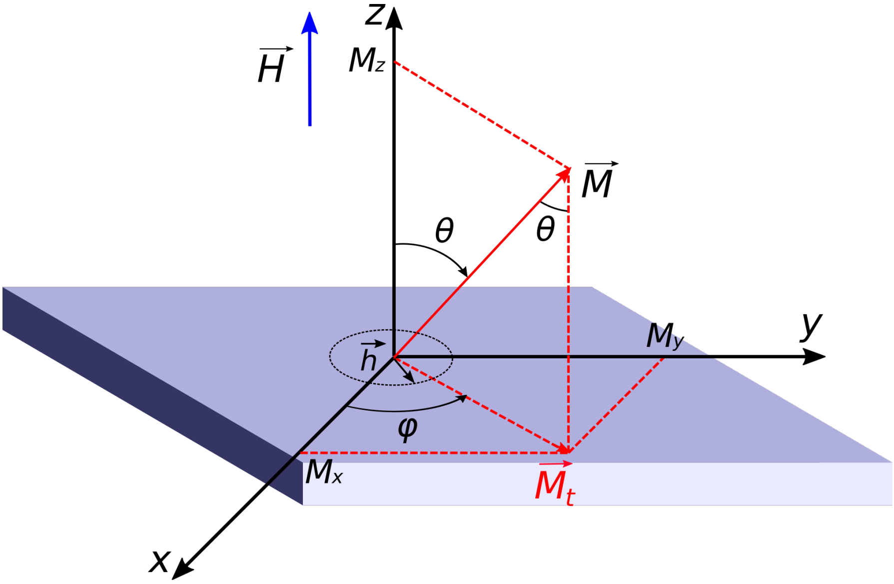

Figure 2.7: Geometry of the thin film.

$$\begin{aligned} \cos\theta &\approx 1-\tfrac{\theta^2}{2} \\ \sin\theta &\approx \theta \end{aligned} \tag{2.55}$$

Finally, it is found [10] :

$$\theta^2 = \frac{h^2(1-\theta^2/2)}{\left[\left((H-M_{eff})-\frac{\omega}{\gamma}+M_{eff}\frac{\theta^2}{2}\right)^2+\left(\frac{\alpha\omega}{\gamma}\right)^2(1-\theta^2/2)^2\right]} \tag{2.56}$$

Neglecting the higher-order terms $h^2\theta^2$ and $\alpha^2\theta^2$, equation (2.56) becomes the well-known form of cone angle in the nonlinear regime :

$$\theta^2 = \frac{h^2}{(H-H_0+M_{eff}\theta^2/2)^2+\frac{\Delta H^2}{4}} \tag{2.57}$$

where $H_0 = \omega/\gamma + M_{eff}$ is the resonance position in the linear regime (i.e at $h \to 0$) which can be extracted in the resonance relation (2.19), and ΔH is the FMR linewidth generalized to $\Delta H = 2\alpha\omega/\gamma + \Delta H_0$, ΔH_0 being the FMR line-shape broadening due to the sample imperfections (see equation (2.33)). When h is stronger than a critical field h_{th}, FMR response shows the discontinuity of θ at $d\theta/dH = \pm\infty$ indicated by the arrows in Figure 2.8 f. Differentiating[3] equation (2.57) with respect to H, we have :

$$\frac{d\theta}{dH} = -\frac{\theta\Big(H - H_0 + \frac{1}{2}M_{eff}\theta^2\Big)}{\Big(H - H_0 + \frac{1}{2}M_{eff}\theta^2\Big)\Big(H - H_0 + \frac{3}{2}M_{eff}\theta^2\Big) + \frac{\Delta H^2}{4}} \tag{2.58}$$

Therefore the up and down jumps can be determined from the quadratic equation of θ^2,

$$(H - H_0 + \frac{1}{2}M_{eff}\theta^2)(H - H_0 + \frac{3}{2}M_{eff}\theta^2) + \frac{\Delta H^2}{4} = 0 \tag{2.59}$$

which has two real roots, namely, θ_{up} and θ_{down} for $h \geq h_{th}$. The corresponding fields, H_{up} and H_{down}, indicated by the arrows in Figure 2.8 f, represent the upward jump and downward jump points in the response curve, respectively. The threshold field h_{th} corresponds to $\theta_{up} = \theta_{down} = \theta_{th}$ and $H_{up} = H_{down}$.

By setting $X = H - H_0$ and $\beta = \theta^2$, the equation (2.59) becomes :

$$\frac{3}{4}M_{eff}^2\beta^2 + 2M_{eff}X\beta + X^2 + \frac{\Delta H^2}{4} = 0 \tag{2.60}$$

which is a second degree equation in β. Its discriminant is given by :

$$\Delta = M_{eff}^2X^2 - \frac{3M_{eff}^2\Delta H^2}{4} \tag{2.61}$$

The equation has only one solution $\theta_{up}^2 = \theta_{down}^2$ if $\Delta = 0$ i.e. if $X^2 = \frac{3\Delta H^2}{4}$ which gives :

$$X = H_{up,down} - H_0 = \pm\frac{\sqrt{3}\Delta H}{2} \tag{2.62}$$

And in this case :

$$\beta_{th} = \theta_{th}^2 = -\frac{4X}{3M_{eff}}. \tag{2.63}$$

- Thus if $M_{eff} < 0$, since θ_{th}^2 must be positive, we deduce that in (2.62) X is the positive solution $\frac{\sqrt{3}\Delta H}{2}$ and we find :

$$\beta_{th} = \theta_{th}^2 = -\frac{2\sqrt{3}\Delta H}{3M_{eff}} \tag{2.64}$$

---

[3] See Appendix A.1 for the calculation.

$X > 0 \Rightarrow H_{up,down} > H_0$: the resonance line shifts towards high fields when the excitation is increased (see Figure 2.8 d & f).

- On the other hand, if $M_{eff} > 0$, X must be negative for θ_{th}^2 to be positive. We then find :

$$\beta_{th} = \theta_{th}^2 = \frac{2\sqrt{3}\Delta H}{3M_{eff}} \tag{2.65}$$

$X < 0 \Rightarrow H_{up,down} < H_0$: the resonance line shifts towards low fields when the excitation is increased (see Figure 2.8 c & e).

In the case $M_{eff} < 0$, Substituting (2.62) (the positive value) and (2.64) in (2.57), one finds :

$$h_{th}^2 = -\frac{2\sqrt{3}\Delta H^3}{9M_{eff}} \tag{2.66}$$

which is the same value deduced by Anderson and Suhl $3.08\Delta H^3/\mu_0 M$ [57], who used the half linewidth. Due to the approximations used this result is slightly different from the exact result which has been calculated by Bertotti et al. in [61].

The characteristic fields are H_R (the field where θ is maximum and equal to θ_R), H_{up} and H_{down}, which correspond to $d\theta/dH = 0$, $d\theta/dH = +\infty$, and $d\theta/dH = -\infty$, respectively. From equation (2.58), we find :

$$H_R = H_0 - \frac{1}{2}M_{eff}\theta_R^2 \tag{2.67}$$

And noting from (2.57) that at resonance :

$$\theta_R^2 = \frac{4h^2}{\Delta H^2} \tag{2.68}$$

one finds :

$$H_R = H_0 - \frac{2h^2 M_{eff}}{\Delta H^2}. \tag{2.69}$$

Equation (2.68) shows that for small precession angles, the precession angle at resonance is proportional to h^2 i.e. to the microwave power. The amplitude of the signal that we will measure in experiments is the reduction of the longitudinal component of the magnetization ΔM_z (given by equation 2.42). Since $\Delta M_z = M_s(1 - \cos\theta)$ (see equation 2.28), one finds $\Delta M_z \approx M_s\theta^2/2$ for small angles. Thus at resonance and for *small precession angles*, one gets

$\Delta M_z \propto \theta^2 \propto h^2 \propto P$, P being the microwave power : the signal amplitude linearly increases with the microwave power.

H_{up} and H_{down} can be solved as functions of h and have no analytical solution in general. We can simplify the solution of equation (2.59) as $\theta^2_{up} \approx -2(H_{up} - H_0)/3M_{eff}$ and $\theta^2_{down} \approx -2(H_{down} - H_0)/M_{eff}$, for $h \gg h_{th}$, and then get [10] :

$$\begin{aligned} H_{up} &\approx H_0 - \frac{3}{2}h^{2/3}M_{eff}^{1/3} \quad at \quad \theta_{up} = (h/M_{eff})^{1/3}, \\ H_{down} &\approx H_0 - \frac{2h^2}{\Delta H^2}M_{eff} \quad at \quad \theta_{down} = 2h/\Delta H. \end{aligned} \tag{2.70}$$

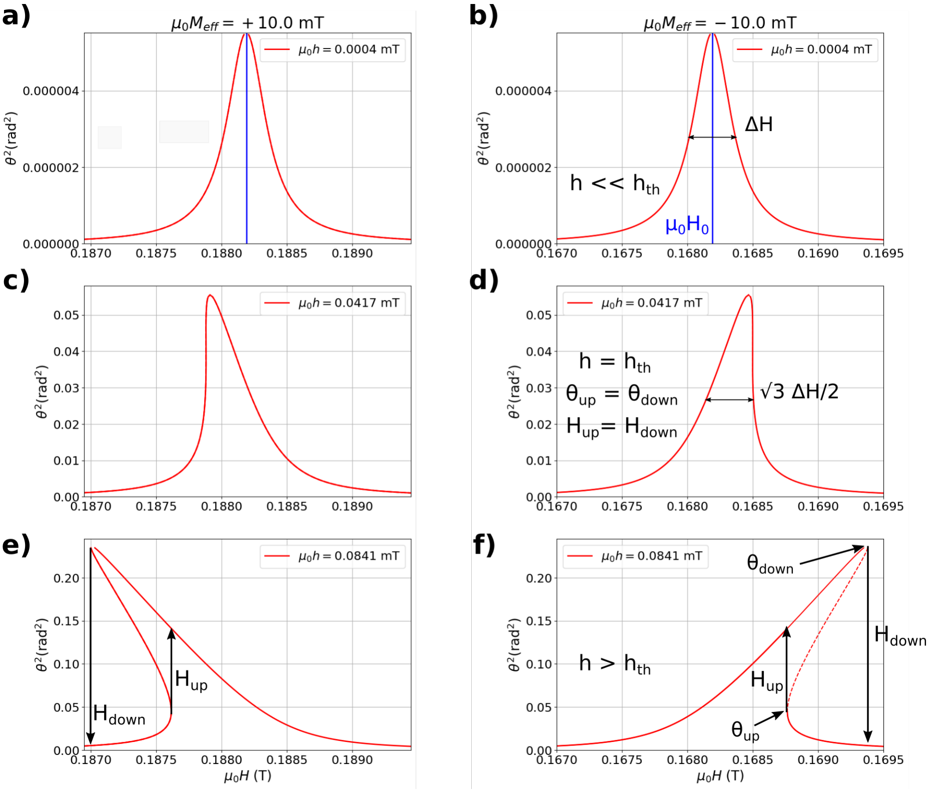

Figure 2.8: The calculated θ^2 for a FMR at f = 5 GHz, at three values of h, $h = 0.01h_{th}$, $h = h_{th}$ and $h = 2h_{th}$ for $M_{eff} > 0$ (a-c-e) and for $M_{eff} < 0$ (b-d-f). The parameters used are $\mu_0 M_{eff} = \pm 10$ mT, $\alpha = 0.001$, $\gamma/2\pi = 28$ GHz/T.

The calculations in Figure 2.8 are done at 3 different values of h, $0.01h_{th}$, h_{th} and $2h_{th}$ for the 2 signs of M_{eff}, at f = 5 GHz. The parameters used are the typical parameters of the BiYIG film and BiYIG nanodisks that we will measure : $\alpha = 1\times10^{-3}$, $\mu_0 M_{eff} = \pm$ 10 mT and $\gamma/2\pi$ = 28 GHz/T. With such parameters, we find $\mu_0\Delta H$ = 0.36 mT at 5 GHz and $\mu_0 h_{th}$ = 0.042 mT (Figure 2.8 c & d). The sign of M_{eff} governs the direction of the foldover in the nonlinear regime. Note that the linear resonance field H_0 also depends on M_{eff}. The existence of two stable solutions of the LLG equation in the interval [H_{up},H_{down}] results in a hysteretic behavior in this interval : the value of $M_z(H)$ measured in this interval depends on the direction of the static field sweep.

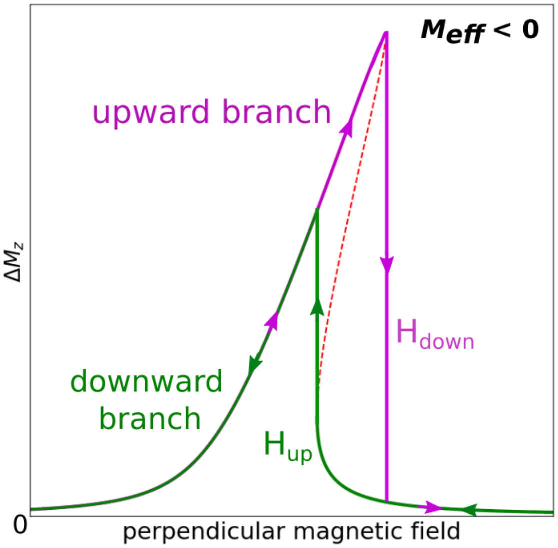

Figure 2.9: Resonance line measured in the experiments in the case M_{eff} < 0.

Figure 2.9 shows an illustration of the resonance line that one expects to measure in experiments in the case $M_{eff} < 0$, the microwave excitation being maintained ON during the measurement. One expects to see two branches according to the scanning direction of the magnetic field. We will call upward and downward the branches corresponding to sweeps towards high fields (magenta curve) and low fields (green curve) respectively. The upward branch contains the field H_{down} (downward jump from the upward branch to the downward branch) while the downward branch contains the field H_{up} (upward jump from the downward branch to the upward branch). Note that when the resonance line is shifted towards low fields (Figure 2.8 e for example), the upward branch rather contains H_{up} and the downward branch contains H_{down}. If the microwave field is modulated ON/OFF, then only the lowest amplitude branch is measured (the downward branch if $M_{eff} < 0$ and the upward branch if $M_{eff} > 0$).

In the analysis of the experimental results, we will speak abusively of foldover for any distorted resonance line but keeping in mind that the foldover threshold specifically corresponds to the resonance line with a vertical tangent (i.e. H_{up}=H_{down}, see Figure 2.8 d), whose onset critical field is given in equation (2.66).

2.5.2 Nutation of magnetization in nonlinear dynamics

Besides the foldover effect desribed above, the above analysis performed in the macrospin approximation demonstrates that it is possible to stabilize a large angle of precessing magnetization by driving it with a microwave field of sufficiently large amplitude and conveniently sweeping the applied field or microwave frequency. The magnetization $\boldsymbol{M}_0$ is then precessing at an angle θ_0 and a phase lag φ_0 (see the right hand scheme of Figure 2.10 a) : the well-known **P**-mode (Periodic mode). In the steady state, these angles satisfy the relationship $\gamma\mu_0 h_1 \sin\varphi_0 = \alpha\omega_1 \sin\theta_0$ which translates the balance between the rates of energy absorbed from the microwave field and of energy dissipated by the precessing magnetization (this is nothing else than equation (2.51) with $\varphi_0 = \omega_1 t - \varphi$).

We can then ask the question of the stability of this **P**-mode. Bertotti et al. studied analytically the stability of large magnetization motions in ellipsoid bodies with uniaxial symmetry and showed that in such systems, large enough motions are always stable [62]. For an excitation field $\boldsymbol{h}_1$ at ω_1 and a **P**-mode at (θ,φ), if the magnetization is slightly perturbed from its trajectory on this P-mode limit cycle, it will come back to it with a characteristic frequency given by [61]:

$$\frac{\omega_n}{\gamma^2} = \frac{\mu_0 h_1 \cos\varphi}{\sin\theta}\left(\frac{\mu_0 h_1 \cos\varphi}{\sin\theta} + \mu_0 M_s \sin^2\theta\right). \tag{2.71}$$

In the frame precessing with the microwave field (or, equivalently, with the magnetization), the magnetization vector is spiraling around its stable equilibrium (cf. Figure 2.10 c), which corresponds to a nutation trajectory in the laboratory frame : a combination of the large periodic coherent motion at a frequency ω_1 and small oscillations at $\omega_n < \omega_1$.

As in the case of a spinning top, the nutation of magnetization demonstrated above is made possible by the specific properties of the dynamics on the unit sphere [63]. Namely, it is topologically allowed for the magnetization to oscillate around its fixed point $\boldsymbol{M}_0(\theta_0,\varphi_0)$ in the rotating frame, which is set by the drive $\boldsymbol{h}_1$. The nutation dynamics discussed here is thus fundamentally connected to the existence of the P-mode. The nutation frequency results from the balance of torques acting on the angular momentum and is given by equation (2.71) in the case of a macrospin governed by the LLG equation [22].

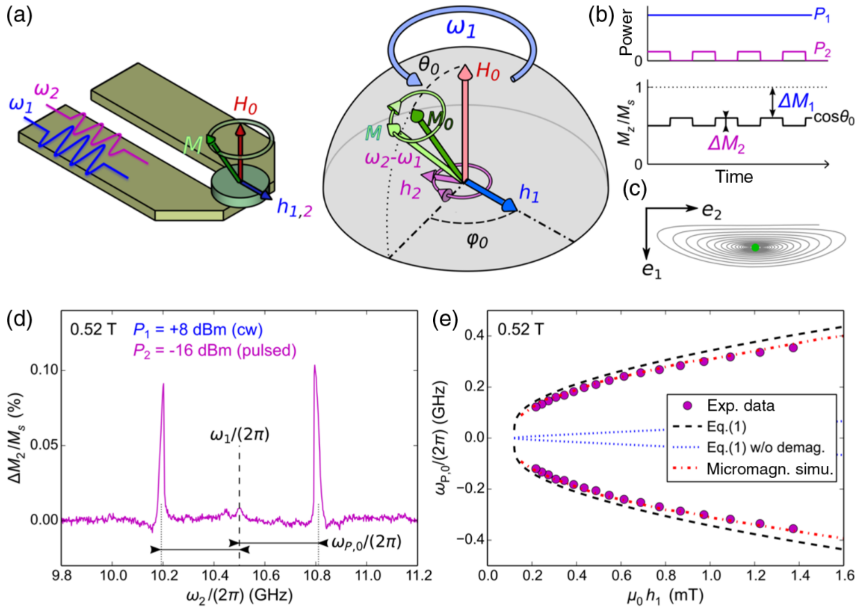

Figure 2.10: Nutation of magnetization. (a,b) Principle of the experiment. A low-power microwave field $\boldsymbol{h}_2$ of pulsation ω_2, which is pulse modulated at the cantilever frequency $f_c \approx 12.3$ kHz, is added to the main pumping cw field $\boldsymbol{h}_1$. This addition enables the spectroscopy in the frame rotating with $\boldsymbol{h}_1$ at ω_1, where the magnetization $\boldsymbol{M}_0$ of the **P**-mode-mode is fixed at an angle θ_0 and a phase lag φ_0. (c) Relaxation trajectory of the magnetization towards in the plane $(\boldsymbol{e}_1,\boldsymbol{e}_2)$ orthogonal to $\boldsymbol{M}_0$. (d) Spectroscopy performed at $\omega_1/2\pi = 10.5$ GHz and $\mu_0 H_0 = 0.52$ T as a function of ω_2. The two resonance peaks that are symmetric with respect to ω_1 correspond to a motion of nutation in the laboratory frame. (e) Evolution of the nutation frequency as a function of the main pumping field h_1 at fixed $\mu_0 H_0 = 0.52$ T. [22].

One way to measure this nutation mode can be to directly monitor the real time evolution of the magnetization after a small disturbance of his steady state trajectory (P-mode) or to detect its frequency by spectroscopy. To illustrate the latter technique, we shortly describe an experiment performed in the lab on the 700 nm diameter YIG nanodisk of Figure 1 C, using the MRFM. A first large microwave field at ω_1 is applied to excite the large amplitude precession. In addition, a second weaker microwave field whose frequency ω_2 is varied around ω_1 is applied to unveil what eventually happens around the large amplitude motion, see Figure 2.10 a.

NB: The details on the use of the MRFM (Figure 2.10 b) for the detection of the 2 signals associated with the two microwave fields will be given later in the presentation of the experimental results, this two-tone spectroscopy having also been used in our works.

Figure 2.10 d shows the spectrum obtained with the second excitation when $f_1 = \omega_1/2\pi = 10.5$ GHz, the static field being fixed at 0.52 T which is in the resonance region at this frequency (see the resonance line with the strong foldover in Figure 1 C) and the frequency f_2 being varied around f_1. One observes two resonance peaks symmetrically distributed around the main frequency f_1 corresponding to the nutation mode, which means that in the frame rotating with the first microwave field $\boldsymbol{h}_1$ at ω_1, the magnetization is precessing at $(\omega_2 - \omega_1)/2\pi = \pm\Delta\omega = 0.3$ GHz around its equilibrium position. The frequency of this nutation mode is well taken into account by equation (2.71), see Figure 2.10 e.

In a general way, the nutation is a periodic motion of the axis of rotation of an object around its average position, which is added to the precession. For example, because of the combined attraction of the Sun and the Moon, the Earth undergoes a nutation which means an oscillation of its rotation axis [64].

2.5.3 Suhl thresholds

We have just studied what happens when we increase the excitation intensity in the macrospin approximation (only the main mode is considered): a foldover of the resonance line occurs. Taking into account the whole spectrum of spin waves can give rise to other effects such as subsidiary resonance and premature saturation of the main resonance, referred to as first and second order Suhl processes respectively. They can be explained by the nonlinear coupling of the uniform precession mode excited by the microwave field with other spin wave modes. Indeed in the perpendicular pumping configuration, the microwave field couples linearly to the uniform mode ($k = 0$) and one observes a FMR

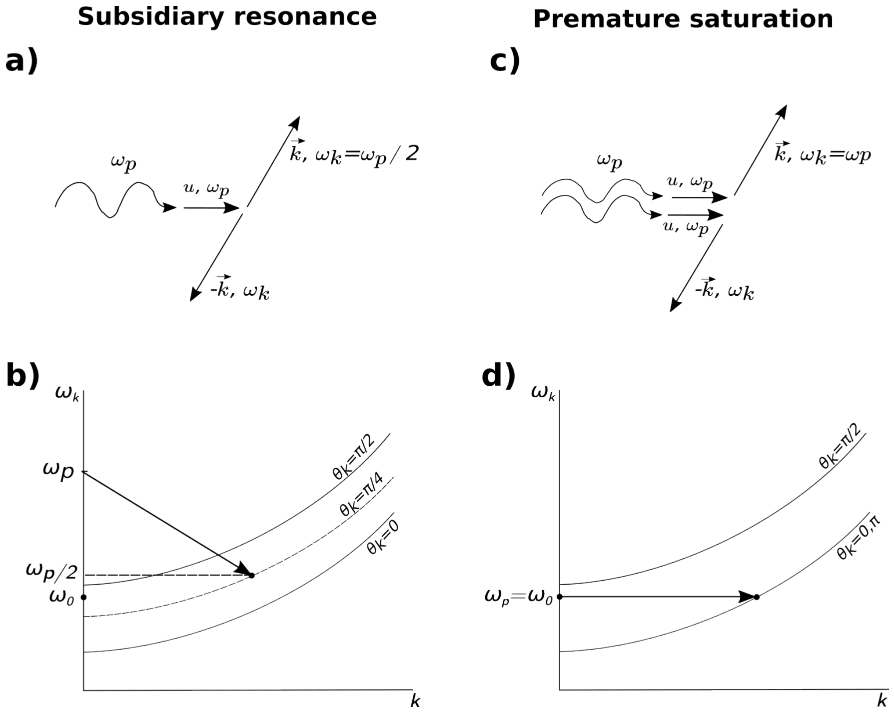

Figure 2.11: a) Diagram of the first order Suhl process b) Illustration of a case of corresponding dispersion relation: at low field ($\omega_p > \omega_0$), the first instability leads to the excitation of magnons at $\omega_p/2$ and $\theta_k = \pi/4$ by uniform magnons excited off-resonance at ω_p. This process results in experiments in a low field subsidiary resonance. c) Diagram of the second order Suhl process. d) At higher fields, when the condition $\omega_p = \omega_0$ is satisfied, the second order process becomes possible. Two uniform magnons excited at resonance are annihilated to create two degenerate magnons at $\theta_k = 0$ and $\theta_k = \pi$. This results in a saturation of the susceptibility χ'' [65]. In schemes a) and c), (u, ω_p) means the uniform magnon of frequency ω_p.

absorption at $H_0 \approx \omega_p/\gamma$. Although spin waves with $k \neq 0$ do not couple directly to the radiation, they can be excited via magnon-magnon interactions [17]. Suhl proposed a theory [12] that explained the first experimental observations of premature saturation by Damon [66] and of subsidiary resonance by Bloembergen and Wang [36]. He did it using a classical approch, expanding the magnetization into a spatial Fourier series [12]. Without giving the details of his calculations, I briefly present here the 2 mechanisms he arrived at as results and which allow to explain subsidiary resonance and premature saturation.

In the first-order Suhl process, spin waves with $\omega_k = \omega_p/2$ in a $\boldsymbol{k}$, -$\boldsymbol{k}$ pair can be driven parametrically by the uniform mode by means of the three-magnon interaction as shown in Figures 2.11 a & b. In this case the uniform mode is driven far off-resonance with $\omega_0 \approx \omega_p/2$. So when the pumping exceeds a certain threshold one observes a *subsidiary* resonance at a field H_0, roughly half the value for the main resonance.

In the second order Suhl process a spin wave pair $\boldsymbol{k}$, -$\boldsymbol{k}$, is driven by two uniform mode magnons with frequency $\omega_0 \approx \omega_p \approx \omega_k$ pumped by the microwave radiation. This is made possible by the four-magnon interaction as illustrated in Figures 2.11 c and d. This process limits the growth of the FMR absorption with increasing microwave power and is therefore called the *premature saturation* of the main resonance [17].

Like the foldover, these Suhl processes are characterized by certain thresholds. The mechanisms involved in these processes must conserve energy and momentum. However the larger the sample, the higher the density of spin waves and the more probable it will be to find spin waves that can satisfy the conservation relations. Thus, the Suhl threshold will generally be smaller as the sample is larger. Since they can couple the uniform mode to other spatially non-coherent modes, they can lead to spin-wave instabilities that will limit the achievement of large angles of uniform precession. For example, only few degrees of uniform precession of the magnetization was achieved in a YIG disk of 160 μm diameter and 4.75 μm thickness in which spin wave instabilities appeared even before the foldover threshold [67] ($h_{Suhl} < h_{foldo}$). A more recent study made on a YIG nanodisk of 700 nm diameter and 30 nm thickness has allowed to reach very large uniform precession angles (of the order of 30°) by significantly postponing the Suhl threshold to an order of magnitude beyond the foldover threshold ($h_{Suhl} > 10\times h_{foldo}$) [22]. This is explained by the strong confinement of the spin wave spectrum following the nanopatterning, which drastically limits the possible nonlinear interactions between the spin waves.

2.6 Other nonlinear effects in ferromagnetic systems

In this section we present other nonlinear effects and some particular configurations that the spin system of ferromagnetic structures can adopt under certain excitation conditions. We have seen that the LLG equation is strongly nonlinear. It is at the origin of a great diversity of nonlinear phenomena that can be observed in ferromagnetic systems. They are part of the large family of nonlinear dynamical systems that can be found in many fields of study such as fluid dynamics (weather for example), astronomy, evolution of reactions in chemistry etc... So it will not be a surprise to find behaviors or phenomena common to these other fields by studying these ferromagnetic systems. They indeed contain a lot of spin wave modes which interact with each other. These interactions lead to various dynamical phenomena including auto-oscillations, period-doubling cascades, quasiperiodicity, turbulence and chaos. For example, Suhl described the premature saturation of the resonance line and the subsidiary resonance, explained previously in section 2.5, as being due to the fact that the spin waves are coupled in second and higher orders to the uniform precession by the demagnetizing fields and, to a less significant extent, by the exchange fields accompanying the spin waves. The coupling is such that certain of the spin waves extract power out of the uniform precession. At ordinary signal levels, this effect merely imposes a small additional loss on the uniform motion; but above a certain threshold signal, the power transfer becomes catastrophic, causing the relevant spin waves to grow with time, initially in an exponential manner. Their growth takes place at the expense of the uniform precession and causes the decrease of the precession angle, until it attains a final value just below that appropriate to the threshold signal. By that time the spin waves have attained a large nonthermal value [12]. Suhl remarked "This situation bears a certain resemblance to the turbulent state in fluid dynamics" [12], which already underlined the similarities that spin waves dynamics could have with fluid dynamics in the nonlinear regime. Other nonlinear effects (auto-oscillations, period-doubling cascades, chaos etc...) are expected at very high excitation and their study will therefore require to go into the deeply nonlinear regime, *beyond* the thresholds of the nonlinear effects described previously in section 2.5 (foldover, subsidiary resonance and pemature saturation).

Among the seminal experimental works on the study of these different nonlinear phenomena, one can mention that of P. Bryant, C. Jeffries and K. Nakamura on a 0.66 mm diameter yttrium iron garnet sphere [68]. They have achieved a kind of phase diagram presenting regions and boundaries of types of observed behavior in the parameters space (P_i,H_0), where P_i and H_0 are respectively the microwave power of the excitation at a frequency f = 9.2 GHz and the applied static field. This is shown in Figure 2.12. We can see that there is a great variety of effects depending on the position in this phase space.

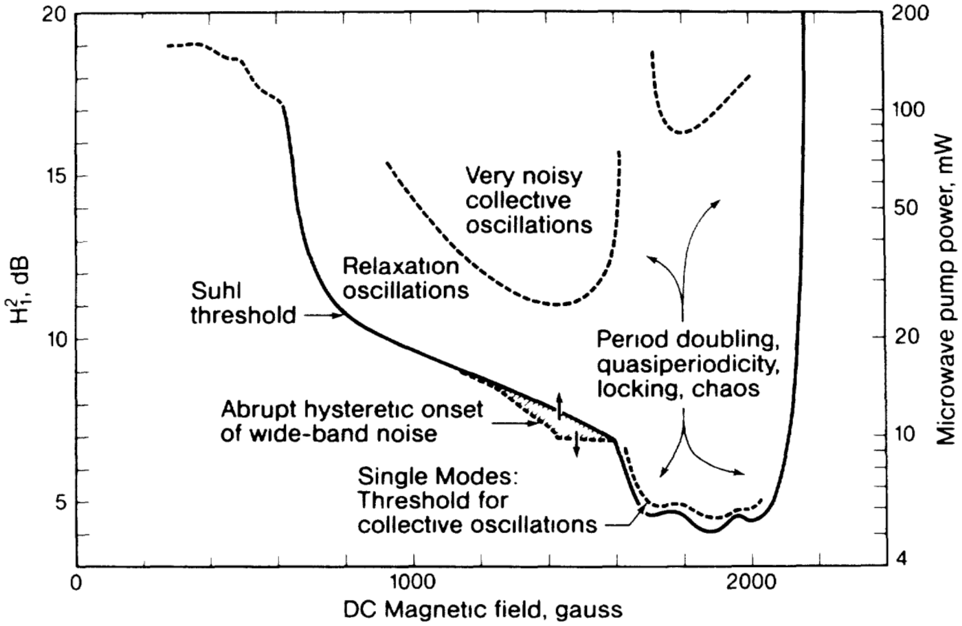

Figure 2.12: Regions and boundaries of types of experimentally observed behavior in the perpendicular-pumped spin-wave instability in an yttrium iron garnet sphere; dc field H_0 vs microwave pump power $P_i \propto H_i^2$ [68]

.

2.6.1 Auto-oscillations, period-doubling route and chaos

The "collective oscillations" in Figure 2.12 are in the range 10^4 to 10^6 Hz and arise from the coupling between microwave spin-wave modes (10^{10} Hz) and are also called auto-oscillations. Indeed, since the earliest studies of spin wave pumping, it is known that as the microwave power is increased beyond the Suhl instability, the radiation absorbed by the sample develops low-frequency (10^4 to 10^6 Hz) coherent oscillations. Their shape and frequency depend on the pumping level, static field value, crystal axis orientation with respect to the static field, and also on sample shape, dimensions, surface polishing, and temperature [17]. Over the years several explanations were proposed for these auto-oscillations. Zakharov, L'vov and Starobinets who were the first to use a nonlinear dynamics approach to the problem, established that the auto-oscillations arise from the back-and-forth dynamic power exchange between parametric modes due to the nonlinear interaction between them [69], the essential ingredient for the nonlinear dynamics being the coupling between two pairs of parametric magnons [17]. These auto-oscillations of the magnetization have been observed in many other experimental works; in micrometer garnet films by directly measuring the temporal variations of the precession angle of the magnetization thanks to optical techniques [24] and in large disks (thickness = 0.45 μm, diameter = 0.6 mm) of YIG by inductive techniques with a microwave cavity [70]. Figure 2.13 shows an example of results obtained by Lührmann et al. in [24]. It can be seen that despite an excitation at f_{ex} = 1420 MHz, the precession of the magnetization shows low frequency auto-oscillations, with a frequency in the order of MHz.

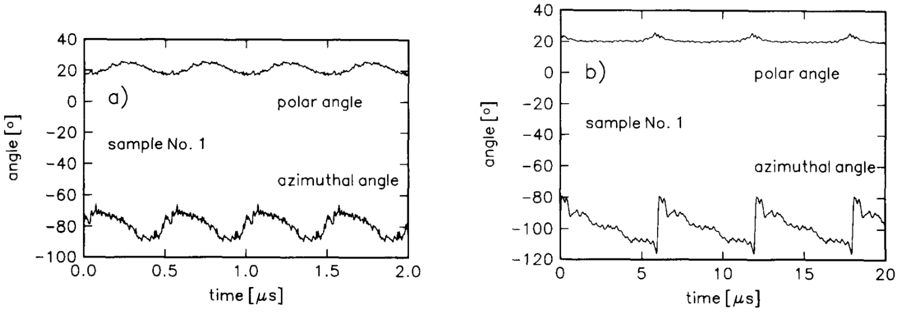

Figure 2.13: Real-time variations of the polar angle θ(t) and azimuthal angle φ(t) at instability conditions. Excitation frequency f_{ex} = 1420 MHz. [24].

In contrast to auto-oscillations, the other manifestations of the nonlinear dynamic behavior such as period doubling, intermittency, chaos are not so easy to observe. They appear only under certain conditions of crystal orientation, static field value and sample shape. This is probably the reason why it took so many years for these phenomena to be observed in spin-wave instabilities [17]. In the standard experimental setup to investigate these manifestations, a magnetic sample is driven by a microwave rf field either parallel or perpendicular to the static magnetic field. The nonlinear dynamic effects are then observed in the amplitude modulation which appears in the microwave field returning from the sample when the pumping is well above the instability threshold [12].

The first observation of a complete period doubling route to chaos was made by Gibson and Jeffries in a ≈ 1 mm diameter gallium-doped yttrium iron garnet (Ga-YIG) sphere [71]. Figure 2.14 shows some results they obtained. These are traces of the modulation appearing in the microwave transmission signal when the incident power exceeds the threshold for the premature saturation. First, they observed auto-oscillations of the magnetization with a frequency 16 kHz (Figure 2.14 a). Then, they found that this mode at 16 kHz displayed a route to chaos. As they increased the driving field, successive period-doubling bifurcations were observed (Figures 2.14 b & c) leading finally to chaos (Figure d). Their results were explained independently by Rezende et al. using a numerical solution of a two-mode model [72, 73] and by Zhang and Suhl [74] with an analytical treatment of essentially the same model. The model assumes that the oscillation results from the dynamic nonlinear interaction between the uniform mode and a degenerate $k \neq 0$ spin wave pair mode.

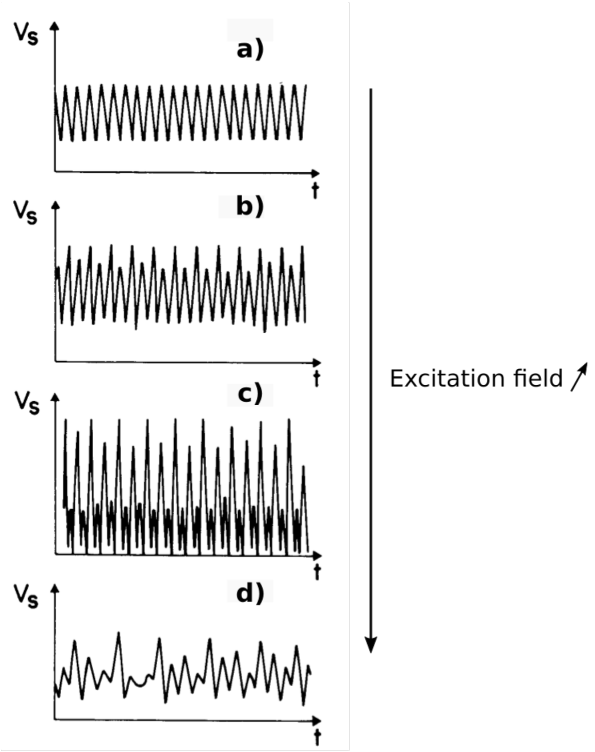

Figure 2.14: Real-time signals for auto-oscillations : a) auto-oscillation frequency f $\approx$ 16 kHz; b) at higher excitation field, bifurcation to f/2; c) bifurcation to f/4; d) chaos. Extracted in [17] adapted from [71].

Several other experimental works have demonstrated such routes to chaos in yttrium iron garnet spheres with typical diameter 1 mm, both for perpendicular-pumped spin waves [75, 76, 77] and for parallel-pumped spin waves [78, 75] and even simulations works [79]. Becker et al. highlighted different types of intermittency between different types of chaotic behavior even within the chaotic regime itself [80]. Bragart et al. calculated the complete phase diagrams of an anisotropic magnetic nanoparticle using the LLG equation and found that even such nanoparticle presents multiple transitions between regular and chaotic behaviors [81].

2.6.2 Bullets and droplets

In a ferromagnet, under certain conditions, rather high excitations can give rise to localized magnetization states. Any localized stable solutions of the dynamical equation of magnetization are called magnetic solitons. Thus, they are nonlinear spin wave modes which appear only at large excitation and which can stabilize under certain conditions. They are therefore completely different from the linear spin wave eigenmodes such as the Bessel-like functions described previously in the case of a perpendicularly magnetized disk. The soliton can be seen as a solitary wave that can propagate without deformation in a nonlinear and dispersive medium. They exist in many fields of physics, for example hydrodynamic solitons involving waves that propagate over several kilometres without weakening. Magnetic solitons can be quasi-one-dimensional, two-dimensional or three-dimensional depending on the ferromagnet dimension. Among the two-dimensional magnetic or spin-wave (SW) solitons, magnetic bullets and droplets have attracted a particular interest because of their unusual properties. Both these types of nonlinear solitonic SW excitations are now considered as promising “working objects” in modern magnonics and spintronics, and could be used for the development of a new generation of microwave information processing devices [82]. Quasi-one-dimensional and two-dimensional SW envelope solitons were first experimentally observed in YIG films [83] just after its theoretical prediction [84].

2.6.2.1 Bullets

Spin-wave bullets are the two-dimensional SW soliton pulses strongly localized in space and time by self-focusing. They are similar to light bullets in optics which are localized pulses of electromagnetic energy that can travel through a medium and retain their spatiotemporal shape in spite of diffraction and dispersion which tend to spread the pulse. This is made possible by a balance between the nonlinear self-focusing and spreading effects brought about by the medium in which the pulse beam propagates. SW bullets were experimentally observed by Bauer et al. in [85]. They studied a large (1.8 x 2.6 cm) sample of a high-quality epitaxial YIG film magnetized to saturation by a tangential bias magnetic field. Thanks to a microwave antenna, they excited a two-dimensional SW packet. The spin waves were created in the YIG film by the propagating wave packets. The distributions of SW intensity were measured by a space- and time-resolved BLS technique which allow them to deduce the two-dimensional distributions of propagating SW bullet intensity. In the experiment, the SW bullets were formed as a result of a spatiotemporal self-focusing, similar to the self-focusing effect in optics, as the two-dimensional input SW packets were self-focused for both in-plane directions (y and z), while propagating along z direction, see Figure 2.15. The self-focusing of dipolar SW bullets in YIG films was stabilized by dissipation [85].

Indeed, it is well-known that in the absence of dissipation, two dimensional self-focusing of an initial wave packet leads to the packet collapse only if the packet's amplitude is sufficiently large for nonlinearity to overcome the effects of diffraction and dispersion [86]. Such a two-dimensional collapse is a threshold process, and it has an amplitude threshold. But, in the presence of dissipation, the amplitude of a self-focusing wave packet decreases exponentially with time, and with the decrease of the amplitude, the focusing effect of nonlinearity also decreases. This leads to a collapse stabilization, and a subsequent defocusing of the packet when its amplitude becomes smaller than the collapse threshold [86].

This is what happens in YIG films where the influence of dissipation on SW bullets is even much stronger than the similar dissipative effect on light pulses in optical fibers. Thus, the two-dimensional collapse of dipolar spin waves in YIG films is rapidly stabilized by dissipation, and a quasi-stable SW bullet is formed. Such a bullet propagates for a certain distance without changing its spatial sizes (but constantly losing energy due to dissipation). Then, at some point it starts to diverge in space, when its amplitude is not anymore sufficient for self-focusing. It is important to stress that a SW bullet is not a stable two-dimensional envelope soliton, but a quasi-stable self-focusing wave packet whose the collapse has been stopped by dissipation [83].

At almost the same time when SW bullets were observed in magnetic films [85], it has been theoretically predicted [87, 88, 89] and experimentally observed [33, 90, 91, 92, 93, 94, 95] that spin-polarized current passing through a thin "free" magnetic layer of a magnetic bi-layered structure, can excite microwave magnetization oscillations. Then, this discovery made possible SW excitations driven by a spin-polarized current in an in-plane magnetized magnetic nanocontact (NC). These excited spin waves indeed modulate the magnetoresistance of the NC and can be therefore detected as a microwave voltage signal

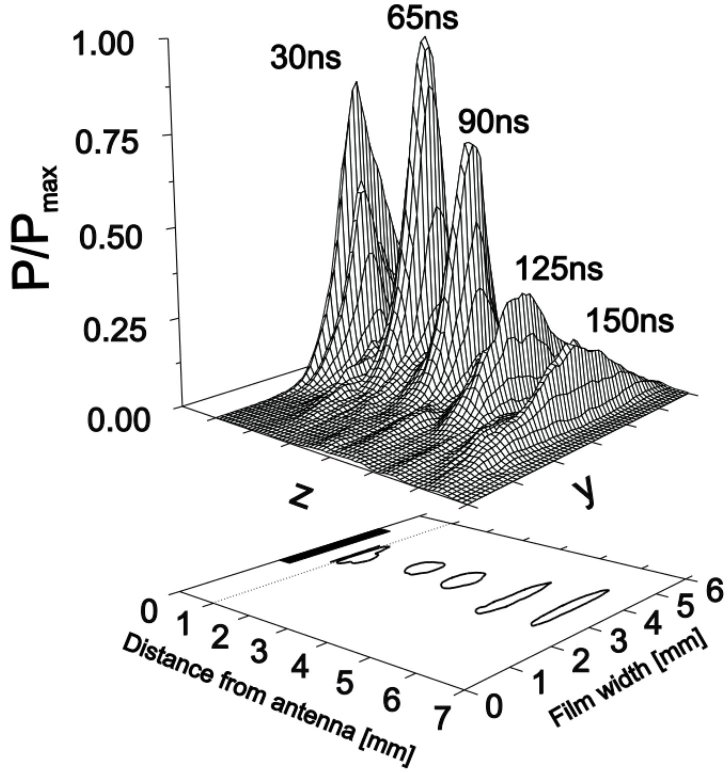

Figure 2.15: Two-dimensional (y,z) distributions of normalized intensity in propagating dipolar spin wave packets, corresponding to five different values of the propagation (delay) time as indicated in the figure. The distributions were experimentally measured by space- and time-resolved BLS technique for T = 29 ns and P_{in} = 460 mW. The cross sections of the propagating wave packets taken at half-maximum power are shown on the (y,z) plane below [85].

: it is then referred to as a nanocontact spin transfer oscillator (NC-STO). By studying the angular dependence of spin wave excitations in such a NC-STO, Bonetti et al. demonstrated that two distinct spin wave modes can be excited, an exchange-dominated propagating spin wave and a self-localized nonlinear spin wave bullet [96]. Figure 2.16 shows the result they obtained, for an external magnetic field of constant magnitude ($\mu_0 H_e = 1.1$ T) applied to the sample[4] at an angle θ_e with respect to the film plane.

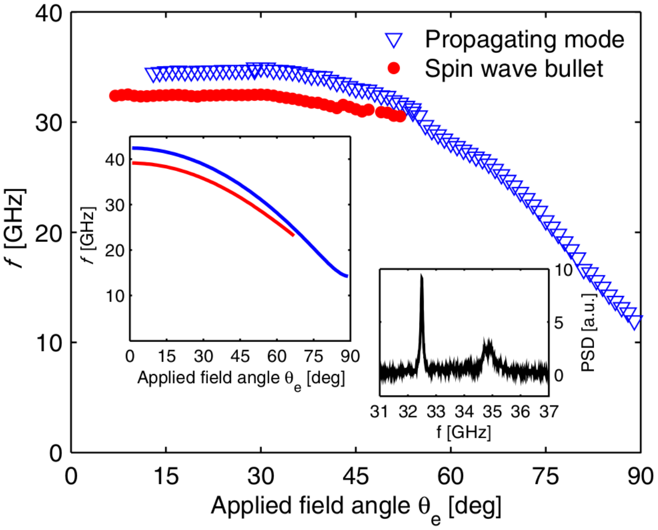

Figure 2.16: Measured frequencies of the observed spin wave modes as a function of the applied field angle θ_e at $I = 14$ mA and $\mu_0 H_e = 1.1$ T. Left inset: theoretically calculated frequencies of the propagating (upper curve) and bullet (lower curve) modes at the current threshold, for nominal parameters of the nanocontact STO. Right inset : power spectrum at $\theta_e = 30$ deg, $I = 14$ mA [96].

.

This excitation of a propagating mode or a SW bullet mode according to the applied static field angle can be explained by the sign of the nonlinear frequency shift coefficient N, characteristic parameter of the NC-STO which is a nonlinear oscillator [34]. It turns out that this nonlinear frequency shift coefficient N of spin-torque oscillators strongly depends on the direction of the bias magnetic field and can be positive or negative. Figure 2.17 shows an

---

[4] A $Co_{81}Fe_{19}$(20nm)/Cu(6nm)/$Ni_{80}Fe_{20}$(4.5 nm) thin film trilayer with on top a circular Al nanocontact having a 40 nm nominal diameter.

example of the evolution of N for an isotropic magnetic film, as a function of the out-of-plane angle θ_0 of the external bias magnetic field for several values of the magnitude of this field [34]. One can see that N is a monotonically increasing function of θ_0, and is negative for an in-plane magnetized film ($\theta_0 = 0°$) and positive for a normally magnetized film ($\theta_0 = 90°$). This is also the change of the sign in front of M_{eff} between equations (2.19) and (2.25) when going from a normally magnetized film to an in-plane magnetized film. There is therefore a critical angle θ_{cr} between 0 and 90° where $N = 0$.

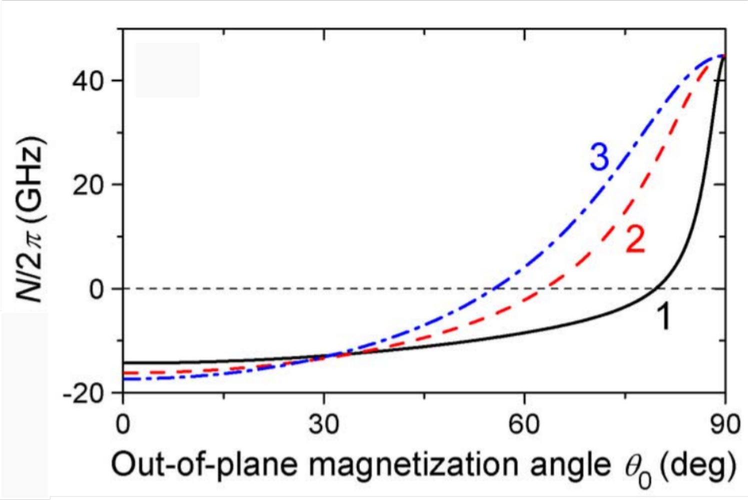

Figure 2.17: Nonlinear frequency shift coefficient for an isotropic magnetic film (saturation magnetization $4\pi M_0 = 8$ kG) as a function of the out-of-plane magnetization angle θ_0 for several magnitudes of the external bias magnetic field H_0 : 1) $H_0 = 10$ kOe, 2) $H_0 = 15$ kOe, 3) $H_0 = 20$ kOe. [34].

Whatever the direction of the applied field (and thus the value of N), it is possible to excite spin waves which will propagate from the nanocontact to the rest of the film due to the exchange interaction. This corresponds to the progagating mode, blue curve on Figure 2.16. The frequency of this mode is indeed given by [97]:

$$\omega(k) = \omega_0 + Dk^2 + N(\theta_0)|a|^2 \tag{2.72}$$

where k and a are the wave number and the complex amplitude of the excited mode respectively, ω_0 is the FMR frequency of the free layer, and D is the spin wave dispersion coefficient determined by the exchange interaction.

For this mode, ω is typically higher than ω_0 [96], which makes possible the propagation to the rest of the film.

When $\theta_0 < \theta_{cr}$, the nonlinear frequency shift $N < 0$ and can therefore counteract the spread of the spin wave profile related to the dispersion [96]. We can thus have the formation of a mode whose frequency ω is *below* the frequency ω_0 of the film. Consequently, it will not be able to propagate and will have a non-propagating evanescent character [97]. This is a standing SW bullet : a self-localized nonlinear spin wave mode of finite amplitude a_0 [96], see the red curve in Figure 2.16. Thus, on Figure 2.16, we find $\theta_{cr} \approx 55°$. The frequency of the SW bullet mode is [97] :

$$\omega(k) = \omega_0 - |N(\theta_0)||a_0|^2 \tag{2.73}$$

which confirms that its frequency is shifted by nonlinearity below the spectrum of propagating linear spin waves.

2.6.2.2 Droplets

Magnetic droplet solitons are a localized region of highly excited spin waves that form in thin films with perpendicular magnetic anisotropy [98]. They were predicted to occur in materials without magnetic damping and to require a non-equilibrium spin-wave (or magnon) population [99, 11]. For these reasons, it was not possible to study them experimentally until the discovery of spin torques associated with spin current mentioned previously. Such spin torque can indeed compensate the magnetic damping in a magnetic material, thus creating the conditions for the formation of "dissipative droplet solitons" [100] which were predicted to occur in a nanocontact to a ferromagnetic layer [101]. Spin-current flowing through the nanocontact leads to spin-wave excitations that localize in the nanocontact region, forming a droplet soliton.

A droplet is nearly a circular region of suppressed z-component of magnetization in which spins precess about the z axis, in the x–y plane (Figure 2.18). At its center, the spin-precession amplitude is minimal and the magnetization is nearly reversed (i.e $m_z \approx$ -1), while at the droplet boundary (i.e $m_z \approx$ 0), the spin-precession amplitude is maximal [98]. A profile indicating the spin precession is shown in Figure 2.18.

As stated above, the formation of a droplet requires a spin-transfer torque. For this purpose, the typical sample for an experiment consists of two ferromagnetic layers separated by a non-magnetic layer. One of the ferromagnetic layers, the free layer (the magnetic layer that responds to the spin torques), has perpendicular magnetic anisotropy (PMA) and the other ferromagnetic layer, the fixed or polarizer layer, usually has in-plane magnetic anisotropy

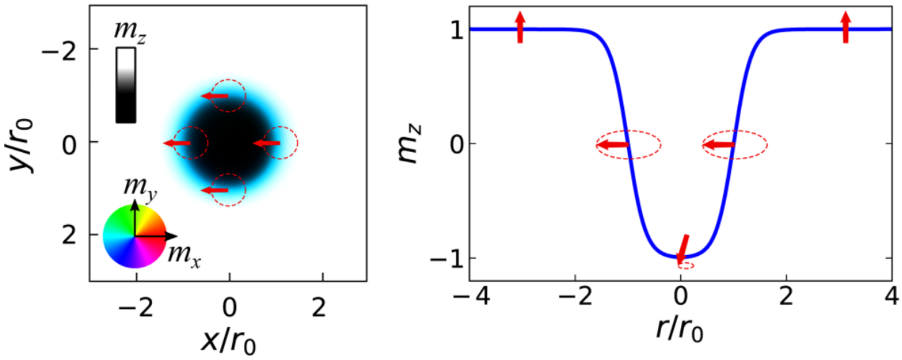

Figure 2.18: Schematic of a droplet soliton. Left : droplet in a nanocontact with radius r_0 . The color indicates the direction of magnetization. Right : Profile through the droplet core. Spins precess about the anisotropy field, i.e., normal to the film plane. At the droplet boundary, the precession amplitude is maximum, as indicated by the red arrows [98].

[98]. The PMA comes from interface effects resulting from such a stacking of layers. Mohseni et al. performed the first demonstration of droplet formation using such a sample configuration with a Co fixed layer and a [Co/Ni multilayer] free layer with a magnetization along the film normal because of the PMA sufficiently strong to overcome the demagnetization field [100].

Since these first works, many other experimental studies have highlighted the formation of magnetic droplets generated using the spin-transfer torque driving mechanism and studied among other things, the influence of temperature, their strong hysteretic response to fields and currents [102], their drift instability [103], the parametric autoexcitation of magnetic droplet soliton perimeter modes [104], the direct imaging of a droplet using scanning transmission x-ray microscopy [105], the freezing of droplets solitons [106].

Moreover, dissipative solitons are often robust attractors and can exhibit exotic dynamics, such as time-periodic breathing [107].

2.7 Conclusion

We have demonstrated the two variants of the Kittel formula for a thin film with perpendicular anisotropy in the two cases where it is magnetized along its normal and in-plane. These two relations will be used in the analysis of the experimental results in the linear regime. The eigenbasis of the standing spin waves of a perpendicularly magnetized thin nanodisk, described here, will later form the foundation of our spectroscopic studies on BiYIG nanodisks. In the same way, the detailed study of the foldover and the presentation of the associated previous experimental results in the case of the YIG nanodisk will allow us to analyse the experimental results of BiYIG nanodisks in the non-linear regime while putting them in perspective with those of YIG and some of the nonlinear effects we have briefly presented in section 2.6.

Summary

- Derivation of the Kittel formula for a thin film with perpendicular magnetic anisotropy in both cases of a static field applied in-plane and perpendicular to the film.
- Brief description of ferromagnetic relaxation and microwave field driven FMR.
- Presentation of the spin waves eigenbasis of a normally magnetized thin nanodisk: focus on the internal field profile within the disk.
- Detailed study of the nonlinear effect of foldover of the resonance line and nutation of magnetization around the large amplitude precession coherent motion.
- Brief presentation of nonlinear effects such as auto-oscillations and chaos, nonlinear spin wave modes droplet and bullet magnetic solitons.

Chapter 3

Methods : experimental setup and sample

"Great things are not done by impulse, but by a series of small things brought together."

Vincent van Gogh, **October 1882**

Contents

In this chapter, we present the material on which this study is based. On the one hand, it is the experimental setup used for all our measurements, namely the magnetic resonance force microscope (MRFM) and on the other hand, the sample studied, consisting of BiYIG nanodisks. We will present the MRFM basic principle as well as a brief summary of its experimental realization. Then we will highlight the characteristics and performance of the main elements that constitute this microscope and we will underline the peculiarities of the sample. Finally we will show the influence that the probe can have on the measurements and how we are able to overcome it.

3.1 Magnetic resonance force microscopy

3.1.1 Origins of the technique

The basic idea of the MRFM is to use a mechanical detection of the ferromagnetic resonance to measure the static component of the magnetization. The first mechanical detection of the longitudinal component of the magnetization was carried out in 1956 by Evans on a system of paramagnetic spins, using a Faraday balance type device. However, it required a strong static magnetic field gradient at the sample for a good sensitivity, which limited the resolution of the technique. For these reasons, it was not developed at that time. It is only in the 1980s and the development of near-field microscopies such as Atomic Force Microscopy (AFM) and Magnetic Force Microscopy (MFM) that the idea of a mechanical detection of the longitudinal component was again considered. This is how Sidles, who was searching for a precise technique of measurement to study the structure of biological objects, proposed a technique in 1991. He suggested the idea to couple a highly sensitive force detector like a micrometer sized cantilever to the longitudinal component of magnetic moment of either nuclear or electronic spins [108]. Dan Rugar's team (IBM Almaden) detected for the first time in 1992 an NMR signal by MRFM [109], while Phil Wigen and Chris Hammel's team, in 1996, measured a FMR signal by the same technique [110]. The MRFM therefore clearly appears as a powerful technique that can detect the longitudinal component of the magnetization of a ferromagnetic sample [111, 112, 52, 113, 114, 115, 116, 65].

3.1.2 Principle of mechanical detection

MRFM has similar principles as magnetic force microscopy (MFM) in which the interaction between a probe (a magnetic tip) and a magnetic sample is used to reconstruct the magnetic structure of the sample surface. This technique is also called mechanical-FMR, since a mechanical setup is used for the detection of FMR, as shown in Figure 3.1. The detector is a very soft cantilever with a magnetic particle at its end, both constitute the probe. It is first placed at a certain distance above the studied sample which is itself magnetic. The whole system is placed in a static magnetic field. A dipolar interaction occurs between the two. The probe, of magnetic moment m_p then undergoes the force :

$$\boldsymbol{F} = m_p.\nabla \boldsymbol{B} \tag{3.1}$$

where $\boldsymbol{B}$ is the magnetic field created by the sample at the location of the probe. Then, under the appropriate conditions, the excitation field $\boldsymbol{h}$ produced by a microwave antenna usually integrated during the sample fabrication (see section 3.3) allows to excite the FMR in the sample. This leads to a decrease in the static (longitudinal) component of the magnetization M_z and therefore a modification of the static interaction between the probe and the sample. We can then measure ΔM_z by detecting the variations in the amplitude vibrations of the cantilever using a laser beam that reflects at the end of the cantilever towards a two-quadrant photodiode.

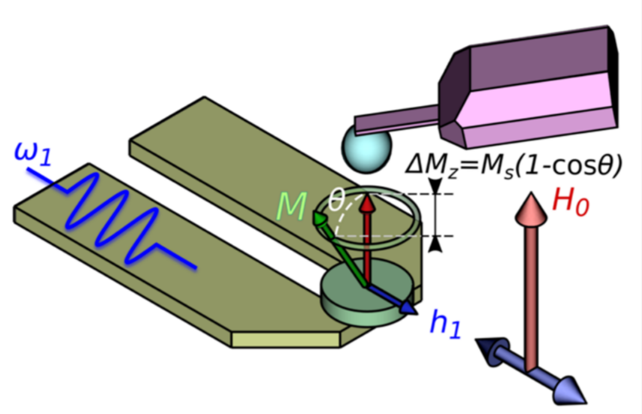

Figure 3.1: Schematics of the experiment. A microwave field $\boldsymbol{h}_1$ of pulsation ω_1 drives the magnetization $\boldsymbol{M}$ of a nanodisk into FMR, opening a precession angle θ around the perpendicularly applied field H_0. The associated variation in the longitudinal component of the magnetization, ΔM_z, is mechanically detected by the cantilever of a magnetic resonance force microscope.

$$h_{rf} \xrightarrow[\textcircled{1}]{\substack{\boldsymbol{M \wedge H_{eff}} \\ \text{(LLG)}}} \Delta M_z \xrightarrow[\textcircled{2}]{m_p.\nabla \boldsymbol{B}} \Delta F \xrightarrow[\textcircled{3}]{k.\Delta z} \Delta z$$

Figure 3.2: Summary of the signal detection steps.

Figure 3.2 summarizes the signal detection steps.

① The application of a rf field induces a torque $\boldsymbol{M}\text{x}\boldsymbol{h}_{rf}$ on the magnetization of the sample through the gyroscopic term $\boldsymbol{M}\text{x}\boldsymbol{H}_{eff}$ of the LLG equation ($\boldsymbol{h}_{rf}$ is included in $\boldsymbol{H}_{eff}$). At the resonance, this torque opens a precession angle θ of the magnetization, which decreases its longitudinal component by ΔM_z.

② This variation of M_z in the sample modifies the field $\boldsymbol{B}$ created by the sample on the probe at the apex of the cantilever and therefore the corresponding force $m_p.\nabla\boldsymbol{B}$.

③ This variation of force creates a variation of deflection of the cantilever of Δz which one measures finally through an optical detection.

3.1.3 Experimental realization

Figure 3.3 shows images of the MRFM (a & b) and a drawing of its design conception (c). It consists of two blocks. There is the optical block, the upper part in Figure a, which includes the laser and the cantilever, and which allows to measure its deflection. Then there is the bottom block which includes the microwave circuit, the sample and the piezoelectric scanner which allows to move it; a zoom is shown in b.

The microscope is placed between the poles of an electromagnet that can apply a homogeneous magnetic field H, which can reach 1.1 T, the current flowing through the coils being about a hundred Ampere. So they need to be cooled continuously. This field can be applied perpendicular (see Figure 3.3 a) or in the plane of the sample. A crucial point in our experiments is to place the probe quite close above the sample (the typical separation is between 1 and 2 μm). To achieve this, the cantilever is first roughly aligned with the sample over a few tens of micrometers using piezoelectric motors. After this first step, a more precise alignment is done using a piezoelectric tube on which the sample is mounted (see (3) in Figure 3.3 c) and which allows lateral displacements of a few tens of microns and vertical displacements of about 2 microns with a nm resolution. This tube requires the application of high voltage to the electrodes. The whole set is placed in a vacuum chamber with a pressure of about 10^{-5} to 10^{-6} mbar which allows to gain several orders of magnitude on the quality factor of the cantilever, which will allow to amplify the measured signal. The microscope operates at room temperature. It is stabilized at a value around 15°C using Peltier modules. Finally, the fine positioning of the probe above the sample is done by minimising (in the perpendicular configuration) the frequency of the cantilever above the sample as will be explained later.

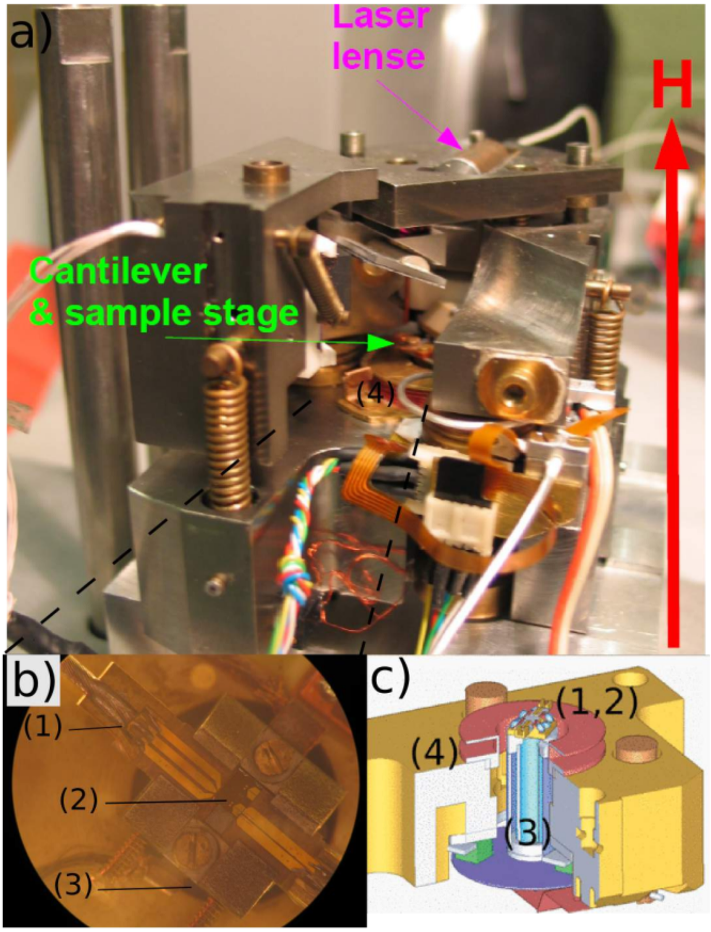

Figure 3.3: a) General view of the MRFM microscope used during this thesis. The MRFM is placed in the middle of a 1.1 T electromagnet. b) image of the MRFM bottom. c) Drawing of the MRFM design conception. The top part with the cantilever and the optical detection is not shown. The numbers indicate the visible parts that are shown in b) - (1) microwave circuit, (2) sample location (3) piezoelectric scanner, (4) modulation coil (not used in this thesis).

3.1.4 MRFM signal measurement

As explained previously, the measurement of the cantilever motion is done by optical deflection using a laser and a photodiode split in two quadrants A and B (see Figure 3.4 a). It is then possible to access to two signals, a signal "A+B" proportional to the total light intensity received by the photodiode and thus gives access to the power of the laser, and a signal "A-B" proportional to the difference in light intensity received by the two quadrants and thus gives a direct access to the deflection of the cantilever. This voltage "A-B" in mV can then be converted into the deflection of the cantilever in nm as we will see later.

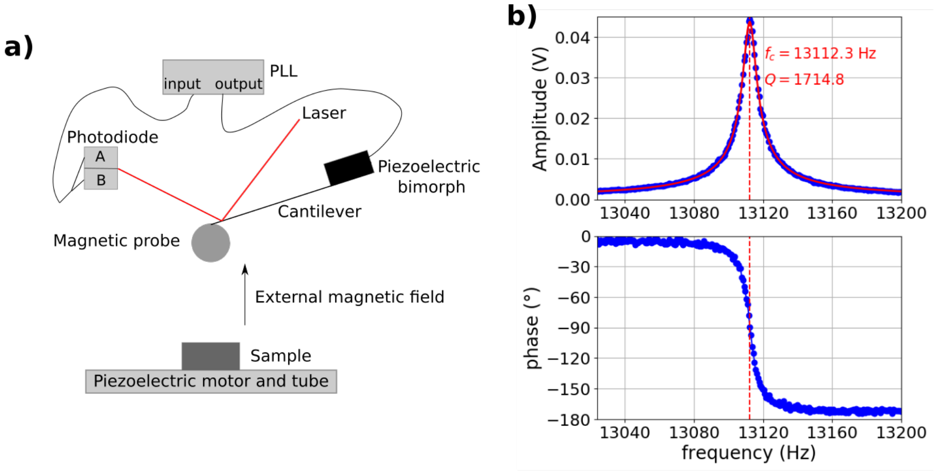

Figure 3.4: a) Principle of MRFM signal detection. b) Typical curves of the amplitude and phase response of the cantilever as a function of the output frequency of the piezoelectric bimorph.

In MRFM, the cantilever of frequency f_c is used as a detector and to increase the signal to noise ratio, the microwave excitation within the sample is modulated at the frequency f_c in order to make the cantilever sensitive to the magnons created in the sample. To monitor f_c permanently, we use a phase-locked loop (PLL) which has as input the A-B signal while its output is connected to a piezoelectric bimorph which excites the cantilever as shown in Figure 3.4 a. Using the phase difference between input and output as a feedback signal, it adjusts its output frequency so that the phase shift between input and output corresponds to -90°, synonymous with the resonance of the cantilever. The motion of the cantilever is indeed the one of a damped harmonic oscillator in forced regime as show the typical curves of its amplitude and phase response in Figure 3.4 b. A Lorentzian fit of the amplitude curve gives it resonance frequency $f_c = 13$ kHz and its quality factor $Q = 1715$. Q varies with vacuum and can reach 2000 in the best vacuum conditions in our experiments (cf. Figure 3.6).

So, the resonance of the cantilever is tracked in real time. It is also possible to keep the amplitude of the cantilever oscillations constant by controlling the amplitude of the excitation voltage of the piezoelectric bimorph through a proportional-integral-derivative (PID) loop. When the microwave resonance is excited in the sample, magnon excitations are created in the GHz range as explained in the previous chapter. The cantilever frequency being in the kHz range, it is first not sensitive to the magnetization dynamics. So it is necessary to modulate the magnetization dynamics in the sample at f_c. This is done by directing modulating the microwave excitation at this frequency f_c : in the experiment the microwave source is alternatively turned on and off at the cantilever frequency. The probe of the cantilever becomes therefore sensitive to an additional force induced by the decrease of the longitudinal magnetization ΔM_z in the sample (force which oscillates at f_c). The PID loop which until then applied a constant voltage to maintain the amplitude of the oscillations constant will then adapt to this new force by changing the amplitude of the excitation voltage. It is this voltage variation that constitutes our MRFM signal. The new force being created at f_c, with this modulation technique the vibrations amplitude of the cantilever is multiplied by its quality factor Q.

Notice that since the modulation period $1/f_c$ in the μs range is large compared to the relaxation time of the magnetization in the ns range, the MRFM measurement is always a static measurement of the magnetization dynamics.

3.2 Characteristics of the setup

This thesis followed my master internship which was done in the same lab. Until the beginning of the internship, the same magnetic probe, a spherical FeSi particle of 700 nm diameter which was glued at the apex of the cantilever [56], was used in the set-up for 12 years, between 2007 and 2019. This cantilever broke during my internship. For all the work done during this thesis, we used a new generation of mechanical detectors for the MRFM. It consists of cobalt nanospheres grown directly on cantilever tips by focused electron beam induced deposition (FEBID) [117], fabricated by our collaborator Dr Soraya Sangiao of Departamento de Fisica de la Materia Condensada of Universidad de Zaragoza in Spain.

3.2.1 Cantilever

Let's consider a simple beam clamped on one side. Applying a force perpendicular to the beam at its end will bend it. A knowledge of the beam characteristics allows to deduce the associated displacement. Our goal being to measure very small forces, such a simple beam appears to be the ideal force detector and can therefore be used as a cantilever. Figure 3.5 shows a schematic of such a model cantilever, of length l, width w and thickness t.

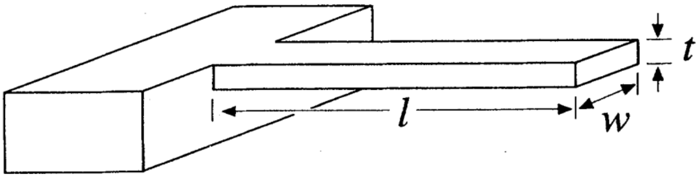

Figure 3.5: Modelisation of a simple cantilever [118].

Even in the absence of any external force, the cantilever vibrates due to the thermal energy associated with the temperature T at which the entire experimental setup is maintained. This Brownian motion of the cantilever is related to its intrinsic characteristics which are its resonance frequency f_c, its quality factor Q and its spring constant k. It is this thermal noise that defines the detection limit of the cantilever. We can show that the minimum detectable force, in a detection bandwidth B is given by [118] :

$$F_{min} = \sqrt{\frac{4k_BTBk}{\omega_c Q}} \tag{3.2}$$

where k_B is the Boltzmann constant and $\omega_c = 2\pi f_c$. The conditions for the highest cantilever sensitivity are a high quality factor Q, a high resonance frequency f_c and a nominal spring constant k. To this thermal force is associated the thermal amplitude of the vibrations of the cantilever :

$$a_{min} = \sqrt{\frac{4k_BTBQ}{\omega_c k}} \tag{3.3}$$

For our cantilever, we use a commercial Olympus biolever, with a design similar to the one shown in Figure 3.5 and a typical spring constant $k = 6$ mN.m^{-1}. Using the values of $Q \approx 2000$ and $f_c = 13$ kHz calculated previously, at $T = 290$ K one finds $F_{min} = 0.77$ fN/$\sqrt{Hz}$ which means that the force sensitivity is less than 1 fN/$\sqrt{Hz}$ at room temperature. One also finds a_{min} = 2.6 Å/$\sqrt{Hz}$.

The characteristics of the cantilever (with the probe at the apex) can also be determined from its thermomechanical noise. It can directly be recorded as a function of frequency in $\mathrm{mV}/\sqrt{Hz}$ thanks to a demodulator. It is shown in Figure 3.6. The measurement is done under vacuum (10^{-6} mbar) and at $T = 290$ K. The Lorentzian shape confirms the quality of the oscillator. The cantilever frequency and its quality factor are extracted from the Lorentzian fitting curve in red. Using the nominal spring constant ($k = 6$ mN.m^{-1}), the amplitude a_{min} in $\mathrm{nm}/\sqrt{Hz}$ is calculated thanks to the equation (3.3). One deduces the conversion factor $conv$ between a_{min} and the measured amplitude in $\mathrm{mV}/\sqrt{Hz}$, see Figure 3.6. We find $conv$ on the order of 1 nm/mV.

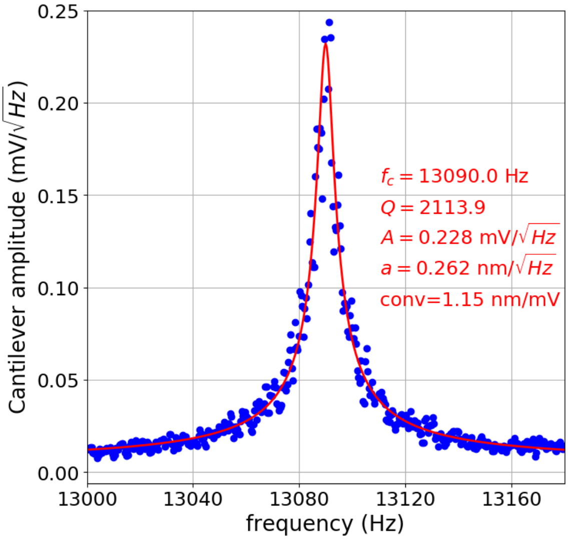

Figure 3.6: Thermo-mechanical noise of the cantilever : the measurement is done at zero field and by positioning the probe very far away from the sample, i.e. in the absence of interaction between the probe and the sample.

3.2.2 Magnetic probe

The probe used in this thesis is a 500 nm diameter Cobalt nanosphere. It is one of a batch of probes grown in September 2019. Based on previous experience of using probes fabricated in the same way, for the sake of stability, it was grown on top of a small roughly cylindrical Co-FEBID pedestal as shown on Figure 3.7 c. One of the main advantages of the spherical shape is that it has no shape anisotropy and preserves the axial symmetry of the studied samples. However, the spherical probe is no longer magnetized at zero field, which limits or even prevents MRFM measurements at very low field. This small pedestal also allows to circumvent this limitation since it makes it possible to keep a non-zero magnetization even at almost zero field because of the cylindrical shape. Before using it to measure samples, we need to characterize the magnetic probe to determine its magnetic moment as a function of the applied field. We have used two methods to do this.

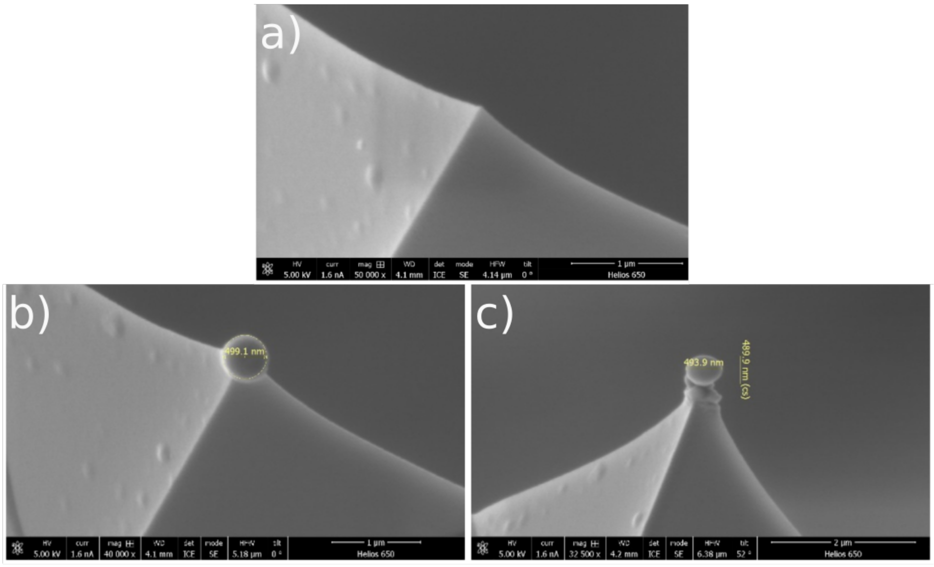

Figure 3.7: a) Scanning electron microscopy (SEM) image of the bare Biolever cantilever. SEM images of the 500 nm diameter Co nanosphere grown by FEBID - b) top view and c) front view.

In the first one, a sample whose characteristics are well known is used. It is a cylinder of $Co_{64}Fe_{65}Ni_{15}Si_{14}B_{14}$ alloy with a saturation magnetization of 5.1×10^5 A/m determined by SQUID magnetometry [119], about 16 μm in diameter and 1 mm long, surrounded by a glass sheath which protects it from oxidation as shown in Figure 3.8. To characterize the probe, magnetometry measurements are performed with the MRFM. They consist in monitoring the mechanical resonance frequency of the cantilever as a function of the applied magnetic field. One plunges the tip of the cantilever in the field gradient produced by the magnetic cylinder, as indicated in the sketch of Figure 3.8. The effective spring constant of the cantilever depends on the magnetic force acting on it, which is proportional to both the nanomagnet's magnetic moment

m_p and the field gradient $\partial B_z/\partial z$, considered to be along z [120], see equation (3.1). We can show that (see appendix A.2 for the calculation) the resulting cantilever frequency shift due to the presence of the magnetic moment at its end then writes [120]:

$$\frac{\Delta f_c}{f_c} = -\frac{m_p}{2k}\left[\frac{\partial^2 B_z}{\partial^2 z}\right]_{z_0} \tag{3.4}$$

where z_0 indicates the equilibrium position of the nanomagnet in the field gradient. It follows that if k and $\partial^2 B_z/\partial^2 z$ are precisely known in equation (3.4), a quantitative determination of m_p is possible. Owing to its shape anisotropy, the magnetic cylinder is expected to be fully saturated along its symmetry axis z even at low applied magnetic field. One measures the variation $\Delta f_c/f_c$ at different altitudes of the probe above the cylinder. In order to calibrate these measurements, we used as reference similar measurements made with the 700 nm FeSi probe and under the same experimental conditions (same probe-cylinder separations). The characterization of this probe gave a magnetization $M_{\text{FeSi}} = (1.55 \pm 0.07)\times10^{6}$ A/m, which for a radius $R = (350 \pm 30)$ nm determined by SEM imaging, corresponds to a magnetic moment $m_{\text{FeSi}} = (2.8 \pm 0.7)\times10^{-13}$ A/m^2 [120].

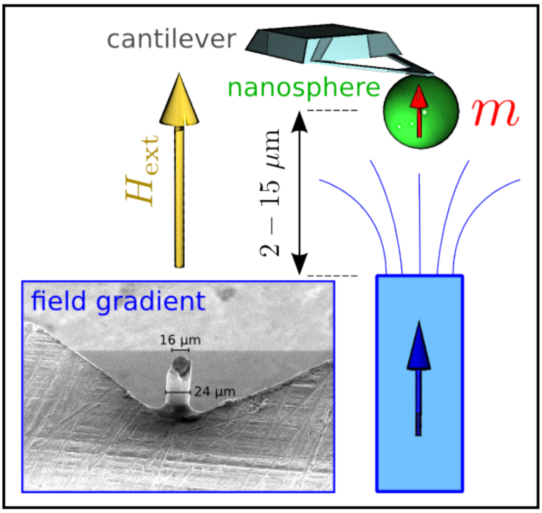

Figure 3.8: Sketch of the experimental setup to perform the probe magnetometry. The cantilever with the magnetic nanosphere at its tip is plunged in the field gradient of a magnetic cylinder (see SEM image in lower left inset). [120]

In Figure 3.9, we show the typical relative frequency shifts measured as a function of field for the Co-FEBID nanosphere. We can compare the relative frequency shifts measured to the one measured for the reference FeSi probe at the same separation with the magnetic cylinder. Since they are positioned roughly at the same altitude above the cylinder, the field gradient in which the two nanomagnets are plunged is approximately the same. From these measurements, we can infer the ratio between the magnetization of the 500 nm Co sphere and the one of the well-known 700 nm FeSi reference sphere. For better accuracy, we have repeated these measurements at different tip-cylinder separations, between 10 and 30 μm. We extract that on average $(\Delta f_c/f_c)_{[700\text{ nm FeSi}]} = (6 \pm 1)\ (\Delta f_c/f_c)_{[500\text{ nm Co-FEBID}]}$. Finally, from the magnetic moment of the reference probe, we deduce the one of the Co nanosphere $m_{\text{Co-FEBID}} = m_p = (4.7 \pm 1)\times 10^{-14}$ A/m^2.

In the second method, we use the saturation field of the probe. The variations in the relative frequency shift in Figure 3.9 directly correspond to the variations of the probe magnetic moment (the spherical part and the pedestal magnetic moments) as shown by the images. At high field, we observe a saturation of the frequency shift above $H_s = 0.5$ T. Above this field, the probe is saturated, the probe-cylinder interaction is constant and the frequency variation is therefore constant. From this field, there is a linear increase of $\Delta f_c/f_c$ when the field is reduced, which corresponds to the desaturation of the spherical part. At low field the linear variation continues until a given field around 0.1 T where there is a change in the slope : this is the saturation field of the pedestal. Due to the presence of a pedestal, the direct reading of the saturation field is less obvious than the case of a perfect sphere[1]. As explained previously, we can see that the pedestal allows to keep the magnetization of the probe at low field. For example, at 0.1 T, the probe still has almost 50% of its total magnetization, a value which would be less than 25% if the sphere was alone. Assuming that we only have a sphere, from the saturation field $H_s = 0.5$ T, we can calculate its magnetization M_p. For a perfect sphere without crystalline anisotropy, it is indeed only governed by demagnetizing effects, and is given by $H_s = \mu_0 M_p/3$. With this formula we deduce M_p. Then by multiplying by its volume $4\pi R_p^3/3$, we deduce its magnetic moment. The measurement of its radius is made on the SEM images in Figure 3.7. We find $R_p = 495/2 = 247.5$ nm and $m_p = (7.6 \pm 1)\times 10^{-14}$ A/m^2.

Combining the two methods gives $4.7\times 10^{-14} < m_p < 7.6\times 10^{-14}$ A/m^2.

---

[1] We obtain the two saturation fields by taking the intercept of the tangent of the curve at large field and of the transition region between the 2 saturation fields for the high saturation field, and between the transition region and the tangent of the curve at zero field for the low saturation field. We find respectively 0.09 T and 0.5 T.

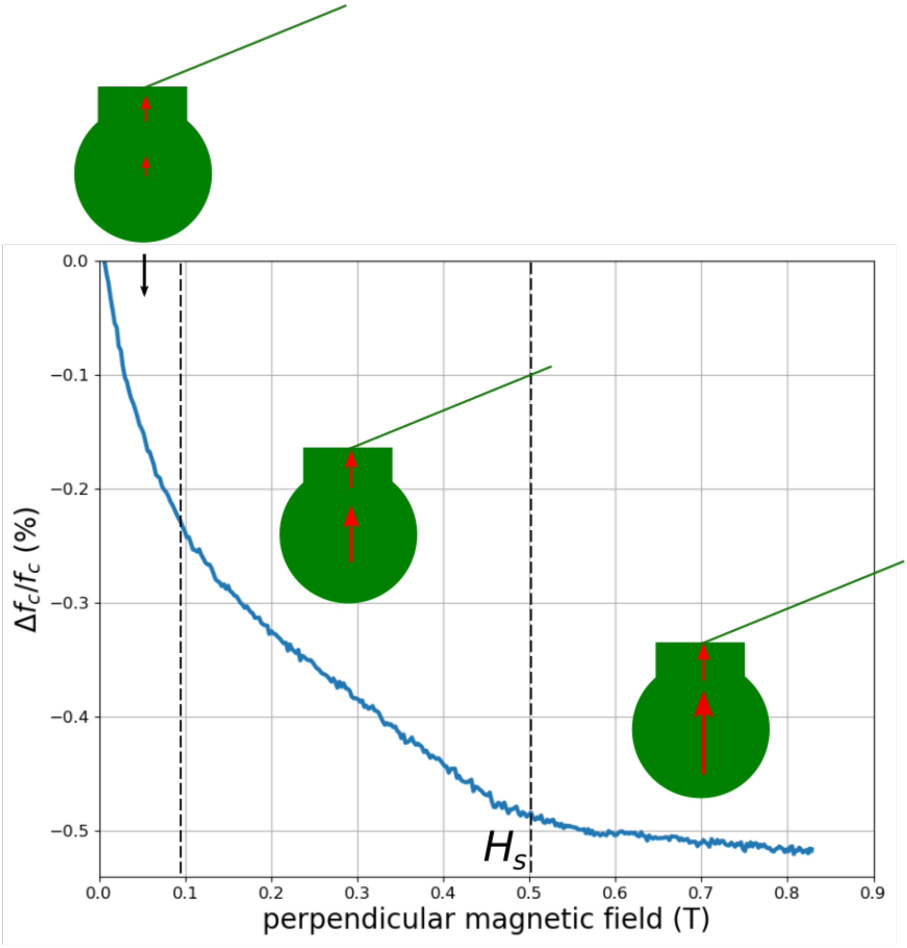

Figure 3.9: Typical relative frequency shift of the cantilever with the 500 nm Co-FEBID nanosphere as a function of the applied perpendicular magnetic field. The images show the variation of the magnetic moments of the spherical part and the pedestal.

The difference between the two measurements, using the variation $\Delta f_c/f_c$ and using the saturation field H_s, can be explained by different elements. First of all, the equation (3.4) is strictly valid for a spherical probe. Secondly, the error on the probe-disk separation in the experiment described in Figure 3.8 is $\approx 1\ \mu m$. So, the separation[2] from one experiment with the FeSi reference probe to a second one with the Co-FEBID sphere is not exactly the same. Finally, due to the presence of a pedestal, the relation $H_s = \mu_0 M_p/3$ is only an approximation here.

Previous results may allow us to refine this determination. Indeed, from previous systematic measurements of the magnetization of Co-FEBID nanospheres as a function of the percentage of Co after nanofabrication and the diameter of the nanosphere [117], we estimate the magnetization of the Co-FEBID sphere used here $M_p = 1.05\times10^6$ A/m. We deduce its magnetic moment $m_p = \frac{4}{3}\pi R_p^3 \times M_p = 6.7\times10^{-14}$ A/m^2. This value is intermediate between the two values determined previously and seems to be most realistic since the only assumption here is to neglect the magnetic moment of the pedestal (by considering that the probe is only a sphere). This value will therefore be used in the rest of the study.

3.3 Sample

3.3.1 BiYIG film growth

Due to its very low damping, yttrium iron garnet (YIG), which is a ferrimagnetic insulator, is the ideal material for the study of spin waves. Its importance in understanding the mechanisms involved in the magnetization dynamics of ferri- and ferromagnetic insulators and the associated relaxation processes led Kittel to say that YIG is to the ferromagnetic resonance research what the fruit fly is to genetics research [121]. The sample studied in this thesis, consisting of BiYIG nanodisks, was fabricated in Thales lab by Abdelmadjid Anane and his thesis students Diane Goueré and Hugo Merbouche, our partners in the Maestro ANR project.

Bismuth (Bi) doping which, under appropriate conditions induces a perpendicular magnetic anisotropy in YIG is performed; a Bi$_x$Y$_{3-x}$IG (BiYIG) target where x=1 is the Bi doping level is obtained. The 30-nm thick reference film is then grown by pulsed laser deposition (PLD) of this target on a substrate : a laser beam is focused inside an ultra-high vacuum chamber on the BiYIG target. BiYIG is then vaporized from the target, as plasma, and is deposited

---

[2] With the magnetic cylinder.

as a thin film on the substrate as described in [27]. Here, the substrate used is a 300 μm thick and one cm square piece of sGGG (substituted gadolinium gallium garnet, $Gd_3Ga_5O_{12}$) (111). It is a non-magnetic garnet whose growth plane and lattice parameter are compatible with those of BiYIG. Before the nanofabrication, a mm square piece was cut in a corner of the 1 cm square film, to measure the thin film magnetic parameters.

3.3.2 Cavity-FMR characterisation

The thin film characterisation was done in the lab by Hervé Hurdequint using a microwave resonant cavity experiment. The resonant cavity is fixed at a frequency of 9.725 GHz. The thin film is placed between the poles of an electromagnet and the magnetic field is swept while the resonant absorption intensity of FMR is detected. The applied field is modulated at low frequency, which explains the shape of the resonance line, the one of the derivative of a Lorentzian, see Figures 3.10 a & b. When the magnetization precession frequency and the resonant cavity frequency are the same, absorption increases sharply. This FMR signal is measured as a function of the angle θ_H between the static field H and the normal to the thin film, see the inset in Figure 3.10 a. Figures 3.10 a & b show the FMR signal at $\theta_H = 54°$ and 8° while Figures 3.10 c & d present the variations of the resonance field H_{res} and the peak-to-peak linewidth ΔH_{pp} as a function of θ_H (it is shown in Figure 3.10 a how they are extracted). We observe that at $\theta_H = 8°$ i.e near the out-of-plane configuration ($\theta_H = 0°$), the resonance signal has a complex shape with the appearance of "decorations" on the resonance line which are due to the spatial inhomogeneities in the film.

One observes that $H^{//}_{res}$ ($\theta_H = 90°$) is larger than $H^{\perp}_{res}$ ($\theta_H = 0°$) which proves that the thin film has a negative M_{eff} according to Figure 2.1. Moreover $H^{//}_{res}$ - $H^{\perp}_{res} < 180$ Oe $= 18$ mT, an indication that M_{eff} is quite small. From a complete analysis of the results , the effective magnetization of the thin film $\mu_0 M_{eff} = -10.9$ mT and the gyromagnetic ratio $\gamma/2\pi = 28.15$ GHz/T are deduced. Knowing the magnetization of the thin film $M_s = 1.35\text{x}10^5$ A/m measured by SQUID magnetometry at UMPhy CNRS Thales (i.e $\mu_0 M_s = 170$ mT) and taking into account the small cubic anisotropy of BiYIG, one deduces the uniaxial (perpendicular) magnetic anisotropy field $\mu_0 H_u = 2K_u/M_s = 0.18$ T i.e an anisotropy constant $K_u = 12150$ J/m^3.

The linewidth shows variations due to the inhomogeneous linewidth. This is due to the spatial distribution of the magnetic properties of the thin film due to imperfections. So, even at the minimum, the linewidth does not give the damping, but a higher value. The minimum value of $\Delta H_{pp} = 2.9$ Oe (at

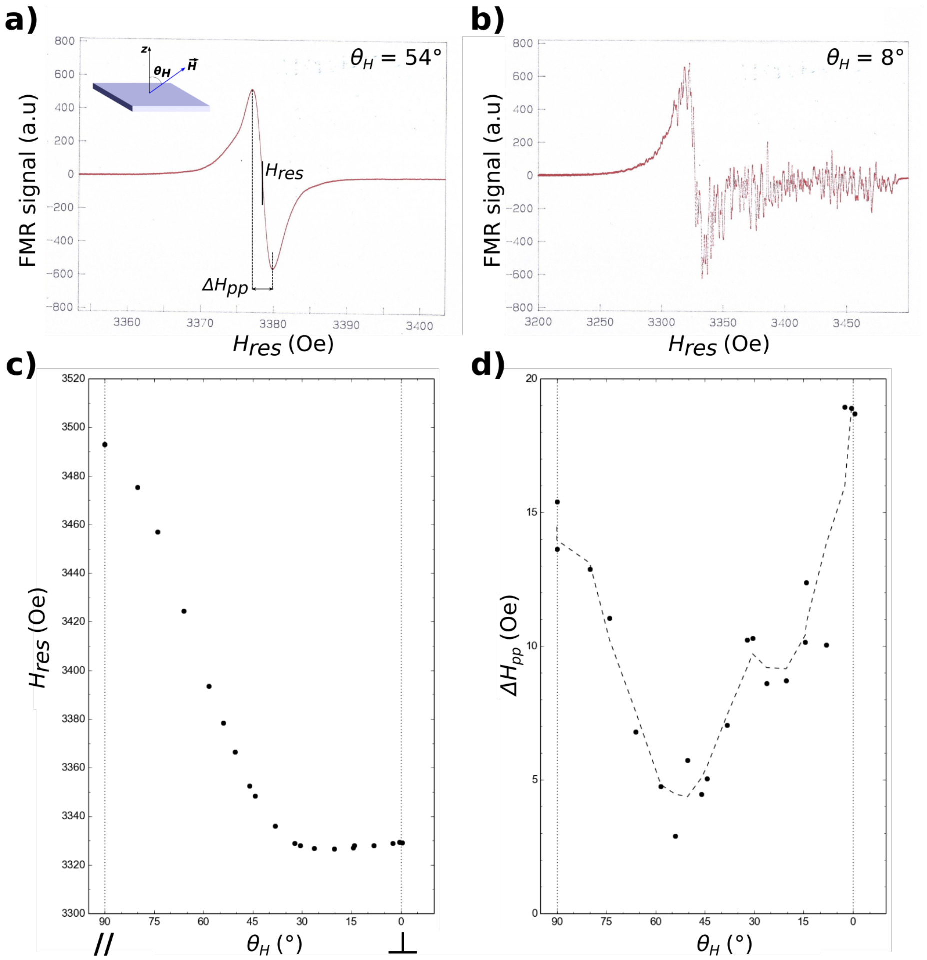

Figure 3.10: a) FMR absorption signal of the BiYIG thin film at $\theta_H = 54°$. The inset shows the configuration of the resonant cavity experiment, θ_H being the angle between the static field and the normal to the thin film. b) FMR absorption signal of the BiYIG thin film at $\theta_H = 8°$. The signal shape is more complex. c) Variation of the resonance field as a function of θ_H. d) Variation of peak-to-peak linewidth as a function of θ_H.

$\theta_H = 54°$) allows therefore to find an upper bound for the damping of the thin film $\alpha = 7.5\text{x}10^{-4}$.

3.3.3 Patterning of nanodisks and microwave antenna

Subsequently, BiYIG nanodisks of different sizes were defined by electron lithography using a negative resist for which the exposed areas are resistant to development and then patterned by ion beam etching. Then, with this resist layer acting as an insulator, a 150-nm-thick and 5 μm wide Titanium/gold (Ti/Au) antenna was deposited on top to allow microwave excitation. The idea is to pass a microwave current in a metallic stripline to create an ortho-radial microwave field in its surrounding. To fulfill the various constraints of reduced dimensions, generation of a homogeneous and maximum field at the location of the samples, impedance matching at 50 Ω which is necessary to minimize the parasitic reflections, the design in Figure 3.11 a is used for the sample fabrication. Similar designs have been used in previous experimental works in the lab [21, 52] and have been described in details before [52].

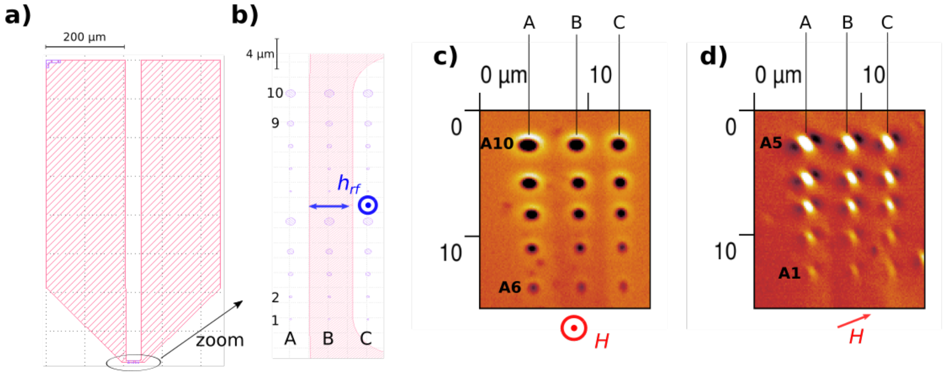

Figure 3.11: a) Image of the design used for the fabrication of the studied sample; the nanodisks are located at the constriction of the microwave antenna. b) Zoom on the constriction : there are 3 disks rows which we label A, B and C, and 10 disks per row which we number from 1 to 10. The rf field is linearly polarized and is in-plane for disks B and out-of-plane for disks A and C. c) MRFM image of the part of the sample with disks numbered 6 to 10 for an applied field 0.6 T perpendicular to the sample. We can distinguish the antenna on the image. d) MRFM image of the part of the sample with disks numbered 1 to 5 for an applied field 0.6 T in the plane of the sample.

The 50 Ω matching of the antenna is ensured by the 30 μm distance between the two electrodes whose flared shape prevents the microwave current to be reflected to the source before the constriction. This microwave circuit is powered by a broadband source, a 100 kHz - 20 GHz Anritsu synthesiser. The 5 μm wide and 50 μm long constriction short-circuits the 2 electrodes, see Figure 3.11 a. To deliver the microwave current from the synthesizer to the antenna we use coaxial cables, connected with SMA connectors.

Figure 3.11 b shows a zoom of the constriction of the microwave antenna on the design image, where the disks are located. The sample consists of 30-nm thick BiYIG disks divided into 3 rows which we call A, B and C. Each row consists of 10 disks numbered from 1 to 10. The disks have diameters of 200, 300, 500, 700 and 1000 nm. Each row has 2 series of disks of the same sizes arranged in the same order. For example, A1,A6, B1,B6 and C1,C6 are disks of 200 nm diameter, A2,A7, B2,B7 and C2,C7 are disks of 300 nm diameter etc... In a row, two neighboring disks are separated by 4 μm. The separation between the rows is 5 μm. As shown in the image the disks B under the antenna are subjected to a linearly polarized rf field h_{rf} in-plane while the disks A and C are subjected to an out-of-plane rf field. Figures 3.11 c & d show MRFM images in both out-of-plane and in-plane static field configurations, with the probe saturated with a field 0.6 T.

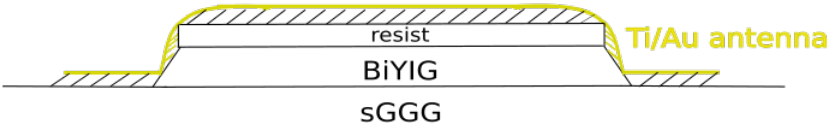

Figure 3.12: Profile view of a disk B under the antenna showing the contact between the edges of the disk and the Ti/Au antenna at the lateral boundaries.

It is known that due to the etching process, the real profile of the disks is not perfectly cylindrical but is slightly trapezoidal with not exactly vertical edges as shown in Figure 3.12. So, the disks B under the antenna are protected from the antenna on top by the resist layer but are in contact with the antenna at their edges, in contrast to disks A and C which are far from the antenna.

Notice that the disks B located under the antenna are subjected to a uniform microwave field while the disks A and C are subjected to a spatially non-uniform field, see Figure 3.13.

These remarks will be important in the analysis of the experimental results.

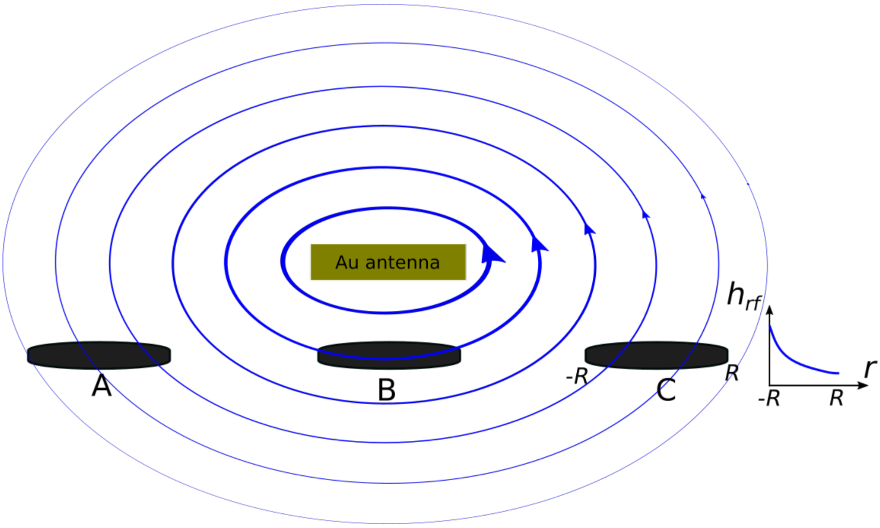

Figure 3.13: Illustration of the spatial distribution of the microwave field around disks A, B and C produced by the antenna. For each loop, the thickness of the line is associated with the field intensity. The disks B are subjected to a uniform field while disks A and C are subjected to a spatially non-uniform field as shown an illustration of its variation profile within disk C. This effect is less important for the smaller disks.

3.4 Effects of the MRFM probe on the measurements

3.4.1 Analytical estimation of the probe's stray field

In a typical MRFM experiment, the probe is positioned above a disk, the static field is swept at a fixed microwave frequency and the resonance spectrum of the disk is recorded. Figure 3.14 a shows a typical experimental configuration with the probe at a distance *sep* above a disk, in this case a 700 nm diameter disk. They are both plunged in a perpendicular static magnetic field $\boldsymbol{H}$. The probe, with a magnetic moment $\boldsymbol{m}_p$ creates an additional stray field $\boldsymbol{H}_{probe}$ on the disk during the experiment. An illustration of the corresponding field lines is shown in Figure 3.14 a. It can have an effect on the MRFM spectrum. So before measuring the different disks in detail, it is necessary to know with precision the influence of the probe.

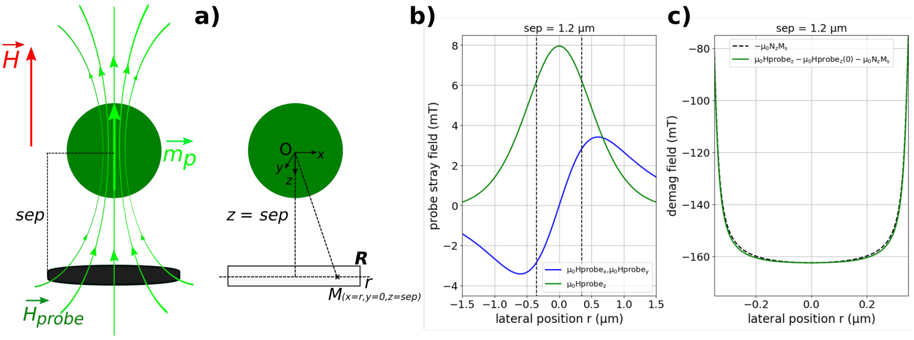

Figure 3.14: a) Typical experimental configuration for measuring the MRFM spectrum of a disk. Here, the 500 nm diameter probe is positioned at a distance $sep = 1.2\ \mu$m above a 700 nm diameter disk. The figure is on the scale except for the disk thickness (30 nm). The probe creates a stray field $\boldsymbol{H}_{probe}$ on the disk. The geometry used for the calculation of $\boldsymbol{H}_{probe}$ is shown. b) Spatial profiles of the 3 components of $\boldsymbol{H}_{probe}$. c) Spatial profile of the internal field in the disk (in black dashed line) and of the internal field modified under the effect of $\boldsymbol{H}_{probe}$ (in green) : The influence of the probe is negligible.

The aim is to calculate the magnetic field created by the magnetic dipole $\boldsymbol{m}_p$ at a point $M(x, y, z)$ in the disk. The geometry used for this calculation is shown in Figure 3.14 a, with a reference frame centered at the probe center. Thus, the field $\boldsymbol{H}_{probe}$ in M is given by:

$$\mu_0 \boldsymbol{H}_{probe} = \frac{\mu_0}{4\pi} \frac{3(\boldsymbol{m}_p.\boldsymbol{u})\boldsymbol{u} - \boldsymbol{m}_p}{OM^3}. \tag{3.5}$$

where $\boldsymbol{u}$ is the unit vector $\boldsymbol{u} = \frac{\overrightarrow{OM}}{OM}$. In the reference frame (x, y, z), see Figure 3.14 a, $\boldsymbol{u}$ and $\boldsymbol{m}_p$ are written $\boldsymbol{m}_p = (0{,}0{,}\text{-}m_p)$ and $\boldsymbol{u} = (\frac{x}{OM}, \frac{y}{OM}, \frac{z}{OM})$. (3.5) becomes :

$$\mu_0 \boldsymbol{H}_{probe} = \frac{\mu_0}{4\pi} \left(\frac{3m_p \frac{z}{OM}.\boldsymbol{u} - \boldsymbol{m}_p}{OM^3} \right). \tag{3.6}$$

One deduces the 3 components of $\boldsymbol{H}_{probe}$:

$$\begin{cases} \mu_0 H_{probe_x} &= -\frac{3\mu_0 m_p}{4\pi} \frac{z.x}{OM^5} \\ \mu_0 H_{probe_y} &= -\frac{3\mu_0 m_p}{4\pi} \frac{z.y}{OM^5} \\ \mu_0 H_{probe_z} &= \frac{\mu_0 m_p}{4\pi} \left(-\frac{3z^2}{OM^5} + \frac{1}{OM^3} \right) \end{cases} \tag{3.7}$$

where $OM = \sqrt{x^2 + y^2 + z^2}$. Figure 3.14 b shows the profiles of these fields calculated at a point M in the median plane of the disk as shown in Figure 3.14 a. The calculation is done for $z = 1.2$ μm and we assume that the probe is saturated (i.e $m_p = m_p^{max}$). The vertical dashed lines are the boundaries of the 700 nm disk. One observes that the stray field is only of the order of a few mT and varies by a few mT at the disk scale, between -3 and 3 mT for H_{probe_x} and H_{probe_y} (blue curve in Figure 3.14 b) and between 6 and 8 mT for H_{probe_z} (green curve in Figure 3.14 b). Figure 3.14 c shows the profiles of the internal field within the disk in the absence of the probe (in black dashed line)[3], and in the presence of the probe (in green). The comparison shows that the influence of the probe is very weak.

For this disk size (700 nm diameter), our experiments were performed most often for separations with the probe of 1.4 μm and at magnetic fields for which the probe has only half of its maximum magnetic moment. So the stray field of the probe is even lower than the one calculated. The stray field of the probe can therefore be considered as homogenous at the scale of the disk i.e. $H_{probe}(r) = H_{probe}(0)$. H_{probe} can be reduced to the value of its z component at the disk center :

$$\mu_0 H_{probe} = \frac{\mu_0 m_p}{2\pi z^3} \tag{3.8}$$

by taking $OM = z$ in the expression of $\mu_0 H_{probe_z}$.

---

[3] Similar to the profile shown in Figure 2.4 a.

3.4.2 Extraction of the resonance parameters without the influence of the probe

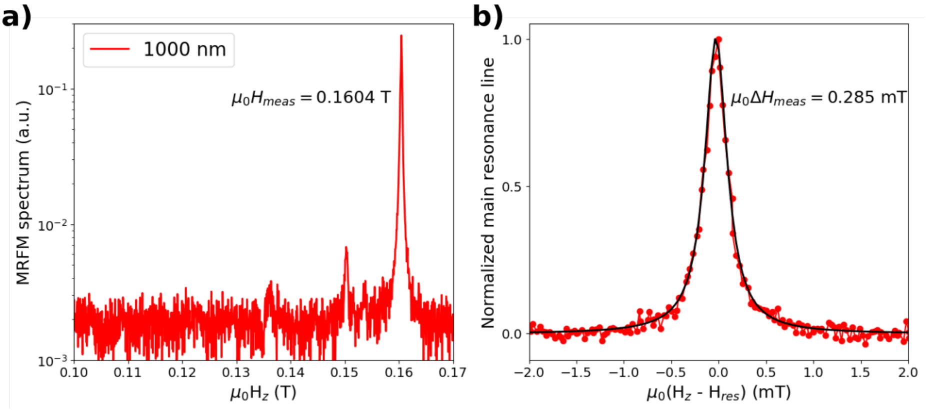

Figure 3.15: a) MRFM spectrum at f = 5 GHz and P = -1 dBm of the 1000 nm diameter B5 BiYIG disk. b) Linewidth measurement of the main mode at f = 5 GHz and P = -10 dBm. The resonance line has been shifted with respect to the resonance field.

It is possible to calculate this stray field in experiments. Figure 3.15 shows the MRFM spectrum and the linewidth measurement of the 1000 nm diameter disk B5 at a microwave frequency f = 5 GHz, for a static field normal to the disk. The presence of the probe induces a downward shift of H_{probe} in the measured resonance spectrum. In addition, the probe located at the end of the cantilever oscillates with an amplitude of a few nm which is kept constant thanks to the PID loop. So in addition to the static stray field H_{probe}, there is also a modulated stray field given by :

$$\mu_0 \Delta H_{probe} = \frac{3\mu_0 m_p}{2\pi z^4} dz \tag{3.9}$$

which has the effect of broadening the resonance line of ΔH_{probe}. dz is the amplitude of vibration of the cantilever which is directly linked to the excitation voltage *pid* of the PID loop by the conversion factor *conv* determined in Figure 3.6 :

$$dz = conv \times pid \tag{3.10}$$

Finally, if ΔH and H_{res} are respectively the intrinsic linewidth and resonance field of the disk in the absence of the probe, the parameters measured on the experimental MRFM spectrum are :

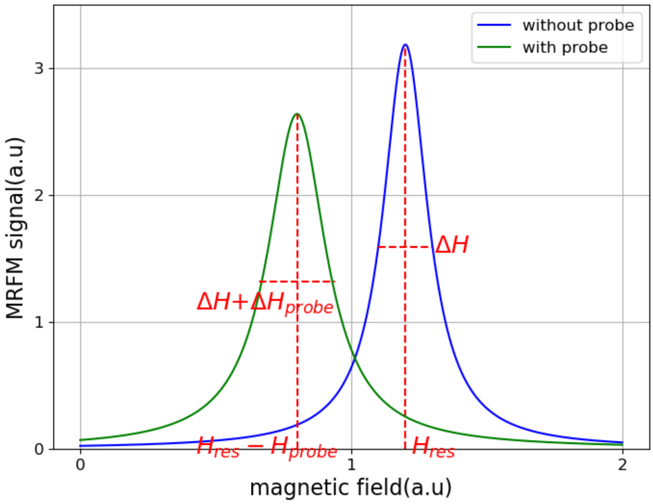

Figure 3.16: Effects of the probe on the resonance line. The figure is not to scale: the effects of the probe are exaggerated for a better visualization.

$$\begin{aligned} H_{meas} &= H_{res} - H_{probe} \\ \Delta H_{meas} &= \Delta H + \Delta H_{probe}. \end{aligned} \tag{3.11}$$

Figure 3.16 shows these effects of the probe on the resonance line. Obviously, the linewidth being affected, it is also the case of the signal amplitude. However, this variation of amplitude is a second order effect and is negligible. Our MRFM experiments, like those of Figure 3.15 are made at separations z ranging from 1 to 1.5 μm depending on the size of the disk. For the disk B5 we find a linewidth of 0.285 mT. It is a very small value, as expected from the low damping of the reference thin film. For a typical separation $z = 1.4$ μm and an ocillation amplitude $dz = 4$ nm, one finds $\mu_0 \Delta H_{probe} = 0.042$ mT. We therefore have $\mu_0 \Delta H_{probe}$ of the order of 15% of the linewidth. It is clear that concerning the linewidth, it is necessary to know the influence of the probe in our measurements.

Measuring such small intrinsic linewidths turned out to be one of the main challenges of our experiments. Indeed, one could say that we only need to have the probe far away to measure the intrinsic parameters of the different disks since in equations (3.8) and (3.9), H_{probe} and $\Delta H_{probe} \longrightarrow 0$ when $z \longrightarrow \infty$. But one would have to increase the microwave power to compensate the weak probe-disk interaction in order to have a good signal to noise ratio. However, since the threshold power for the foldover is related to the linewidth as shown in section 2.5.1, there is a power threshold if we want to keep measurements in the linear regime in order to measure linewidths. On the other hand, one can decrease the power and bring the probe closer to the disk, in which case we will broaden the resonance line (increase of ΔH_{probe}). So a compromise must be found between the separation z and the microwave power in order to limit the influence of the probe as much as possible while having a good signal to noise ratio.

It is now admitted that the farther the probe is from the disk (i.e. the larger z is), the closer the spectrum obtained will be to the intrinsic spectrum. One way to determine the intrinsic parameters H_{res} and ΔH is therefore to make measurements as a function of z and to deduce them by extrapolation.

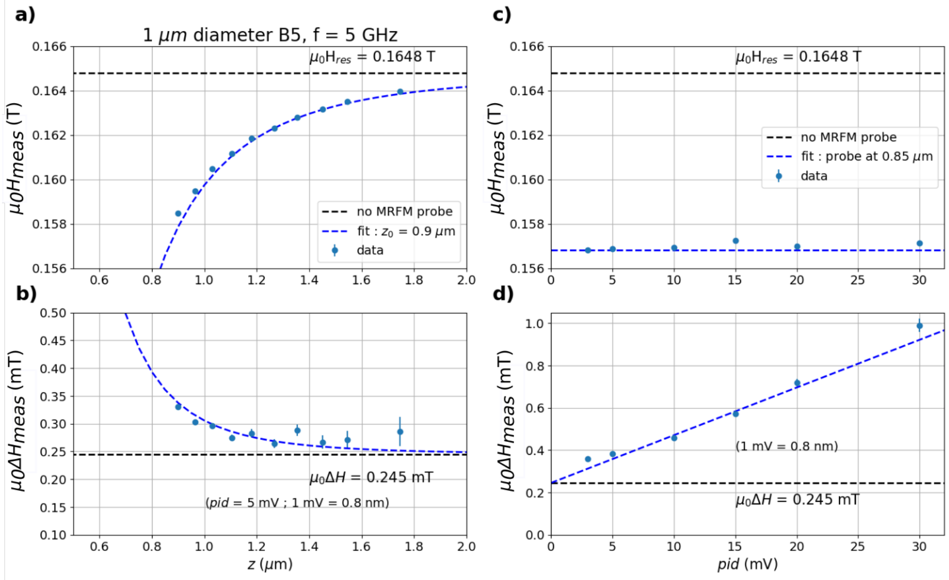

Figure 3.17: a) Resonance field of disk B5 evolution as a function of probe-sample separation z. b) Linewidth evolution as a function of the probe-sample separation z. c) Resonance field evolution as a function of the cantilever vibration amplitude. d) Linewidth evolution as a function of the cantilever vibration amplitude.

We start by positioning the probe at an altitude z_0 above the disk then we measure the resonance line at f = 5 GHz. Thanks to the piezoelectric tubes, the probe is moved away from the disk in steps of Δz and at each position we measure the resonance line. The resonance field and the linewidth are extracted from Lorentzian fits for each position (see equation (2.42)). Figures 3.17 a & b show their evolution as a function of z in the case of the disk B5.

As expected, the effects of the probe are more important close to the disk. Replacing H_{probe} and ΔH_{probe} by their expressions (3.8) and (3.9) in (3.11), one finds :

$$\begin{aligned} \mu_0 H_{meas} &= \mu_0 H_{res} - \frac{\mu_0 m_p}{2\pi(z_0+\Delta z)^3} \\ \mu_0 \Delta H_{meas} &= \mu_0 \Delta H + \frac{3\mu_0 m_p}{2\pi(z_0+\Delta z)^4} \times conv \times pid. \end{aligned} \tag{3.12}$$

In Figures 3.17 a & b, the initial separation z_0 and the calibration factor *conv* are determined in equations (3.12) by adjusting them to best fit the experimental data. The best fit is obtained for $z_0 = 0.9$ μm and $calib = 0.8$ nm/mV, close to the value determined previously from the thermal noise of the cantilever in Figure 3.6, 1.15 nm/mV[4]. The intrinsic resonance field and the linewidth without probe are then deduced at 5 GHz : $\mu_0 H_{res} = 0.1648$ T and $\mu_0 \Delta H = 0.245$ mT.

NB: The linewidth $\mu_0 \Delta H = 0.245$ mT is the real linewidth at 5 GHz, without probe perturbation, but contains nevertheless the inhomogeneous or extrinsic contribution ΔH_0 (see equation (2.33)).

An additional measurement based on the vibration amplitude of the cantilever allows to check the results obtained. Now, we set the probe-disk separation to a fixed value z and then vary the voltage of the bimorph excitation (*pid*). The resonance field and the linewidth are extracted in each case. Figures 3.17 c & d show the values obtained as a function of the *pid*. From equations (3.12) and with the same parameters of fit as before, we find exactly the same results $\mu_0 H_{res}$ and $\mu_0 \Delta H$. Let us emphasize that here, the separation is deduced directly from the first measurement of the value of the stray field which is constant : we thus note the agreement between the Figures 3.17 a & c on which the resonance field is 0.157 T for $z = 0.85$ μm.

Returning to Figures 3.15, we note that the disk B5 has for resonance field and linewidth $\mu_0 H_{meas} = 0.1604$ T and $\mu_0 \Delta H_{meas} = 0.285$ mT. The comparison of these values with the values without probe allows us to accurately deduce the stray field of the probe on B5 $\mu_0 H_{probe} = \mu_0 H_{res} - \mu_0 H_{meas} = 4.4$ mT and the broadening of the line $\mu_0 \Delta H_{probe} = \mu_0 \Delta H_{meas} - \mu_0 \Delta H = 0.04$ mT which corresponds to a line modulation of $p = \frac{\mu_0 \Delta H_{meas} - \mu_0 \Delta H}{\mu_0 \Delta H} = 16\%$. Similar measurements were made on all the disks B1-B5. The results will be presented in the next chapter.

---

[4] The difference may be due to the uncertainty of the nominal spring constant given by the manufacturer and used in the calculation of Figure 3.6.

3.4.3 Direct experimental measurement of the intrinsic resonance signal

Furthermore, the experimental data give us direct access to the intrinsic resonance fields of some disks. It turns out that under certain experimental conditions, in addition to the resonance signal of the disk located below the probe, an opposite signal of smaller amplitude is measured, see Figure 3.18 a & c. It is indeed the signal of the largest disk next to the measured disk as shown in Figure 3.18 b. Its negative sign is due to the repulsive coupling between the probe and this neighbouring disk, in opposition to the attractive coupling between the probe and the disk straight below. A fit allows to extract the corresponding resonance field which is $\mu_0 H_{res}$ = 0.1651 T for B5 and $\mu_0 H_{res}$ = 0.167 T for B4. For B5, the value is in excellent agreement with the value of 0.1648 T extrapolated previously. We will see in the next chapter that there is also a perfect agreement for B4. However, the probe being very far from this neighbouring disk, we have to pump sufficiently hard to measure its signal. For these reasons, the quality of the signal is not good enough to extract the intrinsic linewidth (the detected negative signal is already in the non linear regime). We can then understand the difference in power between -1 dBm in Figure 3.18 a which makes it possible to measure this opposite signal for B5 and -10 dBm in Figure 3.15 b which allowed to measure its linewidth.

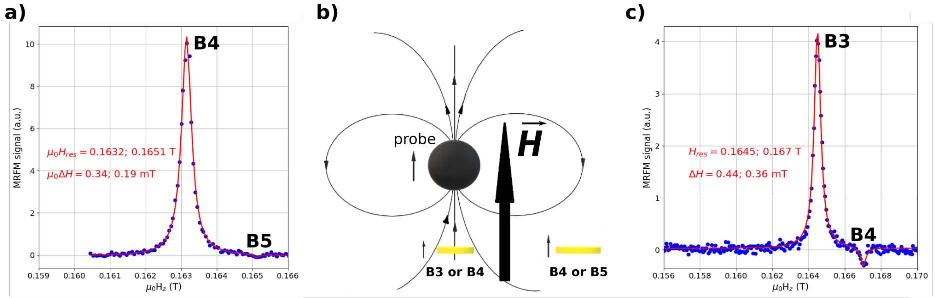

Figure 3.18: a) Presence of a small negative resonance signal on the resonance spectrum of disk B4 at f = 5 GHz and P = -1 dBm : it is the resonance of B5. b) Dipolar coupling between the probe and disk B4 (B5), with the probe above disk B3 (B4). This coupling allows a measurement of the intrinsic resonance of the large disk next to the disk below the probe as shown in a) and c). a) Presence of a small negative resonance signal on the resonance spectrum of disk B3 at f = 5 GHz and P = -3 dBm : it is the resonance of B4.

3.5 Conclusion

We explained the mechanical detection principle on which MRFM is based before showing in practical ways how an MRFM signal is measured. Then we proceeded to the characterization of the magnetic probe, the Co nanosphere. We were able to determine its magnetic moment with a precision of the order of 40%. We explained the influence of the probe in our experimental measurements. We determined the intrinsic resonance field of the 1000 nm diameter disk B5 thanks to the small negative signals measured in the experiments. This experimental intrinsic resonance field is in excellent agreement with the intrinsic resonance parameters of the disk extrapolated from measurements of its resonance line as a function of the probe altitude. Similar results for other disks (see next chapter) confirm the accuracy of our experimental approach to obtain the intrinsic parameters of a disk.

Summary

- Presentation of the experimental setup : the magnetic resonance force microscope (MRFM)
- Characterisation of the MRFM probe : a Co nanosphere
- Detailed description of the sample studied : BiYIG nanodisks
- Careful study of the influence of the magnetic probe on the experimental measurements on a 1000 nm diameter disk : deduction of its intrinsic resonance parameters

Chapter 4

Linear spectroscopy of BiYIG nanodisks

"A hundred years ago, Auguste Comte, ... a great philosopher, said that humans will never be able to visit the stars, that we will never know what stars are made out of, that that's the one thing that science will never ever understand, because they're so far away. And then, just a few years later, scientists took starlight, ran it through a prism, looked at the rainbow coming from the starlight, and said: "Hydrogen!" Just a few years after this very rational, very reasonable, very scientific prediction was made, that we'll never know what stars are made of."

Michio Kaku

Contents

In this chapter, we perform spectroscopy measurements of all the BiYIG nanodisks, focusing mainly on the linear regime, the static field being perpendicular to the disks. The analysis of the spectra characteristics, namely the resonance fields, the linewidths and the amplitudes of the resonance peaks, will give us informations at the local scale on the nanodisks, such as the magnetic anisotropy, the spin waves modes profiles and the damping. In particular, combined with micromagnetic simulations, they will allow to demonstrate that the nanofabrication process yields a spatial modulation of the magnetic anisotropy at the periphery of the disks.

4.1 Spectroscopy of the disks at 5 GHz

We first measured the disks B1 to B5 located under the antenna (see Figure 3.11 b) for a microwave frequency of 5 GHz. In Figure 4.1 we present the spin wave spectra (left column) and the measured linewidths (right column) for these disks. The data for the 1000 nm B5 disk are the ones shown in Figure 3.15. The set of spectra in the first column was measured for the same probe altitude above the disks so as to have the same probe stray field in each case. Thus, the spectra can be directly compared with each other. The three elements that are extracted from a spectroscopy and which give informations on the nature of the excited modes are the resonance field (or the resonance frequency), the linewidth and the amplitude of the resonance peaks.

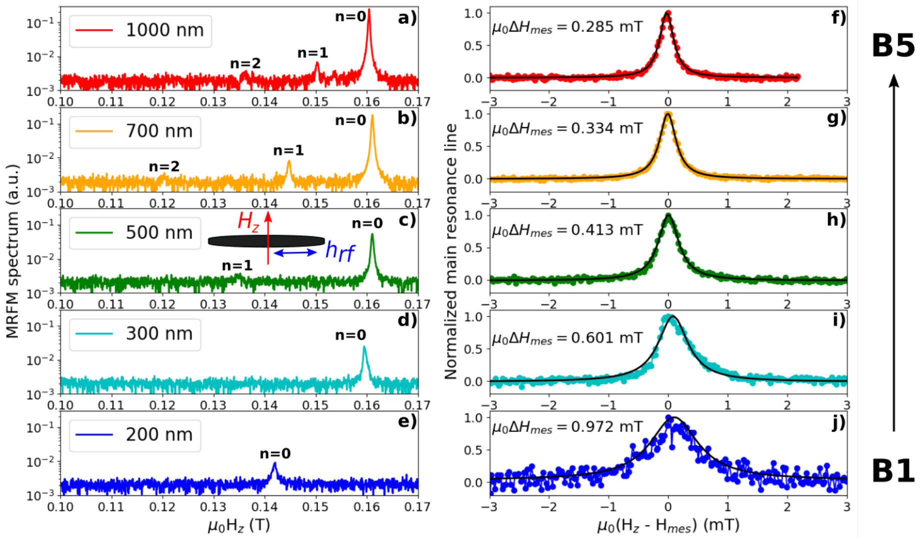

Figure 4.1: (a-e) Mechanical-FMR spectra at f = 5 GHz of the 1000, 700, 500, 300 and 200 nm diameter BiYIG disks (B5-B1) arranged in row by decreasing lateral size. The indices of the modes are shown. The inset in c) shows the configuration of the rf and static fields. (f-j) Values of the linewidths of the uniform mode for each disk size. Each resonance line has been shifted with respect to the resonance field.

- Concerning the eigenfrequencies, the largest peak at high magnetic field corresponds to the lowest energy mode : the so-called uniform mode which we index $n = 0$. Smaller peaks at lower fields (higher frequencies) are those of higher orders (which we index $n = 1, 2, 3$ ...). These are the radial spin wave modes with azimuthal index l =0. For the 5 spectra on the left, the microwave power is P = -1 dBm to allow to observe these smaller peaks. We observe some of these peaks for disks of diameter D $\geq$ 500 nm as shown on the figure. As expected, due to the geometrical confinement, the splitting between higher order modes increases as disk size decreases. But in contrast to previous MRFM studies on nanodisks, where the frequency (field) of the uniform mode clearly increases (decreases) as the size of the YIG disk [21] (see Figure 2.6 b) or permalloy disk [56] decreases, here the position ($\simeq$ 0.16 T) of the uniform mode varies very little with the size of the disk, except for the smallest disk of 200 nm diameter whose resonance field is about 20 mT lower.

- Regarding the linewidth (the full width at half maximum, FWHM) of the main mode, we observe an increase as the size of the disk decreases. Compared to the linewidth of the 1000 nm disk B5, it increases respectively by a factor of 1.17, 1.24, 1.8, and 2.91 for disks 700 nm B4, 500 nm B3, 300 nm B2 and 200 nm B1. For linewidth measurements of the main n=0 mode, one uses much lower powers to remain in the linear regime and not to distort the resonance line. For the data presented in Figures 4.1 f to j, the microwave power used is lower than the corresponding broad spectrum power for disks B3 (2 times smaller), B4 (4 times smaller) and B5 (8 times smaller). On the other hand, the power has been maintained (-1 dBm) for B1 and B2, for which one remains in the linear regime due to their larger resonance linewidths.

- Finally, another striking result is the very low relative amplitude of the higher order modes, compared also to what was measured on YIG nanodisks of similar sizes [21] as shown in Figure 2.6 b.

Then, with measurements as a function of the probe-disk separation, we complete the determination of the intrinsic resonance parameters of these disks (without the influence of the MRFM probe) as explained at the end of the previous chapter in the case of disk B5. The results are shown in Table 4.1.

Table 4.1: Values of intrinsic resonant field and linewidth at 5 GHz. The percentage p of linewidth modulation by the probe and the stray field in the data in Figure 4.1 are also indicated for information.

nanodisk (diam)	$\mu_0 H_{res}$ (T)	$\mu_0 \Delta H$ (mT)	$\mu_0 H_{probe}$ (mT)	p(%)
B5 (1μm)	0.1648	0.245	4.4	16
B4 (700nm)	0.167	0.295	5.9	14
B3 (500nm)	0.168	0.36	6.9	15
B2 (300 nm)	0.167	0.52	5.2	16
B1 (200nm)	0.151	0.75	9.0	29

The slight differences observed in the probe stray field can be explained by the error in the vertical position of the probe above each nanodisk during the experiment, which is of the order of 100 nm. As for B5, it was possible to detect experimentally the intrinsic resonance signals (the small negative signal) of the disks B4 and B3 (the one of B4 was presented in Figure 3.18 c) and thus to measure their intrinsic resonance fields. These values are in excellent agreement with the calculated values in Table 4.1.

4.2 Broadband spectroscopy

Now that we know precisely the influence of the probe on the MRFM spectra, we can proceed to a detailed quantitative analysis of the measurements. For different disks, the MRFM spectrum is measured at frequencies between 0.5 and 10 GHz. Then Resonance fields and FMR linewidths are extracted using a lorentzian fit. During such an experiment, the static field is typically swept between 0 and 0.35 T, which obviously varies the magnetic moment of the probe (see Figure 3.9) and thus its stray field. Knowing the separation between the probe and the disk, the measured data are corrected from the probe stray field.

In Figures 4.2 a & b, we show for all the disks of the first series (B1-B5) the dispersion relation (frequency-field graph) as well as the linewidth evolution with the microwave frequency f. We remind that the resonance condition of a nanodisk in the case of a perpendicular applied field is given by equation (2.43) :

$$\omega = \gamma\mu_0(H - H_K) \tag{4.1}$$

where $\omega = 2\pi f$ is the angular frequency of the microwave, H the resonance field and H_K a characteristic field of the disk which gives the position of the Kittel mode. The linear dependence of the linewidth on the frequency comes from the Landau–Lifshitz–Gilbert theory and is given by equation (2.33) :

$$\mu_0\Delta H = \mu_0\Delta H_0 + \frac{2\alpha\omega}{\gamma} \tag{4.2}$$

where γ is the gyromagnetic ratio and $\mu_0\Delta H_0$ is the extrinsic or inhomogeneous linewidth.

Thus, linear fits based on these two relations allow to extract the magnetic parameters for each disk. All the results as well as those of the disks B6 to B10 are presented in Table 4.2.

As expected, we find an identical gyromagnetic ratio for all the disks, $\gamma/2\pi$ = 28.04 GHz.T^{-1} which is similar to the one of the thin film determined from cavity measurements, 28.15 GHz/T. The characteristic field $\mu_0 H_K$ which causes the variation of the resonance field with the size of the disk for the same applied microwave frequency varies only by 3 mT between B2, B3, B4 and B5. The one of B1 is much smaller. All this confirms the previous observations

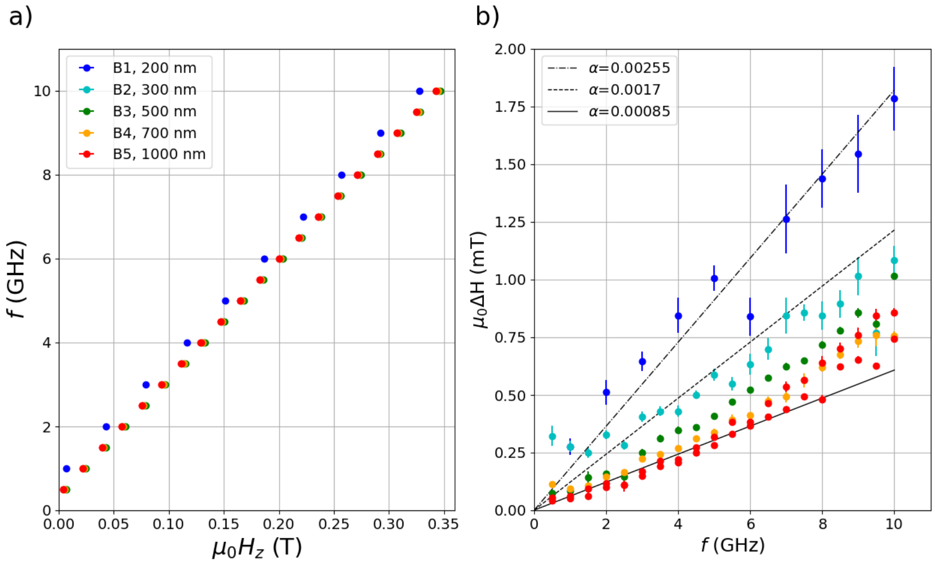

Figure 4.2: a) Frequency-field dispersion curves of all the disks of the series (B1-B5). b) FMR linewidth vs. frequency for all these disks. The three lines that correspond to the equation (4.2) with $\Delta H_0 = 0$ are eye guides that allow to clearly see the increase in damping as the disk size decreases.

Table 4.2: Magnetic parameters of the different nanodisks.

disk (diam)	$\gamma/2\pi$ (GHz.T^{-1})	$\mu_0 H_K$ (mT)	α ($\times$ 10^{-3})	$\mu_0\Delta H_0$ (mT)
B5 (1μm)	28.05±0.01	-13.0±0.1	0.9±0.03	-0.033±0.013
B10	28.03±0.01	-17.3±0.1	1.1±0.05	-0.04±0.02
B4 (700nm)	28.04±0.02	-11.3±0.1	1.04±0.03	-0.04±0.014
B9	28.04±0.02	-11.6±0.2	1.25±0.05	-0.082±0.021
B3 (500nm)	28.04±0.02	-10.2±0.1	1.15±0.04	-0.03±0.015
B8	28.25±0.01	-22.0±0.1	1.5±0.03	-0.09±0.015
B2 (300 nm)	28.04±0.02	-11.3±0,1	1.36±0.08	0.083±0.03
B7	28.04±0.02	-16.4±0.4	2.0±0.06	0.02±0.02
B1 (200nm)	28.04±0.08	-28.0±0.06	2.2±0.2	0.15±0.07
B6	28.04±0.05	-28.3±0.35	2.7±0.2	0.3±0.06

and results at 5 GHz. The damping of the disk B5 is 0.9×10^{-3}. It increases respectively by a factor of 1.16, 1.28, 1.5 and 2.5 for B4, B3, B2 and B1. The extrinsic linewidth $\mu_0 \Delta H_0$ is zero for all the disks with diameter $\geq$ 300 nm[1] and small for the 200 nm diameter disks. This confirms that nanopatterning reduces spatial inhomogeneities. Futhermore, the measurement of the small opposite signal (as shown in the previous chapter and section at 5 GHz) for disks with diameter $\geq$ 500 nm as a function of the frequency allows to have their intrinsic parameters γ and $\mu_0 H_K$. There is also a remarkable agreement between the values obtained in this way and those presented in the table, which confirms the accuracy of our correction model of the stray field induced by the probe.

In summary, there is a quantization of the spin wave spectrum due to the confinement : the splitting between the modes increases when the size is reduced. On the other hand, there is a confirmation of unexpected results compared to previous results on YIG disks of similar size, namely the quasi-invariance of the main resonance field with diameter except for the smallest disk and the very low relative amplitudes of the higher order modes. The damping increases as the disk size decreases.

To get further insight we perform micromagnetic simulations.

4.3 Micromagnetic simulations methods

We used Micromagnum which is a finite-difference/FFT package for the solution of dynamical micromagnetic problems [122, 123]. The magnetic parameters used are as follows : $M_s = 135$ kA.m^{-1}, $A_{ex} = 3.6$ pJ.m^{-1} [124] which corresponds to an exchange length $\lambda_{ex} \simeq 18$ nm, $\gamma/(2\pi) = 28$ GHz.T^{-1} and $\alpha = 10^{-3}$. The nominal geometries of nanodisks with diameters ranging from 200 to 1000 nm and a thickness of 30 nm are defined. Each disk is discretized using a rectangular mesh. The condition is to have a cell size smaller than λ_{ex} and which optimizes the computing time. For this purpose, test simulations were performed and the following meshes were selected : $32 \times 32 \times 1$ for disks with diameters D $\leq$ 500 nm and $64 \times 64 \times 1$ for other disks. Thus, the size of the cells varies between 6 nm for the 200 nm disk and 15 nm for the 1000 nm disk. Then, we use two complementary simulation methods.

In the first one, the equilibrium configuration is pre-calculated at 0.1 T, applied along the normal of the disk. Afterwards, the magnetization of the disk is disturbed by tilting it by 3° with respect to the normal. The FFT of the

---

[1] By setting $\Delta H_0 = 0$ in equation (4.2) one obtains values of damping α equal to those presented in the Table 4.2.

dynamic of the return to equilibrium of the magnetization is then calculated for 100 ns with a time step of the order of 1 ps. This method is very fast but provides only the frequencies of the eigenmodes of the system. It is not directly comparable to our experimental results concerning the linewidths and the relative amplitudes of the modes. Note that here, one obtains a frequency spectrum at a fixed field. Figure 4.3 shows some results as a function of disk size obtained using this method.

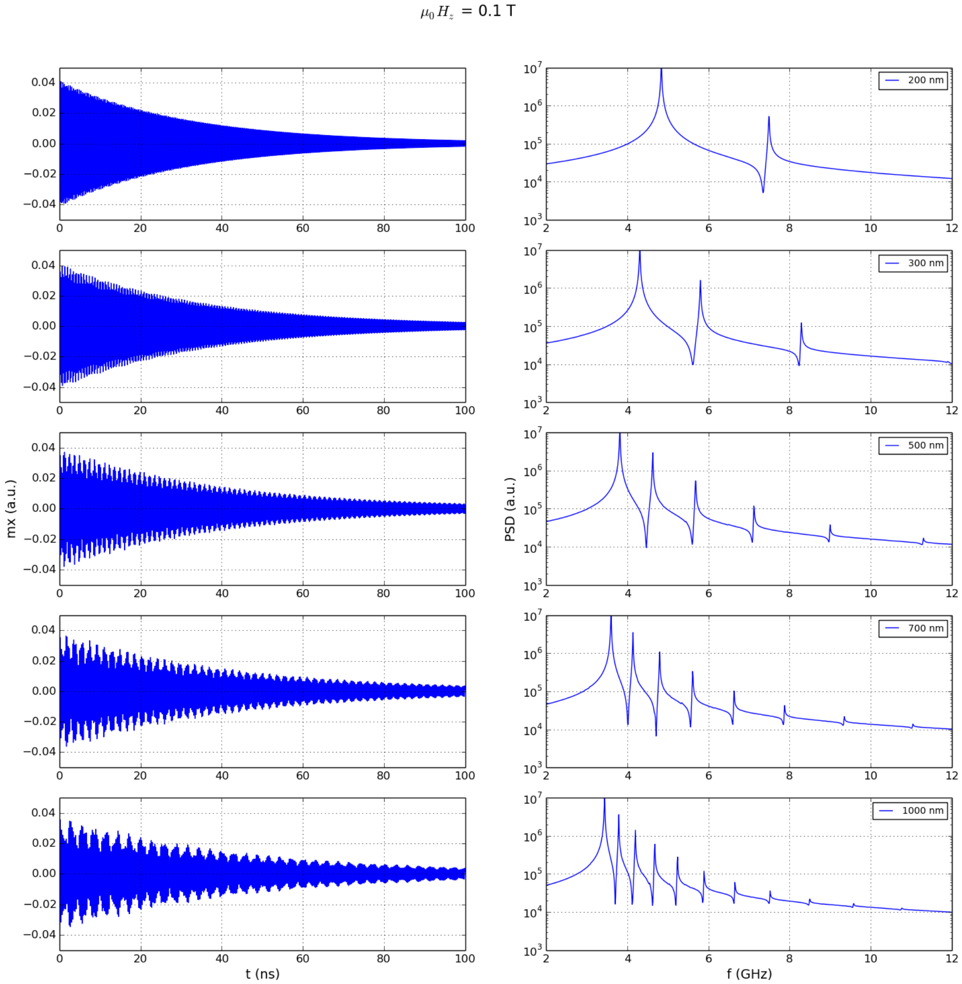

Figure 4.3: Time trace of a component of the magnetization (left) and resonance spectrum (right) as a function of disk size obtained using the first simulation method.

The second method allows to be more precise. Here, we perform a simulation similar to our experimental protocol. The bias magnetic field is applied along the normal of the disk. The static equilibrium configuration of the magnetization is calculated at a given static field. Then, a linearly polarized excitation field of constant and very low amplitude $\mu_0 h_{rf} = 0.008$ mT (to be in the linear regime) is applied at 5 GHz in the plane of the disk, and for each value of the bias magnetic field, which is decreased by steps of 0.05 mT, the resulting magnetization dynamics is calculated over 100 ns with a typical step of 1 ps. Obviously, this method is much longer than the first one. For each static field, one calculates the spatial average of the decrease of the longitudinal component of the magnetization ΔM_z averaged over 50 ns after the 50 ns of transient regime. So, we obtain here a field spectrum at a fixed frequency, directly comparable to our experimental spectra. We have checked that the two types of spectra obtained with the two methods are equivalent concerning the positions and therefore the splitting between the modes.

Let's add that Olivier Klein from Spintec in Grenoble did complementary simulations using SpinFlow 3D [38], a finite element based simulation software platform based on the dynamic matrix approach with as results the direct determination of all the eigenmodes of the system and the associated eigenfrequencies. They presented a perfect agreement with the two mentioned methods.

4.4 Evidence of a spatial modulation of the anisotropy

4.4.1 Dependence of spectral characteristics as a function of diameter

In simulations, we first use for each disk the magnetic properties of the thin film and the damping measured in experiments. We therefore use a constant magnetic anisotropy $K_u = 12150$ J/m^3, which corresponds to the PMA field $\mu_0 H_u = 0.18$ T. On one hand, with the first simulation method one obtains the eigenfrequencies for each size. On the other hand, knowing $\mu_0 H_K$ for each disk in experiments, one can determine the corresponding uniform mode frequency for a field $\mu_0 H_z = 0.1$ T, using the equation (4.1). Thus, one can directly compare data and simulation results. Figures 4.4 a & b show the evolution with the disk diameter of the frequency of the uniform mode and the splitting of the first two SW modes ($n = 1$ and $n = 2$) with respect to the main mode ($n = 0$) in both simulations and experiment for the 2 series of disks under the antenna B1-B5 and B6-B10.

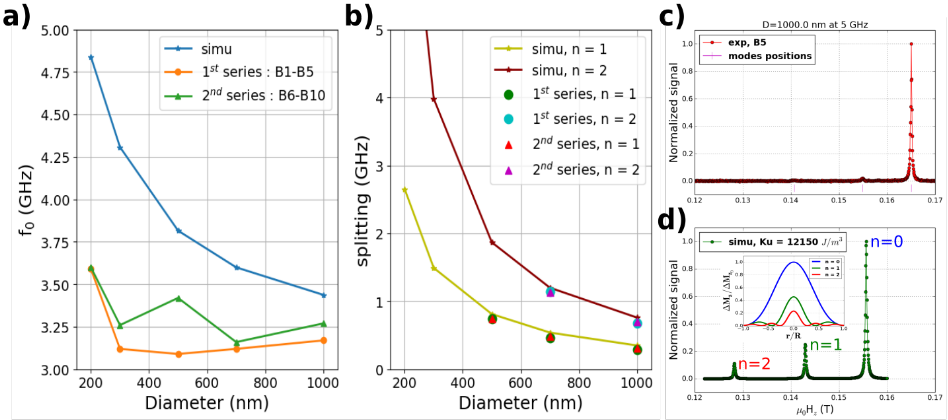

Figure 4.4: a) Evolution of the uniform mode frequency as a function of the diameter in experiments (for the two series of disks under the antenna) and in simulations. b) Variation of splitting between modes as a function of disk diameter : the splitting of each mode is calculated with respect to the main mode n=0. The simulations were made for a normal field to the disk of 0.1 T. c-d) Comparison between the experimental spectrum of the 1000 nm diameter disk B5 in red and the simulated spectrum in green. The inset of figure d) shows the simulated profiles of the 3 modes of the green spectrum.

Regarding the splitting between the modes in Figure 4.4 b, they are similar for the 2 series B1-B5 and B6-B10 and are close to the simulations results.

For the frequency of the uniform mode, as already pointed out previously, it is clear that it is almost independent of the size ($f_0 \approx 3.1$ - 3.25 GHz) except for the 200 nm diameter disks for which $f_0 \approx 3.6$ GHz (orange and green curves in Figure 4.4 a). It is the same behavior for the second series B6-B10 except for the 500 nm diameter B8 which has a frequency quite different from its counterpart, as suggested by its singular value of $\mu_0 H_K$ in the Table 4.2. These results are far from those expected consisting in an increase when the size decreases, clearly highlighted in the simulations (blue curve).

The comparison between the experimental spectrum of the disk B5 and the simulated spectrum of the 1000 nm diameter disk in Figures 4.4 c & d confirms the very low relative amplitudes of the higher order modes compared to the main mode in the experiment. The profiles of the uniform mode and the first two SW modes obtained in this case of a constant anisotropy are presented in the inset of Figure 4.4 d, with the corresponding indices in labels. For this purpose, the three spatial components of the magnetization at each point in the disk are recorded in the simulation. The profiles shown here correspond to the spatial distribution of the reduction of the longitudinal magnetization in the disk at the different resonance peaks. These are the well-known first-order Bessel functions suitable for describing the radial spin waves of disks magnetized out of plane due to axial symmetry [38] and presented in subsection 2.4.3.2. The amplitudes of the spin wave modes are given by the overlap integral between the mode profile and the excitation field, see equation (2.41). For a uniform excitation as it is the case for disks B (see Figure 3.13), the profiles of these Bessel functions must lead to a variation of the mode amplitude in $1/(n+1)^2$ (n being the mode index) as can be seen on the spectrum of Figure 4.4 d with relative amplitudes 1, 1/4 and 1/9. In contrast, on the experimental spectrum, one is rather close to 1/20 for the relative amplitude of the second mode while the third one around 0.14 T is almost invisible. Thus, at this point we can think that the *real spatial profiles of the spin waves in the nanodisks are different from the expected Bessel functions.*

Another striking experimental result is the variation of the damping with the size of the disk. It is reported on Figure 4.5 for the 2 series B1-B5 and B6-B10; the upper bound value for the damping, extracted on thin film by cavity-FMR is also indicated (blue dashed line). One observes the increase of the damping of the disks B when the diameter decreases. One also notes the dependence in ≈1/D (D being the diameter) of the damping of the disks B as shown by the black dashed line, which points towards an effect which appears at the periphery of the disks.

These different results suggest possible adverse effects during the nanopatterning of the thin film to disks B.

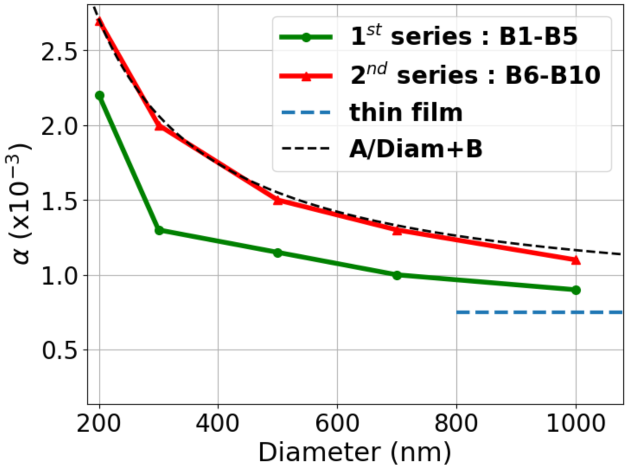

Figure 4.5: Variation of the damping as a function of the diameter for the 2 series of disks B1-B5 and B6-B10. The value of the thin film is indicated. These variations are in 1/Diameter as shown by the black dashed line (for which A=0.385 nm and B = 7.8×10^{-4}).

4.4.2 Spectroscopy of the disks beside the antenna

To check this assumption, an interesting point would be to measure the disks A and C located next to the antenna. In an ideal experimental configuration, the rf field is parallel to the static field at their locations. It would therefore be impossible to excite their FMR. But, if there is a very small angle between these static and rf fields at these locations (see the inset in Figure 4.6 a), it will be possible to measure them. It turns out that we were able to measure them. Figure 4.6 a shows the spectra of the series C1-C5 at f = 10 GHz. The microwave power used is 5 dBm for C5, 10 dBm for C2, C3 and C4 and even 17 dBm for C1. Indeed, these disks having a rf field whose main component is parallel to the static field, it is already necessary to pump them very hard even to measure them in the linear regime. With broadband measurements one can extract their magnetic parameters as for the disks B. One can therefore complete the previous Figures 4.4 a and 4.5 in Figures 4.6 b and 4.6 c below.

One observes that the absolute values of the frequency of the uniform mode of disks C remain close to those of disks B and quite far from the simulations (red curve in Figure 4.6 b).

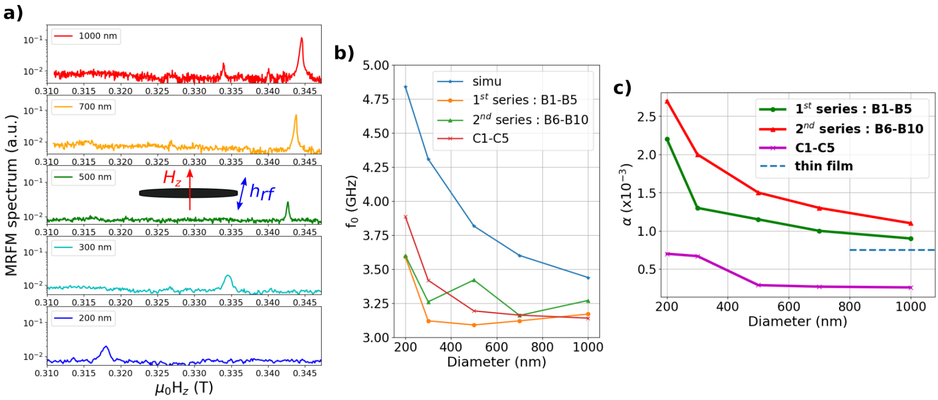

Figure 4.6: a) MRFM spectra at f = 5 GHz of the 1000, 700, 500, 300 and 200 nm diameter BiYIG disks (C5-C1) arranged in row by decreasing lateral size. The spectra have been shifted by the corresponding probe stray field. b) Evolution of the uniform mode frequency as a function of the diameter in experiments (for the 3 series of disks B1-B5, B6-B10 and C1-C5) and in simulations at a normal static field of 0.1 T. c) Variation of the damping as a function of the diameter for the 3 series of disks B1-B5, B6-B10 and C1-C5. The upper bound value of the thin film is indicated.

For these disks C, the spectacular result concerns the damping. On Figure 4.6 c, one observes that their damping is much lower than those of the disks B. It is almost constant and equal to 2.7×10^{-4} for the larger disks ($D \geq 500$ nm) and increases only up to 7×10^{-4} for the smaller ones. We have similar results for the other disks C (C6-C10) and disks A (A1-A10). The difference between the disks A,C and disks B being the presence of the antenna above the disks B, this result clearly shows that the microwave antenna affects the dynamic quality of disks B.

Since the disks B are in contact with the antenna at their edges as explained in Figure 3.12, it can be assumed that the mechanism behind the increase in their damping is the spin pumping at the lateral boundaries of the disk towards the Ti/Au antenna. A similar effect was observed for the confined mode of precessing magnetization in an unpatterned YIG film by finding that its damping scales like its surface-to-volume ratio, indicating an interfacial damping effect, similar to spin pumping, due to the transfer of angular momentum from the confined mode to the spin sink of ferromagnetic material in the surrounding film [125]. The fact that the damping of the disks B varies in $\approx 1/D$ as pointed out previously is in agreement with this hypothesis. Indeed, as the size of the disk decreases, this spin pumping effect at the edges would be more important relative to the volume of the disk and the damping would be larger. However, for the smallest disks, there is a non-negligible part of the increase in damping just due to a more important degradation during the etching process. This explains why the damping still increases for the smallest disks even for disks C (Figure 4.6 c) which are not under the antenna.

4.4.3 Spin wave modes amplitudes

We have seen that the relatives amplitudes of SW modes in disks B are very small in experiments, which suggests a deviation of their profiles from the Bessel functions. To complete these observations, we measure again the spectra of all the disks A, B, and C at higher power to detect the higher order modes. Figure 4.7 a shows the case of the 1000 nm disks. The grey vertical bars indicate the positions of the radial spin-wave modes in which we are interested and which we have discussed so far. We will come back later on the other modes detected.

We take the opportunity to extract the splittings of disks A and C. One completes the results of Figure 4.4 b and obtains Figure 4.7 b. One checks that we have a remarkable reproducibility of the splittings between higher order modes and the main mode n=0 for all the disks of the same size except for the disk 1000 nm B10 for which they are systematically slightly larger. At a given thickness, the splitting between the modes depend on the diameter of the disk. Since in the simulations, the splitting are quite well reproduced for all the sizes (see Figure 4.4 b), we conclude that the nominal disk sizes are their real sizes at least for the largest disks. The dispersion of the splitting for the 300 nm disks (see Figure 4.7 b) is not very surprising and is probably due to differences in the real size since it is much more difficult to be perfectly reproducible in nanofabrication at this scale. One observes that the relative amplitudes of higher order modes in disks A and C are not better than those of disks B. They remain far from the expected ratios 1, 1/4 and 1/9 obtained in the simulation. They seem to be better on the disk C5 but the other modes (non-radial modes) also have larger amplitudes than for the disks B.

4.4.4 Spatial modulation of magnetic anisotropy

According to equation (4.1), the quasi-invariance of the uniform mode frequency with the size at a given field can only be due to the characteristic field $\mu_0 H_K$ which is reduced to the demagnetizing field and the perpendicular anisotropy field for the uniform mode. Since the demagnetizing field $\mu_0 N_z M_s$ varies with the size of the disk (due to the variation of N_z with the size as shown in subsection 2.4.3.1), it follows that this quasi-invariance can only be due to the perpendicular magnetic anisotropy K_u. So, the deviation of the mode profiles from the Bessel functions suggests a spatial modulation of K_u. Such a modulation would come from the etching process, which affects the edges of the disk more than its center. One can therefore adopt a spatial modulation model in which the anisotropy is maximal in a central region and decreases to a minimum value in an external crown (see the inset in Figure 4.8 c).

The comparison of the results obtained on disks B and disks A,C allows to distinguish the different origins of the unexpected results and to refine the hypothesis on K_u.

- Damping : it is larger for disks B and increases as the disk size decreases, attributed to spin pumping effect at the lateral boundaries towards the Ti/Au antenna. The increase of the damping of the smaller disks for the disks C show that this increase can also be due to a degradation during the etching, more important for the smaller disks.

- Uniform mode frequency : for all the disks A, B and C, the values are similar (see Figure 4.6 b) and remain far from the simulations ones. The relative amplitudes of higher order modes compared to the main mode are very small and similar for all the disks. The splitting between the

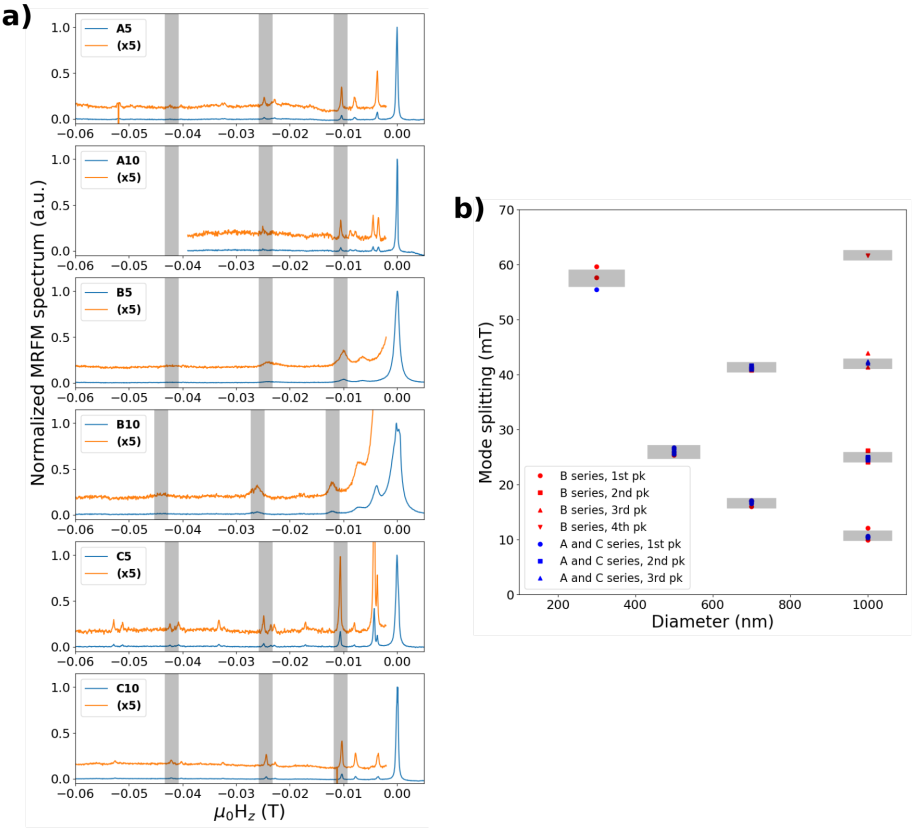

Figure 4.7: a) Variation of the relative amplitude of the spin wave modes for all the 1000 nm diameter disks A, B and C. The spectra are measured at f = 10 GHz. The grey vertical bars indicate the positions of the radial spin wave modes ($l = 0$). The orange spectra are a 5 times zoom on the spectrum except the main mode, to better see the relative amplitudes. b) Splitting between the spin wave modes for all the disks A, B and C: the splitting is reproducible for disks of the same size.

> modes is reproducible for all the disks of the same size and in good agreement with simulations. The spatial modulation of K_u is thus present in all the disks (A, B and C) and comes from the nanopatterning.

In the following, we try to determine this spatial modulation. An intense work on the choice of a suitable spatial modulation function and its optimization has been done. The modulation function finally chosen is given by the following expression (see Appendix B) :

$$K_u(r) = K_u \left[1 - \beta \left(exp(-(\frac{R-r}{\sigma})^2) + exp(-(\frac{R+r}{\sigma})^2) \right) \right] \tag{4.3}$$

where K_u is the maximum value of the anisotropy at the centre of the disk, R the radius of the disk, r the radial position. σ and β are two parameters that allow to adjust the spatial modulation and define respectively the size of the external crown where K_u is lowered and the difference between the anisotropy at the center of the disk and at the edges. The optimized parameters obtained are $\sigma = 150$ nm and $\beta = 0.1$ (see Appendix B for the optimization protocol). In the MicroMagnum code used, it is possible to directly adopt a spatial dependence of a magnetic parameter. Figure 4.8 c shows the new simulated spectrum obtained using the modulation function (4.3) with $K_u = 11685$ J.m^{-3}, for a 1000 nm diameter disk.

First, since the millimeter-sized piece of film on which the thin film properties were measured was far and therefore different from the nanopatterning region, one can think that the magnetic anisotropy of the disks is not exactly the one measured on this piece (12150 J.m^3) due to the strong inhomogeneity at these spatial scales. One checks that the only effect of a simple modification of anisotropy value (no spatial modulation) is to shift the spectrum by a field corresponding to the difference between the two anisotropy values. So, the anisotropy can be adjusted to find exactly the experimental main resonance field of the main mode. This is what has been done for the blue spectrum in Figure 4.8 b for which $K_u = 11500$ J/m^3.

Then, using the spatial modulation, the red experimental spectrum is better reproduced by the yellow spectrum in Figure 4.8 c, both in absolute position of the uniform mode and in relative amplitudes of the other modes. It is even slightly better reproduced in splitting. For example, the splitting between the first two modes is now 10.5 mT instead of 12.65 mT (in the green or blue spectrum in Figure 4.8 b), in even better agreement with the 10.3 mT of the experiment (red spectrum).

A similar effect was observed a long time ago by Hoekstra et al. in 5 μm thick substituted YIG films [126]. They observed in the measured spectra

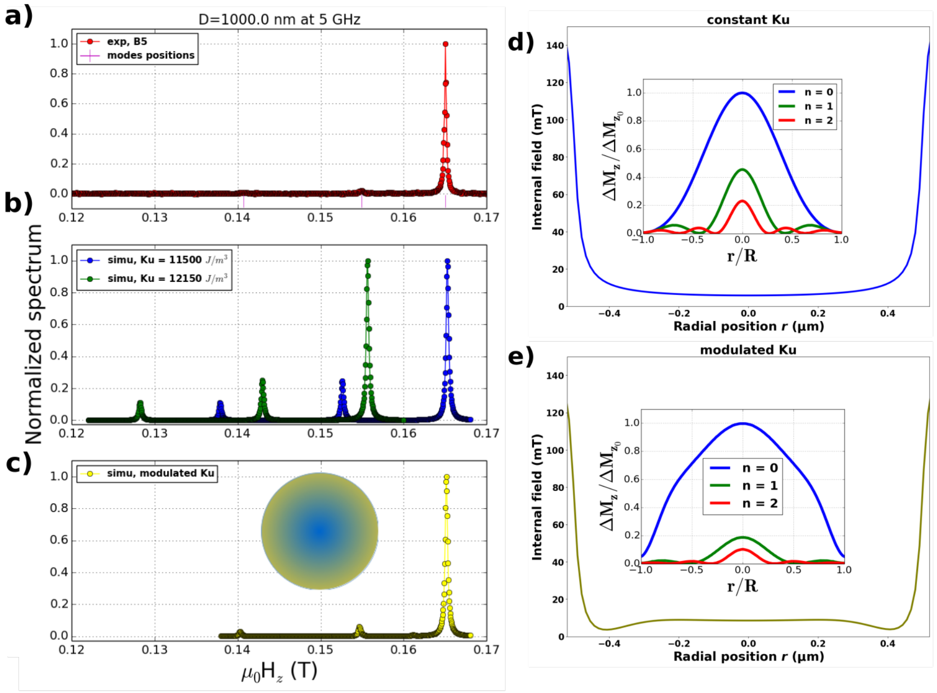

Figure 4.8: a) Experimental spectrum of the disk B5. b) Simulated spectra of a disk of 1000 nm diameter for two spatially uniform values of the magnetic anisotropy K_u : the only effect of a change in K_u is a shift in the spectrum. c) Simulated spectrum obtained by introducing the appropriate spatial modulation of K_u. Inset : model of spatial modulation of K_u within the disk: the central region keeps a constant K_u close to that of the thin film while the external crown has a lower K_u due to the etching during the nanofabrication and the effect of the antenna in the case of disks B. d-e) Profile of the internal field within the disk in the two cases of the constant and spatially modulated anisotropy. In each case, the simulated profiles of the main mode and the first two spin wave modes are shown.

a large number of thickness modes with large deviations from the expected quadratic spacing, interpreted in terms of a volume inhomogeneity of the uniaxial anisotropy constant. They were able to explain their results using two models of anisotropy modulation. One model in which the film is considered to be composed of two exchange coupled layers with different uniaxial anisotropy constants, and a second one in which it is assumed that the uniaxial anisotropy constant varies linearly with the distance from the substrate under the film, but with different slopes in different regions.

The internal field profile in the disk and the associated simulated profiles of the uniform mode and the first two spin wave modes with the corresponding indices in both case of constant and modulated anisotropy modulation are presented in Figure 4.8 d & e. The constant anisotropy modes profiles are those shown in Figure 4.4 d. There is clearly a deformation of the modes profiles with the spatial modulation of K_u. Indeed, this modulation affects the internal field, in particular in the external crown where the inhomogeneous internal dipolar field is partially compensated by the modulation of K_u, which flattens or slightly sinks the profile on a part of the periphery, see the yellow curve in Figure 4.8 e. This results in a significant modification of the profile of the uniform mode by increasing the volume under its curve and thus the corresponding amplitude. For the other modes, this volume decreases. This leads to a decrease in the relative amplitudes of these higher order modes, which explains the yellow spectrum in Figure 4.8 c.

With our model we were also able to slightly better reproduce the results of the 700 and 500 nm diameter disks. The higher order modes were not even detected for the smallest disks. In any case, with the parameters used, we realize that K_u would even be slightly lower at the center of the 200 nm disk than at its edges. This is not surprising since the radius R = 100 nm is now smaller than the external crown size $\sigma = 150$ nm. Let us mention that even for the 500 and 700 nm disks it is necessary to vary the value K_u in the equation (4.3) in order to reproduce the resonance field of the uniform mode. This is certainly due to the spatial inhomogeneities of K_u in the initial thin film already witnessed in the cavity-FMR data (see Figure 3.10 b) as mentioned previously.

4.5 Experimental investigation of the origin of the non-radial spin wave modes

We have previously observed that the spectra of Figure 4.7 a also exhibited resonance peaks different from those corresponding to the radial spin-wave modes we have studied so far. In this section we explain their origin.

4.5.1 Hidden modes

It is known that appart those radial modes $l = 0$, there are azimuthal modes of non-zero azimuthal index l, whose some of index $l = 1$ were shown in Figure 2.5. In a MRFM experiment using a uniform rf field, it should be impossible to excite such modes since the overlap integral of their profiles with a uniform field is zero (see equation (2.41). These modes are then said to be "hidden". However they can be excited for different reasons and in different ways.

This is possible due to an axial symmetry breaking in the experiment. This symmetry breaking can be intrinsic to the studied sample whose shape can slightly deviate from the perfect cylindrical geometry due to the nanofabrication process for example. It can also be caused by a small deviation of the static field from the disk normal. Taking into account such a deviation of the static field in analytical and numerical models allowed to better reproduce the experimental spectra of permalloy disks previously measured in the lab. Such a deviation indeed induces a symmetry breaking which in addition to the radial modes makes possible the excitation of azimuthal modes or even linear combinations of different modes [56]. In MRFM experiments, one can also break or even restore the axial symmetry using the probe stray field, by moving the probe laterally above the disk. Thus, in experiment it is possible to check the axial symmetry by studying the evolution of the amplitude of these hidden modes with the lateral position of the probe. In the case of a perfect probe-disk alignment (axial symmetry) there are no hidden modes at all (zero amplitude).

Finally, it is possible to excite the non radial modes using a non-uniform excitation field in the sample.

4.5.2 Evolution of the spectrum with the lateral position of MRFM probe

In the spectra of Figure 4.7 a, one notes that the positions of these "unexpected" modes are reproducible from one disk to another. The most obvious are those at -4 and -8 mT with respect to the main mode. To understand their origin, measurements of the amplitude (the spectrum) of the mode at -4 mT is performed as a function of the lateral position of the probe. Figure 4.9 a & b show the results for the 1000 nm disks C10 (beside the antenna) and B10 (under the antenna). In each case, the probe is positioned above the disk at

$X_0 = 0$ and then shifted laterally by 100 nm steps. The grey bars show the mode at -4 mT (common to both disks).

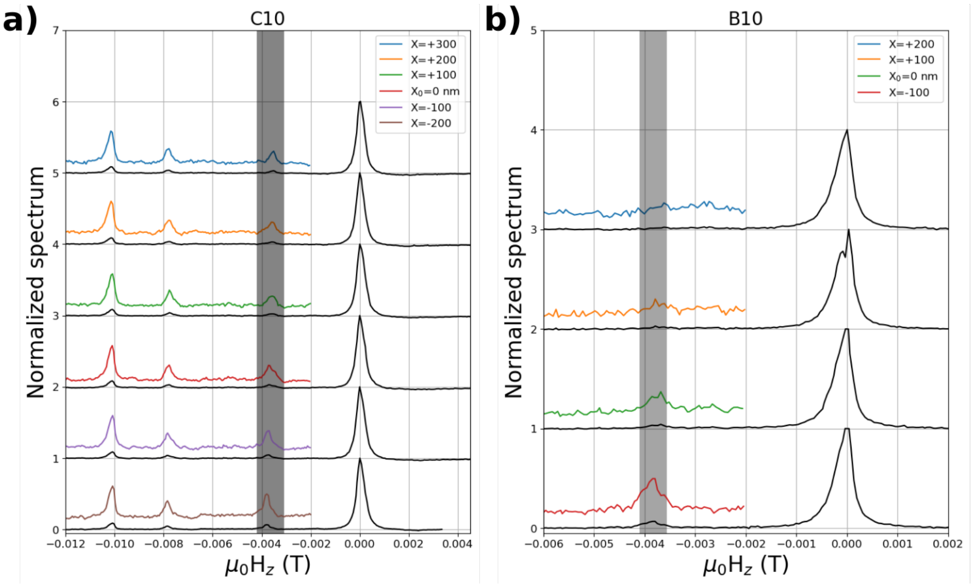

Figure 4.9: Evolution of the MRFM spectrum as a function of the lateral position of the probe for the 1000 nm diameter disks a) C10 and b) B10. The colored spectra correspond to a 5 times zoom. The distorted shape of the main mode at X=+100 in b) is an experimental artefact due to an instability of the MRFM phase-locked loop feedback.

One observes that this symmetry breaking almost does not affect mode amplitude in the case of disk C10. But in the case of B10, it is possible to almost suppress this mode at X=+100 and 200 nm. These results suggests that the detection of these modes in disks B located under the antenna and subjected to a uniform excitation field (see Figure 3.13), is simply due to a breaking of axial symmetry, an effect which can be corrected in the experiment by playing on the position of the probe.

The disks A and C located quite far from the antenna are subjected to a non-uniform rf field decreasing from the edge of the disk near to the antenna to the other edge (see Figure 3.13). This non-uniform excitation is the reason for the simultaneous excitation of the radial and azimuthal modes in disks A and C independently on the probe lateral position.

In micromagnetic simulations performed by Olivier with SpinFlow, one obtains all the modes in the disks, both for radial and azimuthal ones. one checks that the modes (n=0,l=1) and (n=0,l=2) are at -5.5 and -10.8 mT with respect to the main mode (n=0,l=0). These values are in agreement with the experimental values of -4 and -8 mT of the first two hidden modes (see Figure 2.5).

However, even for disks B under the antenna for which the excitation field is uniform, it is almost impossible to completely suppress the amplitudes of these azimuthal modes in experiments. This could be explained by the small deviation of the disks from the perfect cylindrical geometry (see Figure 3.12), another intrinsic source of axial symmetry breaking.

4.6 Conclusion

From the broadband spectroscopy, we measured the magnetic parameters of the different disks. We obtained unexpected results such as the quasi-invariance of the resonance field with the size of the disk, which is obviously not reproduced in basic micromagnetic simulations with a constant anisotropy. These observations, combined with low relative amplitudes of spin wave modes compared to the main mode, were attributed to a spatial modulation of the anisotropy within the disks using the simulations. We believe that this effect comes directly from the degradation of the sample during nanopatterning. We also observe a very strong increase in the damping of the disks under the antenna compared to the others, which we attribute to pumping at their lateral boundaries towards the metallic antenna.

Summary

- Measurement of the resonance spectra of the different disks : extraction of their magnetic parameters.
- Presentation of micromagnetic simulation methods : application to the case of nanodisks.
- Comparison between experimental and simulation results : evidence of a spatial modulation of the magnetic anisotropy.
- Larger damping for disks B : spin pumping at their lateral boundaries towards the metallic antenna.

Chapter 5

FMR driven dynamic instabilities in out-of-plane magnetized nanodisks

"Turbulence is the only way to get altitude – to get lift. Without turbulence the sky is just a big blue hole. Without turbulence, you sink."

Kelly Corrigan, *Lift,* **2010**

Contents

In the previous chapter, one focused on limiting the power of the microwave excitation to perform disks spectroscopy in the linear regime. We now enter the heart of this thesis by going into the nonlinear regime, which means significantly increase the intensity of the excitation. The applied static field is still perpendicular to the disks. The discretization of the spectrum allows to focus on the main mode.

5.1 Evolution of the main resonance line with the excitation amplitude

5.1.1 MRFM experiments

As mentioned in the theoretical part, the FMR foldover that appears in the nonlinear regime has a hysteretic character. It was explained in section 3.1.4 that in the experiment one modulates the excitation at the cantilever frequency by alternatively switching on and off the microwave power to amplify the signal. By doing this, in the hysteretic region one will not have access to the upward branch of the dynamics but only to the downward branch (see Figure 2.9).

Figure 5.1 shows the evolution of the resonance line as a function of microwave power for the 700 nm disk B9 at f = 5 GHz and 7 GHz. Let's focus on the case of the Figure 5.1 a for example. It shows this evolution between -16 dBm and 9 dBm corresponding to a variation of power of more than two orders of magnitude. For clarity, the resonance lines are shifted vertically by the value of the power. As explained in equation (2.68), for very small excitation powers the amplitude of ΔM_z which is our signal, and the corresponding precession angle, linearly increases with the power. One checks for example that the signal amplitude doubles between -16 dBm and -13 dBm and that the linear increase continues until -11 dBm. Then at -10 dBm the resonance line start to distort, which indicates that the nonlinear regime is reached. This distortion of the resonance line continues until -1 dBm. One checks that in this range, the amplitude does no longer evolve linearly with the power since the linewidth increases. As expected, due to the negative characteristic field H_K of the disk, the resonance line shifts towards higher magnetic field as the precession angle increases (see Figure 2.8 d & f), which is opposite to the behavior reported on undoped YIG nanodisk shown in Figure 1 C [22]. The shift remains very small because of the very small value of $\mu_0 H_K$ = -11.6 mT (see Table 4.2).

The dynamics at even higher power (P > 0 dBm) is completely unexpected and seems more complex and interesting, with a rapid saturation of the peak amplitude followed by a kind of splitting of the resonance line into two peaks combined with broadening of the line towards both lower and higher magnetic

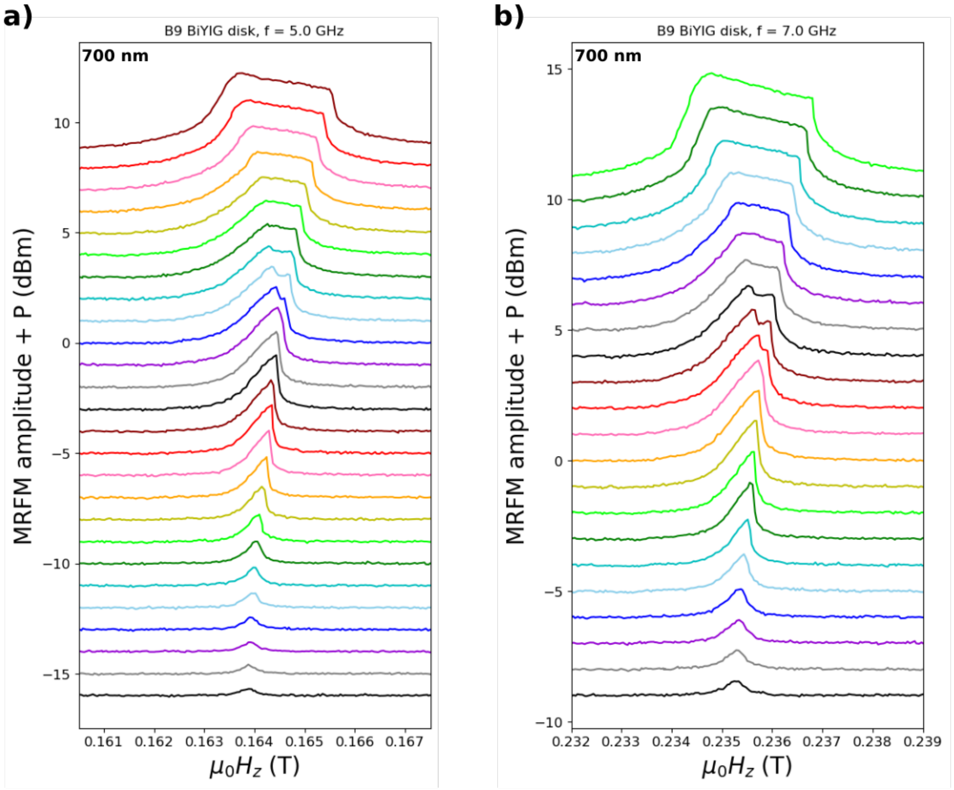

Figure 5.1: Evolution of the resonance line as a function of microwave power for the 700 nm diameter disk B9 at a) f = 5 GHz and b) f = 7 GHz. Each spectrum is shifted by the power level for clarity.

field. Figure 5.1 b shows that these effects are also observed at f = 7 GHz.

Moreover, Figure 5.2 shows that the early saturation of the signal is common to the 1000 nm and 500 nm diameter disks with some particularities.

For the 1000 nm disk B10 (see Figure 5.2 c), the behavior is mainly similar to that of the 700 nm disks except for the amplitude of the azimuthal mode (n=0,l=1) at 0.156 T which also increases until it "merges" with the main mode beyond 10 dBm. Let us mention that the results obtained for the 700 nm disk B4 and 1000 nm disk B5 are similar to those of their twin disks B9 and B10 respectively.

For the 500 nm disks B3 and B8, which already had quite different resonance fields in the linear regime, the behaviors differ a bit more in the nonlinear regime. The one of B8 (Figure 5.2 b) is similar to the 700 nm and 1000 nm disks with a flattened resonance peak at very high power. But for B3, although it also presents a rapid saturation of the signal, the splitting in two of its resonance peak appears more clearly (see the black resonance line in Figure 5.2 a at P = 5 dBm). It even splits in three beyond 8 dBm, in contrast to the flattening of the peak for the other disks. In Figures 5.1 and 5.2, for a better visualization, the signals of the 500 nm disks B3 and B8 were multiplied by two compared to those of the 700 nm disk B9 and 1000 nm disk B10.

So, despite these qualitative differences, all the disks of diameter D $\geq$ 500 nm show an early saturation of the resonance peak amplitude as the power is increased.

As mentionned previously, for the same excitation power, the transverse component of the microwave field for disks A and C located beside the antenna is much smaller than for disks B under the antenna. Therefore, to measure them even in the linear regime it is necessary to use very high powers. For this reason it was not possible to measure them as a function of microwave power in the same detail as for disks B. Nevertheless, we were able to observe the same saturation effect of the resonance peak at lower frequency f = 3 GHz on one of the 1000 nm disk A, the smaller frequency allowing to decrease the threshold of the nonlinear regime.

5.1.2 Comparison with micromagnetic simulations

To understand these unexpected observations in the nonlinear regime, we perform micromagnetic simulations. We obviously follow the second method presented in section 4.3, this time increasing the excitation field and scanning the static field in both directions to get the full dynamics, since we do not need to modulate the microwave field in the simulation.

Figure 5.3 shows the results obtained for the 700 nm disk for different

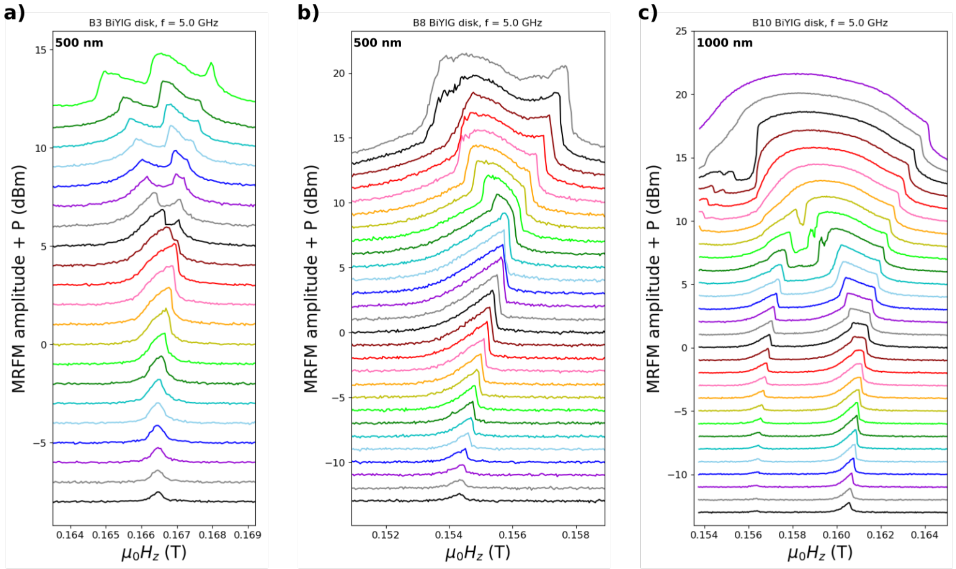

Figure 5.2: Evolution of the resonance line as a function of microwave power at f = 5 GHz for the 500 nm diameter disks a) B3 and b) B8, and for the c) 1000 nm diameter disk B10. Each spectrum is shifted by the power level for clarity.

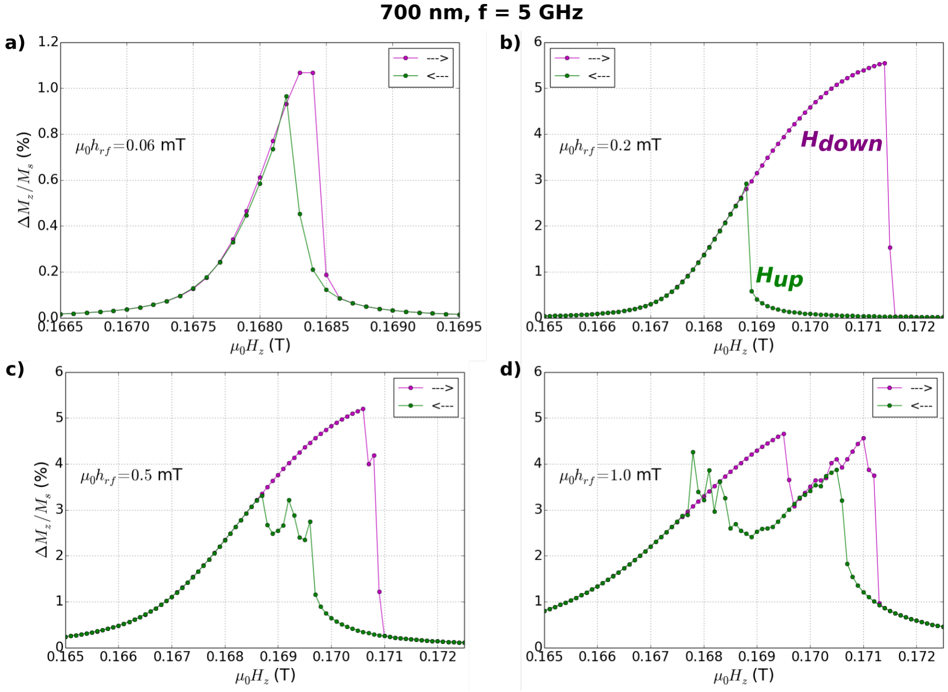

Figure 5.3: Hysteresis cycle of the FMR resonance line of the 700 nm disk at different excitation fields in the simulation. At high excitation, a rapid saturation of the two branches of the dynamics appears.

excitation fields at f = 5 GHz. It displays the spatial average of the decrease of the longitudinal component of the magnetization ΔM_z averaged over 50 ns after the 50 ns of transient regime, calculated for each static field as explained in section 4.3. If at the beginning there is the expected behavior of the resonance line with the classical hysteretic response, one observes from $\mu_0 h_{rf}$ = 0.2 mT that the amplitude of the upward branch (with H_{down}) in magenta tends to saturate. This observation is confirmed with a decrease of H_{down} between $\mu_0 h_{rf}$ = 0.2 mT and $\mu_0 h_{rf}$ = 0.5 mT combined with a saturation of the downward branch in green. Finally, at $\mu_0 h_{rf}$ = 1.0 mT, both branches have saturated. One notes that this saturation is almost at the same amplitude, at $\Delta M_z/M_s \approx$ 5%.

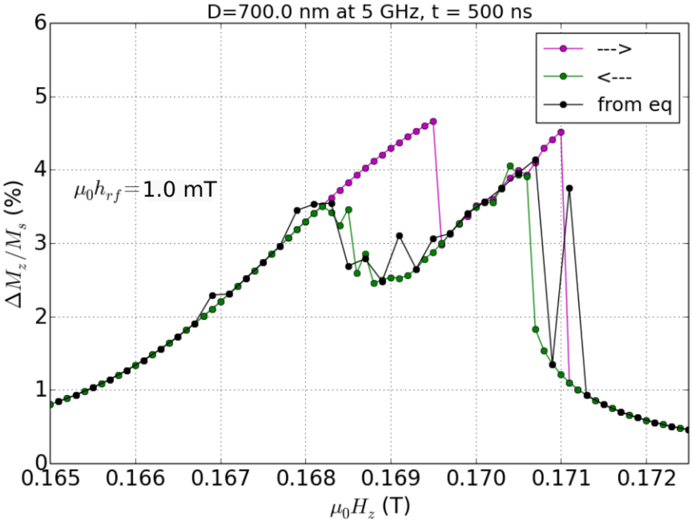

Figure 5.4: Resonance lines of the 700 nm disk at f = 5 GHz and $\mu_0 h_{rf}$ = 1.0 mT, obtained for different simulation protocols. In green and magenta : the result of the simulation at each point is used as the initial state for the simulation of the next point, the field is scanned in both directions. In black : each point is simulated starting from the equilibrium i.e. at $\Delta M_z = 0$. In both cases, each field is simulated during 500 ns.

On the resonance line of Figure 5.3 d, one observes some kind of small oscillations in the saturation zone, around 0.168 T for the green curve and around 0.1705 T for the magenta curve. This is simply a numerical noise which comes from the simulation time of 100 ns at each static field (see the description of the simulation protocol in section 4.3), insufficient to really reach the steady state in these regions of the resonance line. The result obtained with an identical simulation but using 500 ns at each field and presented in Figure 5.4 (green and magenta curves) confirms this explanation : these oscillations are smoothed. Moreover, since in the experiment, one modulates the excitation, one starts from the equilibrium at each static field. We have performed a simulation in which we do exactly that, i.e. at a given field, instead of taking the state obtained at the end of the simulation of the previous field as the initial state for the calculation of the dynamics, we start from the equilibrium each time (which we calculate in a first step). This method obviously requires a much longer simulation time for each field since one starts each time from a state much further away (equilibrium state i.e. $\Delta M_z = 0$) from the final state. The black curve in Figure 5.4 shows the result obtained with a simulation time of 500 ns. It can be seen that the curve obtained is almost identical to the green curve corresponding to the downward scan of the field, except a slight shift in the position of H_{up}. Using this method with a simulation time of 100 ns as in Figure 5.3 gives however a much noisier result than the one in Figure 5.3 d. For all these reasons, we will keep the bidirectional scan simulation protocol with a simulation time of 100 ns, sufficient to compare the results with our experimental results.

In Figures 5.5 a & b, one compares the simulation results with the previous experimental results of the 700 nm disk B9, the resonance lines being now normalized and shifted vertically with the rf field. In simulations, one takes the downward branch which we are supposed to measure in the experiment. One observes a good qualitative agreement with a small distortion of the resonance line towards high fields, followed by the broadening of the resonance line and the saturation of the peak amplitude despite the fact that the flattening is not well reproduced.

It is interesting to evaluate the amplitude of the microwave excitation to know quantitatively the thresholds of the various nonlinear effects that we observe (foldover, splitting of the resonance peak, saturation of the line...). At a given power, the efficiency of the excitation depends on the microwave frequency. The microwave power P being proportional to $(\mu_0 h_{rf})^2$ where $\mu_0 h_{rf}$ is the excitation field, let's introduce the factor of proportionality S :

$$S = \frac{\mu_0 h_{rf}}{\sqrt{P}} \tag{5.1}$$

One can calculate S from the geometry of the antenna using the Biot-Savart law, see Appendix C.1. One finds in the absence of microwave losses in the circuit $S = 0.8$ mT/$\sqrt{mW}$. One can now deduce S by comparing experimental and simulation results quantitatively. This involves matching the experimental and simulated resonance lines in pairs at remarkable locations such as the appearance of the foldover (when there is a vertical tangent), the peak splitting and the saturation. This is done in Figures 5.5 a & b. This leads to $S = 0.25$ mT$/\sqrt{mW}$. One also measured S by measuring H_{up} as a function of microwave power, see Appendix C.2. One found a value of the same order of magnitude, $S = 0.17$ mT$/\sqrt{mW}$.

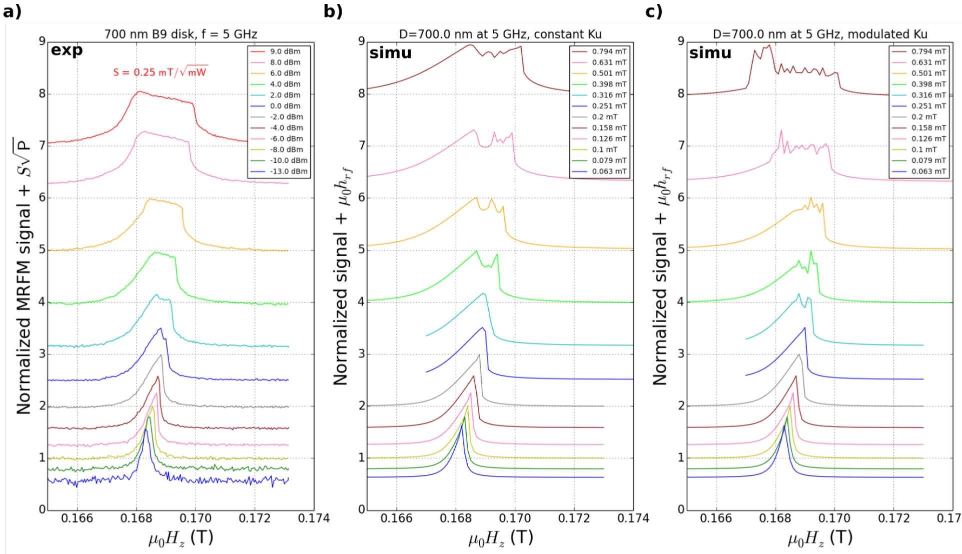

Figure 5.5: a-b) Comparison between the experimental results and the simulation : deduction of the calibration factor S between the excitation power and the microwave field from a qualitative comparison. The simulation results are obtained for a constant anisotropy K_u. c) Case of a modulated anisotropy using the spatial modulation model demonstrated in the linear regime : the results are similar to the case of a constant anisotropy.

Having this matching of resonance lines between experiment and simulations, one can then determine the amplitudes reached in the experiment by multiplying the data by an appropriate factor to well reproduce the amplitudes of the corresponding simulated resonance lines. This is what has been done in Figure 5.6 with the data of the 700 nm disk B9 shown previously. One observes that the saturation of the amplitude occurs for $\Delta M_z/M_s$ of the order of 4%, which corresponds to mean precession angles θ of maximum 20° (cos $\theta = 1 - \Delta M_z/M_s$). This result is completely different from $\Delta M_z/M_s$ of the order of 100% i.e a mean precession angle of almost 90° previously measured in the YIG disk of the same size [22] as shown in Figure 1 C.

Note that these simulation results (Figures 5.3, 5.4 and 5.5 b) for the 700 nm disk were obtained with a constant anisotropy. Figure 5.5 c shows the results obtained when using the spatial modulation model of the anisotropy demonstrated in the linear regime, see equation (4.3). The results are similar to those obtained for a constant anisotropy except for the amplitude of the peak which is greater in the case of the modulation since the linear regime as we have seen. In that case, the saturation is rather at $\Delta M_z/M_s \approx 8\%$, which corresponds to precession angles lower than 25°. Thus this saturation of the resonance line is independent of the spatial modulation of the anisotropy. This is why, in the following, in simulations we limit the study to the spatially uniform case. The values of anisotropy and damping used in the simulations for all disk sizes are given in appendix D.

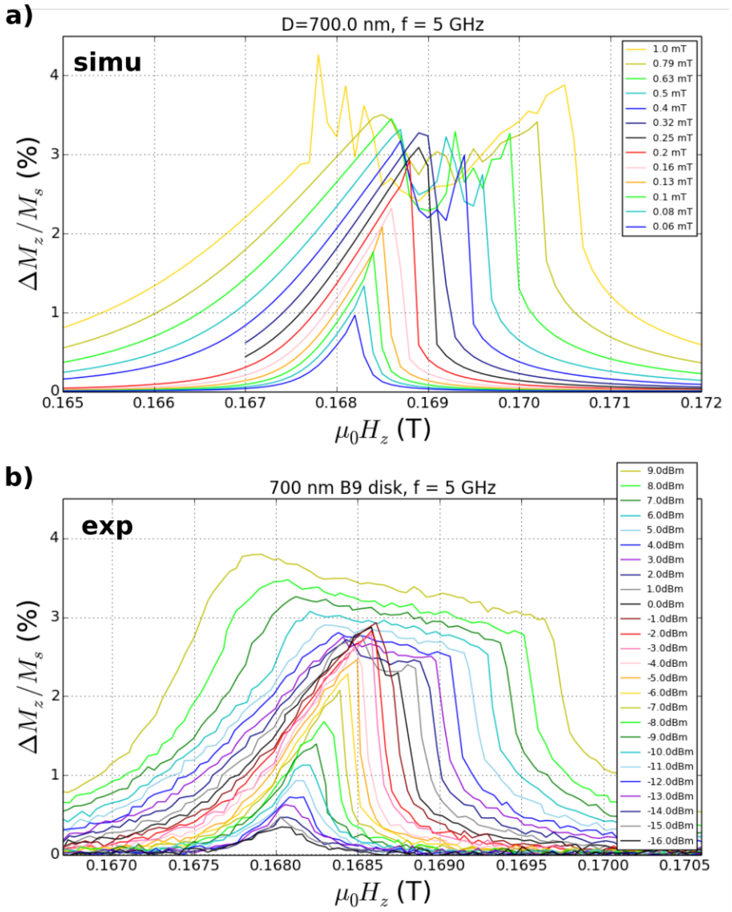

Figure 5.6: Comparison between the experimental results and the simulation of the evolution of the resonance line as a function of the excitation field for the 700 nm disk B9 at f = 5 GHz.

We obtained similar results using MicroMagnum on the 1000 nm disk concerning the evolution of the resonance line, the hysteretic behavior followed by the rapid saturation of the amplitude and the calibration of the rf field. One finds that for the maximum excitations in the experiment, $\Delta M_z^{max}/M_s \approx 3$ %, even smaller than for the 700 nm disk.

5.2 Analysis of the simulated temporal dynamics

As mentioned before, the reduction of longitudinal component of magnetization ΔM_z that we measure in the experiment corresponds to a spatial average over the whole disk; the sizes of the disks being of the same order of magnitude as the size of the probe, we do not have spatial resolution. Furthermore, because of the modulation of the microwave power at the cantilever frequency, the integration time of our measurements is in the order of 50 μs (the cantilever frequency f_c of the order of 10 kHz corresponds to a period of 100 μs). So we don't have time resolution. This is not the case in simulation where one can have access to both the temporal dynamics and the spatial profiles of the spin wave modes. So, in order to understand the main effect observed in the experiment and reproduced in the simulation, namely the rapid saturation of the resonance peak amplitude, one can now focus on what happens in time in the simulation. One focuses on the 700 nm diameter disk.

5.2.1 Time evolution of the average components of magnetization

Figure 5.7 a shows the simulated downward branch of the resonance line in the simulation at a field $\mu_0 h_{rf}$ = 1.0 mT at f = 5 GHz, already shown in Figure 5.3 d. Then one visualizes in Figures 5.7 b to j the time evolution of the normalized average components of the magnetization, the x and y components $m_x = M_x/M_s$ and $m_y = M_y/M_s$ (in green), the longitudinal component m_z $= M_z/M_s$ (in skyblue) and the transverse one $m_t = \sqrt{m_x^2 + m_y^2} = M_t/M_s$ (in red) at nine fields through the resonance line. The selected points are colored on the resonance line. And in Figure 5.8, one presents for 3 of these fields, 0.167, 0.168 and 0.1685 T, zoom curves of m_z, m_x and m_y, and m_t at the end of the 100 ns of simulation. They allow to distinguish m_x and m_y, to check that they oscillate at 5 GHz and that they are in phase quadrature (see Figures 5.8 d, e & f). We call the saturation region the area of the resonance

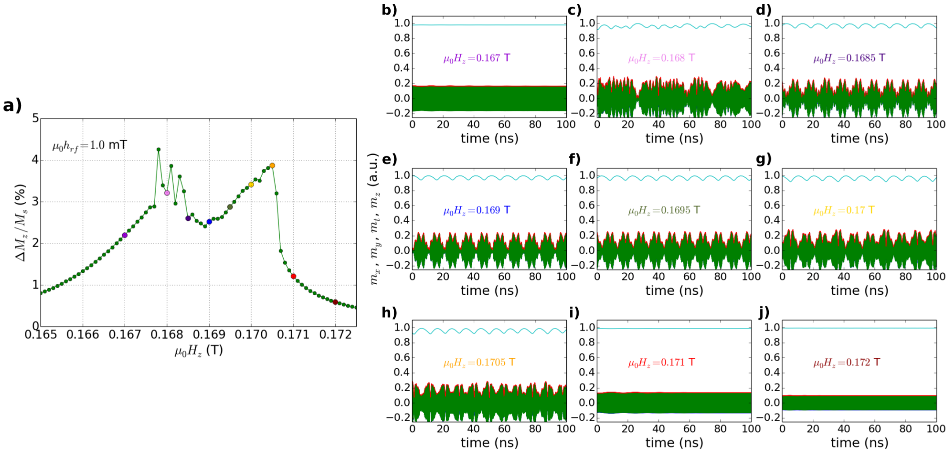

Figure 5.7: a) Resonance line in the simulation at $\mu_0 h_{rf} = 1.0$ mT for the 700 nm disk. b) to j) Time evolution of the normalized average components of the magnetization during the 100 ns simulation at different fields through the resonance line shown in a). The fields from b) to j) correspond in this order to the colored points of the resonance line in a). The longitudinal component m_z is in light blue, the m_x and m_y components in green and the transverse component m_t in red.

line located between 0.1678 T and 0.1705 T. One observes that for the fields outside this area (0.167, 0.171 and 0.172 T), there is nothing special in the time evolution (Figures 5.7 b, i & j). A zoom on the curves allows to check that after a transient regime, a steady state where m_t and m_z are constant is reached, see Figures 5.8 a & g.

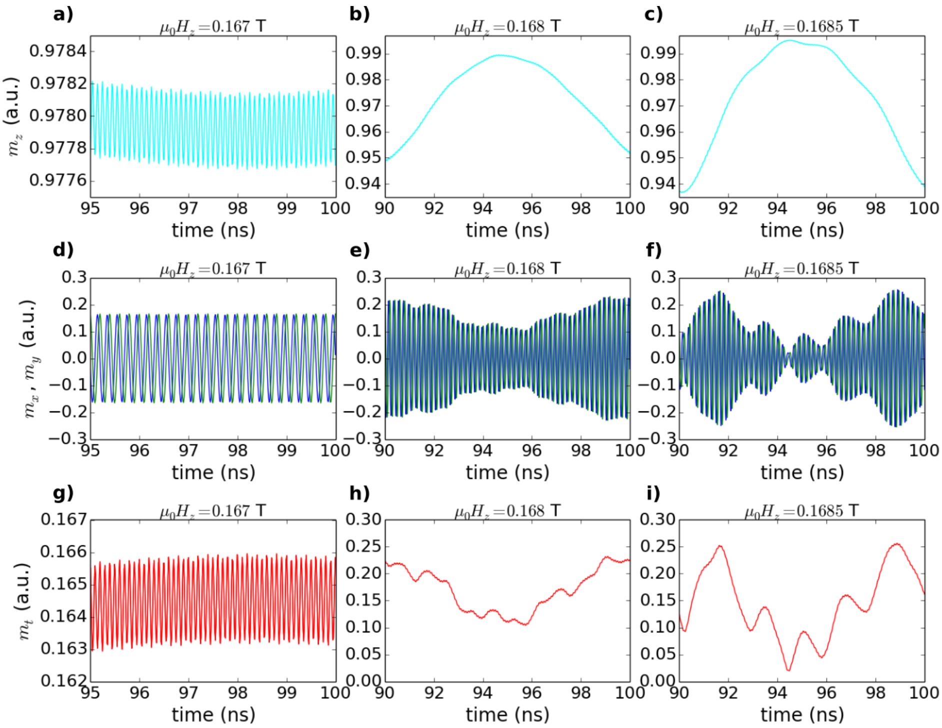

Figure 5.8: Zoom on the time evolution of the components m_z, m_x, m_y and m_t of the magnetization at three different fields : 0.167, 0.168 and 0.1685 T, for the 700 nm disk.

On the other hand, for the fields located inside the saturation zone (between 0.1678 T and 0.1705 T), one observes the onset of low frequency instabilities in the time evolution. At 0.1685 T for example, one observes quasi-periodic oscillations of the longitudinal component m_z with a period in the order of 10 ns, which corresponds to a frequency of 100 MHz. It is obviously very far from the excitation frequency of 5 GHz. This quasi-periodicity can be seen in Figure 5.8 f with the amplitude of m_x and m_y varying over time at a slower time scale than the 5 GHz drive. In Figures 5.8 c & i, one also observes that at 94.5 ns, $m_t \approx 0$ and $m_z \approx 1$: this corresponds to a kind of extinction of the precession of the magnetization ($\theta \approx 0$). In Figure 5.7 d, m_z reaches almost 1 during its ocillations. These different points are all points of quasi-extinction of the precession : there is a periodic quasi-extinction of the dynamics. Such points are also present for other fields located in the saturation region except at 0.1705 T (see Figure 5.7 h) where we can see that m_t never approaches 0 (red curve).

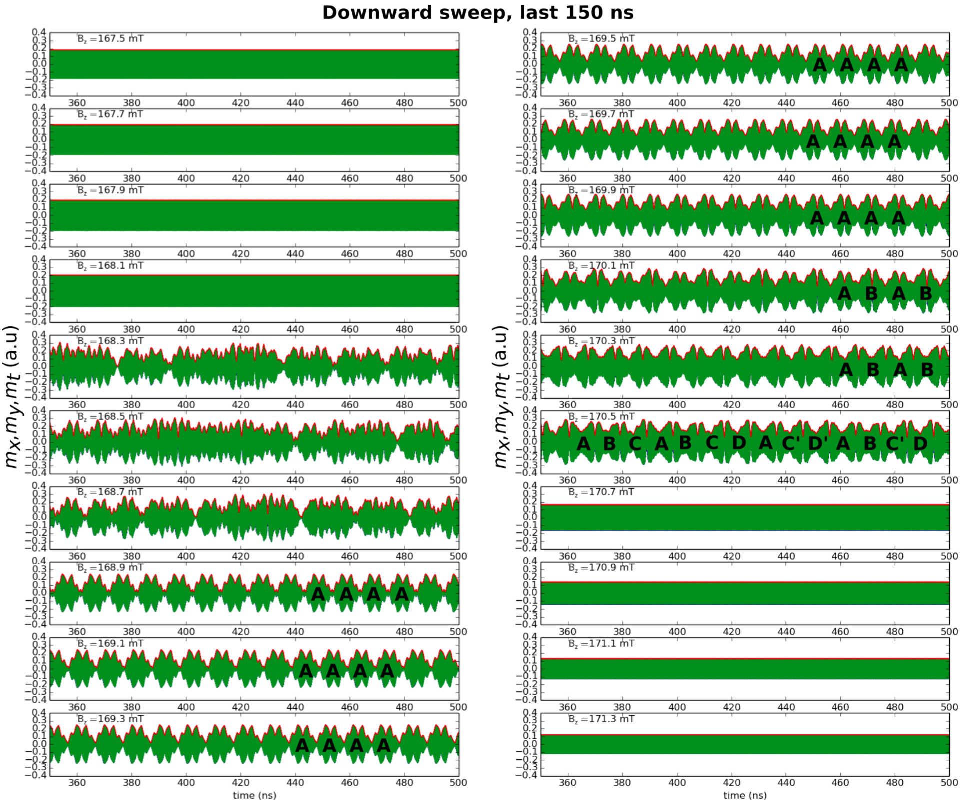

Figure 5.9: Zoom on the last 150 ns in time evolution of the components m_x, m_y and m_t of the magnetization at different fields trough the resonance line for the 700 nm disk, each field having been simulated 500 ns. The simulation was done with a downward sweep of the field. For each field, the initial state is the final state of the previous field.

We have seen in Figure 5.4 that with a simulation time of 500 ns at each field, one obtains almost the same resonance line as with 100 ns, except the small oscillations in the saturation zone which are smoothed. Figure 5.9 shows a zoom of the evolution of the components m_x, m_y and m_t (in red) of the magnetization on the last 150 ns at different fields through the resonance line. This is the case of a downward sweep of the field (green curve in Figure 5.4).

The values of the field are indicated in mT. One notes that depending on the static field in the saturation region, there is a rich variety of temporal profiles. For example, let's focus on the transverse component in red. It can be seen that the profiles for the fields between 168.9 mT and 169.9 T show a similar periodic repetition of type AAAA... of an elementary pattern A, the exact shape of the pattern can be different from one field to another. For example a careful inspection allows to check that the pattern is different between the fields 169.1 and 169.7 mT in particular concerning the value reached by m_t at the extinction points. For the fields 170.1 and 170.3 mT one rather has a quasi-periodic behavior with a repetition of type ABAB... A and B being of different amplitudes. At 170.5 mT, it seems that the dynamics is still not stable after 500 ns and one should simulate on a longer time. At 168.3, 168.5 and 168.7 mT, it is not possible to identify a pattern. The temporal evolution seems to present a chaotic behavior. Here too there are extinction points, but they are not quasi-periodic as at the other fields. The dynamics of the magnetization thus presents commensurate (quasi-periodic) or incommensurate (chaotic) states depending on the conditions of excitation of the resonance. The detailed study of the time evolution of the profiles highlights a rich generation of patterns that could be analyzed by symbolic dynamics and encoded in bit sequences, as was done in nanocontact vortex oscillators by unveiling and characterizing their waveform patterns [127].

Comparisons with time evolution in the case of a simulation starting from equilibrium at each field (see black curve in Figure 5.4) are shown in the appendix E. They show that the steady state is easier to reach in the case of a point to point sweep. One notes that at certain fields, the final state can be very different according to the initial state. Even when the final dynamics at a field is a periodic repetition of the same type in both cases (for example AAA...) a detailed inspection shows that the pattern A can be different depending on the case. In all cases, these instabilities are associated with a periodic decrease of the longitudinal magnetization m_z.

5.2.2 Time evolution of the precession profile

5.2.2.1 Self-localized ultra-large precession : dynamic instability

One can then go a little further in the analysis by visualizing the entire spatial profile of the precession mode during the resonance. The profile is obtained by storing the 3 components of the magnetization in all the 64x64 cells. Since this requires storing a very large amount of data, it is only done at the end of the 100 ns simulation of each field. For the different magnetic fields selected in Figure

5.7 a, the profile is presented in Figure 5.10, the transverse component m_t in light blue and the longitudinal component m_z in red. For the fields outside the saturation zone (the first and the last two), the precession profile corresponds to the classical Bessel function (see the inset in Figure 5.10 a) whose amplitude depends on the selected field in the resonance line, while remaining low. Inside the saturation region, the precession mode increases in amplitude, becoming more and more localized in the center of the disk. This is particularly clear on the profiles of the fields 0.168, 0.1685, 0.1695 and 0.17 T in Figures 5.10 b c e & f. At 0.1685 T, the localization is so huge that mz becomes negative at the center of the disk, which means a crossing of the equatorial plane by the magnetization at the center of the disk, meaning a local precession angle larger than 90°.

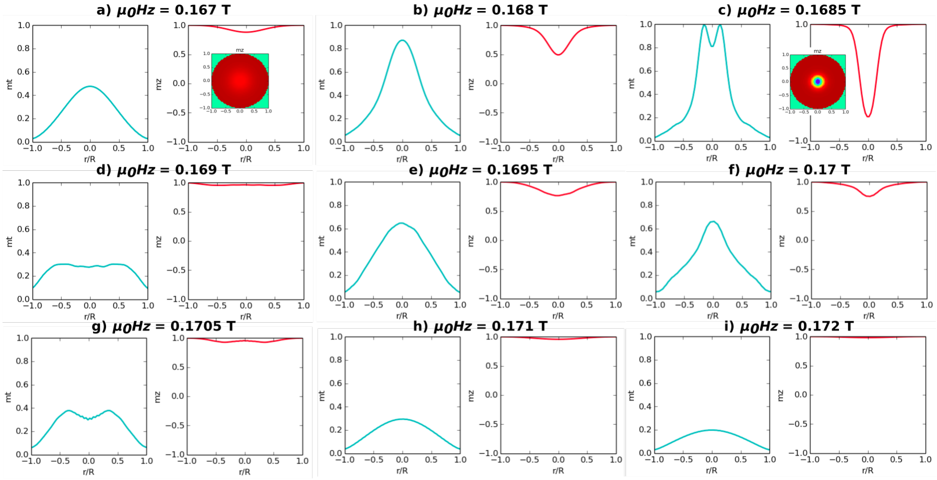

Figure 5.10: Snapshots of spatial profiles of the transverse (light blue) and longitudinal (red) components of magnetization at the different colored points of the resonance line of Figure 5.7 a for the 700 nm disk.

Then it is necessary to see how this profile evolves in time. The result obtained at $\mu_0 H_z = 0.169$ T located in the saturation region is shown in Figure 5.11 for the longitudinal component of magnetization. It shows the strong localization of the precession profile at the disk center, see Figure 5.11 g. Note that the six Figures 5.11 b to g show the profile evolution over 5.5 ns. The profiles obtained during the next 5.5 ns (and not shown here) are almost identical, repeating in the opposite order : from 11.56 ns, the amplitude of the profile decreases until it reaches an almost zero amplitude as in t=6.08 ns (Figure 5.11 b) around 17 ns and so on. There is clearly a dynamic instability corresponding to time oscillations of the profile during which its amplitude varies significantly. Indeed, at t = 11.56 ns which corresponds to the maximum decrease of m_z, the profile of m_z in Figure 5.11 g shows that there is no precession at the edges of the disk while at the center $m_z \approx$ -0.5, which corresponds to a precession angle of 120°. This confirms that at the center of the disk, the magnetization vector even crosses the xy plane ($\theta > 90°$). But one has to keep in mind that this is a precession strongly localized spatially at the center of the disk. Moreover it is also time localized since at a given field, it takes place only at certain moments as clearly shown in Figure 5.11. We have checked that even with a simulation time of 500 ns we find the same dynamics and the same time variations of the magnetization. The comparison between Figure 5.11 g and Figure 5.10 c shows that the onset of this strong localization of the precession profile at the disk center occurs at all the fields in the saturation region.

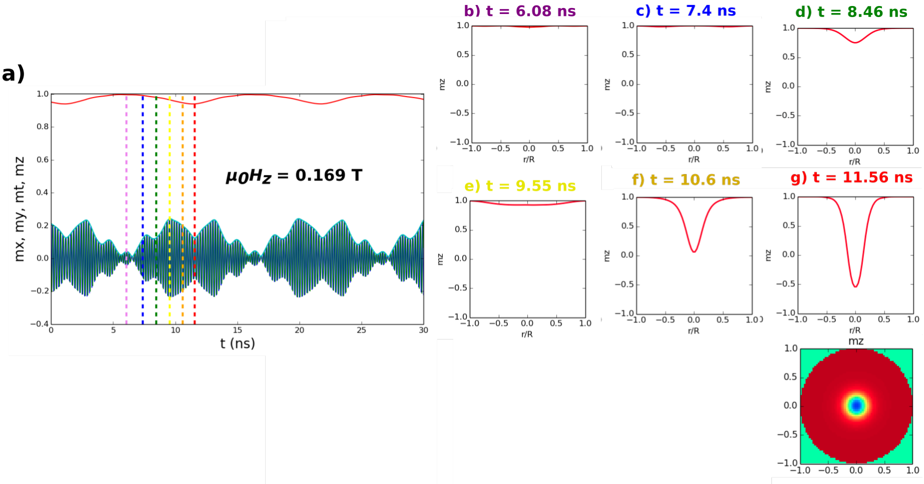

Figure 5.11: **a)** Time evolution of average components of magnetization for the 700 nm disk, at $\mu_0 H_z = 0.169$ T during 30 ns (zoom of Figure 5.7 e). **b-g)** Spatial profile of the longitudinal normalized magnetization at different times of the dynamics corresponding to the different colored dashed lines of Figure a. The 2D profile is shown for the last case.

Thus, even when very large precession angles are reached (case of the profile at 0.1685 T), the fact that the corresponding precession mode remains strongly localized both spatially and temporally explains why the mean ΔM_z[1] which we

---

[1] Which is averaged both spatially and temporally.

measure in experiments remains very small, which explains the rapid saturation of the signal.

This dynamic instability is similar in a certain way to the nonlinear spin-wave modes bullets and droplets described in section 2.6.2 as they also correspond to a strong spatial localization of a precession mode of the magnetization in a ferromagnetic sample under an excitation, usually a spin current in the case of a nanocontact. But in contrast to droplets and bullets which remain both spatially and temporally stable once formed, the dynamic instability observed here evolves both spatially (it deforms within the disk) and temporally (it forms, then disappears, then reappears and so on).

5.2.2.2 Possible mechanism at the origin of the dynamic instability

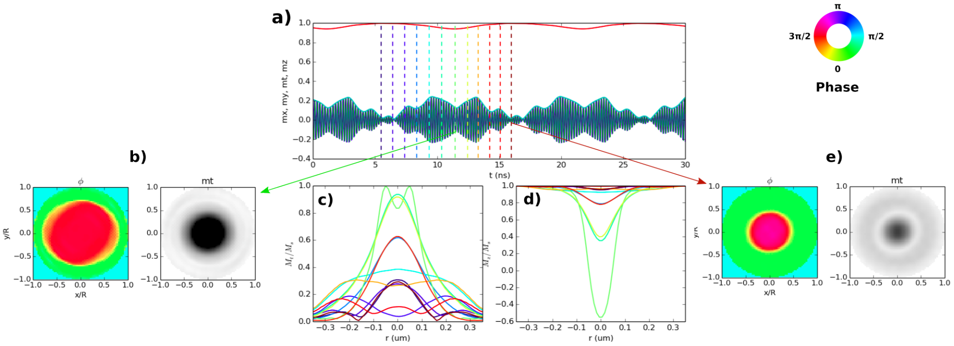

Figure 5.12: **a)** Time evolution of average components of magnetization for the 700 nm disk, at $\mu_0 H_z = 0.169$ T during 30 ns (same as Figure 5.11 a). **c-d)** Spatial profiles of the transverse (c) and longitudinal (d) normalized magnetizations at different times of the dynamics corresponding to the different colored dashed lines of figure a. The 2D profiles of the phase and the transverse component of the magnetization are shown for t = 11.56 ns when the reduction of m_z is maximum **b)** and for t =16 ns **e)**. The color code for the phase is shown. For the transverse magnetization amplitude : dark color = high amplitude, white color = zero amplitude.

Figure 5.12 now shows on the same figures the temporal evolution of both the spatial profiles of the longitudinal magnetization (5.12 c) and the transverse magnetization (5.12 d). The strong localization of m_z (see Figure 5.12 d) is well recognized. The phase profile at t = 11.56 ns (Figure 5.12 b) when the reduction of m_z is maximum shows that there is a small external crown in which the magnetization precesses in phase opposition with the central region. So it is not a perfectly uniform phase mode. The observation of the temporal evolution of the transverse magnetization profile (Figure 5.12 c) shows that during the dynamics the precession profile changes from the uniform mode $n = 0$ to other modes. For example, at certain moments the precession profile is clearly identifiable as the radial mode $n = 1$, see Figure 5.12 e. At other moments, these modes are apparently different from eigenmodes of the system but may be linear combinations of eigenmodes (like the modes $n = 0$ and $n = 1$). Since at the beginning it is the mode $n = 0$ that is excited, these oscillations of the precession profile between different modes means that once excited by the rf field, the mode $n = 0$ can transfer the stored energy to other low order eigenmodes like the mode $n = 1$. It is interesting to notice that this phenomenon of transfer of energy among low order eigenmodes of a system bears similarities with the Fermi-Pasta-Ulam-Tsingou behavior [128, 129] , a standard problem of dynamical systems and chaos. Lewis et al. found that in magnetic systems, it appears in particular in those having a uniaxial anisotropy [130].

This oscillation of the profile between different modes is due to the nonlinear couplings between modes, which can emerge due to the long-range dipolar or short-range exchange interactions. Here, a likely mechanism is the non-uniform dipolar stray field created by the magnetization precession. The uniform rf field primarily excites the $n = 0$ fundamental mode with uniform phase and Bessel-like distribution. When the amplitude of the $n = 0$ mode increases, it tends to localize in the center of the disk. The resulting in-plane dipolar stray field at the periphery of the disk increases, being in phase opposition with the precession at the center of the disk, see Figure 5.13. The transverse magnetization being of the order of the total magnetization M_s at the disk center, this dipolar stray field can be very strong, and has the appropriate symmetry to couple to the $n = 1$ mode, which can be excited at rather high amplitude even if it is non-resonant (the static field is far from the resonance field of this mode). When the $n = 1$ mode is excited at large amplitudes, it tends to suppress the mode $n = 0$ which provides its source of energy. Therefore, the $n = 1$ mode will not be stabilized, and decreases in amplitude. The uniform rf field becomes dominant again, and the $n = 0$ mode is mainly excited, until it grows too much, and start to radiate again a strongly non-uniform dipolar field. This process can repeat periodically (or not) over time, which produces the auto-oscillation instability corresponding to the transfer of energy between modes. Of course, there are not only the $n = 0$ and $n = 1$ modes in the system. This picture is oversimplified, but the underlying mechanism remains

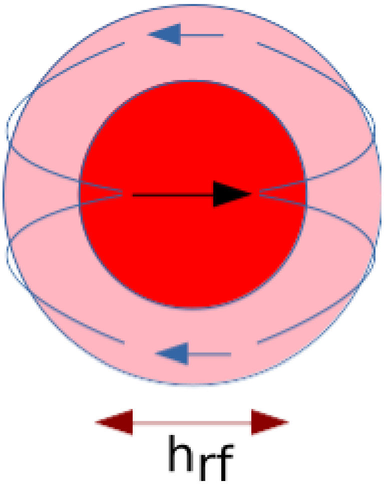

Figure 5.13: Generation of a non-uniform dipolar stray field at the periphery of the disk by the precession of the magnetization after the excitation by the rf field. Top view of the nanodisk showing the transverse magnetization m_t (snapshot when m_t is maximal at the center of the disk) in black arrow and the dynamic dipolar stray field created by this transverse magnetization in the disk plane. This dipolar field is in the same direction as m_t in the central region of the disk in red but is opposite to it in the periphery.

the same.

5.2.3 Extraction of dynamic instability frequencies

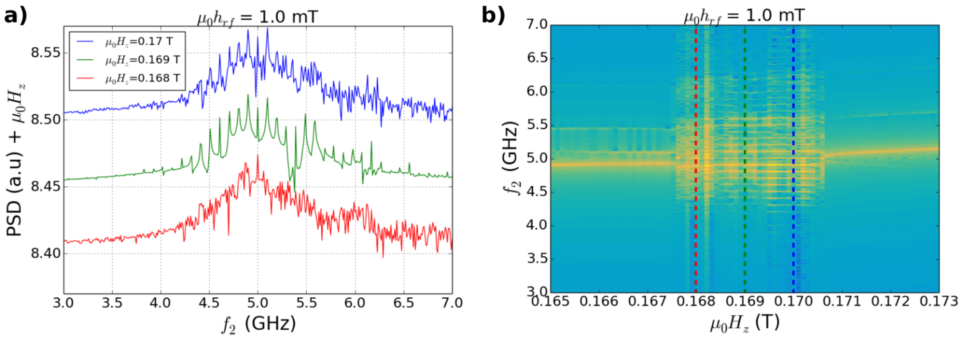

Figure 5.14: a) Power Spectral Density (PSD) obtained by doing a FFT of m_x and m_y at three fields H_z trough the simulated resonance line at $\mu_0 h_{rf} = 1$ mT. b) Spectroscopy map obtained by taking these spectra at all the fields. We note these frequencies f_2 to differentiate them from the excitation frequency $f = 5$ GHz and in anticipation of additional experimental measurements presented later. The positions of the 3 fields of the curves in figure a) are indicated by lines of the same colors.

Finally, one can extract the frequencies of these dynamical instabilities in the simulation. This is done by doing a fast Fourier transformation (FFT) of the time evolution of the average components of magnetization m_x and m_y simulated at each bias field after subtracting the component at 5 GHz[2]. Let us consider for example the temporal profiles of m_x and m_y of Figure 5.7 c at 0.168 T. By making their FFT, one obtains the complex red spectrum of Figure 5.14 a with a large density of peaks, which suggests a chaotic state. The spectra obtained for 0.169 T and 0.17 T are also shown. Then, this operation can be repeated for all the fields H_z through the resonance line of Figure 5.7 a. One obtains the map of Figure 5.14 b. It shows a linear dispersion on both sides of the dynamic instabilities region. And within this region, one observes an interesting frequency modulation pattern with a modulation frequency of the order of 100 MHz. The linear dispersion corresponds to the Kittel mode (main mode) which varies slightly with the static field H_z around the excitation

---

[2] The main component in the time evolution, coming from the frequency of the excitation field $f = 5$ GHz.

frequency of 5 GHz. The positions of the 3 fields of the curves in Figure 5.14 a are indicated on the map by lines of the same colors.

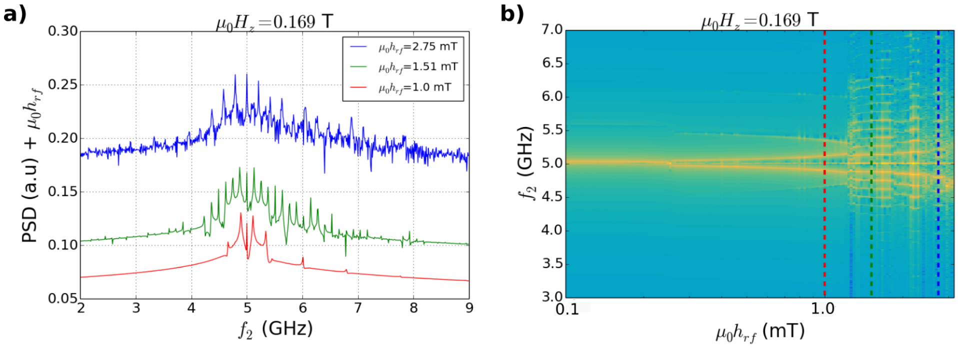

Figure 5.15: a) Power Spectral Density (PSD) obtained by doing a FFT of mx and my at three fields h_{rf} trough the simulated resonance line at $\mu_0 H_z = 0.169$ T. b) Spectroscopy map obtained by taking these spectra at all the fields. The positions of the 3 fields of the curves in figure a) are indicated by lines of the same colors.

Since the resonance line almost doesn't shift in the nonlinear regime, another way to study the instabilities is to fix the static field in the instability region and observe how the instabilities appear and develop with the rf field. This is what is presented in Figure 5.15 for $\mu_0 H_z = 0.169$ T. At low excitation, one finds the excitation frequency of 5 GHz. Then when one increases h_{rf}, two modes appear around 5 GHz before the emergence of the complex frequency modulation.

We will explain these observations in details later with additional experimental results.

5.3 Two-tone measurements : experimental evidence of the formation of dynamic instabilities

5.3.1 Single microwave frequency continuous wave excitation

It was already mentioned that with microwave modulation one does not have access to the upward branch of the dynamics : one measure H_{up} but not H_{down}.

To measure the full dynamics, one uses a continuous wave (cw). In this case the amplification of the signal by the quality factor of the cantilever $Q \approx 2000$ is lost. The signal is no longer coded in the amplitude of the vibrations of the cantilever. One uses the second detection mode of our MRFM in which the signal is coded in the variations of the cantilever frequency f_c.

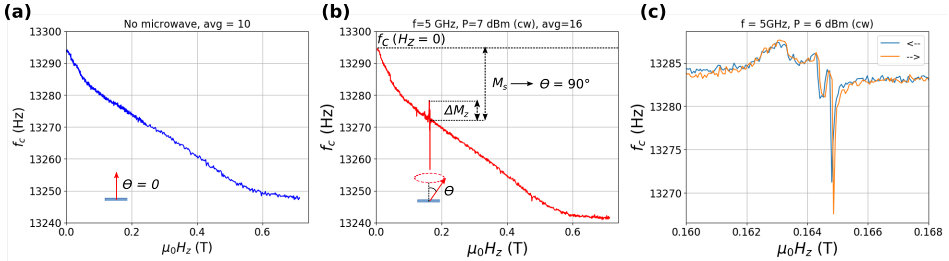

Figure 5.16: Variation of the cantilever frequency when the probe is above the 700 nm disk B4 a) without microwave and b) with microwave. The insets show a zoom on the resonance signal and the procedure used for a direct calibration of the signal in mean precession angle. c) Resonance signal for both directions of field sweep: absence of hysteresis cycle.

Figure 5.16 a shows the variation of f_c when the static field is decreased, the probe being above the 700 nm disk B4 and in the absence of microwave field[3]. These variations are characteristic of the variations of the magnetization of the probe as explained in the section 3.2.2. Then, one repeats the same experiment with the microwave field switched on in cw mode at $f = 5$ GHz and $P = 7$ dBm, see the red curve in Figure 5.16 b. One observes the appearance of a signal around 0.16 T. It is the resonance of the disk. Indeed, when the resonance field is reached, the cw microwave pumping excites the dynamics of the magnetization in the disk, which opens a precession angle θ as shown on the inset; the longitudinal magnetization then decreases by ΔM_z. Thus, the dipolar static force between the disk and the probe decreases and the cantilever frequency increases. The associated change in f_c provides quantitative magnetometry of the disk [120, 22].

Moreover, an advantage of this method is that it allows a direct calibration of ΔM_z in precession angle of the magnetization. At zero field the cantilever has a frequency $f_c(H_z = 0)$ shown on the figure. This is the frequency in the absence of interaction since the probe is almost not magnetized at zero field. If during a given resonance, f_c increases until the value $f_c(H_z = 0)$, it means that there is no more interaction between the probe and the disk, which

---

[3] The microwave source is turned off.

means that $M_z = 0$, i.e. $\Delta M_z = M_s$. In other words, this means that the mean precession angle $\theta = 90°$ has been achieved. From there we can directly convert any frequency shift into ΔM_z.

On Figure 5.16 c, one checks that this signal is not hysteretic. Moreover, the signal has a complex shape with a negative peak compared to what was measured on the YIG disk with exactly the same experimental protocol, like the resonance line shown in Figure 1 C. This complex shape obviously makes the ΔM_z calibration more difficult. This signal shape is due to complex feedback from the probe oscillations on the probe-disk interaction during the measurements. The detailed explanation is given in Appendix F.

We did not observe hysteresis cycles on the large disks with D $\geq$ 700 nm. This is not unexpected since even in the simulation, the hysteresis cycles obtained for these disks at intermediate excitation fields are of very low amplitude (3 mT maximum) before almost disappearing at higher excitation, the amplitude of the two branches becoming equal (cf Figure 5.3 d).

5.3.2 Double frequency spectroscopy in nonlinear regime

Since there is no spatial or time resolution with the MRFM but a good spectral (frequency) resolution, one way to access the dynamic instabilities in the experiment would be to try to measure their frequencies. To experimentally determine these frequencies, we need to investigate in details the nonlinear regime. Now, instead of simply looking at what happens around the static equilibrium position as it was done so far, one probes the susceptibility of the system around the nonlinear or deeply nonlinear regime of the magnetization dynamics. For this purpose, we perform two-tone measurements whose principle was already presented in Figure 2.10 a and is reminded in Figures 5.17 a & b. One starts by applying a first continuous excitation (cw) at a power P_1 and a fixed frequency $f_1 = \omega_1/2\pi = 5$ GHz for example, to bring the magnetization into the nonlinear regime. Then, to probe this regime, a second excitation whose frequency $f_2 = \omega_2/2\pi$ is varied around f_1 is applied, at a power P_2 weaker than P_1 and modulated at the cantilever frequency (see Figure 5.17 b). The power P_1 induces an average decrease in longitudinal magnetization of ΔM_1 while the second excitation induces an additional variation ΔM_2 on top of ΔM_1. For different P_1-P_2 combinations, one measured ΔM_2 by scanning f_2 at different fields through the resonance line corresponding to ΔM_1.

The results obtained for the 700 nm disk B4 are presented in Figures 5.17 c to g. In each case we present the resonance line ΔM_1 at the bottom and just on top the ΔM_2 spectroscopy map, the values of P_1 and P_2 are indicated. ΔM_1

can be coded in the variations of the cantilever frequency while ΔM_2 is coded in its vibrations amplitudes as it has been the case for all our experimental measurements so far. However for the representation of ΔM_1, we do not use the signal measured with the variations of f_c which is of poor quality as explained previously but we use the signal measured with a modulated excitation alone, at the indicated power. Indeed, since there is no hysteresis, the two signals measured with the two detection modes are equivalent.

Figures 5.17 c & e correspond to the results obtained for P_1 = -6 dBm and P_2 = -19 dBm. At high fields ($\mu_0 H_z > 0.1645$ T), the magnetization dynamics is excited out of resonance by $\boldsymbol{h}_1$ and has a very low amplitude. Thus, the field $\boldsymbol{h}_2$ simply excites the standard linear Kittel mode on top of the weak ΔM_1, which explains the bright linear dispersion $\omega_2 = \gamma\mu_0(H_z - H_K)$ observed in this region[4]. One observes the same situation at low field ($\mu_0 H_z < 0.1637$ T). It is different for 0.1637 T $< \mu_0 H_z <$ 0.1645 T. In this region, $\boldsymbol{h}_1$ excites the nonlinear regime of the foldover demonstrated earlier and $\boldsymbol{h}_2$ excites the dynamics of the magnetization on top of this regime. One notes the appearance of two symmetrical signals with respect to $f_1 = 5$ GHz (see the black spectrum in Figure 5.17 g extracted at 0.1642 T) which means that in the frame rotating with $\boldsymbol{h}_1$ at ω_1, the magnetization is precessing at $(\omega_2 - \omega_1)/2\pi$, of the order of 20 MHz, around its equilibrium position in this frame. In other words, in a similar way to what was observed in the case of the YIG disk [22], the magnetization is subjected to a slow nutation motion in the laboratory frame (see Figure 2.10 d) : a combination of the large periodic motion at frequency ω_1 (the **P**-mode) and the small oscillations at frequencies $< \omega_1$. This result shows that at 0.1642 T, the precession is coherent (the angle θ_0 is constant during the precession) and the macrospin approximation can be used to describe the evolution of the system.

But the situation is already getting non trivial only by changing the field H_z in the same experiment. As shown the green spectrum of Figure 5.17 g taken at 0.1644 T, each nutation mode seems to split into several modes of much larger amplitudes and opposite signs.

At higher excitation P_1 = 6 dBm, see Figures 5.17 d & f, the result is also interesting. One has reached the regime of saturation of the resonance peak amplitude, see Figure 5.17 f, and one observes in the saturation region a complex map as illustrated by the red spectrum in Figure 5.17 h extracted at 0.16424 T.

Similar experiments performed on the 500 nm disk B3 led to more comprehensive results. One reminds that it already had a singular behavior with a splitting of the resonance line into 3 peaks at high excitation (see Figure 5.2

---

[4] Where H_K is the characteristic field of the disk.

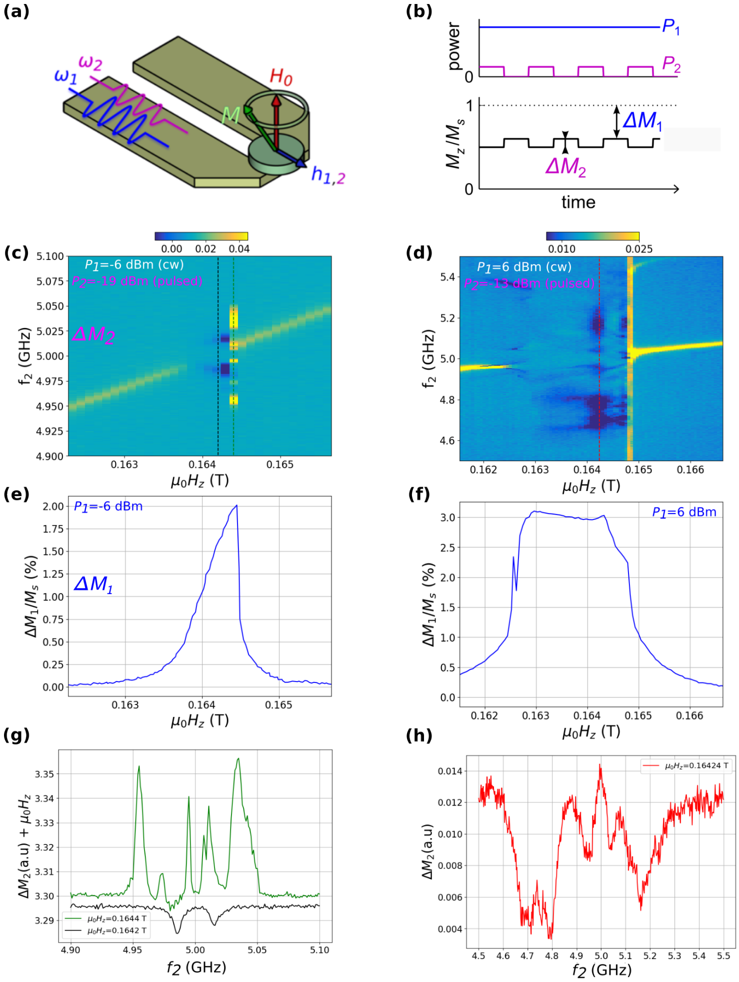

Figure 5.17: (a,b) Principle of the experiment. A low-power microwave field $\boldsymbol{h}_2$ of pulsation ω_2, which is pulse modulated at the cantilever frequency $f_c \simeq 13\,\mathrm{kHz}$, is added to the main pumping cw field $\boldsymbol{h}_1$. $\boldsymbol{h}_1$ induces a decrease of the longitudinal magnetization ΔM_1 and $\boldsymbol{h}_2$ of variable frequency $\omega_2/2\pi$, allows to probe the excitations on top of it in the frame rotating with $\boldsymbol{h}_1$ at ω_1, by measuring an additional variation ΔM_2. (c-e) and (d-f) Measurement for the 700 nm disk B4 for two different combinations (P_1,P_2) at $\omega_1/2\pi = f_1 = 5$ GHz of the ΔM_2 spectroscopy map as a function of the field H_z, swept through the resonance induced by $\boldsymbol{h}_1$. This resonance line is indicated in each case at the bottom of the map. g) Spectra extracted at two given fields in figure c. h) Spectra extracted at a given field in figure d. For each spectrum, the position of the field is indicated on the spectroscopy map by a dashed line of the same color as the spectrum.

a). At low excitation $P_1 = 1$ dBm in Figure 5.18 a, one has a result similar to that of the 700 nm disk B4 with only a nutation mode in all the resonance region now. As P_1 is increased, the dynamics becomes more complex as shown in Figure 5.18 b. One still observes the bright linear dispersion of Kittel when $\boldsymbol{h}_1$ is out of resonance. For $P_1 = 4$ dBm, the resonance peak measured with the continuous excitation splits in two (see Figure 5.18 e). Here, in the area where $\boldsymbol{h}_1$ excites the dynamics, one first observes at low field a splitting of the Kittel mode into two apparent nutation branches similar to what was observed for $P_1 = 1$ dBm (see the lime spectrum in Figure 5.18 h extracted at 0.16511 T). But, as the field increases, one observes successive separations of each of these branches into much more complex spectra. The sign of these signals and their distribution around ω_1 are non-trivial, see the black and orange spectrum in Figure 5.18 h.

Finally, for $P_1 = 12$ dBm (Figures 5.18 c & f) one notes very striking results. Here, the amplitude saturation regime reached by exciting the dynamics with P_1 is different from what was observed in the 700 nm disk (flattening of the peak). In the saturation region, there is a strong frequency modulation which is similar even quantitatively to the simulations. On the spectrum of Figure 5.18 i extracted at $\mu_0 H_z = 0.165$ T on the map in Figure 5.18 c, one determines a frequency modulation of 60 MHz, of the same order as the hundred of MHz obtained in the simulation on Figure 5.14 b. This similarity confirms that as in the simulations, the origin of the rapid saturation of the signal is the formation of dynamic instabilities directly resulting from the way the precession profile deforms when the resonance is excited.

One can also fix the static field and observe the formation of these instabilities as a function of the microwave power. Figure 5.19 shows the results obtained for disks B3 and B4 at $f_1 = 10$ GHz. Figures 5.19 a & b show the evolution of the resonance line as a function of a pulsed excitation, with the now well known behavior (splitting and saturation at high power). Then, the static field is fixed at the value indicated by the magenta dashed lines, chosen to be in the saturation region at high power, and with a two-tone experiment the ΔM_2 spectroscopy as a function of the cw power P_1 is obtained, see Figures 5.19 c & d. Some spectra are shown in Figures 5.19 e & f. One observes the formation of the frequency modulation when P_1 is increased, which is similar to simulation results in Figure 5.15 b. One recovers the intermediate regime with two nutation branches before the frequency modulation regime.

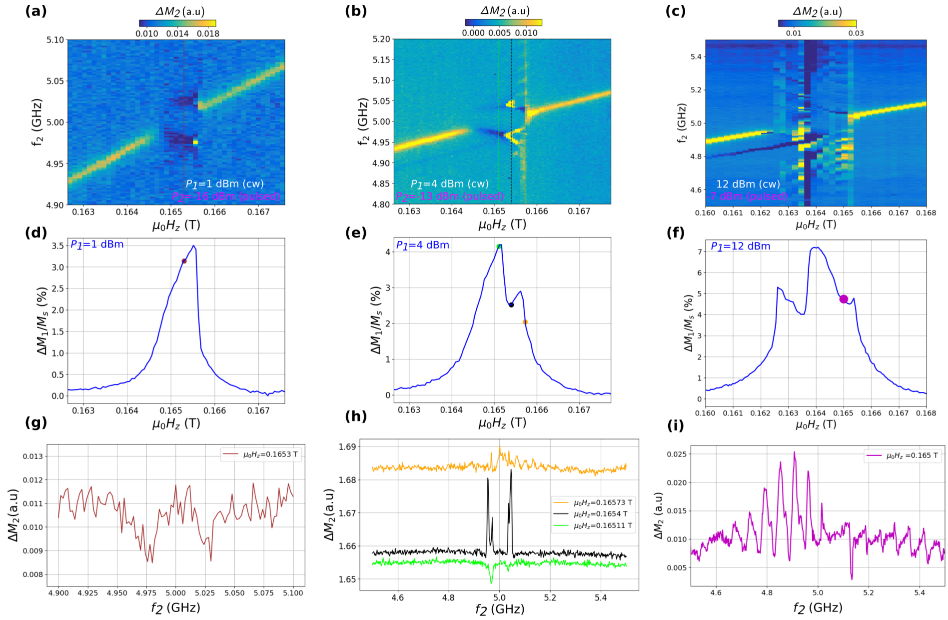

Figure 5.18: (a-d),(b-e) and (c-f) Measurement for the 500 nm disk B3 for three different combinations (P_1,P_2) at $\omega_1/2\pi = f_1 = 5$ GHz of the ΔM_2 spectroscopy map as a function of the field H_z, swept through the resonance induced by $\boldsymbol{h}_1$. This resonance line is indicated in each case at the bottom of the map. g) Spectrum extracted in figure a) at $\mu_0 H_z = 0.1653$ T. h) Spectra extracted in figure b) at three fields inside the resonance region. h) Spectrum extracted in figure c) inside the instability region, at $\mu_0 H_z = 0.165$ T. For each spectrum, the position of the field is indicated on the spectroscopy map by a dashed line of the same color as the spectrum.

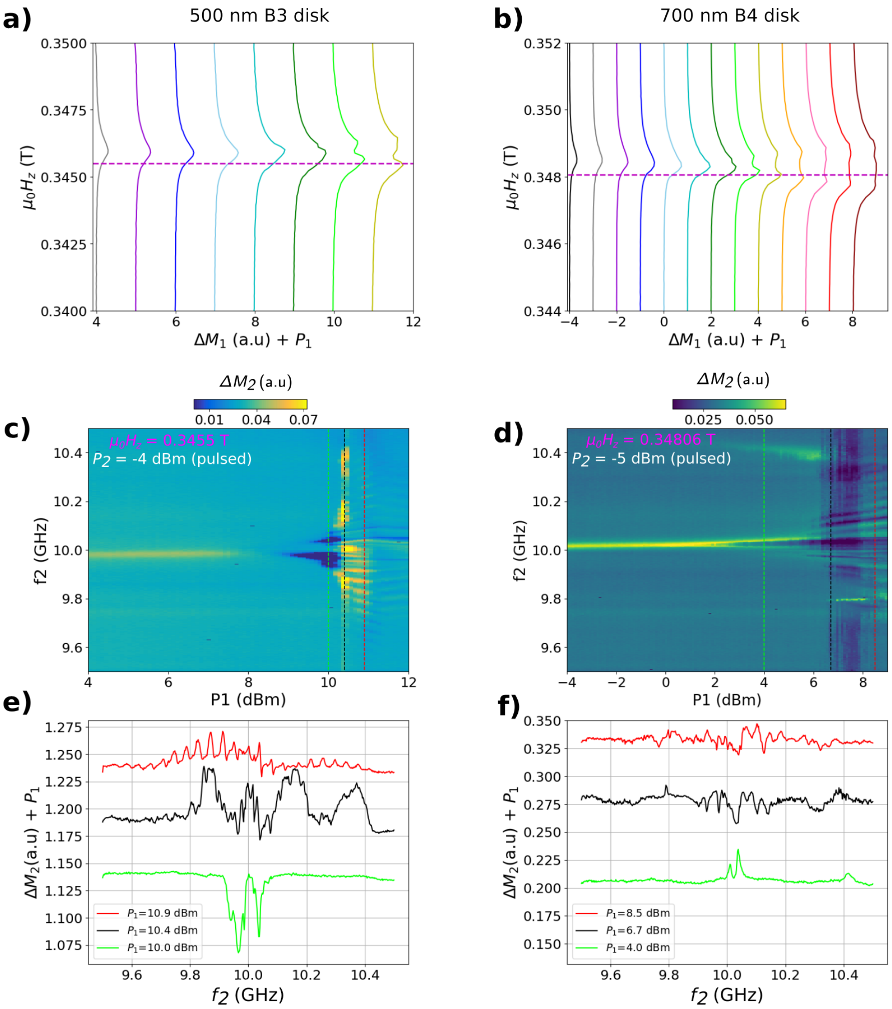

Figure 5.19: a-b) Resonance line versus microwave power for a pulsed excitation, for the 500 nm B3 and 700 nm B4 disks. c-d) ΔM_2 spectroscopy map at a fixed field as a function of P_1. The field and power P_2 are indicated on the figures. The field is fixed at the value indicated by the dashed line on the figures above. e-f) Spectra extracted at some fields indicated on the maps of figures c) and d) by dashed lines of the same color. The measurements have been performed at $f_1 = 10$ GHz.

5.4 Comparison between YIG and BiYIG disks

Despite the achievement of ultra-large precession in large BiYIG disks with diameter 500, 700 and 1000 nm, the fact that it remains strongly localized both spatially at the disk center and temporally at certain times of the dynamics explains the rapid saturation of the spatial average of the reduction of longitudinal component of magnetization ΔM_z. One explained that a large amplitude of magnetization precession ($\Delta M_z/M_s \approx 100$ % i.e $\theta \approx 90°$) was achieved in the 700 nm YIG disk but with a strong frequency shift due to the foldover (see Figure 1 C). One expected to improve this aspect of the results in BiYIG by almost suppressing the resonance line shift in the nonlinear regime thanks to an effective magnetization $M_{eff} \approx 0$. It is not the case. We try to understand in this section the origin of the drastically different result between YIG and BiYIG nanodisks.

5.4.1 YIG disk : spatial extension of the precession profile

For this purpose we performed additional analysis of the simulations on the 700 nm YIG disk which were done previously in the lab [22]. Figure 5.20 a shows the resonance line for a rf field of 1.0 mT. The simulation protocol is exactly the same as the one we used for the BiYIG disks with the same MicroMagnum code. It is done at $f = 10.5$ GHz, the frequency at which the main experimental measurements were made, like the one presented in Figure 1 C. We focus on the large amplitude branch which in the YIG case is now the downward branch since $M_{eff} = M_s > 0$ (no uniaxial anisotroy), as explained in Figure 2.9. The damping used is 5×10^{-4}, which was extracted from experiments. As we did for the 700 nm BiYIG disk, see Figures 5.7 and 5.10, we visualize in Figure 5.20 the time evolution of the average components of the magnetization for four fields through the resonance line and the corresponding precession profiles. Here, from 0.574 T, m_z (in light blue) decreases significantly until 0.45 T. In contrast to BiYIG, where dynamic instabilities already appeared in the transverse component m_t (in red) as soon as $m_t = 0.2$, here the increase of m_t reaches $m_t = 0.6$ (at $\mu_0 H_z = 0.508$ T) before the instabilities appear (see the red curve in Figure 5.20 c). But despite these instabilities, m_z continues to decrease, which was not the case for the BiYIG nanodisk.

Looking at the precession profile, the comparison with Figure 5.10 allows to understand the difference between the results obtained. In contrast to the

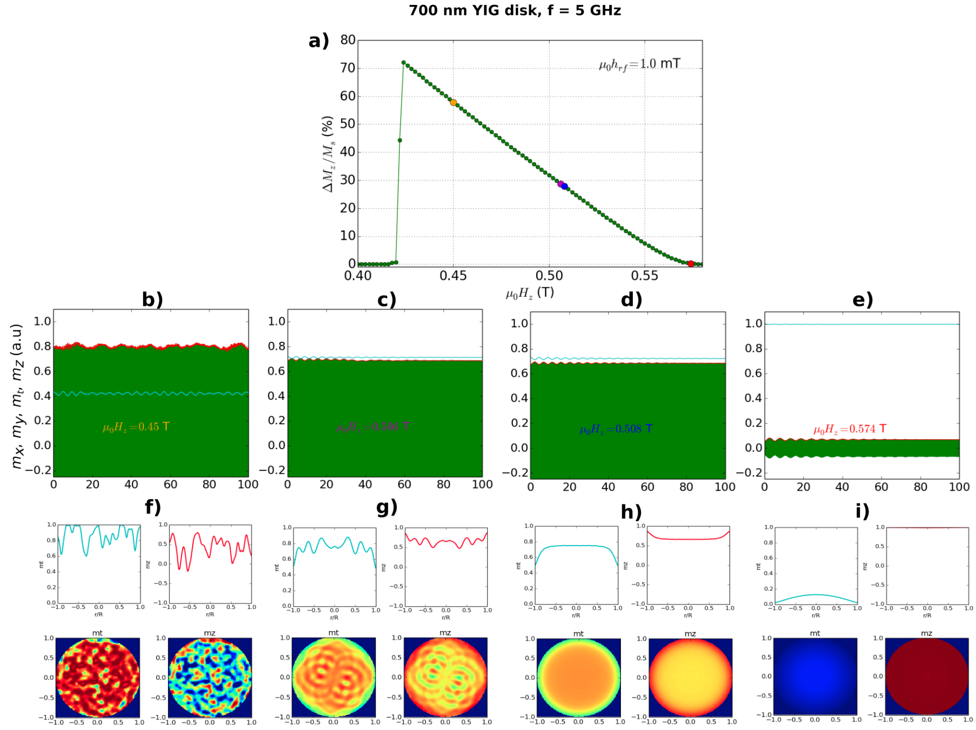

Figure 5.20: a) Resonance line in the simulation at $\mu_0 h_{rf} = 1.0$ mT for the 700 nm YIG disk. b) to e) Time evolution of the normalized average components of the magnetization during the 100 ns simulation at four different fields through the resonance line shown in a). The fields from b) to i) correspond in this order to the colored points of the resonance line in a). The longitudinal component is in light blue, the m_x and m_y components in green and the transverse component in red. f-i) 1D spatial profiles of the longitudinal magnetization mz (in red) and the transverse magnetization m_t (in light blue) at the four selected fields. In each case the corresponding 2D profile is shown below.

strong localization of the precession profile at the disk center which leads to the formation of dynamic instabilities and to the saturation of ΔM_z in the case of the BiYIG disk, here there is a spatial extension of the precession profile at the beginning. From the starting Bessel-like function at 0.574 T, see Figure 5.20 i, one reaches a quasi-uniform mode in amplitude at 0.508 T, see Figure 5.20 h. Then one observes that the instabilities which appear from 0.506 T are the well-known spin waves instabilities (see Figure 5.20 g) associated with very higher order spin wave modes. They are similar to Suhl instabilities, but in confined geometries. They are therefore intrinsically different from the dynamic instabilities highlighted in the BiYIG disk which mainly concern the low order spin wave modes. Despite these spin wave instabilities which explain the deviation from the macrospin model, m_z continues to decrease and large mean precession angles are reached. For example, for the case presented here, $\Delta M_z^{max}/Ms = 72\%$ (see Figure 5.20 a) which corresponds to a mean precession angle $\theta = 74°$.

5.4.2 Origin of the distortion of the precession profile in the nonlinear regime

To understand the difference in the evolution of the precession profile, one can go back to the internal field profile within the disk. The typical shape of this profile, already shown in Figure 3.14 c, is reminded here in Figures 5.21 a & c, which is the same for both YIG and BiYIG disks. The blue line corresponds to the frequency of the excitation needed to excite the main mode n=0. It is slightly higher than the frequency at the center of the disk. The dashed line indicates the profile of this mode. Due to nonlinear frequency shift, the resonance line shifts towards low fields, i.e. towards high frequencies for YIG, whereas it shifts towards high fields, i.e. towards low frequencies for BiYIG.

So when the excitation is increased, in the case of YIG it is like ω_0 shifts upwards. Thus more and more spins at the edges of the disk satisfy the resonance condition and start to precess. This results in the spatial extension of the precession profile which tends to become uniform, see Figure 5.21 b. In the case of BiYIG, it is totally different. $\omega_0/2\pi$ shifts downwards when the excitation is increased. Thus this results in an increase of the precession amplitude localized at the center of the disk which can lead to the formation of dynamical instabilities within the disks, see Figure 5.21 d. This change in the spatial distribution of the main spin wave mode by increasing the microwave power is similar to what was observed previously in YIG films [131].

To confirm these explanations, we performed additional simulations in which the value of the anisotropy K_u is varied so as to change the sign and the

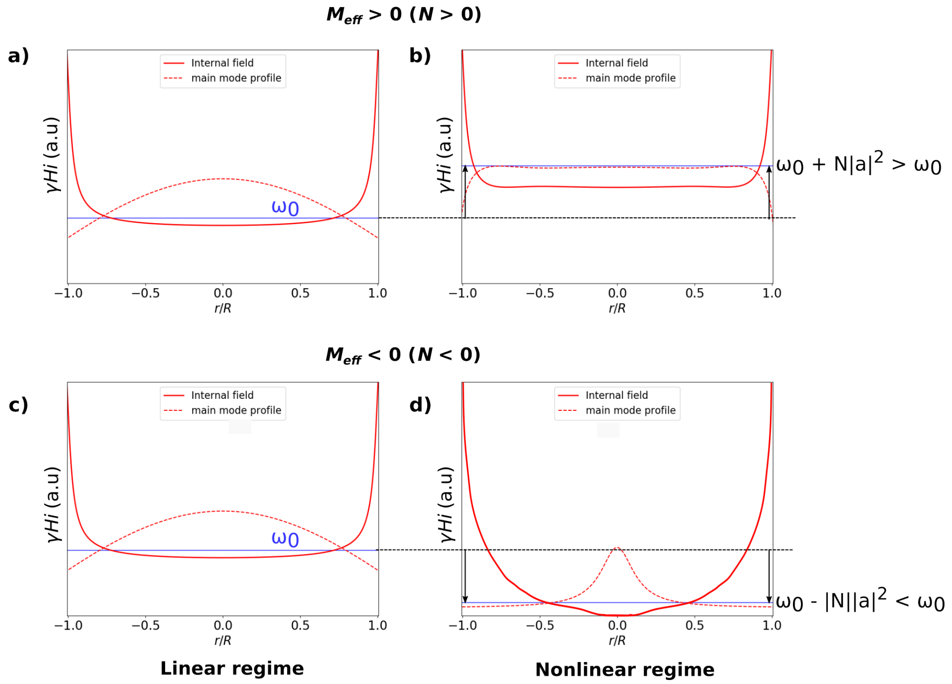

Figure 5.21: a-c) Typical profile of the internal field H_i in a disk in the linear regime (very low excitation). The FMR is excited by applying a microwave field of frequency ω_0 indicated by the horizontal blue line; slightly higher than the frequency at the center of the disk. The dashed line indicates the profile of the main mode. b-d) Modification of the internal field profile in the nonlinear regime according to the sign of the effective magnetization M_{eff}. This modification leads to a spatial expansion of the precession profile when $M_{eff} > 0$ (b) and to a localization of the precession profile at the disk center when $M_{eff} < 0$ (d). N is the nonlinear frequency shift and a is the spin wave amplitude.

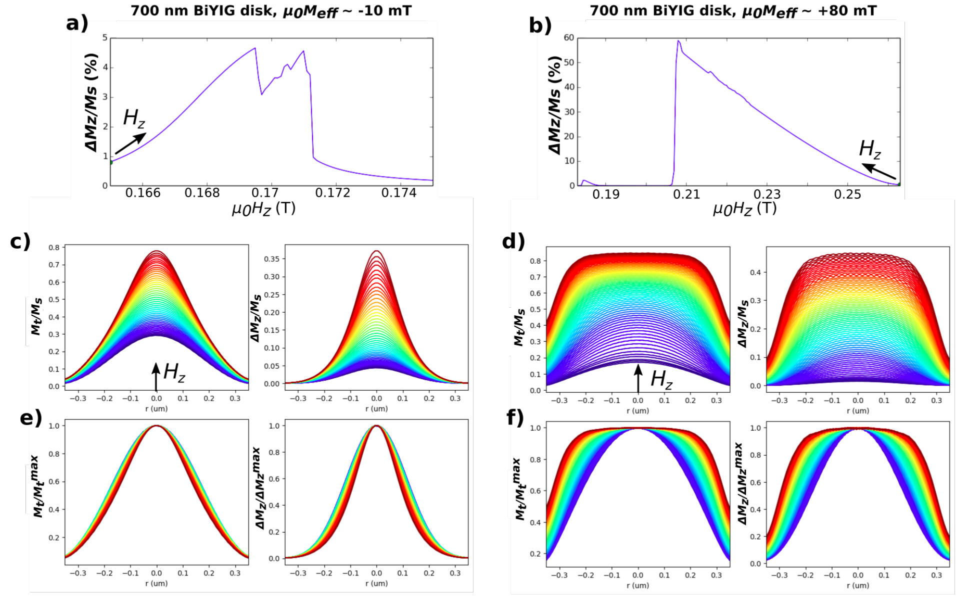

Figure 5.22: a-b) Resonance line in the simulation at $\mu_0 h_{rf} = 1.0$ mT for the 700 nm YIG disk for two different values and signs of M_{eff} 0. c-d) Evolution of the spatial profiles of the transverse magnetization $m_t = M_t/M_s$ and longitudinal magnetization (the reduction $\Delta m_z = \Delta M_z/M_s$) when the resonance line is swept in the direction indicated in figures a) and b). The profiles are represented from dark blue to dark red. e-f) Representation of the same profiles as in figures c) and d), each profile being normalized by its maximum.

value of $\mu_0 M_{eff}$. Figure 5.22 b shows the results obtained for $\mu_0 M_{eff} \approx +80$ mT. Figure 5.22 d shows the evolution of the spatial profiles of the longitudinal and transverse magnetization when the resonance line is swept in the direction indicated in Figure 5.22 b, the profiles being represented from dark blue to dark red. Figure 5.22 f shows the same profiles, normalized by their maximum amplitude at the center of the disk. Figures 5.22 a c & e show the same plots for the 700 nm BiYIG disk we have studied so far, with $\mu_0 M_{eff} \approx$ -10 mT, for the upward branch (whose the amplitude is slightly larger than the one of the downward branch).

In Figure 5.22 b, as expected from the sign of M_{eff}, the direction of the foldover shift is now towards the low fields. While for $M_{eff} < 0$, $\Delta M_z/M_s$ saturates at less than 5%, here $\Delta M_z/M_s$ reaches 60%, which corresponds to a mean precession angle of more than 65°. We note that for this positive value of M_{eff}, it is possible to reach the quasi-suppression of M_z ($\theta = 90°$) at higher excitation field. Moreover one observed the classical hysteretic behavior (not shown on the figure) with two characteristic fields H_{up} and H_{down} by sweeping the field in the two directions. These results are clearly opposite to those of BiYIG with $M_{eff} < 0$ but similar to those of YIG. The representation of the profiles shown in Figures 5.22 c to f is made until the threshold of onset of the instabilities (the spin wave instabilities for $M_{eff} > 0$ and the dynamical instabilities studied previously for $M_{eff} < 0$). One observes a spatial extension of the precession profile within the disk for $M_{eff} > 0$ (see Figures 5.22 d & f) as in the YIG case (Figure 5.20 h) and a localization of the precession profile at the center of the disk in the case $M_{eff} < 0$. Moreover, in the case $M_{eff} > 0$ one notes that m_t=M_t/M_s and Δm_z=$\Delta M_z/M_s$ increase significantly at the edges of the disk during the spatial extension whereas they remain respectively very small and almost zero in the case $M_{eff} < 0$, meaning a strong pinning of the magnetization (there is almost no precession at the edges).

Theses observations suggests that the difference in behavior comes from two elements : the sign of M_{eff} which defines the direction of frequency shift in the nonlinear regime and the distortion of the linear precession profile of the main mode, itself due to the profile of the internal field. For $M_{eff} < 0$, due to the strong inhomogeneity of the internal field and therefore the precession profile, and the resonance conditions, the increase of the precession amplitude remains localized in the center and leads to the formation of dynamic instabilities, see Figure 5.11. Switching from $M_{eff} < 0$ to $M_{eff} > 0$ modifies the precession profile in the nonlinear regime by making it less inhomogeneous. The non-uniform precession profile $\Delta M_z(r)$ reduces the demagnetizing field compared to the equilibrium situation $M_z(r) = M_s$ in such a way that the internal field not only increases, but also gets more homogeneous in the disk. It results that the precession profile tends to be more homogeneous (uniform) when the precession amplitude increases, i.e., an opposite behavior with respect to the case with $M_{eff} < 0$.

5.5 Nonlinear dynamics in smaller disks

Let's mention that for the 1000 nm BiYIG disk ($M_{eff} < 0$), we have very similar simulation results to the 700 nm disk with even a more rapid saturation of the peak amplitude at mean precession angles of a few degrees in agreement with experimental results, and the formation of the same dynamic instabilities.

The analysis of the simulated nonlinear dynamics shows differences for the 500 nm disk. In this case, there is also a strongly localized precession profile at the center of the disk, but the reduction of the disk size makes it less peaked at the center. This results in a more stable profile in time, which allows to reach larger mean precession angles of the magnetization of the order of 30° in experiments. The detailed results of the 500 nm disk are presented in appendix G. The values of damping and anisotropy used in the simulations for all disk sizes are given in appendix D.

The simulation results on the smallest 200 and 300 nm disks are presented in appendix H. In these disks, one finds that a maximum $\Delta M_z/M_s$ of the order of 20 % can be reached, i.e. mean precession angles of 40°, only limited by the excitation field and their large damping.

So there are no more dynamic instabilities of oscillations of the precession profile when the disk size is reduced[5] although they all have a negative M_{eff} too. These results seem to be in agreement with the previous explanation in terms of inhomogeneity of the internal field as a parameter influencing the development or not of the dynamic instabilities. Figure 5.23 shows the normalized profile of the uniform mode $n = 0$ as a function of the disk size for the longitudinal and transverse components of magnetization. In Figure 5.23 a, one observes that while the dipolar pinning is almost maximal and equal for the 1000 and 700 nm disks (almost no precession at the disk edges), it slightly decreases for the 500 nm and much more for the 300 and 200 nm disks. Indeed, the precession amplitude at the edges climbs to 10% of the amplitude at the centre for the 300 nm disk and to more than 20% for the 200 nm. This difference in amplitude at the edges of the disk with the size is even more important for the transverse magnetization, see Figure 5.23 b. This is due to the fact that the internal field profile is much less inhomogeneous in small disks (D $<$ 500

---

[5] Note that there is nevertheless an instability of saturation of the downjump field at much higher excitation - see appendices G and H.

nm) than in large ones (D $>$ 500 nm). This effect of reduction of the dipolar pinning with size is well known and has been reported recently in nanoscopic ferromagnetic waveguides [132].

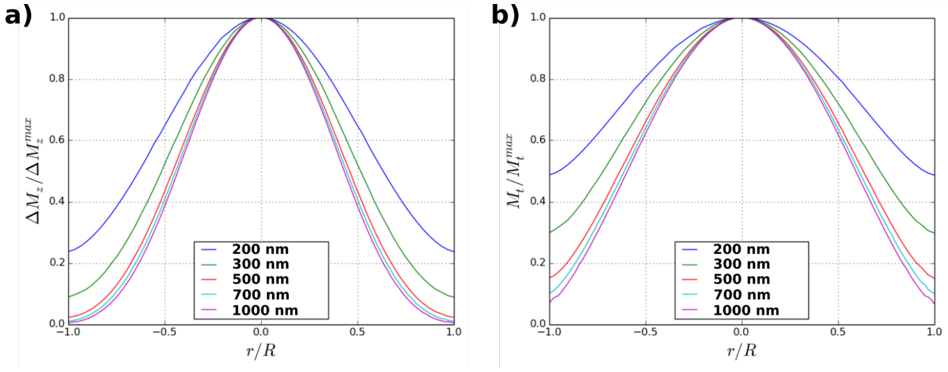

Figure 5.23: Normalized uniform mode profile of the a) longitudinal magnetization (ΔM_z) and b) transverse magnetization (M_t) as a function of the disk size.

So, in the large 1000 and 700 nm BiYIG disks, at high excitation, the negative sign of M_{eff} and the strong inhomogeneity of the internal field allow the strong localization of the precession profile and the development of the dynamic instability. The latter leads to the rapid saturation of the peak amplitude. The decrease of the disk size changes the linear internal field profile and the corresponding precession profile, makes the precession profile more stable in time and prevents the formation of the dynamic instability at high excitation.

Concerning the evolution of the precession profile in the nonlinear regime, the detailed analysis of the simulation results obtained showed that this general picture of strong localization or extension of the precession profile depending on the sign of M_{eff} is much more complex in the smaller disks (D $<$ 500 nm). This is certainly due to finite size effects which become more important. The way the profile deforms results from a fine balance between these finite size effects, the internal field profile and the effective magnetization M_{eff} which are themselves inter-dependant.

Finally, in other complementary simulations, we tried to treat the case $M_{eff} = 0$ for a nanodisk. If at the beginning there is no shift of the resonance line, one observes quite quickly a shift of the resonance line in one direction and then in the other one at higher excitation. One observes that the precession profile is also distorted when the excitation is increased. In fact it turns out that it is impossible to obtain and even less to keep a uniform precession profile for such a non-ellipsoidal geometry (a disk here) since the starting linear profile (Bessel-like function) is already non-uniform due to the non-uniform profile of the internal field (demagnetizing field) within the disk. If one had real ellipsoidal BiYIG samples, the precession profile would be uniform and could remain uniform at high excitation. So, the origin of the deformation of the precession profile in the nonlinear regime is the *non-ellipsoidal* geometry of the samples, which yields a non-uniform internal field.

5.6 Summary of the results : drafts of phase diagrams

With these results, one can draft a phase diagram of the 700 nm diameter disk at 5 GHz for a perpendicular static field. Figures 5.24 a & b show its 2D maps of the evolution of the simulated upward and downward branches of the resonance line as a function of the microwave power. The phase diagram is shown in figure b) and shows a rich dynamics with regions of bistability, quasi-periodicity and/or chaos, as demonstrated by the study of the time traces of the magnetization dynamics and the time evolution of the precession profile. Figure 5.24 c recalls the good qualitative agreement with the experimental results.

Figure 5.25 shows a draft of the phase diagram in parameter space (M_{eff}, D) equivalent to (K_u, D), the perpendicular magnetic anisotropy constant K_u and the effective magnetization M_{eff} increasing in opposite directions as shown on the abscissa axis. Figures 5.25 a to e show the simulated resonance lines of the 700 nm disk at f = 5 GHz and $\mu_0 h_{rf} = 1.0$ mT, for a perpendicular static field, for different values of M_{eff}, ranging from highly negative to highly positive as shown by the corresponding points a) to e) on the phase diagram. In each case, it is the large amplitude branch that is shown, the maximum amplitude of the $\Delta M_z/M_s$ signal reached before the appearance of instabilities is indicated[6] and a typical precession profile (phase and amplitude) in the instabilities regime is shown below the resonance line. On the phase diagram, the blue stars correspond to the experimental study[7] done in this thesis on BiYIG nanodisks with $\mu_0 M_{eff}$ slightly negative. The sign of M_{eff} is associated with the sign of the nonlinear frequency shift N as indicated on the abscissa axis.

---

[6] It appears that the more negative the nonlinear frequency shift, the lower the threshold of reduction of the longitudinal component, beyond which an instability develops.

[7] Completed by micromagnetic simulations in good agreement.

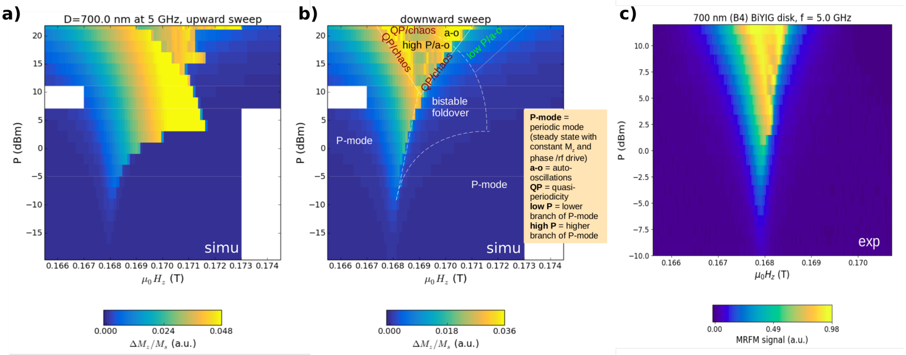

Figure 5.24: a-b) 2D map of the evolution of the resonance line as a function of microwave power in the simulations for the 700 nm BiYIG disk at f = 5 GHz, for a perpendicular static field, for the two upward (a) and downward (b) branches. Boundaries of characteristic nonlinear regimes met in this phase diagram are superposed in panel (b). b-c) Comparison between the simulated results of the downward branch (b) and the experimental results of the 700 nm B4 disk (c): there is a good qualitative agreement. Figure b) is a 2D plot of Figure 5.6 a.

At D = 700 nm and N very negative, in a), one notes a stronger localization of the precession profile which even splits into two "solitons"[8] at the center of the disk. The detailed analysis shows a very turbulent dynamics. At N slightly negative, in b), one has the case that we have studied in detail with the auto-oscillation instability of the precession profile. At $N \approx 0$ ($M_{eff} \approx 0$) one gets the case where there is no nonlinear shift of the resonance line at low excitation. But as mentioned previously, the resonance line finally distorts at high excitation. Being at the boundary of different regions of the phase diagram, the dynamics is difficult to characterize here and is certainly very sensitive to small variations of M_{eff} (i.e. K_u) or the disk diameter. In d) and e) the transition to $N > 0$ changes the behavior of the precession profile in the non-linear regime, spatial expansion rather than localization at the center of the disk, and results in a totally different dynamics, with large amplitude of magnetization precession and spin-wave instabilities beyond a certain amplitude. The green star corresponds to the 700 nm YIG disk (M_{eff} = M_s, no perpendicular anisotropy) studied in [22]. By decreasing the size of the BiYIG disks (blue stars), the development of dynamic instabilities is

---

[8] Here we name soliton a localized region with strong reduction of the longitudinal magnetization.

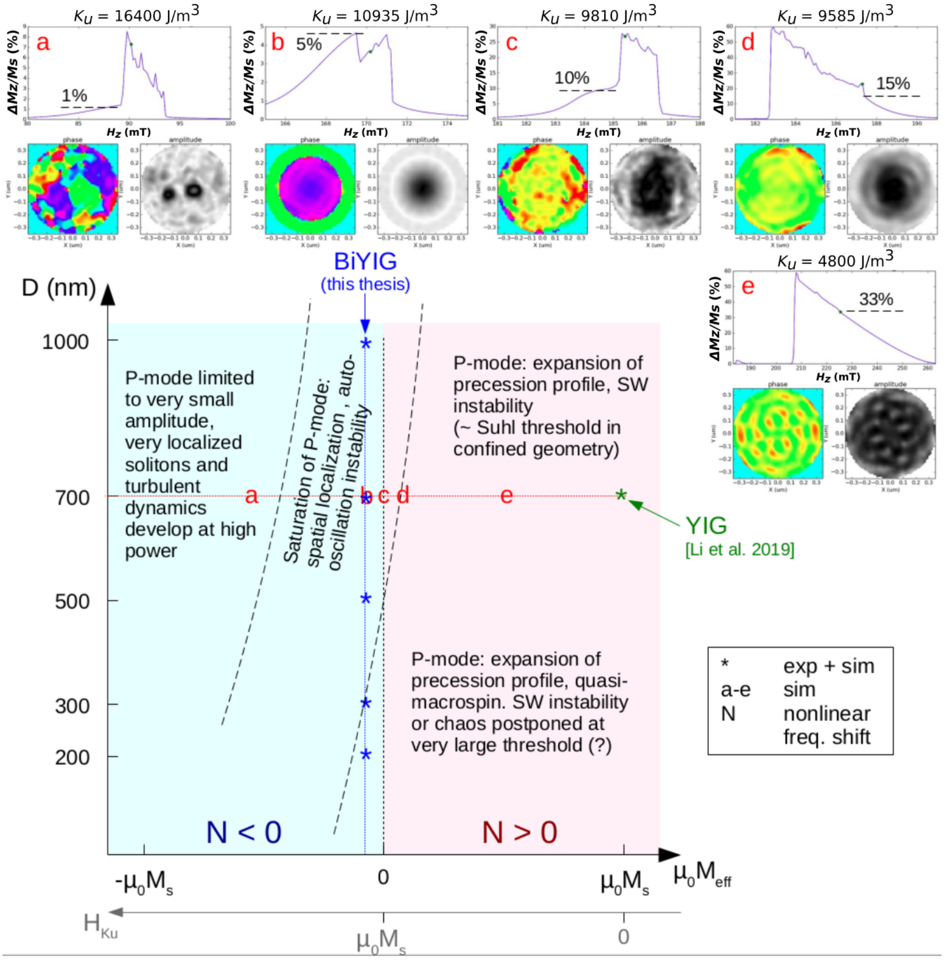

Figure 5.25: Draft of the phase diagram in parameter space (M_{eff},Diameter) equivalent to (K_u,Diameter), with the perpendicular magnetic anisotropy constant K_u and the effective magnetization M_{eff} increasing in opposite directions as shown on the x-axis. a-e) Simulated resonance lines of the 700 nm disk at f = 5 GHz and $\mu_0 h_{rf} = 1.0$ mT, for a perpendicular static field, for different values of the effective magnetization M_{eff}, ranging from highly negative to highly positive as shown by the corresponding points a) to e) on the phase diagram. In each case, the large amplitude branch is shown, the maximum amplitude of the signal $\Delta M_z/M_s$ reached before the onset of instabilities is indicated and a typical precession profile (phase and amplitude) in the instabilities regime is shown below the resonance line.

prevented as showed by the experimental and simulation results.

On the basis of this diagram, one can expect to reach large amplitudes of coherent magnetization precession in small disks with $N > 0$ (i.e. $M_{eff} > 0$), the eventual instabilities being postponed to very large thresholds. It would also be interesting to see what happens in small disks with highly negative N. Such complementary simulations or experiments would allow to complete the phase diagram.

5.7 Conclusion

We measured the main resonance line of the differents disks located under the antenna while increasing the microwave power. One observes for the large disks (D $\geq$ 500 nm) a rapid saturation of the resonance peak amplitude soon after the onset of the foldover. Micromagnetic simulations similar to our experimental protocol reproduce this unexpected behaviour. The comparison between experiments and simulation shows reduction of the spatial average of the longitudinal component of magnetization limited to 5% in the 700 and 1000 nm disks. The analysis of the temporal dynamics in the simulation shows that this early saturation is due to the strong localization of the precession profile at the disk center. This localization combined with the strong dipolar pinning in the 700 nm and 1000 nm disks due to the inhomogeneous internal field result in temporal oscillations of this ultra-large precession self-localized at the disk center. In some simulations where a well-defined periodic auto-oscillation occurs, one can notice a self-modulation of the precession profile that oscillates back and forth between low order eigenmodes and possibly linear combinations of these modes. This phenomenon bears similarities with the Fermi-Pasta-Ulam-Tsingou behavior, a standard problem of dynamical system. A rich generation of patterns in the temporal dynamics depending on the excitation conditions of the resonance was also identified.

We then extracted the frequencies of these instabilities in the simulations. Two-tone measurements in which two microwave fields are used allow to perform a spectroscopic study of the nonlinear regime of instabilities and remarkably give frequency modulation spectra similar to simulations results, which experimentally demonstrates that the phenomenon of auto-oscillation dynamics instability is in fact well occurring in the BiYIG nanodisk samples.

Then, the comparison of the simulation results on the 700 nm BiYIG disk with those obtained previously on the 700 nm YIG disk allowed to understand the outstanding difference between the two cases. The key element is the way the precession profile deforms when the resonance is strongly excited, which is in fact directly related to the sign of the effective magnetization M_{eff}. In

YIG, $M_{eff} > 0$ leads to a spatial extension of the precession profile while in BiYIG with $M_{eff} < 0$, the precession profile becomes strongly spatially localized at the disk center and eventually forms the dynamical instability at higher excitation.

Additional simulations in BiYIG disks performed while changing the sign and value of M_{eff} ($M_{eff} > 0$) give results in agreement with this explanation. Simulation results in smaller disks (200 and 300 nm) where the internal field is less inhomogeneous showed the absence of these dynamical instabilities, which confirms that the strong inhomogeneity of the internal field in large disks governs the development of the dynamic instabilities.

A compilation of all the results allowed to draft two phase diagrams at f = 5 GHz, the first one for the 700 nm disk in the parameter space (microwave power, static field), and the second one in the parameter space (diameter, effective magnetization).

Summary

- Measurement of the main resonance line of the 500, 700 and 1000 nm diameter disks as a function of microwave power : unexpected rapid saturation.
- Micromagnetic simulations : reproduction of the rapid saturation of the signal amplitude.
- Analysis of the temporal dynamics in the simulation : rich patterns generation depending on the conditions of excitation of the resonance; evidence of the appearance of dynamic instabilities corresponding to oscillations of the precession profile between the low order eigenmodes.
- Two-tone experiments : measurement of the frequencies of these instabilities - results similar to those of the simulation.
- Detailed comparative study with previous results on the 700 nm diameter YIG disk : one of the major ingredients at the origin of the drastic difference in results is the way the precession profile deforms during resonance, directly related to the sign of the effective magnetization.
- Summary of results (experimental and simulations) of smaller disks (200 and 300 nm diameter) : confirmation of finite size effects, non-uniform internal field profile, sign of effective magnetization as critical parameters for the formation or not of the dynamic instabilities depending on the size of the nanodisk.
- Drafts of two phase diagrams at f = 5 GHz : one for the 700 nm disk in the parameter space (microwave power, static field), and the second one in the parameter space (diameter, effective magnetization).

Chapter 6

Ferromagnetic resonance of nanodisks in in-plane configuration

"A small change can make a big difference."

Ankita Singhal

Contents

All the experimental results presented so far have been obtained for a static field applied perpendicular to the disks. We have seen that in the large disks of diameter D $>$ 500 nm there is a rapid saturation of the resonance peak at mean precession angles of only 20°. We saw that these results could be explained by the negative sign of the effective magnetization M_{eff} (more precisely the sign of the nonlinear frequency shift) and finite size effects (non-uniform internal field profile, dipolar pinning). Switching to an in-plane applied static field configuration will change the sign of the nonlinear frequency shift and possibly modify the finite size effects; different results can therefore be expected. We present here some results obtained in this configuration.

6.1 Linear regime

6.1.1 Spectroscopy of individual disks

First, let's note that for an in plane static field, the magnetization dynamics can be pumped both with an in-plane rf field or a perpendicular one. Moreover, due to the quasi compensation of the magnetization by the perpendicular magnetic anisotropy in the sample ($M_{eff} \approx 0$), the precession is quasi circular in the disks. For this reason, using an in-plane or out-of-plane rf field is equivalent. Figure 6.1 shows the normalized MRFM spectra of the five disks of the A1-A5 series at f = 5 GHz (one reminds that the disks B are under the antenna, and the disks A and C are next to it). They are very different and more complex than those measured in the perpendicular configuration. The mode of highest amplitude is at higher field only for the 200 nm. There is an inversion of the relative amplitudes of the two modes between 200 and 300 nm. For disks of diameter $\geq$ 300 nm, there are modes of resonance fields larger than the one of the main mode, in contrast to the perpendicular configuration where it is always at higher field. Not surprisingly, the splitting between modes always increases as the disk size decreases. By measuring all the disks, we noted for a given size, a remarkable reproducibility of results between disks A and C and some differences for disks B. We present and explain these results in the appendix I.

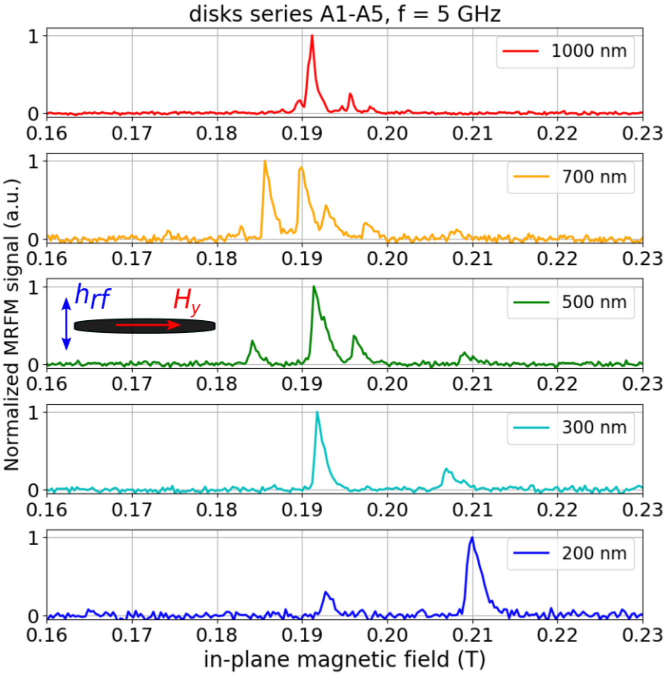

Figure 6.1: Normalized MRFM spectra at f = 5 GHz of the 1000, 700, 500, 300 and 200 nm diameter BiYIG disks (A5-A1) arranged in row. The inset shows the configuration of the rf and static fields.

We also performed a detailed spectroscopy of the different disks to extract their magnetic parameters in this configuration. Note that the extraction of the damping for the 700 nm and 1000 nm disks is very complex in this case because of the high density of spin wave modes as can be seen on the red spectrum in Figure 6.1 (see also the spectra of Figures I.5 and I.6 of the Appendix I). Because of this, during the broadband measurements, it is difficult to follow with accuracy the evolution of the different modes as a function of the frequency, the spectrum showing slight differences from one frequency to another as very small variations of the relative amplitudes of the modes. For these disks, we therefore end up with an order of magnitude of their damping rather than their exact damping. Nevertheless, the results are essentially similar to those obtained in the perpendicular configuration. The damping is higher for the disks B and increases systematically for the smallest disks. The dispersion relations in this case are fitted using the relation (2.24) :

$$\omega = \gamma\mu_0\sqrt{H(H+H_K)} \tag{6.1}$$

and allow to extract the characteristic field H_K of the disks in this new configuration. It is worth to point that if the effective magnetization M_{eff} of the thin film does not depend on the direction of application of the magnetic field, this is not the case of its equivalent for the nanodisks, namely the characteristic field H_K. Indeed, the profile of the demagnetizing field in the disk, the main contribution in H_K, changes when one moves from the perpendicular static field to the in-plane static field (see Figure 6.3). In addition, there is also the small contribution of the cubic anisotropy that we neglect but which is not exactly the same for a perpendicular or in-plane field. It is thus expected that H_K varies slightly, which is confirmed by the experimental results. For this in-plane configuration, one finds that this characteristic field is negative for all the disks and varies between -18 and -35 mT, and is thus of the same order of magnitude as those found out-of-plane and presented in Table 4.2.

6.1.2 Micromagnetic simulations and interpretation

As in the perpendicular case, we have performed micromagnetic simulations using the second method which reproduces our experimental protocol. The parameters used are the same as those used in the perpendicular case, with a constant anisotropy. Figure 6.2 shows the spectra obtained. Comparing with the experimental spectra of Figure 6.1, one notes a quite good qualitative agreement except for the 300 nm concerning the relative amplitudes of the two peaks. We also present on this figure the profiles of the modes of the 200 and 300 nm disks and the profiles of some modes for the other disks. The profiles are numbered and the corresponding peaks have the same number on the spectra (from 1 to 12). For each mode, we show on the right the profile of the amplitude and on the left the profile of the phase of the precession of the magnetization within the disk. The corresponding colorwheel is shown. The static field is applied along the y axis.

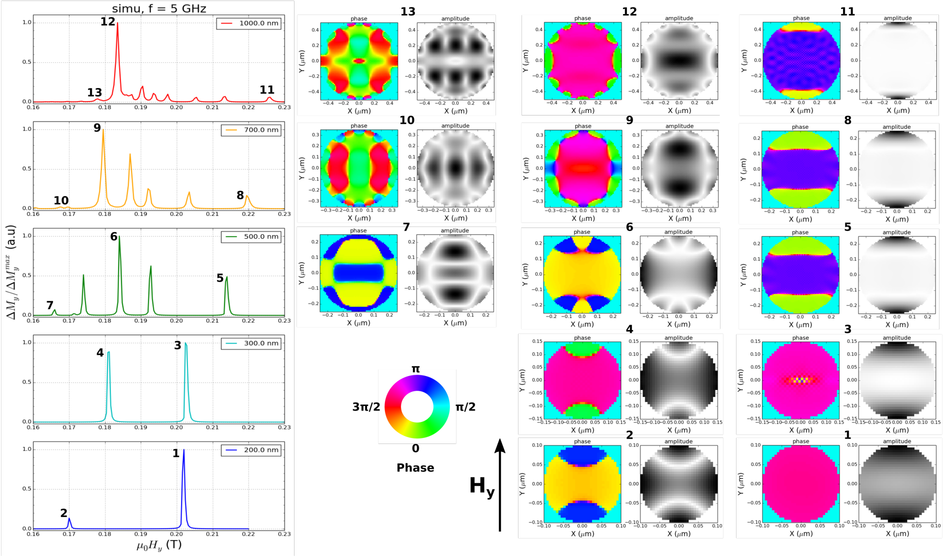

Figure 6.2: Normalized simulated spectrum at f = 5 GHz of the different disks sizes arranged in row by decreasing lateral size. The 2D profiles (phase and amplitude : dark = high amplitude, white = zero amplitude) of the modes corresponding to the numbered peaks on the spectra are shown on the right. The field is applied along the y axis.

Figure 6.3 shows the profile of the demagnetizing field within the 1000 nm diameter disk calculated analytically, in the perpendicular field and in-plane field configurations as shown on the insets. The blue curve is the one already shown in red in Figure 2.4 a. The field is calculated in the median plane of the disk $z = 0$ (see Figure 2.4 b). In the in-plane case, the profiles are different in the x and y directions. This is due to radial symmetry breaking as expected. Considering the profile of the field along the direction of application of the field, one notes the switch from a "bowl" profile in the out-of-plane case to a kind of "inverted bowl" in the in-plane case (red curve). The field is now weaker at the edges of the disk than at the center. This profile obviously has the same behavior for the other disk sizes (larger in the center than at the edges) even if the size reduction leads to different quantitative variations.

With such a profile, one expects to localize spin wave modes on the edges of the disk along the static field. This is the case for the mode 1 of the 200 nm disk in Figure 6.2. One observes that the amplitude is larger at the edges of the disk along the y axis and decreases at the center of the disk but without going exactly to zero. On the other hand, this mode of greater amplitude (greater than mode 2) is the one with a perfectly uniform phase as shown by the phase profile. Mode 2 has a precession node between the center and the edges along y. Edges and center are in phase opposition.

Profiles 3 and 4 allow to understand the change in relative amplitudes of the two peaks between 200 and 300 nm. In the 300 nm, with the increase of the size, the amplitude of mode 1 is more localized on the edges and is much weaker in the center of the disk (mode 3). The phase is uniform in the disk. Mode 2 now takes more space in the center of the disk (mode 4). These changes result in almost equal amplitude for peaks 3 and 4.

With the increase of the size one notes a large variety of spin wave modes. Starting from the 500 nm disk (peaks and modes 5, 8 and 11), the edge mode is more and more localized at the edges, has now zero precession amplitude in the central region of the disk and has smaller relative amplitude. In all the cases the largest amplitude mode (6, 9 and 12) is the mode with the most uniform phase in the central region within the disk. The uniform phase mode remains the fundamental edge mode 5, 8 and 11 (the phase is not defined in the central region where the magnetization does not precess). There are modes like 7 and 10 with precession nodes in the x direction perpendicular to the static field. Indeed, in this geometry, there can be spin waves of wave vector both perpendicular and parallel to the magnetization i.e to the static field.

However, there is no quantitative agreement between experiments and simulations concerning the position of the modes but especially the splitting between the modes. For example, there is almost a factor 2 of difference between

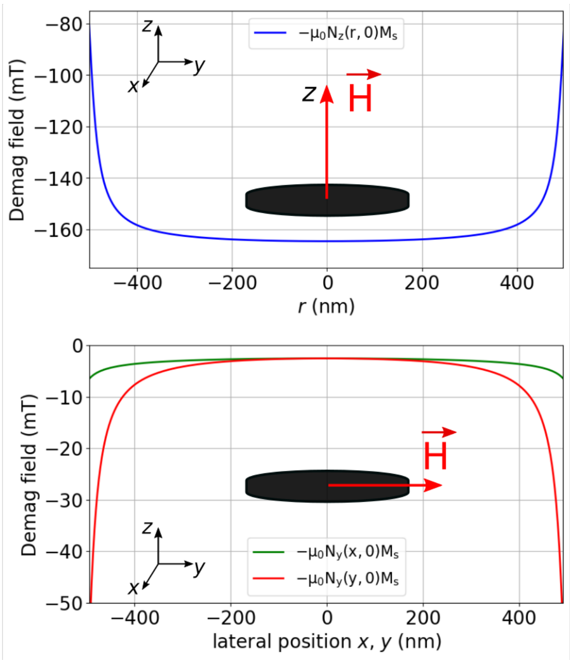

Figure 6.3: Profile of the internal field within the disk for an applied field perpendicular and in the plane of the disk as shown on the insets. In the in-plane case, the field is calculated in both x and y directions. In each case the field is calculated in the median plane z =0.

the splitting between the two peaks of the 200 nm (see the blue spectra of Figures 6.1 and 6.2). The differences are less important when the size of the disk increases. Our attempts to elucidate these observations have been unsuccessful, in particular even using the model of spatial modulation of the anisotropy demonstrated in the perpendicular configuration. We had already seen that the model only slightly affects the splitting between the modes (see Figure 4.8 b & c).

6.2 Nonlinear regime

6.2.1 Experimental results

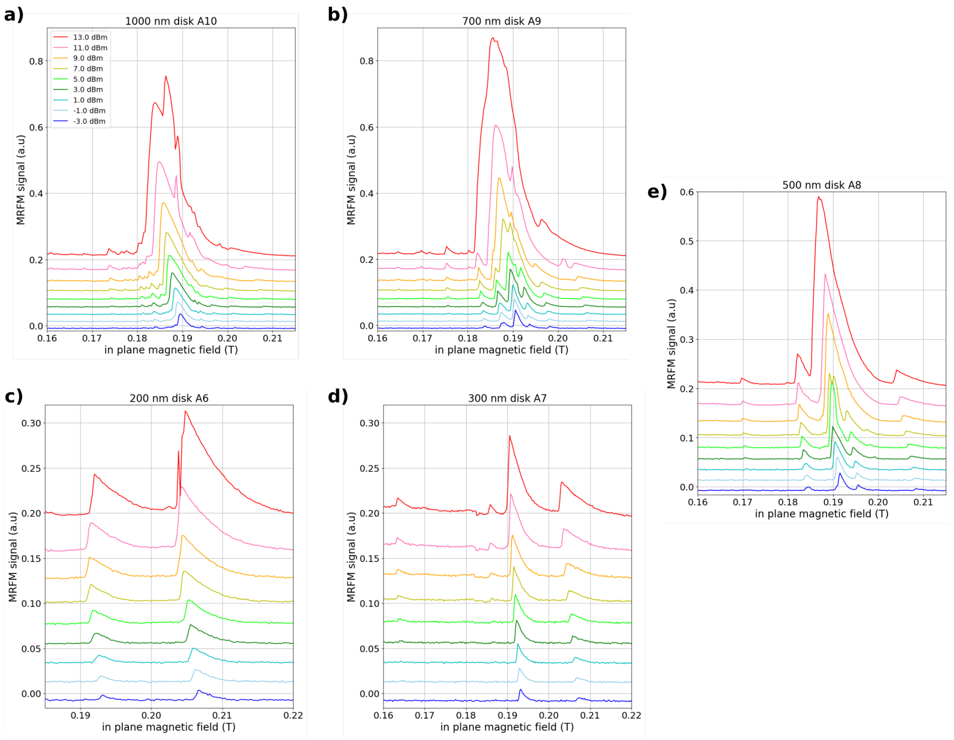

Figure 6.4: Evolution of the MRFM spectra of disks A6-A10 at f = 5 GHz as a function of the microwave power.

We now study the evolution of the spectrum as we increase the microwave power. Figure 6.4 shows the results obtained for the A6-A10 series, the microwave excitation being modulated. The resonance signals are therefore measured with the amplitude of the cantilever vibrations and correspond to the low amplitude branch of the dynamics. The power is increased between -3 and 13 dBm. One notes a foldover of the resonance lines towards the low fields in contrast to the perpendicular case where the foldover was towards the high fields. This can be understood by the change of sign in front of the characteristic field H_K in the resonance relation (6.1) compared to the perpendicular case. This change leads to a change of sign of the nonlinear frequency shift. Then one notes a clear increase of the amplitude of the resonance peaks even for disks of diameter $\geq$ 500 nm, in contrast to the out-of-plane case where we observed a rapid saturation of the resonance line amplitude. For large disks, one also observes a kind of merging of the resonance peaks at very large microwave powers.

We also measured the resonance spectra of the disks using a continuous microwave excitation and the signal being coded in the cantilever frequency. This gives access to the full dynamics by sweeping the field in the two directions. In this case, the signal can be directly calibrate into mean precession angle of the magnetization as explained in Figure 5.16. Figure 6.5 shows the results obtained for the A1-A5 series, at P $=$ 12 dBm. One notes that at this power, there is no hysteresis for the large disks, a very small hysteresis for the 500 nm and 300 nm and a clear hysteresis for the 200 nm. The strange signal shape for the 700 nm A4 and 1000 nm A5 comes from the feedback due to probe oscillations on the probe-disk interaction during the measurements, due to the presence of many modes in the resonance line. This is similar to what was already observed in the perpendicular configuration (see Appendix F). However, even for large disks, it is possible to calibrate the signal in precession angle. One finds $\Delta M_y^{max}/M_s \approx 40\%$ for the 1000 nm disk and 75% for the 200 nm disk, which correspond respectively to mean precession angles of 53° and 75°.

6.2.2 Micromagnetic simulations

6.2.2.1 Case of 700 nm diameter disk : "merging" of the different spin wave modes

Figure 6.6 shows the evolution of the spectrum as a function of rf field in the simulation for the 700 nm diameter disk. There is a qualitative agreement with Figure 6.4 b, the different modes tending to merge at high excitation. One also observes at high excitation, a very weak hysteresis at $\mu_0 h_{rf} = 1.26$ mT and then almost no hysteresis at 2.0 and 3.16 mT. This is also the case in experiments, see the yellow curve in Figure 6.5. Quantitatively, for the maximum rf fields reached in the experiment of the order of 1.6 mT, $\Delta M_y^{max}/M_s$ of the order of

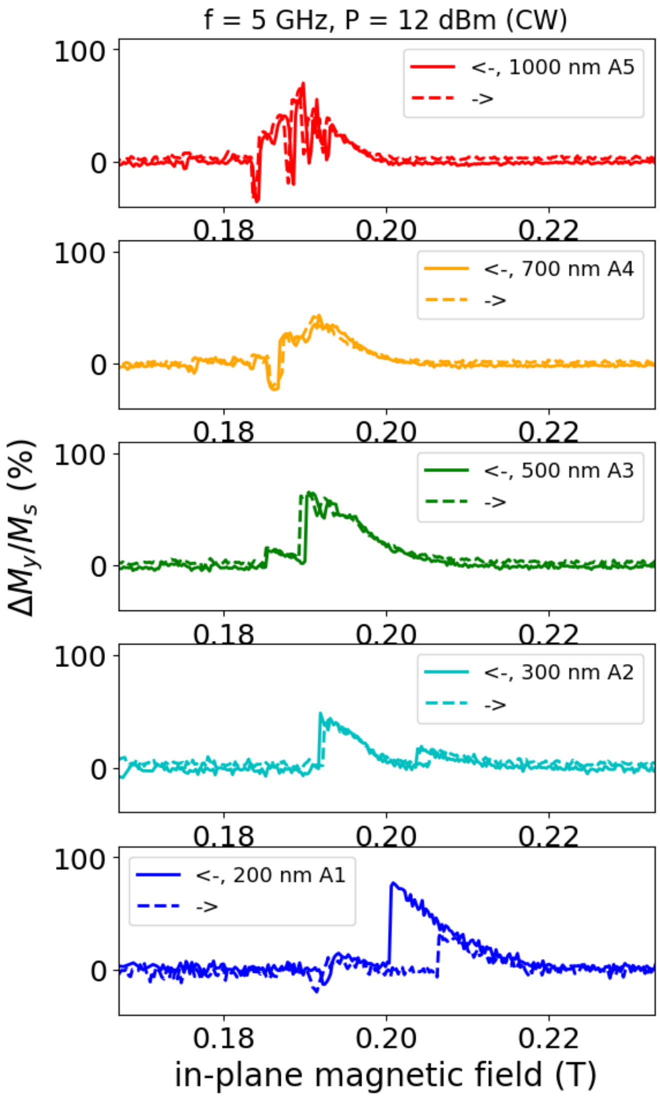

Figure 6.5: MRFM spectra of disks A1-A5 at f = 5 GHz at P = 12 dBm for both scanning directions of the field.

40% are reached, which corresponds to an average precession angle of 53°. This is also the case in experiment, see the yellow curve in Figure 6.5. However, the contribution of several modes to this mean precession angle clearly indicates that it is not a macrospin precession.

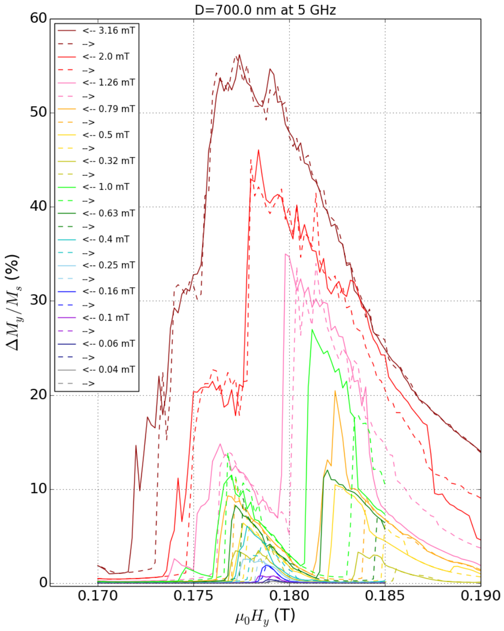

Figure 6.6: Evolution of the simulated spectrum of the 700 nm disk at f = 5 GHz as a function of the excitation field.

6.2.2.2 Case of 200 nm diameter disk : achievement of very large precession angles

Figure 6.7 shows the direct comparison at f = 5 GHz between the experimental spectrum of the 200 nm disk A1 at P = 13 dBm and the simulated spectrum at $\mu_0 h_{rf}$ = 1.0 mT. If the upward branch in red is not well reproduced quantitatively, there is a very good quantitative agreement for the large amplitude downward branch. Experimentally, $\Delta M_y^{max}/M_s = 90\%$ is reached, which means a mean precession angle of 84° i.e. a quasi-supression of the longitudinal component of the magnetization M_y. The figure also shows the 2D profile (phase and amplitude) of the precession mode of the magnetization at 5 fields through the downward branch of the resonance line in the simulation.

These points are indicated and colored on the figure and have the same color as the field on the corresponding profiles. Between 0.2005 T and 0.1805 T, one

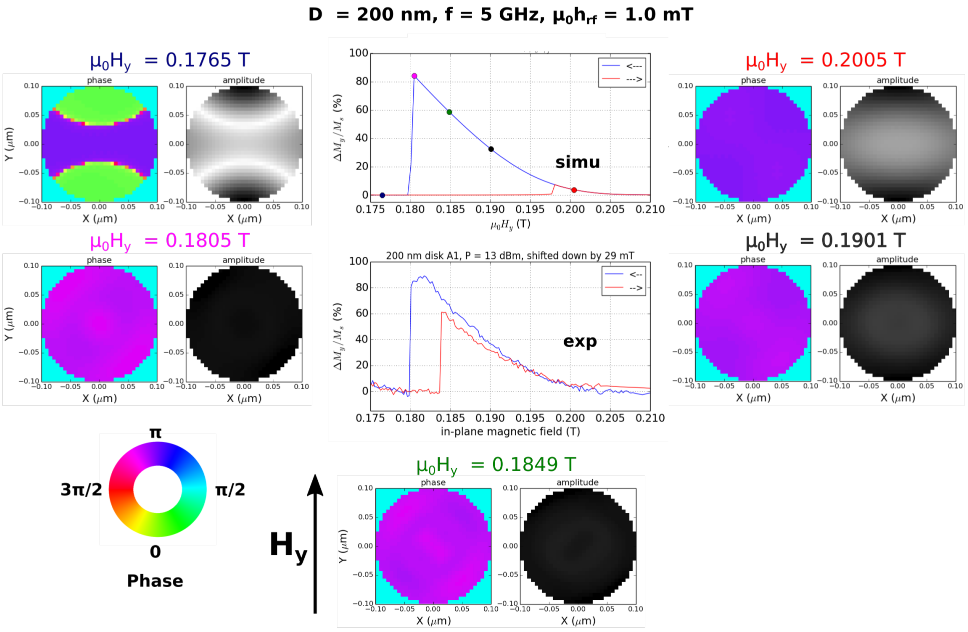

Figure 6.7: Direct comparison at f = 5 GHz between the experimental spectrum of the 200 nm disk A1 at P = 13 dBm and the simulated spectrum at $\mu_0 h_{rf}$ = 1.0 mT. The 2D profile (phase and amplitude) of the precession mode of the magnetization at five fields through the downward branch of the resonance line in the simulation are shown.

moves from the linear mode 1 of Figure 6.2 to a quasi-uniform mode not only in phase but also in amplitude : the precession profile increases in amplitude and extends in the disk. At 0.1765 T one finds the mode 2 in Figure 6.2, after the downward jump on the low amplitude branch. It is therefore clear that, in contrast to the large disks, the excitation of a single mode in this case allows to have a quasi macrospin precession at very large precession angles. The picture is quantitative similar to the one of the normally magnetized 700 nm YIG disk, but is even much better qualitatively, since very large mean precession angles are reached without instabilities and with a shift of the resonance line of only 20 mT in contrast to the YIG disk where the shift of the resonance line was of the order of $\mu_0 M_s = 170$ mT (see Figure 1 C) and where SW instabilities appeared above $\Delta M_z/M_s \approx 30\%$ (see Figure 5.20 a & g). This is due to the fact that the in-plane magnetized BiYIG disk is qualitatively similar to the out-of-plane magnetized YIG disk (same sign of the nonlinear frequency shift). Thus the explanations given in terms of deformation of the precession profile in the case of the YIG disk are valid here (the precession profile extends into the disk during the FMR excitation in contrast to the case of the perpendicularly magnetized BiYIG disks where it was localized at the center). Moreover, the size of the disk, three and a half times smaller here (200 instead of 700 nm), leads to a more drastic confinement of the spin waves which prevent spin waves instabilities to occur. All these ingredients combined allow to reach very large amplitudes of coherent magnetization precession.

6.3 Conclusion

The switch to an in-plane static field radically changes the results obtained. This is due to the change in the sign of the nonlinear frequency shift : in the nonlinear regime the resonance line shifts downwards and the behavior of the precession profile during resonance excitation is no longer the same. Large mean precession angles of the order of 50° are reached in large disks of diameter $>$ 500 nm, which is much larger than those reached in the perpendicular case ($\approx 20°$). But the high spin waves density prevents the achievement of a coherent macrospin precession. The stronger confinement in the 200 nm disk allows to excite a single mode and to reach very large amplitudes of coherent magnetization precession.

Summary

- Measurement of the resonance line of disks magnetized in-plane in linear and nonlinear regimes.
- Micromagnetic simulations : good qualitative agreement but semi-quantitative agreement (the achieved precession angles are well reproduced but not the splitting between modes) with the experimental results.
- Achievement of very large amplitudes of coherent magnetization precession in the 200 nm disk.

Chapter 7

Conclusions & perspectives

"I'm very bad at ending sentences. A lot times I just want to say, 'That's the end of my sentence. I have nothing more to say.'"

Nathan fielder

7.1 General conclusion

The aim of this thesis was to study the nonlinear regimes of Bismuth-doped YIG nanodisks using ferromagnetic resonance. This was done using a magnetic resonance force microscope (MRFM).

We have determined through a spectroscopic study the magnetic parameters of all the disks, the static field being perpendicular to the disks. The negative characteristic field H_K for all the disks confirms the perpendicular magnetic anisotropy of the sample. The analysis of the experimental results and their comparison with the micromagnetic simulations allowed to demonstrate a spatial modulation of the magnetic anisotropy during the nanostructuration. An increase of the damping of the disks located under the antenna, attributed to spin-pumping at their lateral boundaries towards the metallic antenna was observed.

In the nonlinear regime and for a perpendicular static field, we observed for the large disks (700 and 100 nm diameter) a rapid saturation of the amplitude of the resonance peak at mean precession angles of less than 20°. Micromagnetic simulations showed that this saturation is due to the formation of dynamic instabilities corresponding to a strong localization of the magnetization precession profile within the disk followed by oscillations of this profile between different low order spin wave modes. The analysis of the temporal dynamics revealed a rich generation of patterns during the formation of the instabilities, whose shapes depend on the excitation conditions of the resonance. After extraction of the frequencies of these instabilities in simulations, two-tone measurements gave frequency modulation spectra similar to the simulation results, confirming the formation of these instabilities in the experiments. The results obtained in the smallest disks allowed to identify the key elements necessary for the formation or not of these instabilities. These are the sign of the nonlinear frequency shift given by the sign of the effective magnetization M_{eff}, and the non-uniform internal field profile in the disk.

The switch to the in-plane static field configuration allowed to change the sign of the nonlinear frequency shift and to prevent the onset of these instabilities at high excitation, confirming the role of the nonlinear frequency shift in their development. In large disks (D$\geq$ 500nm), due to the lower splittings between SW eigenmodes, one observes a merging of modes at high amplitude, while in small disks, the strong confinement of the spin waves allowed to reach large amplitudes of coherent magnetization precession.

The results obtained allowed to draft two phase diagrams at 5 GHz. The first one for the 700 nm BiYIG disk in the parameter space (microwave power, static field) which presents regimes of coherent precession of the magnetization

(P-mode), auto-oscillations, quasi-periodicity and chaos. A second one in the parameter space (M_{eff},Diameter) which allowed to identify some preliminary perspectives for future studies.

7.2 Perspectives

In this work, we realized that despite the quasi compensation of the magnetization (effective magnetization $M_{eff} \approx 0$) in the BiYIG sample and the resulting small frequency nonlinear shift at high excitation, there is formation of auto-oscillations instabilities of the precession profile in the large disks which lead to a rapid saturation of the signal amplitude. It appears that the non-linear dynamics results not only from the sign and the value of M_{eff}, but mainly from the way the internal field profile in the disk and the corresponding precession profile deforms when the excitation is increased. This profile being already inhomogeneous in the linear regime, due to the non-ellipsoidal shape of the sample, it leads to a complex nonlinear magnetization dynamics.

Although they were not expected at first, interesting perspectives emerge from the obtained results.

Detailed mathematical analyses of the patterns observed in the simulated temporal traces [127] of the magnetization dynamics should be performed in order to accurately characterize the different regimes (commensurate/incommensurate, quasi-periodic/chaotic) and to elaborate more precise phase diagrams.

Concerning the oscillation of the precession profile between different modes observed in certain cases, the influence of nonlinear couplings between the modes could be finely analyzed using recent theoretical developments allowing to compute and decompose the nonlinear dynamics on the basis of a few eigenmodes, such as the vector hamiltonian formalism for nonlinear magnetization dynamics [133] or the computational micromagnetics based on normal modes [134].

BiYIG samples with different uniaxial perpendicular magnetic anisotropy and diameters could be nanopatterned to have M_{eff} strongly negative or strongly positive in order to check some predictions of simulations.

It would be interesting to excite the nonlinear dynamics in these disks by spin-orbit torque (SOT) rather than harmonic excitation (rf). To perform experiments, one would need to add a Pt stripe on top of the BiYIG nanodisks, as it was done to study SOT driven auto-oscillations in YIG microdisks [25]. Micromagnetic simulations including SOT could also be performed. Since SOT excitation requires in-plane magnetization, the small BiYIG disks with $M_{eff} \approx 0$ in which large amplitudes of coherent magnetization precession were achieved in the in-plane configuration appear as the ideal candidate. This would allow to check on hybrid garnet/Pt samples the conclusions of the experimental study performed on fully metallic spin Hall devices [37].

In the case of magnetic garnets with Dzyaloshinskii-Moriya interaction(which may arise from interfacial effects), the perpendicular anisotropy resulting in a negative effective magnetization may allow to stabilize skyrmionic bubbles [135]. Using nanostructuration, one can confine these bubbles and detect their specific signatures in the excitation spectrum [136, 137]. It would also be interesting to investigate experimentally some interesting predictions in the nonlinear regime, such as the parametric excitation of drifting SW patterns due to the antisymmetric exchange interaction [138].

Annexes

"Done right, precision can help clarify, plus it's fun."

Betsy Hodges

Appendix A

Calculations

A.1 Derivation of the precession angle θ with respect to H

From equation (2.57) we have :

$$\frac{d\theta^2}{dH} = \frac{d}{dH}\left(\frac{h^2}{(H - H_0 + M_{eff}\theta^2/2)^2 + \frac{\Delta H^2}{4}}\right) \tag{A.1}$$

$$= \frac{-2(1 + \frac{M_{eff}}{2}\frac{d\theta^2}{dH})(H - H_0 + M_{eff}\theta^2/2)h^2}{\left[(H - H_0 + M_{eff}\theta^2/2)^2 + \frac{\Delta H^2}{4}\right]^2} \tag{A.2}$$

Noting that $(H - H_0 + M_{eff}\theta^2/2)^2 + \frac{\Delta H^2}{4} = \frac{h^2}{\theta^2}$ in equation (2.57), one finds :

$$\frac{d\theta^2}{dH} = \frac{-2(1 + \frac{M_{eff}}{2}\frac{d\theta^2}{dH})(H - H_0 + M_{eff}\theta^2/2)\theta^4}{h^2} \tag{A.3}$$

$$\Longrightarrow \frac{d\theta^2}{dH}\left(1 + \frac{M_{eff}(H - H_0 + M_{eff}\theta^2/2)\theta^4}{h^2}\right) = \frac{-2(H - H_0 + M_{eff}\theta^2/2)\theta^4}{h^2} \tag{A.4}$$

$$\Longrightarrow \frac{d\theta^2}{dH} = \frac{-2(H - H_0 + M_{eff}\theta^2/2)\theta^4}{h^2 + M_{eff}(H - H_0 + M_{eff}\theta^2/2)\theta^4}. \tag{A.5}$$

Knowing that $\frac{d\theta^2}{dH} = 2\theta\frac{d\theta}{dH}$ and replacing h^2 by $\left((H - H_0 + M_{eff}\theta^2/2)^2 + \frac{\Delta H^2}{4}\right)\theta^2$, one finds :

$$\frac{d\theta}{dH}=\frac{-(H-H_0+M_{eff}\theta^2/2)\theta^3}{\left[(H-H_0+M_{eff}\theta^2/2)^2+\frac{\Delta H^2}{4}\right]\theta^2+M_{eff}(H-H_0+M_{eff}\theta^2/2)\theta^4} \tag{A.6}$$

$$=\frac{-(H-H_0+M_{eff}\theta^2/2)\theta}{(H-H_0+M_{eff}\theta^2/2)^2+\frac{\Delta H^2}{4}+M_{eff}(H-H_0+M_{eff}\theta^2/2)\theta^2} \tag{A.7}$$

$$=\frac{-(H-H_0+M_{eff}\theta^2/2)\theta}{(H-H_0+M_{eff}\theta^2/2)(H-H_0+M_{eff}\theta^2/2+M_{eff}\theta^2)+\frac{\Delta H^2}{4}} \tag{A.8}$$

We finally get the equation (2.58) :

$$\frac{d\theta}{dH}=-\frac{\theta\left(H-H_0+\frac{1}{2}M_{eff}\theta^2\right)}{\left(H-H_0+\frac{1}{2}M_{eff}\theta^2\right)\left(H-H_0+\frac{3}{2}M_{eff}\theta^2\right)+\frac{\Delta H^2}{4}} \tag{A.9}$$

A.2 Derivation of variations of the cantilever frequency

The cantilever being a harmonic oscillator and its motion being along the vertical axis Oz (the origin of the axis being taken at the equilibrium position of the cantilever in the absence of a sample), its equation of motion is written :

$$m\frac{d^2z}{dt^2}+\gamma\frac{dz}{dt}+kz=m_p\frac{\partial B_z}{\partial z} \tag{A.10}$$

where m and m_p are respectively the probe mass and magnetization, γ and k are respectively the damping constant and the spring constant of the cantilever. The equilibrium position of the cantilever is the point z_0 such that :

$$kz_0=m_p\frac{\partial B_z}{\partial z}(z_0). \tag{A.11}$$

By expanding $\frac{\partial B_z}{\partial z}$ around z_0, one finds that to first order :

$$m_p \frac{\partial B_z}{\partial z}(z) = m_p \frac{\partial B_z}{\partial z}(z_0) + m_p \frac{\partial^2 B_z}{\partial z^2}(z_0)(z - z_0) \tag{A.12}$$

(A.12) in (A.10) yields :

$$m\frac{d^2 z}{dt^2} + \gamma \frac{dz}{dt} + k_{eff} z = m_p \frac{\partial B_z}{\partial z}(z_0) - m_p \frac{\partial^2 B_z}{\partial^2 z}(z_0).z_0 \tag{A.13}$$

where $k_{eff} = k - m_p \frac{\partial^2 B_z}{\partial^2 z}(z_0)$ is the effective spring constant of the cantilever. The new resonant frequency of the cantilever is :

$$f_{c_{eff}} = \sqrt{\frac{k_{eff}}{m}} = \sqrt{\frac{k}{m}\left(1 - \frac{m_p}{k} \frac{\partial^2 B_z}{\partial^2 z}(z_0)\right)}. \tag{A.14}$$

The vibrations of the cantilever being of very low amplitude (a few nm), one finds :

$$f_{c_{eff}} \approx \sqrt{\frac{k}{m}}\left(1 - \frac{m_p}{2k} \frac{\partial^2 B_z}{\partial^2 z}(z_0)\right) \tag{A.15}$$

i.e :

$$f_{c_{eff}} = f_c - f_c \frac{m_p}{2k} \frac{\partial^2 B_z}{\partial^2 z}(z_0). \tag{A.16}$$

where $f_c = \sqrt{\frac{k}{m}}$ is the cantilever frequency in the absence of probe-sample interaction. The frequency variation of the cantilever is therefore given by :

$$\frac{f_{c_{eff}} - f_c}{f_c} = \frac{\Delta f_c}{f_c} = -\frac{m_p}{2k} \frac{\partial^2 B_z}{\partial^2 z}(z_0). \tag{A.17}$$

One finds equation (3.4).

Appendix B

Optimization of the spatial modulation of the anisotropy

A first study consisting of testing different values of σ (the size of the external crown where the anisotropy is lowered) in expression (4.3) was done. For values of β (which gives the difference between the anisotropy at the center and the edges of the disk) fixed between 0 and 0.3, different values of σ between 50 and 150 nm were tested in each case. For these tests, we use the fisrt simulation method (see section 4.3). Then, the process is repeated in the other sense. For different values of σ fixed between 50 and 150 nm, different values of β between 0 and 0.3 were tested in each case. I present below the case where σ is fixed at 150 nm and the optimization is done on β.

For the chosen value of σ, the evolution of the resonance spectrum of the 1000 nm diameter disk according to different values of β is studied. Figure B.1 shows the results obtained. Figure B.1 b shows the cross-section of the spatial modulation of the anisotropy in the disk for each value of β between 0 and 0.3 in steps of 0.05. The value of K_u taken here is that of the thin film, 12150 J/m^3. One confirms that β defines the difference between the anisotropy in a central region of the disk, maximum and the lower one at the edges. Figure B.1 a clearly shows the effects of these modulations on the resonance spectrum. The experimental spectrum which is the same as the one in Figure 4.1 is recalled (in black). One notes a decrease in the frequency of the main mode when β increases, which is thus close to the experimental frequency. Note that the spectra are normalized. One also notes a decrease of the relative amplitudes of the higher order modes until $\beta = 0.15$ for which one has a quasi-extinction of these modes. On the other hand, from $\beta = 0.2$, the spectrum is intrinsically modified : one notes the appearance of new modes near the main mode, one of which remains localized at 3.5 GHz despite the variations in β. A visualization of the profiles shows that these new modes are located in potential wells which appear in the internal field at the edges of the disk because of the very strong modulation of the anisotropy. Moreover, the quite good reproduction of the splitting between the modes by the simulations without any modulation ($\beta = 0$) remains the case for low values of β (≤ 0.15).

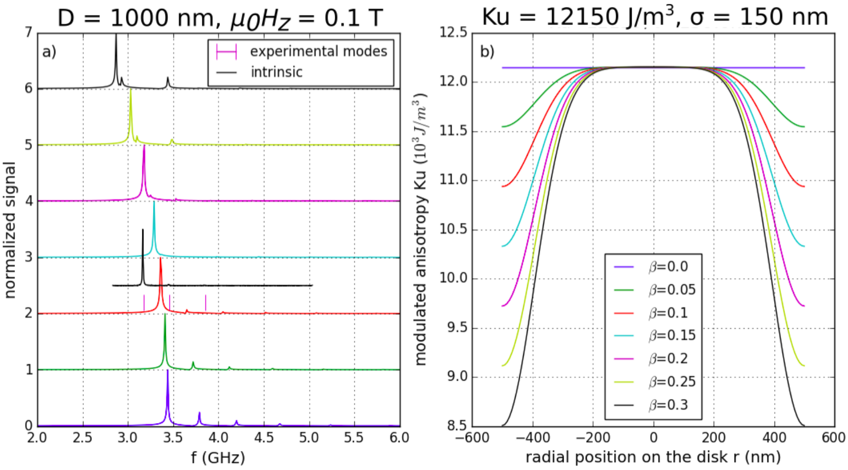

Figure B.1: Evolution of the resonance spectra of the 1000 nm diameter disk when modulating the anisotropy by varying β as indicated.

From all the results obtained in these tests and the comparison with the experimental MRFM spectra, one found optimal parameters $\sigma = 150$ nm and $\beta = 0.1$.

Appendix C

Calibration of the rf field

C.1 Calculation of the conversion parameter S

If i_{rf} is the intensity of the microwave current generated at a microwave power P, the linear amplitude h_{rf} of the microwave field just below the antenna (i.e for disks B) can be estimated from the Biot–Savart law :

$$\mu_0 h_{rf} = \frac{\mu_0 i_{rf}}{2w} \tag{C.1}$$

with $i_{rf} = \sqrt{2}\sqrt{\frac{P}{Z}}$, where $w = 5$ μm is the width of the constriction and $Z = 50$ Ω is the impedance matched to the synthesiser.

This leads to :

$$\mu_0 h_{rf} = \frac{\mu_0}{w}\sqrt{\frac{P}{2Z}}. \tag{C.2}$$

One finds $\mu_0 h_{rf} = 0.8$ mT for $P = 0$ dBm. From equation (5.1), one deduces $S = 0.8$ mT$/\sqrt{mW}$.

C.2 Experimental determination

In a MRFM experiment, the amplitude of the signal depends on the power, i.e. h^2, the magnetic moment of the probe m_p and the linewidth in the linear regime. If A is the peak amplitude, we can write that $A \propto \frac{h^2 m_p}{\Delta H^2}$. Replacing h^2 with its expression (5.1), we find:

$$S^2 \propto \frac{A \times \Delta H^2}{P \times m_p}. \tag{C.3}$$

Therefore, by making a proper measurement of the signal as a function of frequency in which the microwave power is adjusted with frequency, in the same way as the broadband measurements used to extract the disk parameters, and then extracting A and ΔH at each frequency, one can deduce the variations of S with frequency. Figure C.1 shows the result obtained for a measurement performed on the 700 nm disk B4. one finds that the excitation is more efficient at low frequency below 3 GHz, which is a classical behavior of the microwave field, the losses being more important as the frequency increases. One finds that S is almost constant between 3.5 and 9 GHz.

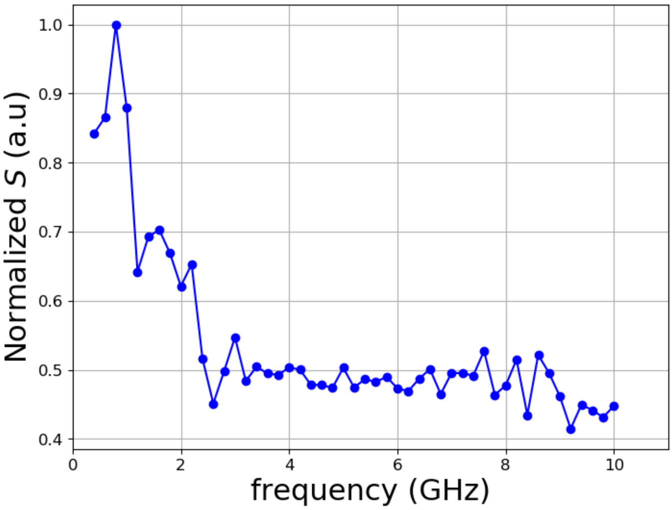

Figure C.1: Evolution of the normalized calibration parameter between power and microwave field as a function of frequency.

We now determine the parameter S at some frequencies. It is possible to use the onset of foldover as a means to calibrate the amplitude of the excitation field produced by the microwave antenna at the sample location [38]. However, to get a better precision, we can also fit the dependence on power of the critical fields H_{down} and H_{up} determined experimentally beyond the onset of the foldover [10]. For this purpose, we have used the formula (2.70) giving H_{up} (we have access only to the downward branch). For this evaluation we restrict the analysis to small disks on which we can follow the evolution of

H_{up} as a function of the power, the large disks showing a rapid saturation of the resonance line. In measurements, one extracts H_{up} as a function of power. The field H_0 is determined in the linear regime, h is replaced by its expression depending on S and P and the effective magnetization M_{eff} (case of the thin film) is replaced by the characteristic field H_K of the disk :

$$H_{up} \approx H_0 - \frac{3}{2} S^{2/3} P^{2/3} H_K^{1/3} \tag{C.4}$$

One plots the evolution of H_{up} which we can then fit by deducing S.

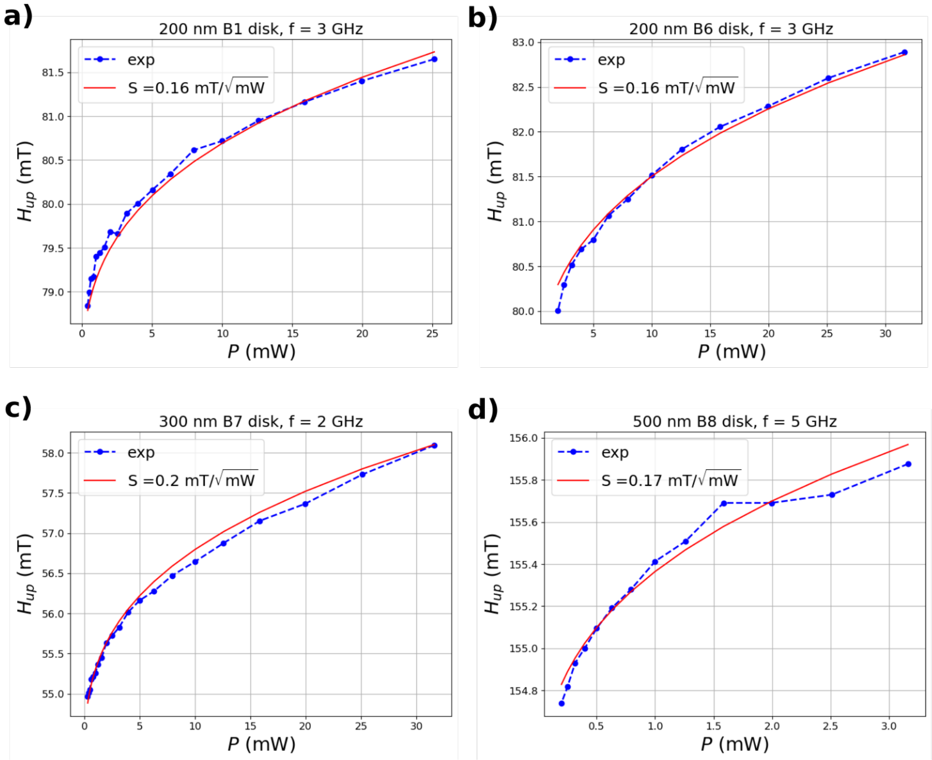

Figure C.2: Estimation of the calibration parameter S between the field and microwave power from measurements of H_{up} vs P made on different disks and at different frequencies : a) on B1 at 3 GHz, b) on B6 at 3 GHz, c) on B7 at 2 GHz and d) on B8 at 5 GHz.

Figure C.2 shows the results obtained. As expected, we find about the same parameter $S = 0.16$ mT$/\sqrt{mW}$ at 3 GHz and 5 GHz independently of the measured disks B since all the disks B undergo the same rf field. One finds that at 2 GHz, $S = 0.2$ mT$/\sqrt{mW}$ which gives a ratio of 1.25 between the values of S at 2 and 5 GHz, a result in agreement with the ratio found in Figure C.1.

Appendix D

Micromagnetic simulations parameters

For the different disk sizes, the Table D.1 summarizes the values of anisotropy constant K_u and damping α used in simulations. Like For the 1000 nm diameter disk in the linear regime (see the blue spectrum in Figure 4.8 b, values of K_u that reproduce the intrinsic resonance fields of disks of the series B1-B5 are used.

Table D.1: Magnetic parameters used in simulations for the different disk sizes.

Diameter (nm)	1000	700	500	300	200
K_u (J/m^3)	11500	10935	10400	9303	9170
α ($\times$ 10^{-3})	0.9	1.0	1.15	1.0	1.0

Appendix E

Sensitivity of simulated temporal dynamics on initial conditions

In this appendix, we present 500 ns simulation traces of the magnetization dynamics computed in the 700 nm disk excited by a microwave field of frequency 5 GHz and amplitude 1 mT.

We compare two situations :

1. "From equilibrium" in which at each field through the resonance line, the initial condition is the equilibrium state.
2. "Downward sweep", in which at each field through the resonance line, the initial condition is the final state of the previous field.

Figure E.2 shows that in the case of a downward scan, after 50 ns, the magnetization has reached a steady state at some fields outside the saturation zone, which is not the case when one starts from the equilibrium (Figure E.1).

The comparison of Figures E.3 and E.4 at 167.9, 168.3, 170.7 and 171.3 mT shows that even after a long time (500 ns correspond to 2500 repetitions of the microwave driving period) the dynamical state can be quite different depending on the initial state which is a typical signature of dynamical systems with chaos.

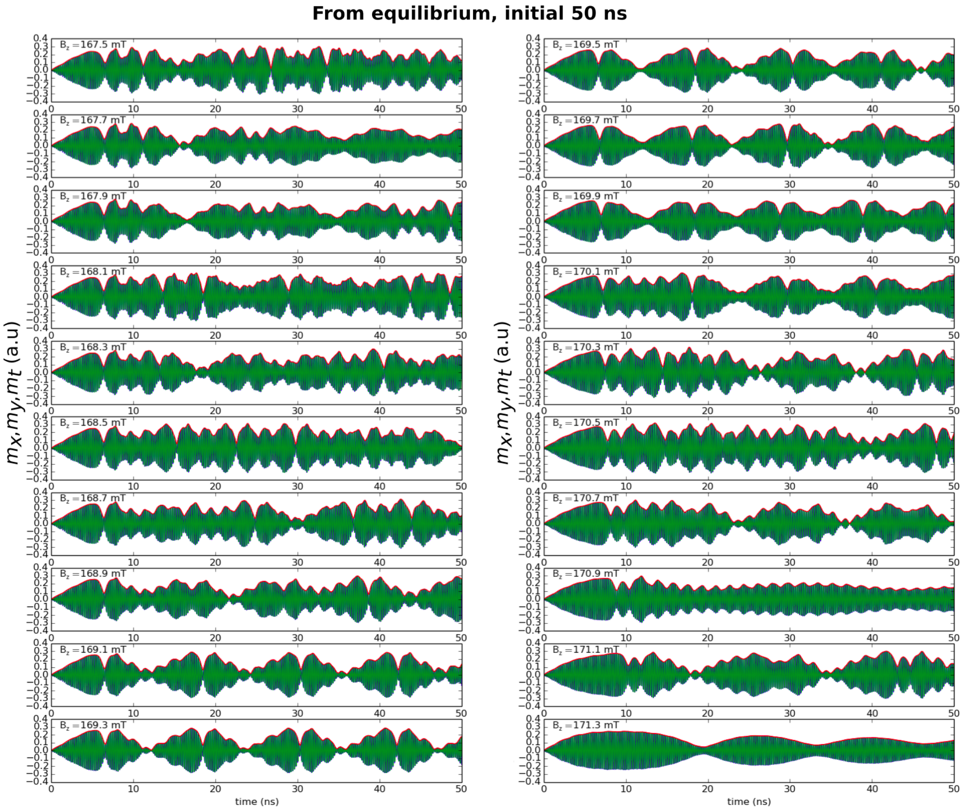

Figure E.1: Zoom on the first 50 ns in time evolution of the components m_x, m_y and m_t of the magnetization at different fields trough the resonance line for the 700 nm disk, each field having been simulated 500 ns. The simulation was done starting from equilibrium at each field : one starts from zero at each field.

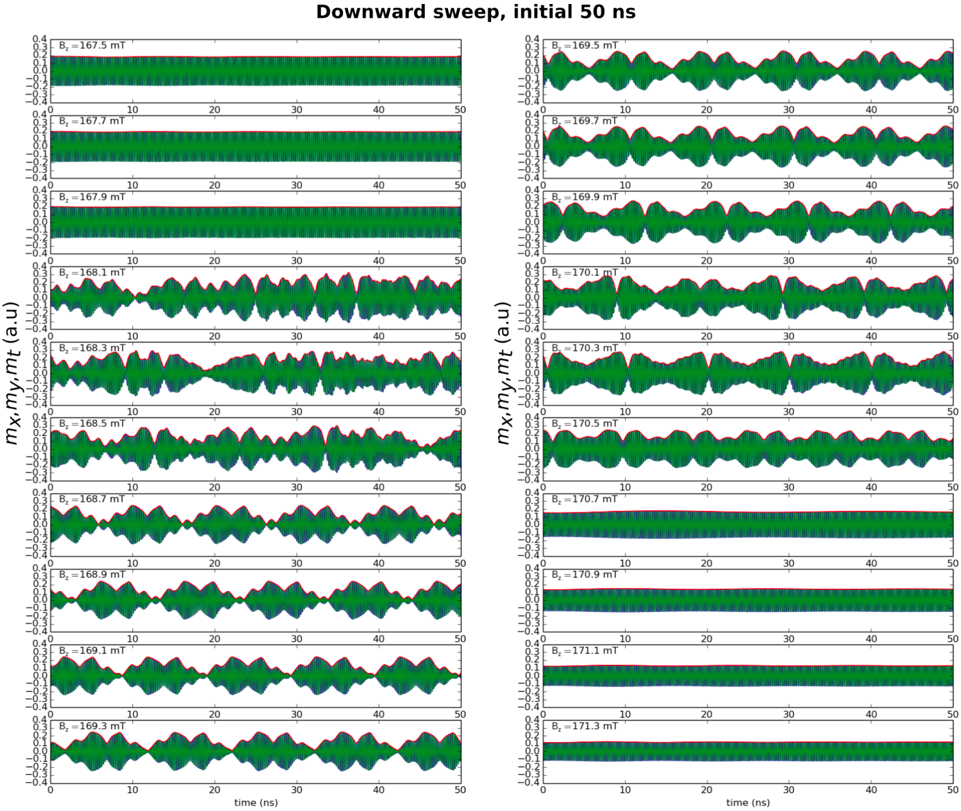

Figure E.2: Zoom on the first 50 ns in time evolution of the components m_x, m_y and m_t of the magnetization at different fields trough the resonance line for the 700 nm disk, each field having been simulated 500 ns. The simulation was done with a downward sweep of the field. For each field, the initial state is the final state of the previous field.

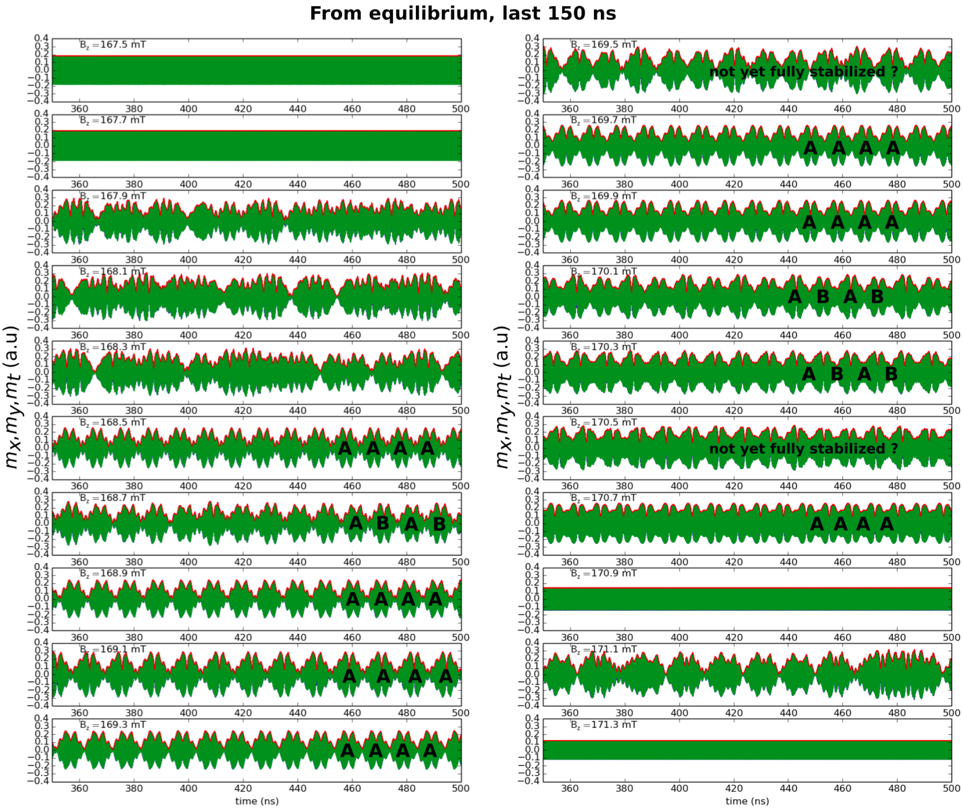

Figure E.3: Zoom on the last 150 ns in time evolution of the components m_x, m_y and m_t of the magnetization at different fields trough the resonance line for the 700 nm disk, each field having been simulated 500 ns. The simulation was done starting from equilibrium at each field : one starts from zero at each field

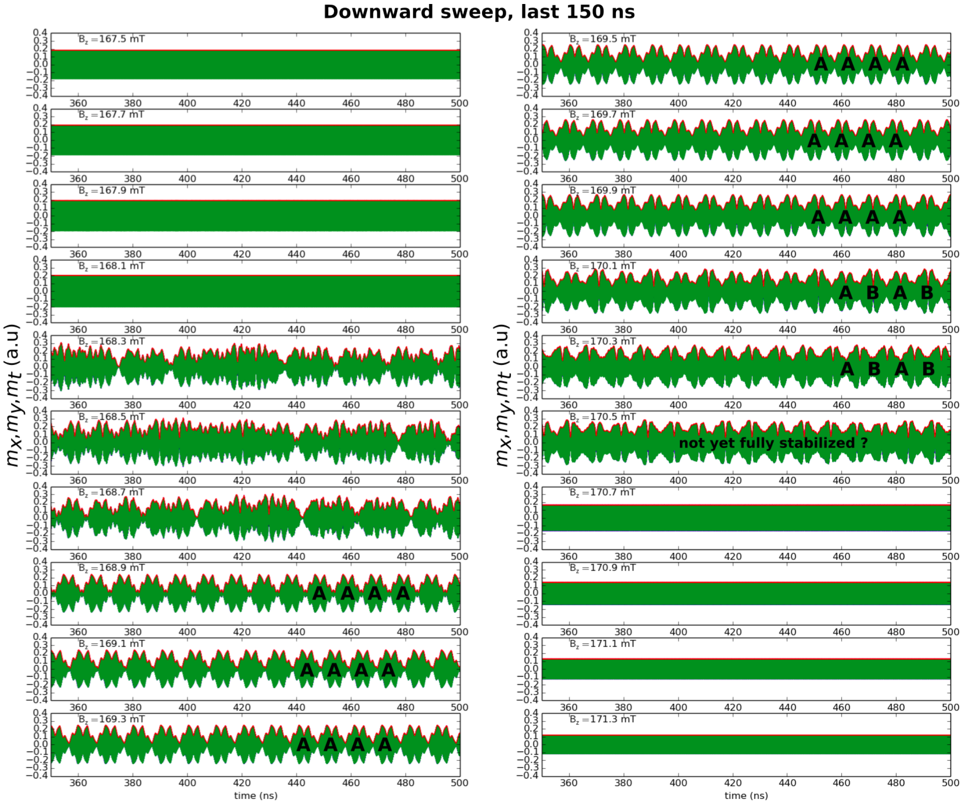

Figure E.4: Zoom on the last 150 ns in time evolution of the components m_x, m_y and m_t of the magnetization at different fields trough the resonance line for the 700 nm disk, each field having been simulated 500 ns. The simulation was done with a downward sweep of the field. For each field, the initial state is the final state of the previous field.

Appendix F

Expected shape of MRFM signal using cantilever frequency mode

Since there is no hysteresis in this regime, there is an equivalence between the signal measured by modulating the microwave (variations of vibrations amplitude of the cantilever) and the one obtained with a continuous wave excitation (variations of the cantilever frequency). We use a small model to deduce de variations of f_c from the pid signal (which also corresponds to ΔM_z). Figure F.1 a shows the pid signal for the 700 nm B4 disk at different microwave powers. We directly convert them in M_z from an appropriate conversion factor. Then we use these data to calculate the expected response for the cantilever frequency.

Now, we know that due to its oscillations, at a position z_0, the probe oscillates between $z_0 + dz$ and $z_0 - dz$. So, inside the resonance line, at a given point, the field oscillates between $H_1 = H_z - H_{probe}(z_0 + dz)$ and $H_2 = H_z - H_{probe}(z_0 - dz)$. It is also the case of the magnetization of the disk which will oscillate between $M_z(H_1)$ and $M_z(H_2)$.

Let's remember that Δf_c depends on the second derivative of the field created by the disk on the probe. This field being a direct function of the static magnetization M_z of the disk, Δf_c signal will be affected by the oscillations of M_z.

On Figure F.1 b, we present the results of these calculations using the datas (M_z) of F.1 a, whitout taking into account these oscillations of M_z in dashed line and taking into account of these oscillations in continuous line. We find a good agreement with the experimental measurements of Δf_c (see Figure 5.16 c), with negative parts of the signal.

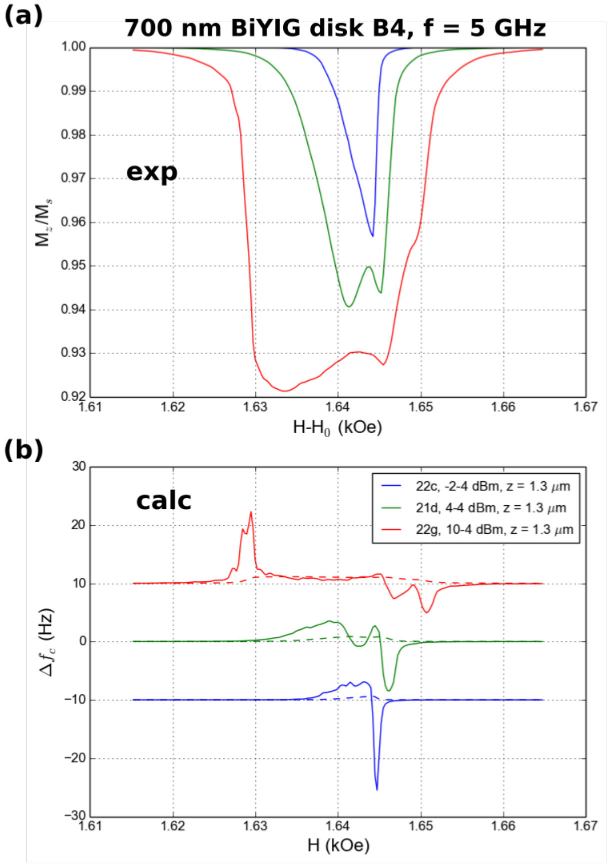

Figure F.1: a) Resonance signal of the disk B4 measured from the variations of the vibrations amplitude of the cantilever for different microwave powers, directly converted in M_z. b) Calculation from the data of figure a) of the variations of the frequency of the cantilever Δf_c. In dashed line: no taking into account of the oscillations of the cantilever. In continuous line: the oscillations of the cantilever are taken into account.

In conclusion, oscillations of the probe create a modulation of the static magnetization of the disk during resonance which is at the origin of the complex shape of the measured signal in the variations of f_c.

This was already present in the case of YIG disk but induced negligible effects. It is for instance the very small negative part of the signal on Figure 1 C at 0.56 T. This effect is amplified here in the BiYIG case because there is almost no resonance line shift in the nonlinear regime. We are constrained to reach very large ΔM_z over lateral shifts of less than 20 mT whereas in the YIG case the shift was on the order of $\mu_0 M_s \approx 200$ mT. The smooth increase of ΔM_z in the YIG case is replaced by an abrupt increase in the BiYIG case, which combined with the oscillations of M_z results in a more complex signal shape.

Appendix G

Simulation results of the 500 nm disk

The static field is perpendicular to the disk.

G.1 Comparison to experimental results

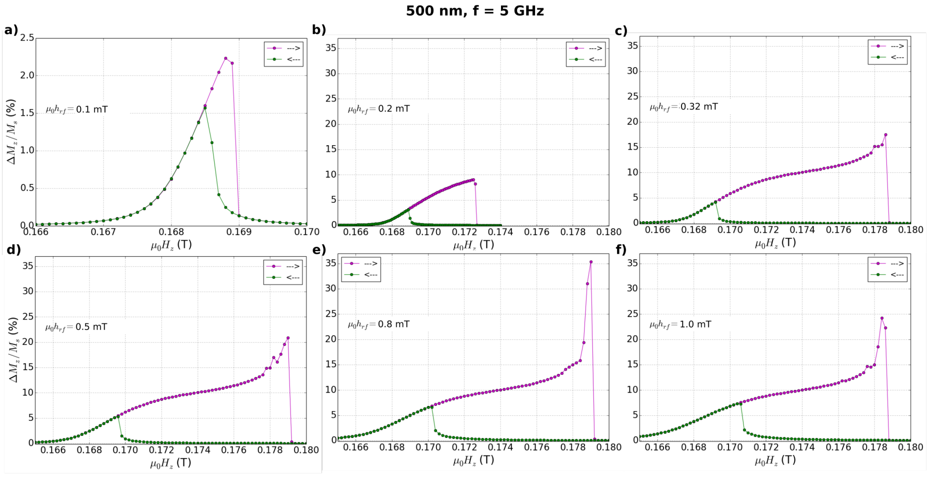

Figure G.1: Hysteresis cycle of the FMR resonance line of the 500 nm disk at different excitation fields in the simulation. At high excitation, the hysteresis cycle is still present but H_{down} saturates as soon as $\mu_0 h_{rf}$ = 0.32 mT and then decreases.

Figure G.1 shows the simulated resonance line at different excitation fields for the 500 nm disk. As the excitation is increased, one moves from the classical hysteretic behavior at low excitation to an apparent saturation of the upward branch at $\mu_0 h_{rf} = 0.2$ mT combined from $\mu_0 h_{rf} = 0.32$ mT to a re-increase of ΔM_z just before the downward jump at H_{down}. Figures G.1 d & e and G.2 e show that H_{down} even start to slightly decrease beyond a certain threshold : one can therefore think that there will be a clear amplitude saturation of this upward branch at higher excitation. On the other hand, we do not observe such an effect for the downward branch which just presents the standard behavior with the increase of H_{up}, see Figure G.2 a.

So it clearly appears that for this particular size of 500 nm diameter, none of the different complex behaviors of the two disks B3 and B8 observed in the experiment at higher excitation (see Figures 5.2 a & b) is reproduced in the simulation. One finds that a maximum amplitude of $\Delta M_z/M_s \approx 14\%$ is reached on B8 (see Figure G.2 b) and even considering the upward branch in simulation, we have at the maximum $\Delta M_z/M_s \approx 20\%$ (see Figure G.1 f), which still remains far from a total suppression of M_z. Concerning the disk B3, the amplitude of the signal reached at high excitation is even lower than that of B8.

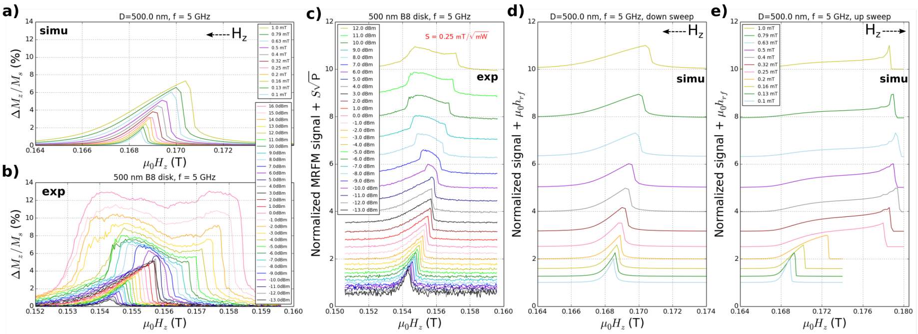

Figure G.2: a-b) Comparison between the experimental results and the simulation of the evolution of the resonance line as a function of the excitation field for the 500 nm disk B8. c-d) Deduction of the calibration factor S between the excitation power and the microwave field from a qualitative comparison of one resonance line to another between experiment and simulation.The experimental results are not reproduced by simulation at high excitation. e) Case of an upward scan of the static field.

G.2 Analysis of the temporal dynamics

G.2.1 Time evolution of the average components of magnetization during resonance

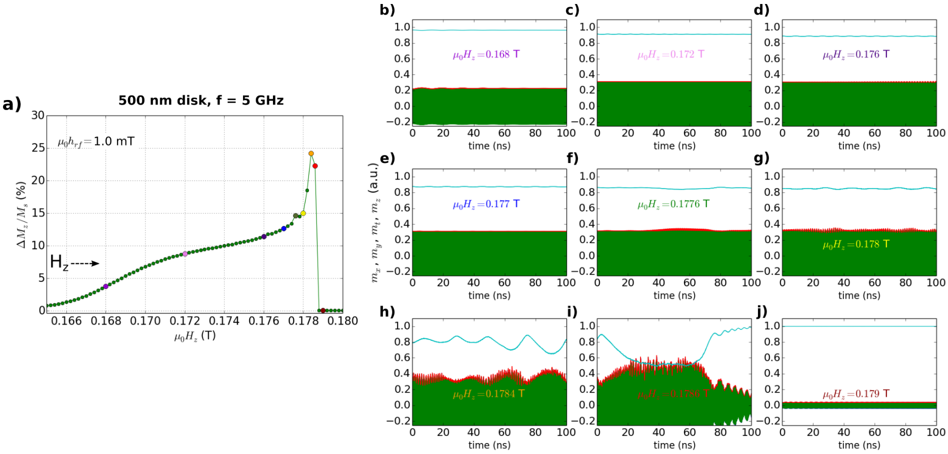

Figure G.3: a) Resonance line in the simulation at $\mu_0 h_{rf} = 1.0$ mT for the 500 nm disk for an upward sweep of the static field. b) to j) Time evolution of the normalized average components of the magnetization during the 100 ns simulation at different fields through the resonance line shown in a). The fields from b) to j) correspond in this order to the colored points of the resonance line in a). The longitudinal component is in light blue, the m_x and m_y components in green and the transverse component in red.

Like Figure 5.7, Figure G.3 shows the time evolution of the average components of the magnetization at certain fields during resonance in the case of the 500 nm disk now and for an upward scan of the field (interesting case in which the saturation of H_{down} occurs). Figure G.4 presents for certain fields, 0.168, 0.178 and 0.1786 T, the zoomed curves of m_z, m_x and m_t at the end of the 100 ns of simulation. One observes that the saturation of H_{down} is due to the formation of other types of instabilities as shown in Figures G.3 g h & i. Up to 0.1776 T, there are oscillations of mz with a continuous decrease of its mean value. Between 0.1776 and 0.178 T one observes the appearance of instabilities in m_t. At 0.1784 T, these instabilities are associated with an increase in the amplitude of the quasi-oscillations of m_z with time, which leads to a sudden decrease in the mean value of m_z. This explains the sharp increase of the signal (ΔM_z) between 0.178 and 0.1784 T on Figure G.3 a. At 0.1786 T, if m_z remains quite low between 20 and 65 ns, it increases significantly from 70 ns, which explains why at this field ΔM_z remains close to the value of the previous field on Figure G.3 a.

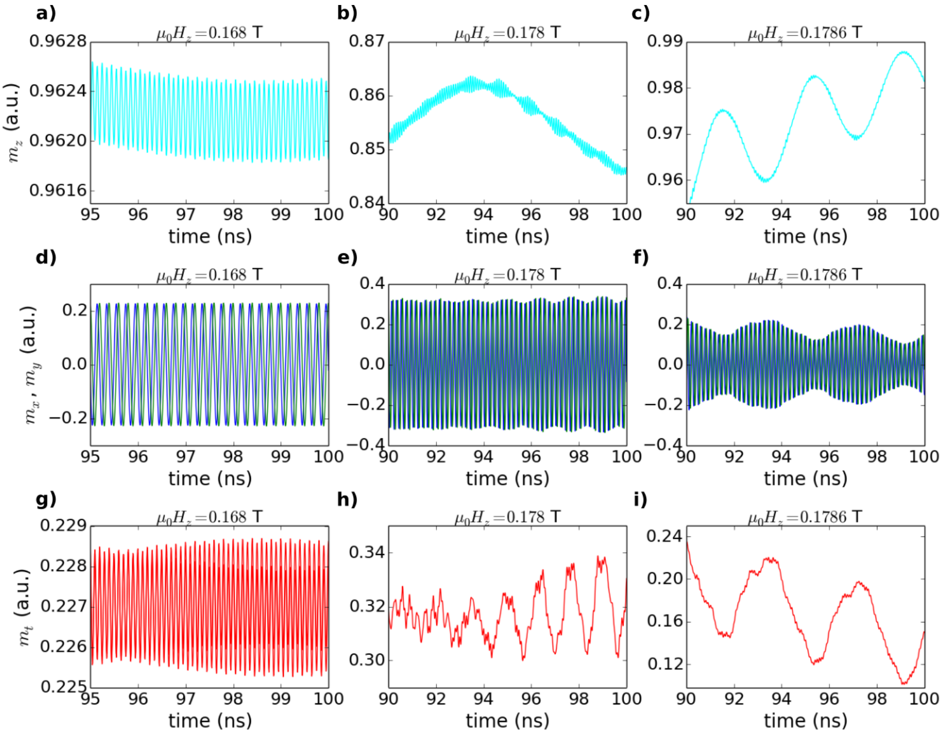

Figure G.4: Zoom on the time evolution of the average components of the magnetization m_z, m_x, m_y and m_t at different fields through the resonance line for the 500 nm disk.

G.2.2 Evolution of the precession profile during resonance

Figure G.5 shows the spatial profiles of the precession mode at the different selected fields. Here also, there is a strong localization of the mode at the disk center when the excitation is increased. From 0.176 T, m_z is already negative at the center of the disk. Then m_z continues to decrease until 0.178 T where ΔM_z increases. At 0.1784 T, ΔM_z increases again (even if the profile seems to indicate the contrary, it is just the snapshot at 100 ns in the time evolution) but then at 0.1786 T one falls on the low amplitude branch.

For this 500 nm disk, the large amplitude profile reached at 0.178 T is less strongly peaked at the center of the disk than in the case of the 700 nm disk, which allows it to be more stable in time. Indeed, the size of the disk being smaller, the precession mode occupies a larger proportion of the disk, which results in a different magnetization dynamics in this case. However, eventually the excitation field can not sustain anymore a precession mode of such large amplitude which results in the downward jump (at 0.1786 T).

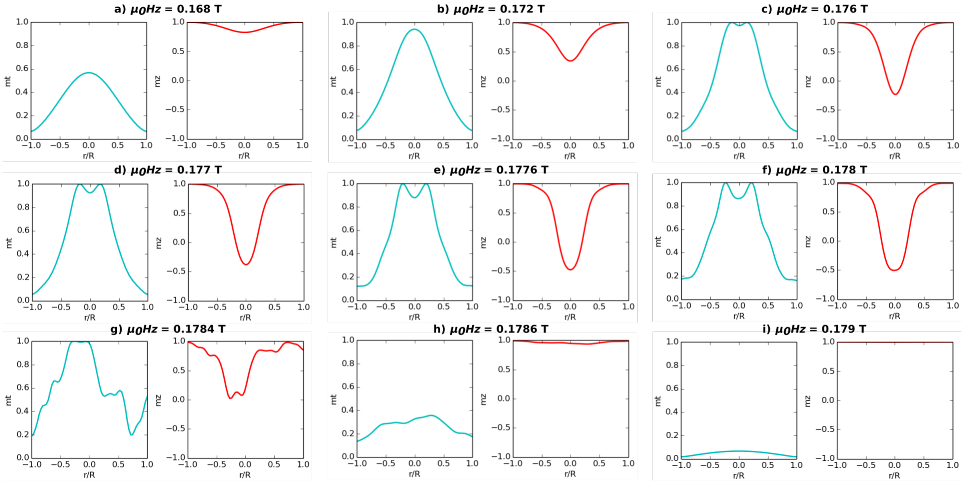

Figure G.5: Snapshots of spatial profiles of the transverse (light blue) and longitudinal (red) normalized magnetizations at the different colored points of the resonance line of Figure G.3 a of the 500 nm disk.

Appendix H

Out-of-plane magnetization dynamics of 200 nm and 300 nm diameter disks : experiments and simulations

We have seen that there is a rapid saturation of the resonance peak amplitude in the 1000 nm, 700 nm and 500 nm disks. Now we want to see what happens when the disk size is reduced. Thus, the experimental approach is exactly the same as the one used in Chapter 5, i.e. measure the resonance line of the different disks when increasing the microwave power. This similarity will allow a faster analysis of the results obtained.The static field is perpendicular to the disks.

H.1 Experimental evolution of the main resonance line with excitation

Figure H.1 shows the results for the 200 nm disk B1 and the 300 nm disks B2 and B7 under the antenna, at f = 5 GHz with a modulated microwave (only the downward branch is measured). At high power there is no longer a saturation of the amplitude of the resonance peak. The other 200 nm disk, B6, has the same behavior as B1. So, except the 300 nm disk B2 (Figure H.1 b), all these disks show the classical behavior of an increase in amplitude and a shift of the resonance line towards high fields associated with the increase of the field H_{up} when the excitation is increased. Surprisingly, the disk B2 shows a strange unexpected behavior. At the beginning, there is a shift towards low fields although this disk has a negative characteristic field $\mu_0 H_K$ as all the other disks (see Table 4.2), before showing at higher excitation (from 1 dBm) a shift towards high fields which results in a broadening of the resonance line. It is therefore obvious that this disk is singular. Despite some hypotheses, we could not find a coherent explanation for this observation. It would be very interesting to understand this intriguing result.

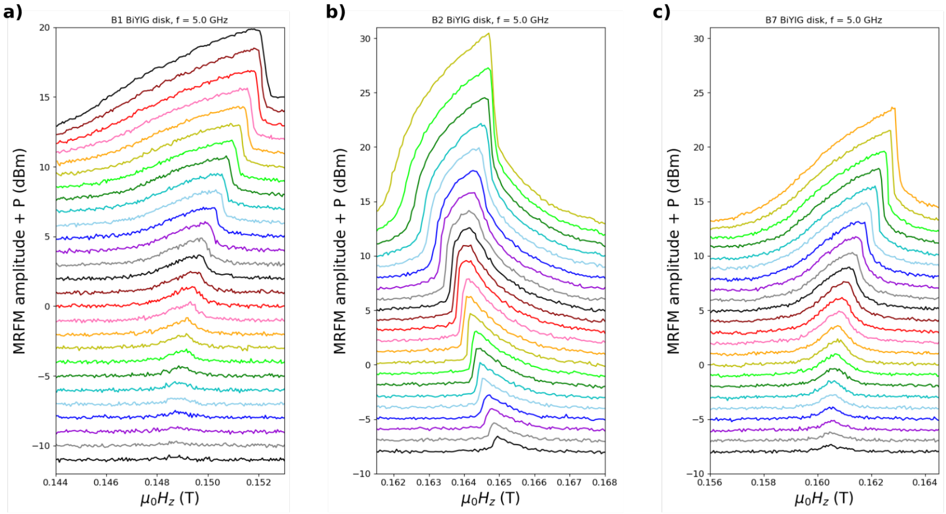

Figure H.1: Evolution of the resonance line as a function of microwave power for a) the 200 nm diameter disk B1 and b-c) the 300 nm diameter disks B2 and B7 at f = 5 GHz.

H.2 Micromagnetic simulations

H.2.1 Comparison to experiments

Figure H.2 shows that the classical behavior observed in experiment is well reproduced by the downward branch (a downward sweep of the field) in simulations for the 200 and 300 nm disks as expected. To compare experimental results to simulations, we used the same calibration parameter S deduced in the experiment with the 700 nm disk in Chapter 5. The only surprise here is on the 300 nm disk, a very quick and sudden increase of the amplitude of the simulation at very high excitation, just before the downward jump at H_{down}, when the excitation field is strongly increased beyond 2.0 mT, see Figure H.2

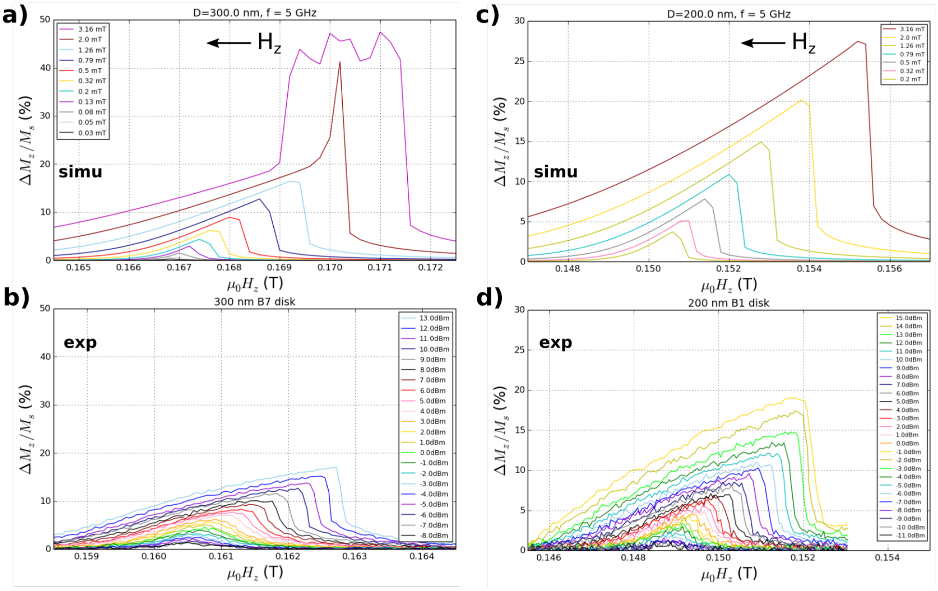

Figure H.2: a-b) Comparison between the experimental results and the simulation of the evolution of the resonance line as a function of the excitation field for the 300 nm disk B7. c-d) Comparison between the experimental results and the simulation of the evolution of the resonance line as a function of the excitation field for the 200 nm disk B6.

a. This regime is not reached in the experiment where the maximum excitation is ≈ 1.7 mT. On these disks, we reach at the maximum in the experiment $\Delta M_z/M_s \approx 20\%$ only limited by the excitation field and their large damping.

Even considering the upward branch in simulations (the high amplitude branch - see Figure 2.9), one realizes that for the 200 nm, $\Delta M_z/M_s$ saturates very quickly at 50% only for $\mu_0 h_{rf} = 0.32$ mT then H_{down} starts to slightly decrease, see Figure H.3 b. And for the 300 nm, there is a sudden increase in amplitude at high excitation. H_{down} slightly decreases between $\mu_0 h_{rf} = 0.32$ and 1.26 mT, before increasing again in 2.0 and 3.16 mT. But here too, $\Delta M_z/M_s$ saturates at 40%, see Figure H.3 a.

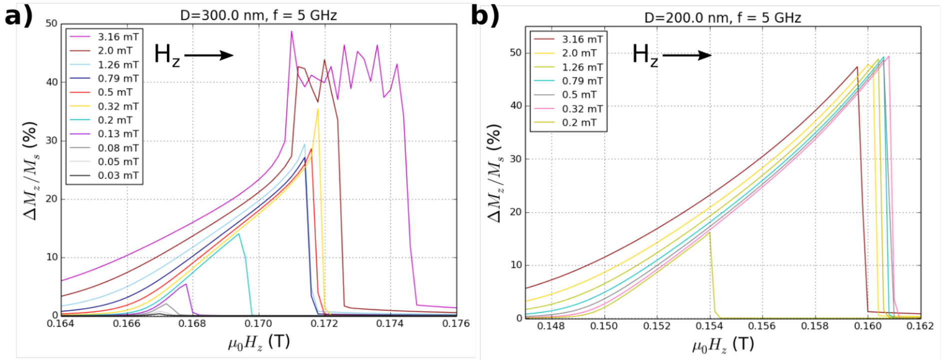

Figure H.3: Evolution of the resonance line as a function of the excitation field in the simulation for an upward sweep of the static field for the 2 sizes a) 300 and b) 200 nm.

H.2.2 Analysis of the temporal dynamics : origin of the saturation of the downjump field

We now analyze the temporal dynamics and the evolution of the precession mode profile during the resonance, in the case of 300 nm. The results obtained are presented in Figures H.4 and H.5 for $\mu_0 h_{rf} = 0.32$ mT for an upward scan of the field. There are no more dynamic instabilities. Because of the smaller size of the disk, the precession mode profile is much less peaked at the center and much less pinned at the edges than for the 500 nm, 700 nm and 1000 nm disks, and remains close to the initial Bessel function. The normalized averaged longitudinal component of magnetization m_z decreases until 0.1718 T, becoming negative at the center at 0.1716 T (Figure H.5). Then, as in the 500 nm case, the large amplitude precession mode can no longer be sustained by the excitation. This different shape of the large precession self-localized at the disk center makes the profile stable in time now and therefore prevents the development of the dynamic instability observed in the 700 nm and 1000 nm disks.

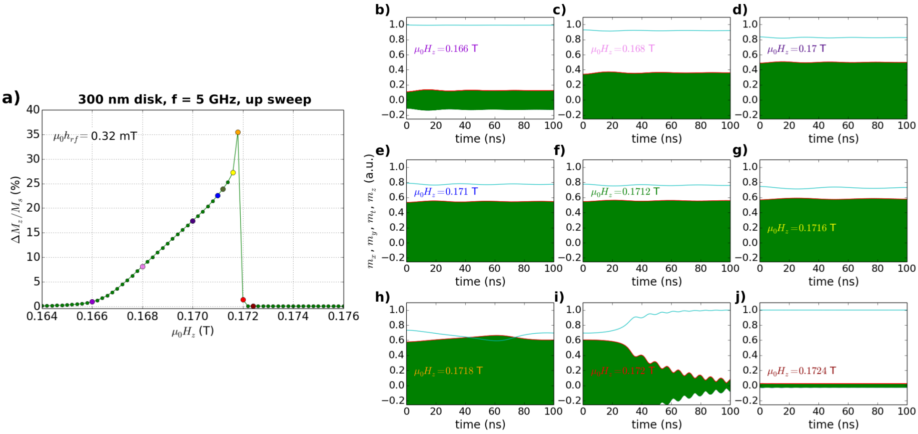

Figure H.4: a) Resonance line in the simulation at $\mu_0 h_{rf} = 0.32$ mT for the 300 nm disk for an up sweep of the static field. b) to j) Time evolution of the normalized average components of the magnetization during the 100 ns simulation at different fields through the resonance line shown in a). The fields from b) to j) correspond in this order to the colored points of the resonance line in a). The longitudinal component is in light blue, the m_x and m_y components in green and the transverse component in red.

For these disks, the saturation of H_{down} observed in some cases from a threshold excitation field is due to the saturation of the precession profile amplitude in the disk. The precession profile does not distort upon increasing excitation, which is attributed to the less inhomogeneous internal field and weaker pinning at the disk periphery, as in larger disks (see the discussion in Figure 5.23). Then with increasing excitation, the resonance condition is still fulfilled but it is no longer possible to increase the amplitude of the precession profile before the downjump. This results in a stagnation of H_{down} or a slight decrease.

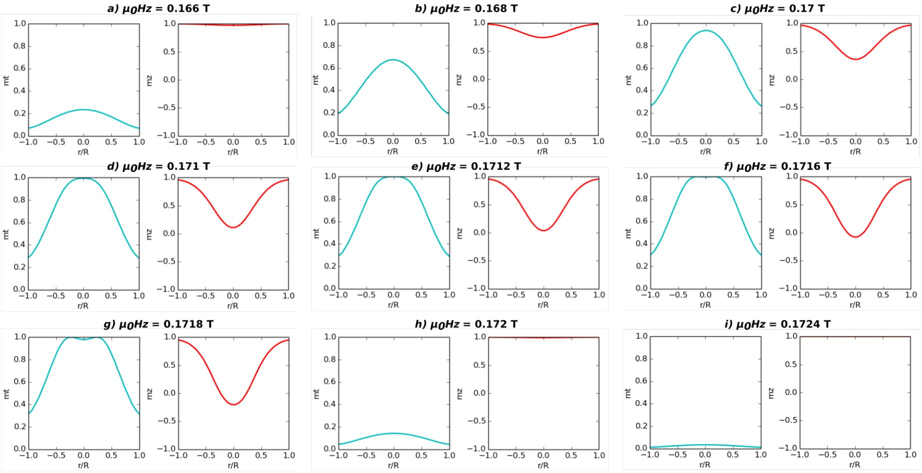

Figure H.5: Snapshots of spatial profiles of the transverse (light blue) and longitudinal (red) normalized magnetizations at the different colored points of the resonance line of Figure H.4 a of the 300 nm disk

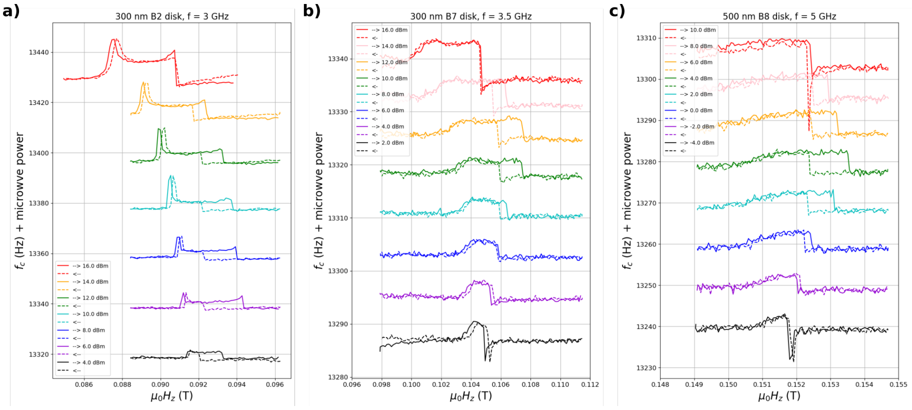

Figure H.6: Measurement of the resonance signal via the variation of the cantilever frequency Δf_c for both field scan directions, as a function of microwave power for a) the 300 nm disk B2 at 3 GHz, b) 300 nm disk B7 at 3.5 GHz and c) 500 nm disk B8 at 5 GHz. In some cases there is evidence of a hysteresis cycle.

H.3 Hysteresis cycles

Using continuous wave excitation and the detection mode of the MRFM where the signal is coded in the cantilever frequency, we could observe hysteresis cycles of nonlinear FMR for the 300 and 500 nm disks as shown in Figure H.6. One notes that for the three disks, at the beginning, the width of the hysteresis cycle increases with the excitation before decreasing beyond a certain threshold. This observation is in agreement with what was sometimes observed in simulation for these sizes of disks 300 and 500 nm with a slight decrease of H_{down} beyond a certain threshold, causing a decrease in the width of the cycle since H_{up} continued on its side to increase.

One can also reveal the hysteresis with the two-tone experiment. This is shown on the data in Figure H.7 for the case of the 300 nm disk B2 at $f_1 = 3.5$ GHz for $P_1 = 6$ dBm and $P_2 =$ -9 dBm. In addition to the spectroscopy maps obtained with $\mathbf{h}_2$ presented on Figures a & b for the two upward and downward sweep of the field, we show on Figures c & d the corresponding variations of the cantilever frequency which correspond to ΔM_1 induced by $\mathbf{h}_1$. Before this experiment, we measured the resonance line with $\mathbf{h}_1$ in the variations of f_c. It is the blue curve of Figures H.7 e & f which clearly shows the hysteresis. The orange curve corresponds to the average of f_c for each field H_z in Figures c and d. One measures the splitting of the Kittel mode into two nutation branches already observed and explained in Chapter 5. But one observes that the field range in which we detect them depends on the scan direction : the spectrum differs between 0.1102 and 0.1118 T for the upward and downward sweep, see Figures a & b; which corresponds exactly to the hysteretic zone, see Figures c, d, e & f.

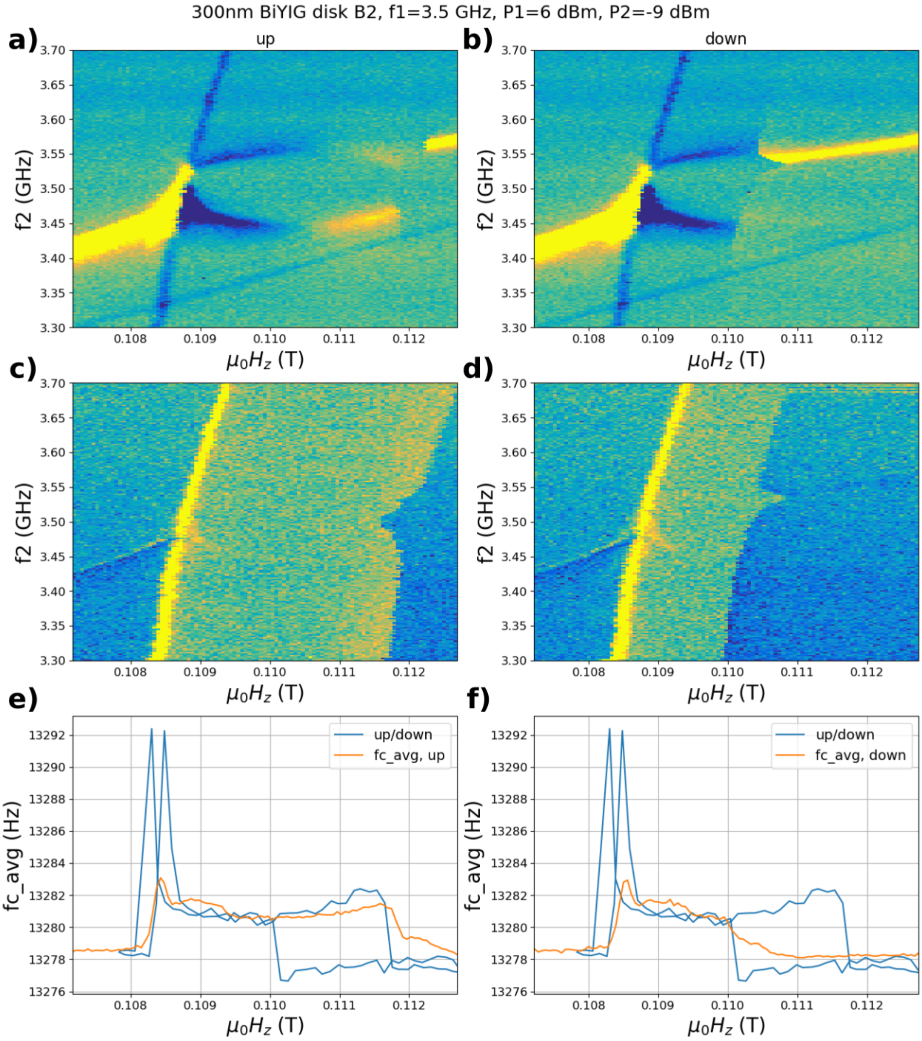

Figure H.7: 500 nm B3

Appendix I

In-plane MRFM spectra of the 30 different disks

Reminder : in the sample design, there are five different disk diameters : 200, 300, 500, 700 and 1000 nm. For each diameter, six distinct disks have been patterned, two of them being located under the microwave antenna (B disks), and four of them being located nearby the antenna.

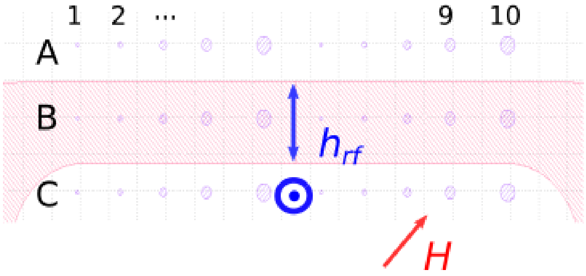

Figure I.1: Different effective excitation fields for disks A and C and disks B for a given microwave power

Figure I.1 reminds an image of the design used to fabricate the sample, already presented in Figure 3.11. The disposition of the sample within the MRFM causes that in this in-plane static field configuration, as shown in the Figure, the static field makes an angle of about 40° with the rf field for the disks B. On the other hand, the two fields are perpendicular for the disks A and C. One understands that for the same microwave power, the effective rf field (the component perpendicular to the static field) is not the same for disks A and C and for disks B. This difference is accentuated by the large difference in damping observed in the out-of-plane measurements, the disks B under the metallic antenna having higher damping than the disks A and C. These elements can explain the differences observed between the spectra.

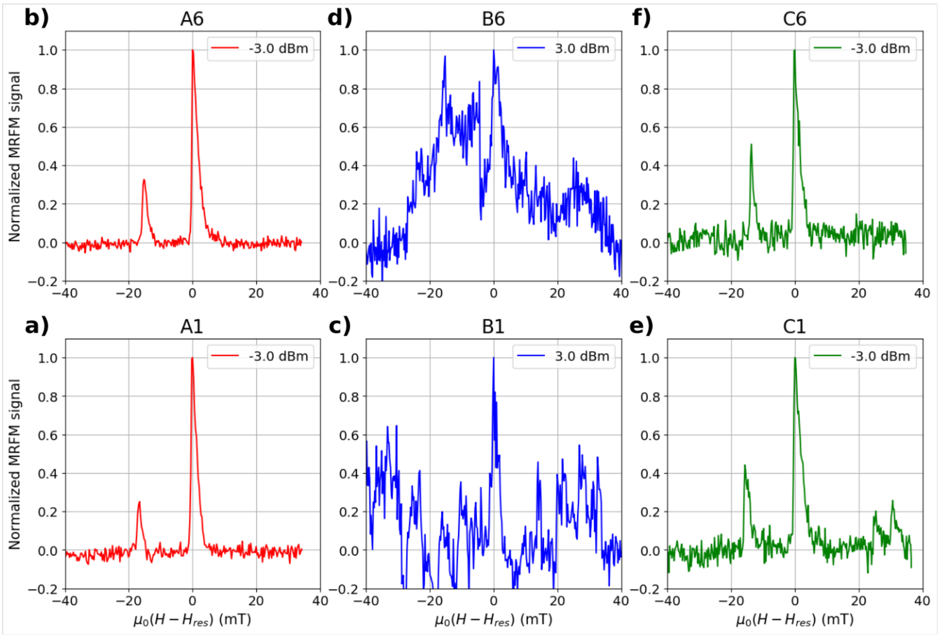

Figure I.2: MRFM spectra of the 200nm diameter disks at f = 5 GHz.

Figure I.3 shows the measured spectra for all the six 300 nm diameter disks. One notes a remarkable reproducibility between disks A and C. The spectra of the disks B are quite different as expected from the differences presented above. Similar results are obtained for all disk sizes, see the other figures.

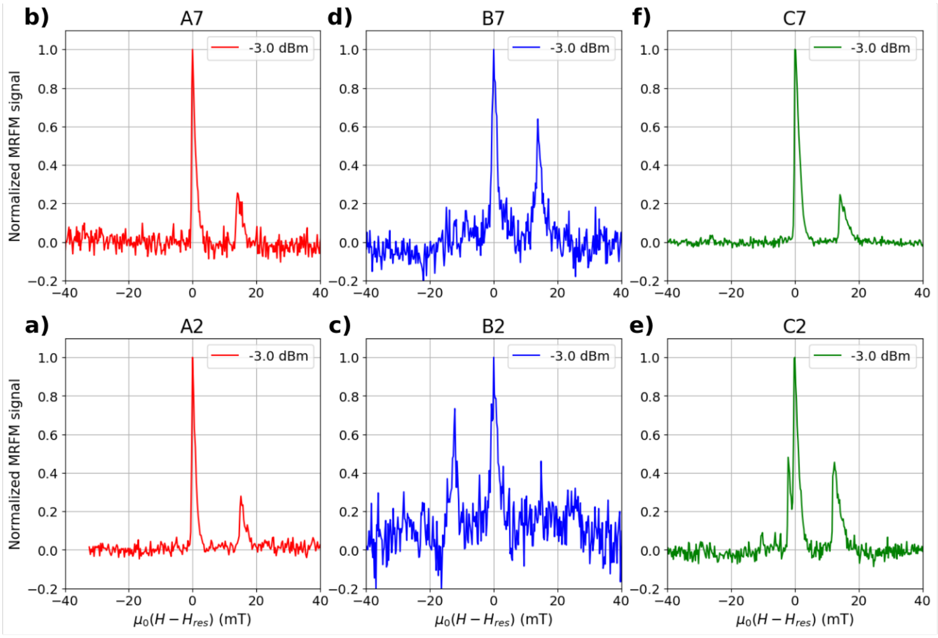

Figure I.3: MRFM spectra of the 300nm diameter disks at f = 5 GHz.

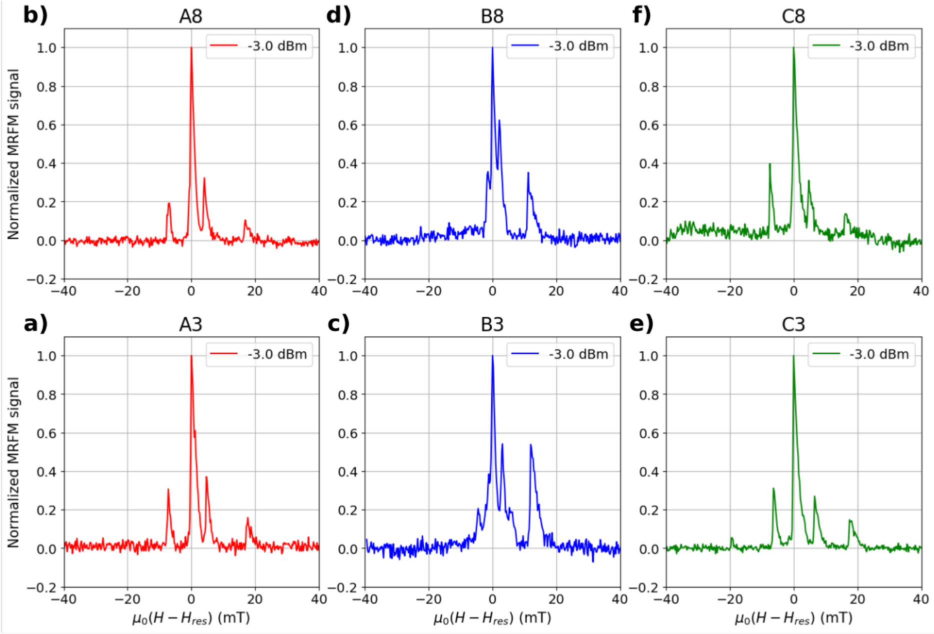

Figure I.4: MRFM spectra of the 500 nm diameter disks at f = 5 GHz.

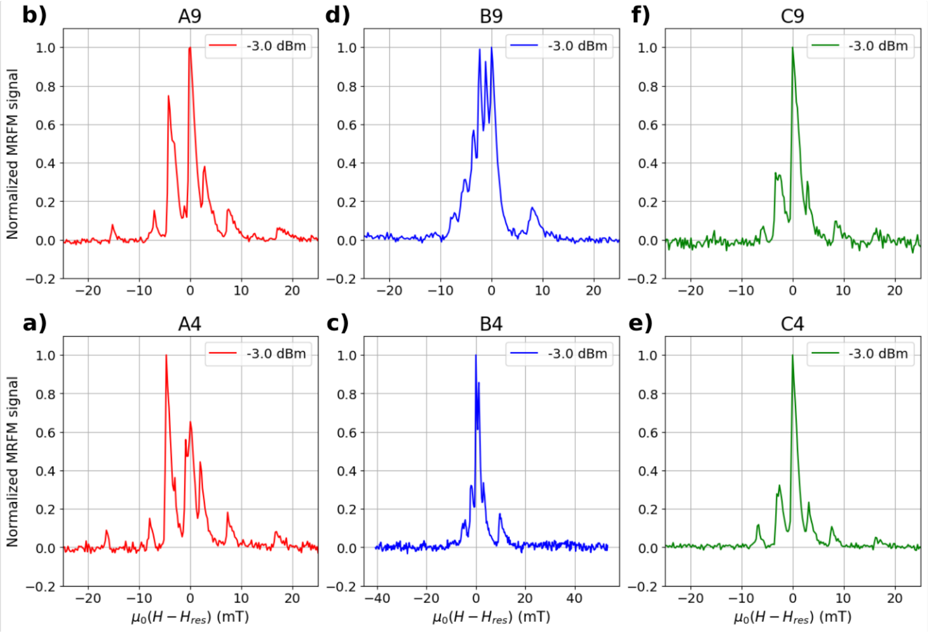

Figure I.5: MRFM spectra of the 700 nm diameter disks at f = 5 GHz.

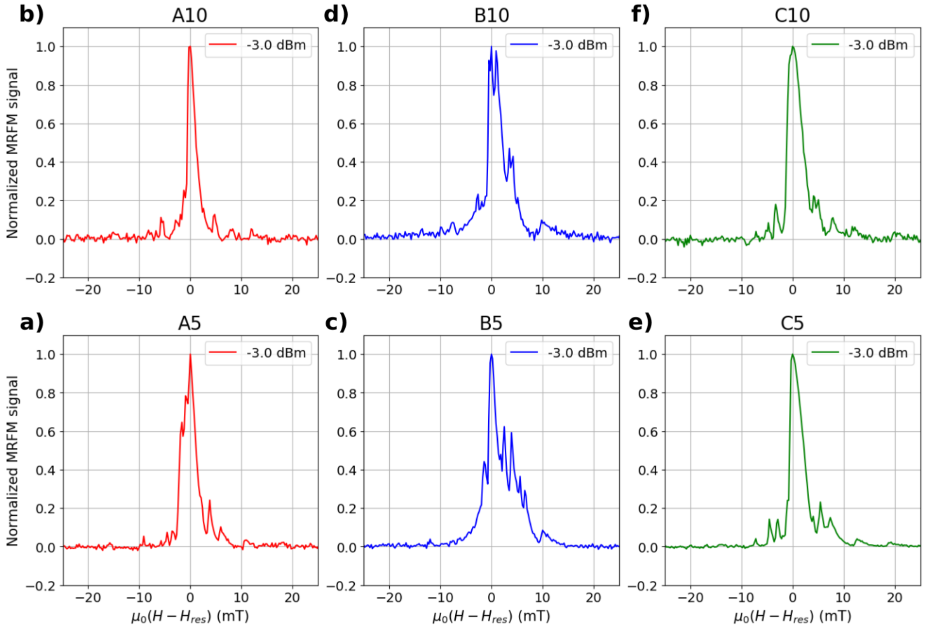

Figure I.6: MRFM spectra of the 1000 nm diameter disks at f = 5 GHz.

Appendix J

Résumé substantiel en français

J.1 Introduction

Dans les matériaux ferromagnétiques, il existe une interaction d'échange forte entre les moments magnétiques qui les aligne. Les excitations de cet état d'équilibre correspondent à des mouvements de précession collective de ces moments appelés ondes de spin ou magnons. Leur étude constitue la branche de la magnonique [3, 4]. Ces excitations peuvent être uniforme, c'est-à-dire de vecteur d'onde nul, ou pas. La physique des ondes de spin est très riche, d'où l'intérêt fondamental de leur étude ; leurs propriétés particulières sont également intéressantes pour de nombreuses applications potentielles. Leur relation de dispersion qui décrit les variations de leur fréquence avec le vecteur d'onde est en effet ajustable à l'aide de plusieurs paramètres : le matériau magnétique utilisé, la forme de l'échantillon étudié, l'amplitude et la direction d'application du champ magnétique statique. Avec des fréquences dans la gamme du GHz et des longueurs d'onde submicroniques elles sont bien adaptées pour du transport et du traitement de l'information et du calcul logique [7]. Elles peuvent par ailleurs transporter de l'information sans déplacement de charges électriques, permettant ainsi de s'affranchir de l'effet Joule, principale limitation de la technologie CMOS (complementary metal oxide semi-conductor) actuelle. Le matériau idéal pour étudier ces ondes de spin est le grenat d'yttrium fer ou YIG ($Y_3Fe_5O_{12}$) [18] en raison de son très faible amortissement magnétique.

À l'heure actuelle il existe un certain nombre d'entraves à la mise en oeuvre de dispositifs à base d'ondes de spin. En raison du caractère non linéaire de la dynamique de l'aimantation qui découle directement de l'équation de Landau-Lifshitz-Gilbert, les ondes de spin deviennent fortement couplées entre elles à forte excitation par des processus d'interaction multi magnons. Une fois le mode uniforme excité, ces processus sont à l'origine d'une redistribution de l'énergie de ce mode vers d'autres modes d'onde spin, ce qui limite l'amplitude de la précession uniforme dans les échantillons macroscopiques[1] à quelques degrés seulement. De tels processus ont été mis en évidence depuis des expériences de résonance ferromagnétique dans les années 50 [36, 12]. Les progrès récents de la nanofabrication offrent la possiblité de discrétiser le spectre d'ondes de spin au sein de nanostructures et par conséquent de limiter voire contrôler ces processus d'interaction multi magnons. La mise en oeuvre de cette discrétisation du spectre d'excitations a permis d'atteindre de grands angles de précession uniforme de l'aimantation dans un nanodisque de YIG de 700 nm de diamètre et 20 nm d'épaisseur [22]. Mais il se produit un décalage non linéaire de la fréquence de résonance ferromagnétique lorsqu'on augmente l'intensité de l'excitation. Il s'agit de l'effet de repliement de la raie de résonance ferromagnétique qui est dû au champ démagnétisant, associé à l'anisotropie de forme de l'échantillon. Il est possible d'ajuster par dopage au Bismuth notamment l'anisotropie effective d'un film de YIG et donc de contrôler cette dépendance non-linéaire de la fréquence de résonance [24]. Ce dopage au Bismuth induit en effet une anisotropie magnétique perpendiculaire qui peut dans les conditions appropriées quasiment compenser l'anisotropie de forme du film [27].

Dans cette thèse, j'ai étudié les régimes fortement non linéaires de la dynamique de l'aimantation dans des nanostructures de BiYIG, la résonance ferromagnétique étant excitée par un champ micro-onde. La combinaison de ces deux stratégies, la nanostructuration d'une part, qui conduit à la quantification du spectre des modes d'onde de spin, et la quasi-compensation de l'anisotropie de forme d'autre part grâce au dopage au Bismuth, qui conduit à un décalage de fréquence non linéaire quasi-nul, est mise en œuvre afin de parvenir à une très grande amplitude de précession cohérente d'un seul mode à fréquence constante lorsqu'on augmente l'intensité du champ micro-onde.

J.2 État d'équilibre

Le magnétisme provient du moment magnétique des éléments qui constituent la matière, en particulier les électrons. Ce moment a une composante orbitale due au mouvement de l'électron autour du noyau et une composante intrinsèque ou spin due à la rotation de l'électron sur lui-même. Dans un matériau, il existe différentes interactions entre les moments magnétiques qui vont définir la nature dia-, para-, ferro- ou ferrimagnétique du matériau.

Dans ce chapitre, on rappelle les principales interactions mises en jeu dans

---

[1] De taille supérieure à la dizaine de microns.

un matériau ferromagnétique, à savoir les interactions Zeeman, d'échange, dipolaire et d'anisotropie. On insiste sur les deux principales interactions d'anisotropie présentes dans les films minces de BiYIG à l'origine des nanodisques étudiés, l'anisotropie démagnétisante associée à la forme du film et l'anisotropie magnétique perpendiculaire ou anisotropie magnétique uniaxiale induite par le dopage au Bismuth. Ensuite, on étudie le cas d'un tel film aimanté par un champ statique faisant un certain angle avec la normale au film, l'objectif étant de trouver l'état d'équilibre de l'aimantation. Cette étude permet d'introduire un nouveau paramètre caractéristique du film, l'aimantation effective définie comme la différence entre l'aimantation et le champ d'anisotropie magnétique perpendiculaire. On trouve en effet que l'énergie totale du film mince ne dépend plus seulement de l'aimantation mais aussi de l'aimantation effective. On peut ainsi modifier l'état d'équilibre en jouant sur la valeur et/ou le signe de l'aimantation effective, c'est-à-dire sur l'anisotropie magnétique perpendiculaire. Cette aimantation effective s'avérera cruciale pour l'analyse et l'interprétation des résultats expérimentaux.

J.3 Dynamique de l'aimantation

Après le premier chapitre où l'état d'équilibre d'un film magnétique a été déterminé, résultat de la compétition entre les différentes interactions magnétiques, il est question ici de déterminer le mouvement de l'aimantation en cas de perturbation de cet état d'équilibre. On trouve que ce mouvement correspond à une précession de l'aimantation autour de sa position d'équilibre, amortie en raison des processus de dissipation de l'énergie du système de spin vers d'autres degrés de liberté transportant du moment angulaire tel que les phonons et les électrons de conduction dans le cas d'un métal. Une résolution analytique de l'équation de la dynamique permet de déduire la fréquence de résonance du mode uniforme dans les deux cas d'un film mince à anisotropie perpendiculaire (cas du BiYIG) aimanté perpendiculairement et dans le plan, fréquence qui est donnée par la formule de Kittel [49]. On trouve sans surprise que cette fréquence dépend désormais de l'aimantation effetive, contrairement au cas d'un film mince sans anisotropie perpendiculaire (cas du YIG) où elle ne dépend que de l'aimantation.

La théorie générale du spectre linéaire des ondes de spin [38, 51] nous renseigne sur le résultat attendu lors de la mesure du spectre de résonance ferromagnétique d'un échantillon à l'aide d'un champ d'excitation micro-onde, à savoir une succession de pics de résonance correspondant aux différents modes d'onde de spin. Les fréquences propres dépendent des profils des modes, les largeurs de raie dépendent du paramètre d'amortissement du matériau et les amplitudes sont données par l'intégrale de recouvrement entre le champ d'excitation et les profils des modes. Par conséquent, l'analyse fine des spectres mesurés peut permettre de remontrer à des informations sur les profils des modes et l'amortissement magnétique.

Dans un film mince aimanté perperpendiculairement, le profil du champ interne directement donné par celui du champ démagnétisant est uniforme. Il s'en suit que le mode de précession est d'amplitude spatialement uniforme lorsqu'on l'excite. Par contre dans un nanodisque aimanté perpendiculairement, le champ démagnétisant devient non uniforme à cause des effets de taille finie. Le mode de précession fondamental devient lui aussi d'amplitude spatialement non uniforme, l'amplitude étant maximale au centre et diminuant lorsqu'on se rapproche des bords du disque. Plus généralement, l'utilisation de la théorie précédente permet de trouver les modes propres du disque qu'on peut décrire à l'aide de deux indices. Un indice radial n qui donne le nombre de fois où la phase de la précession change au sein du disque dans la direction radiale et un indice azimutal qui donne ce même nombre dans la direction azimutale. Ces modes sont bien décrits par les fonctions de Bessel représentées à la Figure 2.5. Par exemple, le mode fondamental (l=0,n=0) bien qu'étant d'amplitude spatialement non uniforme est de phase uniforme. On y fera référence dans la suite avec différentes appelations : mode uniforme, mode principal, mode FMR ou mode de Kittel. On a aussi le mode (l=0,n=1) pour lequel la région centrale et la périphérie précessent en opposition de phase (voir Figure 2.5). Avec un champ micro-onde uniforme, on ne peut exciter que les modes d'indice azimutal $l = 0$, l'intégrale de recouvrement entre un tel champ d'excitation uniforme et chacun des modes d'indice $l \neq 0$ étant égal à 0. Ce profil non uniforme du champ démagnétisant dû aux effets de taille finie est également à l'origine de l'augmentation de la fréquence du mode uniforme lorsque la taille du disque diminue[2] (voir Figure 2.6).

Quelques effets non linéaires qui apparaissent lorsqu'on augmente l'intensité du champ micro-onde excitateur sont présentés. L'effet de repliement de la raie de résonance est notamment présenté en détails dans le cas d'un film mince aimanté perpendiculairement. À faible excitation, la fréquence de résonance dépend de l'aimantation[3] et la raie de résonance est lorentzienne. À forte excitation, la diminution de l'aimantation longitudinale n'est plus négligeable et sa rétroaction sur la fréquence de résonance entraîne un décalage de cette

---

[2] Auquel il faut rajouter la contribution de l'interaction d'échange dans les disques plus petits (de diamètre $<$ 500 nm).

[3] À faible excitation, l'angle de précession est faible, la diminution de l'aimantation longitudinale est faible et l'aimantation longitudinale reste sensiblement égale à l'aimantation.

fréquence à l'origine de la déformation de raie lorentzienne. La résolution analytique détaillée montre comme attendu que le sens de décalage de la raie dépend directement du signe de l'aimantation effective (voir Figure 2.8) tandis que l'amplitude du décalage dépend de sa valeur. Autrement dit pour une aimantation effective nulle, il n'y a pas de décalage de la raie de résonance.

L'étude de la stabilité de la précession de grande amplitude mesurée précédemment dans le nanodisque de YIG de 700 nm d'épaisseur en appliquant deux champs micro-onde a mis en évidence un mouvement de nutation de l'aimantation : une combinaison du mouvement périodique cohérent de grande amplitude (**P**-mode) de fréquence dans la gamme du GHz et de petites oscillations de fréquence de l'ordre d'une fraction de GHz (voir Figure 2.10) [22].

Après cet effet non linéaire de repliement de la raie de résonance décrit pour le mode uniforme seul, d'autres effets mettant en œuvre des interactions entre différents modes d'onde de spin sont brièvement présentés : la résonance subsidiaire et la saturation prématurée de la résonance. Ils s'expliquent tous deux par des processus de Suhl dans lesquels un ou plusieurs magnons uniformes se couplent à des magnons paramétriques de vecteurs d'onde non nuls via des processus multi magnons. L'atteinte de grands angles de précession dans le nanodisque de YIG est notamment due à l'augmentation de plus d'un ordre de grandeur (en champ d'excitation) du seuil d'apparition de ces processus de Suhl par rapport aux structures étendues de YIG [67], cela en raison de la discrétisation du spectre d'ondes de spin.

Ce chapitre s'achève par une mini revue bibliographique d'effets non linéaires apparaissant à plus forte excitation de la dynamique de l'aimantation tels que les auto-oscillations[4], le doublement de période, le chaos. On introduit également des solitons magnétiques qui sont des modes d'onde de spin non linéaires qui se forment à forte excitation et qui peuvent se stabiliser sous certaines conditions. On présente les cas des "bullets" et des "droplets" qui peuvent se former dans des films minces.

J.4 Méthodes : dispositif expérimental et échantillon

La dynamique de l'aimantation est étudiée dans les nanodisques à l'aide d'un microscope de force à résonance magnétique (MRFM). Il repose sur l'idée d'une détection mécanique de la dynamique. Le détecteur est un microlevier très

---

[4] Qui sont des oscillations dans la gamme 10^4-10^6 Hz qui proviennent du couplage entre modes d'onde de spin micro-onde (10^{10} Hz).

souple à l'extrémité duquel est fixée une sonde magnétique, une nanosphère de Cobalt de 500 nm de diamètre. Une fois positionée au-dessus d'un disque, il se produit une interaction entre la sonde et le disque. Lorsqu'on excite la dynamique dans le disque, on mesure la moyenne spatiale de la diminution de l'aimantation longitudinale en mesurant la variation de l'amplitude de vibrations du levier à l'aide d'une détection optique. Cette technique est très sensible et permet de mesurer des angles moyens de précession de l'aimantation très faibles, mais n'a ni de résolution temporelle[5] ni de résolution spatiale[6].

Une description brève de la mise en œuvre du dispositif expérimental est faite en mentionnant l'importance des tubes piézoélectriques qui permettent de déplacer l'échantillon. L'ensemble est placé dans une chambre à vide, à une pression d'environ 10^{-5} à 10^{-6} mbar qui permet de gagner plusieurs ordres de grandeur sur le facteur de qualité du levier. Une boucle de verouillage de phase donne un accès en temps réel à la fréquence de résonance du levier. Pour la mesure du signal de résonance, l'excitation micro-onde est très souvent modulée[7] à la fréquence de résonance du levier, ce qui permet d'amplifier le signal par le facteur de qualité du levier de l'odre de 2000 sous vide. Une calibration de la sonde de nanosphère de Cobalt, utilisée pour la première fois durant cette thèse a été faite et a permis de déduire son aimantation.

L'échantillon consiste en des nanodisques de BiYIG. Il a été fabriqué à l'UMR CNRS-Thales par Abdelmadjid Anane, Hugo Merbouche et Diane Gouéré. Le film mince de Bi_1Y_2IG de 30 nm d'épaisseur est obtenu par croissance par ablation laser pulsé d'une cible sur un substrat approprié, le sGGG (grenat de gallium et de gadolinium subsititué). Un bout de ce film a été utilisé pour des mesures de caractérisations qui ont permis notamment de déduire son aimantation effective, légèrement négative, ce qui signifie que le film est à anisotropie effective perpendiculaire. Le reste du film a servi à la nanofabrication. Les nanodisques sont de diamètres 200, 300, 500, 700 et 1000 nm. Une antenne micro-onde est intégrée au cours de la nanofabrication pour générer le champ d'excitation par passage d'un courant rf. Selon la localisation des disques, le champ rf peut être perpendiculaire ou dans le plan et quant au champ statique, on peut choisir de l'appliquer perpendiculairement ou dans le plan des disques (voir Figure 3.11).

Enfin une étude détaillée de l'influence de la sonde sur les mesures expéri-

---

[5] La fréquence du levier est 13 kHz, soit une constante de temps de l'ordre de la centaine de μs.

[6] La taille de la sonde (500 nm de diamètre) est du même ordre que celle des disques étudiés de diamètres allant de 200 nm à 1000 nm.

[7] On utilise une excitation continue lorsque le signal est suffisant grand pour se passer de la modulation.

mentales a été menée. Il en ressort que ses principaux effets sur les paramètres spectraux des disques sont un décalage du champ de résonance du fait de son champ de fuite statique et un élargissement de la raie de résonance du fait de son champ de fuite dynamique en raison des oscillations du levier mécanique. Il est alors possible de corriger les mesures expérimentales pour déduire les champ de résonance et largeur de raie intrinsèques[8]. Pour les grands disques (diamètre $\geq$ 500 nm), des mesures expérimentales nous donnent directement accès au champ de résonance intrinsèque[9]. Ces résultats sont en excellent accord avec les résultats obtenus en utilisant le modèle de correction du champ de fuite, ce qui valide ce modèle.

J.5 Spectroscopie linéaire de nanodisques de BiYIG

Une étude spectroscopique détaillée dans le régime linéaire est faite pour tous les disques aimantés perpendiculairement. Pour des disques situés sous l'antenne, le champ d'excitation est uniforme et on excite que des modes d'indice azimutal l=0. Sans surprise l'écart entre les modes augmente lorsque la taille du disque diminue, du fait du confinement. On trouve que tous les disques ont un champ caractéristique[10] légèrement négatif comme l'aimantation effective, ce qui signifie qu'ils sont tous à anisotropie effective perpendiculaire comme l'était le film mince. Par contre on note que les amplitudes relatives des modes d'ordre supérieur ($n \geq$1) sont très faibles (voir Figures 4.1 a-e) comparées notamment aux résultats de simples simulations micromagnétiques (voir Figures 4.4 c & d) dans lesquelles sont directement introduits les paramètres magnétiques déduits expérimentalement. De même la position du mode uniforme n'est pas reproduite. Les caractéristiques spectrales dépendant des profils des modes, ces constats nous ont naturellement conduit à formuler une hypothèse d'une déviation des profils réels des modes d'onde de spin par rapport aux fonctions de Bessel. Une telle déviation proviendrait forcément d'une modification du profil du champ interne dans le disque qui peut être due

---

[8] C'est-à-dire sans influence de la sonde.

[9] Dans des conditions où la sonde est très loin des disques de sorte que son champ de fuite sur ceux-ci soit quasiment nul.

[10] Le champ caractéristique est ici l'équivalent de l'aimantation effective du film mince pour le disque de BiYIG. Il corrige l'aimantation effective par la prise en compte des effets de tailles finie.

à une modulation spatiale de l'anisotropie magnétique[11]. Une telle modulation spatiale de l'anisotropie permet finalement de mieux reproduire le spectre expérimental, à la fois la position du mode uniforme et les amplitudes relatives des modes (n ≥1) (voir Figure 4.8 c). Les mesures de l'amortissement magnétique montrent une augmentation sensible de sa valeur pour les disques sous l'antenne micro-onde comparée aux autres disques. Nous l'avons attribué à des effets de pompage de spin latéral aux bords de ces disques où ils sont en contact avec l'antenne.

J.6 Instabilités dynamiques induites par la FMR dans les nanodisques aimantés hors du plan

Dans ce chapitre, on mesure le mode uniforme des différents disques aimantés perpendiculairement en augmentant l'intensité du champ micro-onde excitateur. On observe dans un premier temps le repliement de la raie de résonance avec comme attendu un faible décalage vers les hauts champs en raison de l'aimantation effective légèrement négative, comportement opposé à celui du nanodisque de YIG dans lequel le décalage était très fort et vers les bas champs, l'aimantation effective se réduisant dans ce cas à l'aimantation (pas d'anitropie magnétique perpendiculaire)[12]. Mais à plus forte excitation, très vite au-delà du seuil de repliement, la raie de résonance se fractionne, puis s'aplatit et sature en amplitude (voir Figures 5.1 & 5.2). Les simulations micromagnétiques utilisant les paramètres déduits des résultats expérimentaux et la taille nominale des disques reproduisent assez bien qualitativement ces résultats inattendus et confirment une saturation précoce de l'amplitude à des angles moyens de précession de l'aimantation inférieurs à 20° pour le disque de 700 nm de diamètre (voir Figure 5.6) et même moins pour le disque de 1000 nm de diamètre. L'analyse de l'évolution temporelle dans la simulation montre qu'une instabilité dynamique est reponsable de cette saturation précoce. Celle-ci correspond à une auto-modulation du profil de précession qui se localise très fortement au centre du disque avant d'osciller temporellement entre différents modes d'onde de spin du disque (voir Figures 5.11 & 5.12). Cette oscillation peut se faire de façon quasi-périodique ou chaotique en fonction du réglage fin des paramètres

---

[11] Une variation globale de l'anisotropie a pour seul effet de décaler le spectre de résonance, voir Figure 4.8 b.

[12] L'aimantation effective du film de BiYIG utilisé est négative et vaut 6% de la valeur de l'aimantation.

de contrôle, définissant ainsi des régimes de quasi-périodicité ou de chaos de la dynamique de l'aimantation (voir Figure 5.9). Nous attribuons l'apparition de cette instabilité au champ dipolaire dynamique non uniforme créé par la précession de très grande amplitude localisée au centre du disque susceptible d'avoir la symétrie appropriée pour exciter d'autres modes (voir Figure 5.13). Afin de sonder expérimentalement cette dynamique complexe, une spectroscopie à deux tons est mise en œuvre. Cette dernière révèle des spectres de modulation en fréquence (voir Figure 5.18 c) similaires aux résultats des simulations (voir Figure 5.14 b) et reflétant par conséquent la richesse des variations temporelles de la dynamique de l'aimantation au-delà du seuil d'instabilité.

L'étude comparative des deux cas du disque de YIG étudié avant ma thèse [22] et du disque BiYIG étudié ici, tous deux de 700 nm de diamètre, permet de comprendre l'origine de la dynamique fortement non linéaire différente qui s'explique dans les deux cas par la rétroaction du mode de précession spatialement non uniforme sur le champ interne. Dans le cas du YIG, le coefficient non linéaire[13] est positif et cette action tend à uniformiser le champ interne (voir Figure 5.21 b), il en résulte une extension spatiale du profil de précession lorsque l'amplitude de précession augmente (voir Figures 5.22 d & f) ce qui permet d'atteindre de grands angles de précession[14] (voir Figure 5.22 b). Par contre dans le cas du BiYIG, le coefficient non linéaire est négatif et cette action tend à non-uniformiser davantage le champ interne (voir Figure 5.21 d), il en résulte une localisation spatiale du profil de précession lorsque l'amplitude de précession augmente (voir Figures 5.22 c & e), ce qui conduit à la formation de l'instabilité dynamique responsable de la saturation précoce de l'amplitude du signal de résonance (voir Figure 5.22 a). Dans les plus petits disques (diamètres < 500 nm), les variations du champ interne entre le centre et la périphérie sont plus faibles que dans les grands disques. Il en résulte un profil de précession linéaire moins localisé au centre (voir Figure 5.23), ce qui le rend plus robuste temporellement et empêche le développement de l'instabilité dynamique en dépit de la localisation.

Même en fixant une aimantation effective quasi nulle dans la simulation, la raie de résonance finit par se déformer à forte excitation. Cela est dû à la géométrie non-ellipsoïdale[15] des nanostructures (des disques), qui induit un champ interne non uniforme et par conséquent un mode de précession spatialement non unifome en amplitude dès le régime linéaire.

---

[13] Coefficient qui donne le décalage non linéaire de la fréquence de résonance lorsqu'on augmente l'excitation. Il dépend de l'aimantation dans le cas du YIG et de l'aimantation effective dans le cas du BiYIG.

[14] Suivie par des instabilités d'ondes de spin à plus grande amplitude.

[15] Dans un ellipsoïde le champ interne est uniforme.

Des simulations micromagnétiques complémentaires pour différentes valeurs de l'anisotropie magnétique perpendiculaire et donc de l'aimantation effective ont été faites pour le disque de diamètre 700 nm. On trouve que plus l'anisotropie perpendiculaire est élevée (plus l'aimantation effective est négative) plus on peut localiser des solitons[16] au sein du disque dont les oscillations temporelles induisent une dynamique turbulente à forte excitation. Pour un champ d'anisotropie légèrement supérieur à l'aimantation (aimantation effective légèrement négative) on a le cas étudié expérimentalement avec la formation de l'instabilité dynamique décrite plus précédemment. Ensuite pour un champ d'anisotropie plus faible que l'aimantation (aimantation effective positive) il y a formation à grande amplitude de précession d'instabilités d'ondes de spin. Le seuil d'apparition des instabilités est d'autant plus faible que l'anisotropie perpendiculaire est élevée (que l'aimantation effective est négative). L'ensemble des résultats expérimentaux et des simulations ont permis d'esquisser les diagrammes de phase des Figures 5.24 b et 5.25.

J.7 Résonance ferromagnétique des nanodisques en configuration planaire

Le passage à un champ statique dans le plan des disques donne des résultats intéressants. Les spectres de résonance sont plus complexes que dans le cas d'un champ perpendiculaire en raison de la brisure de la symétrie cylindrique (voir Figures 6.1 et 6.2). La densité de modes d'onde de spin est élevée dans les grands disques. Dans le régime non linéaire, le repliement de la raie de résonance se fait à présent vers les bas champs (voir Figure 6.4) en raison du changement de signe du coefficient non linéaire dû au passage au champ dans le plan. Ce changement permet d'atteindre dans cette configuration des angles moyens de précession dans les grands disques plus importants que dans le cas perpendiculaire, notamment de l'ordre de 50° dans le disque de 700 nm de diamètre. Mais en raison de la forte densité de modes, différents modes d'onde de spin contribuent à l'atteinte de tels angles de précession, il n'est pas possible d'exciter un seul mode. Dans le plus petit disque de 200 nm de diamètre, le confinement plus drastique du spectre d'excitation permet d'atteindre en excitant un seul mode de très grands angles d'une précession cohérente de l'aimantation avec une quasi-suppression de l'aimantation longitudinale, sans apparition d'instabilités d'ondes de spin au-delà d'une certaine

---

[16] On appelle soliton ici le profil de précession d'aimantation longitudinale très fortement localisé au centre du disque.

amplitude comme dans le cas du disque de YIG de 700 nm de diamètre aimanté perpendiculairement.

J.8 Conclusions & perspectives

Dans cette thèse, nous avons étudié les régimes non linéaires de la dynamique de l'aimantation dans des nanodisques de BiYIG en utilisant un microscope de force à résonance magnétique. Une étude spectroscopique linéaire préalable a permis de vérifier que tous les disques sont à anisotropie effective perpendiculaire comme le film mince d'aimantation effective légèrement négative. Dans le régime non linéaire on observe une saturation précoce de l'amplitude du pic de résonance du mode principal dans les grands disques aimantés hors du plan. Cette saturation est due à la formation d'une instabilité dynamique identifiée à l'aide de simulations micromagnétiques qui reproduisent bien les résultats expérimentaux. Cette instabilité est mise en évidence expérimentalement à l'aide de mesures à deux excitations micro-onde qui donnent des spectres de modulation de fréquence similaires aux spectres de fréquences de cette instabilité extraits des simulations. Les résultats obtenus dans les plus petits disques ont permis d'identifier les éléments clés nécessaires à la formation de cette instabilité. Il s'agit du signe du coefficient non-linéaire donné par le signe de l'aimantation effective, et le profil non uniforme du champ interne dans le disque.

Une analyse mathématique détaillée des traces temporelles simulées des composantes moyennes de l'aimantation permettrait de caractériser de façon appropriée les régimes quasi-périodique et chaotique de la dynmaique de l'aimantation au-delà du seuil d'apparition de l'instabilité. Des techniques d'analyse plus récentes combinant méthodes analytiques et simulations micromagnétiques permettraient d'estimer les interactions entre différents modes d'onde de spin mises en jeu lors de la formation de l'instabilité dynamique. Des résultats expérimentaux supplémentaires laissent penser à des processus de doublement de période au sein des nanodisques qu'il faudrait étudier plus finement, de tels processus étant caractéristiques de sytèmes dynamiques exhibant du chaos.

Scientific contributions

Poster

1. **International French-US Workshop on Nanoelectronics**(NYU Paris and C2N) - *Ferromagnetic resonance spectroscopy of BiYIG nanodisks* - 25/09/2019 to 27/09/2019
2. **European School on Magnetism ESM** (online) - *Ferromagnetic resonance spectroscopy of BiYIG nanodisks* - 28/09/2020 to 02/10/2020
3. **Trends in MAGnetism TMAG** (Venice) - *Dynamic instability in high power FMR of a BiYIG nanodisk* - 04/09/2022 to 09/09/2022

Oral contributions

1. **Joint European Magnetic Symposia JEMS** (online) - *Magnetization dynamics of Bi-doped YIG nanodisks* - 07/12/2020 to 11/12/2020
2. **International Magnetic Conference INTERMAG** (online) - *Strongly nonlinear FMR of BiYIG nanodisks* - 26/04/2021 au 30/04/2021
3. **Oxyjeunes** (one week work/break organized by the lab at Les Houches school of physics for the PhD students of the lab) - *Strongly nonlinear FMR of BiYIG nanodisks* - 14/06/2021 to 18/06/2021
4. **International Magnetic Conference INTERMAG** (online) - *Dynamic instabilitiy in high power FMR of BiYIG nanodisks* - 10/01/2022 to 14/01/2022
5. **Colloque Louis Néel XX** (Obernai) - *Dynamic instability in high power FMR of a BiYIG nanodisk* - 28/06/2022 to 01/07/2022

Papers

1. *Spin-wave spectroscopy of BiYIG nanodisks: influence of nanofabrication on magnetic parameters* (to be submitted) - I. Ngouagnia, D. Gouéré, H. Merbouche, T. Srivastava, V. V. Naletov, H. Hurdequint, V. Cros, M. Muñoz, S.Sangiao, J. M. de Teresa, O. Klein, A. Anane, G. de Loubens

2. *Dynamic instabilitiy in high power FMR of BiYIG nanodisks* (in preparation) - I. Ngouagnia, et al.

3. *Resonant dynamics of skyrmion lattices in thin film multilayers: Localised modes and spin wave emission* (submitted to Nature Communications) - T. Srivastava, Y. Sassi, F. Ajejas, A. Vecchiola, I. Ngouagnia, H. Hurdequint, K. Bouzehouane, N. Reyren, V. Cros, T. Devolder, J.-V. Kim, G. de Loubens

4. *Complete identification of spin-wave eigenmodes excited by parametric pumping in YIG microdisks* (to be submitted) - T. Srivastava, H. Merbouche, I. Ngouagnia, V. E. Demidov, S. O. Demokritov, M. Muñoz, J. Ben Youssef, M. d'Aquino, A. Anane, G. de Loubens

Bibliography

[1] F. Bloch. Zur Theorie des Ferromagnetismus. *Zeitschrift für Physik*, 61(3):206–219, March 1930.

[2] Alexander G. Gurevich and Gennadii A. Melkov. *Magnetization Oscillations and Waves.* CRC Press, September 1996. Google-Books-ID: YgQtSvFIvFQC.

[3] V V Kruglyak, S O Demokritov, and D Grundler. Magnonics. *Journal of Physics D: Applied Physics*, 43(26):264001, July 2010.

[4] A. V. Chumak, V. I. Vasyuchka, A. A. Serga, and B. Hillebrands. Magnon spintronics. *Nature Physics*, 11(6):453–461, June 2015.

[5] Anjan Barman, Gianluca Gubbiotti, S Ladak, A O Adeyeye, M Krawczyk, J Gräfe, C Adelmann, S Cotofana, A Naeemi, V I Vasyuchka, B Hillebrands, S A Nikitov, H Yu, D Grundler, A V Sadovnikov, A A Grachev, S E Sheshukova, J-Y Duquesne, M Marangolo, G Csaba, W Porod, V E Demidov, S Urazhdin, S O Demokritov, E Albisetti, D Petti, R Bertacco, H Schultheiss, V V Kruglyak, V D Poimanov, S Sahoo, J Sinha, H Yang, M Münzenberg, T Moriyama, S Mizukami, P Landeros, R A Gallardo, G Carlotti, J-V Kim, R L Stamps, R E Camley, B Rana, Y Otani, W Yu, T Yu, G E W Bauer, C Back, G S Uhrig, O V Dobrovolskiy, B Budinska, H Qin, S van Dijken, A V Chumak, A Khitun, D E Nikonov, I A Young, B W Zingsem, and M Winklhofer. The 2021 Magnonics Roadmap. *Journal of Physics: Condensed Matter*, 33(41):413001, October 2021.

[6] A A Serga, A V Chumak, and B Hillebrands. YIG magnonics. *Journal of Physics D: Applied Physics*, 43(26):264002, July 2010.

[7] Abdulqader Mahmoud, Florin Ciubotaru, Frederic Vanderveken, Andrii V. Chumak, Said Hamdioui, Christoph Adelmann, and Sorin Coto-

fana. Introduction to spin wave computing. *Journal of Applied Physics*, 128(16):161101, October 2020.

[8] Dany Lachance-Quirion, Yutaka Tabuchi, Arnaud Gloppe, Koji Usami, and Yasunobu Nakamura. Hybrid quantum systems based on magnonics. *Applied Physics Express*, 12(7):070101, June 2019. Publisher: IOP Publishing.

[9] M. Chen, C.E. Patton, G. Srinivasan, and Y.T. Zhang. Ferromagnetic resonance foldover and spin-wave instability in single-crystal YIG films. *IEEE Transactions on Magnetics*, 25(5):3485–3487, September 1989. Conference Name: IEEE Transactions on Magnetics.

[10] Y. S. Gui, A. Wirthmann, and C.-M. Hu. Foldover ferromagnetic resonance and damping in permalloy microstrips. *Physical Review B*, 80(18):184422, November 2009. Publisher: American Physical Society.

[11] A. M. Kosevich, B. A. Ivanov, and A. S. Kovalev. Magnetic Solitons. *Physics Reports*, 194(3):117–238, October 1990.

[12] H. Suhl. The theory of ferromagnetic resonance at high signal powers. *Journal of Physics and Chemistry of Solids*, 1(4):209–227, January 1957.

[13] F. B. Mancoff, N. D. Rizzo, B. N. Engel, and S. Tehrani. Phase-locking in double-point-contact spin-transfer devices. *Nature*, 437(7057):393–395, September 2005.

[14] B. Van Waeyenberge, A. Puzic, H. Stoll, K. W. Chou, T. Tyliszczak, R. Hertel, M. Fähnle, H. Brückl, K. Rott, G. Reiss, I. Neudecker, D. Weiss, C. H. Back, and G. Schütz. Magnetic vortex core reversal by excitation with short bursts of an alternating field. *Nature*, 444(7118):461–464, November 2006.

[15] Konstantin Yu. Guslienko, Ki-Suk Lee, and Sang-Koog Kim. Dynamic Origin of Vortex Core Switching in Soft Magnetic Nanodots. *Physical Review Letters*, 100(2):027203, January 2008. Publisher: American Physical Society.

[16] Philip E. Wigen. *Nonlinear Phenomena and Chaos in Magnetic Materials*. World Scientific, 1994. Google-Books-ID: ghS4BJYL7rUC.

[17] S.M. Rezende and F.M. de Aguiar. Spin-wave instabilities, auto-oscillations, and chaos in yttrium-iron-garnet. *Proceedings of the IEEE*, 78(6):893–908, June 1990. Conference Name: Proceedings of the IEEE.

[18] E. G. Spencer, R. C. LeCraw, and A. M. Clogston. Low-Temperature Line-Width Maximum in Yttrium Iron Garnet. *Physical Review Letters*, 3(1):32–33, July 1959. Publisher: American Physical Society.

[19] O. d'Allivy Kelly, A. Anane, R. Bernard, J. Ben Youssef, C. Hahn, A H. Molpeceres, C. Carrétéro, E. Jacquet, C. Deranlot, P. Bortolotti, R. Lebourgeois, J.-C. Mage, G. de Loubens, O. Klein, V. Cros, and A. Fert. Inverse spin Hall effect in nanometer-thick yttrium iron garnet/Pt system. *Applied Physics Letters*, 103(8):082408, August 2013.

[20] Nathan Beaulieu, Nelly Kervarec, Nicolas Thiery, Olivier Klein, Vladimir Naletov, Hervé Hurdequint, Grégoire de Loubens, Jamal Ben Youssef, and Nicolas Vukadinovic. Temperature Dependence of Magnetic Properties of a Ultrathin Yttrium-Iron Garnet Film Grown by Liquid Phase Epitaxy: Effect of a Pt Overlayer. *IEEE Magnetics Letters*, 9:1–5, 2018. Conference Name: IEEE Magnetics Letters.

[21] C. Hahn, V. V. Naletov, G. de Loubens, O. Klein, O. d'Allivy Kelly, A. Anane, R. Bernard, E. Jacquet, P. Bortolotti, V. Cros, J. L. Prieto, and M. Muñoz. Measurement of the intrinsic damping constant in individual nanodisks of Y3Fe5O12 and Y3Fe5O12|Pt. *Applied Physics Letters*, 104(15):152410, April 2014. Publisher: American Institute of Physics.

[22] Y. Li, V.V. Naletov, O. Klein, J.L. Prieto, M. Muñoz, V. Cros, P. Bortolotti, A. Anane, C. Serpico, and G. de Loubens. Nutation Spectroscopy of a Nanomagnet Driven into Deeply Nonlinear Ferromagnetic Resonance. *Physical Review X*, 9(4):041036, November 2019.

[23] JAMAL BEN YOUSSEF. *Elaboration par epitaxie en phase liquide, caracterisation et etude physique des filmsminces de grenats ferrimagnetiques susbstitues par des ions bismuth.* These de doctorat, Paris 6, January 1989.

[24] B. Lührmann, M. Ye, H. Dötsch, and A. Gerspach. Nonlinearities in the ferrimagnetic resonance in epitaxial garnet films. *Journal of Magnetism and Magnetic Materials*, 96(1):237–244, June 1991.

[25] M. Collet, X. de Milly, O. d'Allivy Kelly, V. V. Naletov, R. Bernard, P. Bortolotti, J. Ben Youssef, V. E. Demidov, S. O. Demokritov, J. L. Prieto, M. Muñoz, V. Cros, A. Anane, G. de Loubens, and O. Klein. Generation of coherent spin-wave modes in yttrium iron garnet microdiscs by spin–orbit torque. *Nature Communications*, 7(1):10377, January 2016.

Bandiera_abtest: a Cc_license_type: cc_by Cg_type: Nature Research Journals Number: 1 Primary_atype: Research Publisher: Nature Publishing Group Subject_term: Spintronics Subject_term_id: spintronics.

[26] M. Evelt, V. E. Demidov, V. Bessonov, S. O. Demokritov, J. L. Prieto, M. Muñoz, J. Ben Youssef, V. V. Naletov, G. de Loubens, O. Klein, M. Collet, K. Garcia-Hernandez, P. Bortolotti, V. Cros, and A. Anane. High-efficiency control of spin-wave propagation in ultra-thin yttrium iron garnet by the spin-orbit torque. *Applied Physics Letters*, 108(17):172406, April 2016. Publisher: American Institute of Physics.

[27] Lucile Soumah, Nathan Beaulieu, Lilia Qassym, Cécile Carrétéro, Eric Jacquet, Richard Lebourgeois, Jamal Ben Youssef, Paolo Bortolotti, Vincent Cros, and Abdelmadjid Anane. Ultra-low damping insulating magnetic thin films get perpendicular. *Nature Communications*, 9(1):3355, December 2018.

[28] M. Evelt, L. Soumah, A.B. Rinkevich, S.O. Demokritov, A. Anane, V. Cros, Jamal Ben Youssef, G. de Loubens, O. Klein, P. Bortolotti, and V.E. Demidov. Emission of Coherent Propagating Magnons by Insulator-Based Spin-Orbit-Torque Oscillators. *Physical Review Applied*, 10(4):041002, October 2018.

[29] B. Divinskiy, H. Merbouche, V. E. Demidov, K. O. Nikolaev, L. Soumah, D. Gouéré, R. Lebrun, V. Cros, Jamal Ben Youssef, P. Bortolotti, A. Anane, and S. O. Demokritov. Evidence for spin current driven Bose-Einstein condensation of magnons. *Nature Communications*, 12(1):6541, December 2021.

[30] Hugo Merbouche. *Magnonic circuits based on nanostructured ultra-thin YIG for radiofrequency applications.* phdthesis, Université Paris-Saclay, May 2021.

[31] Y. Kajiwara, K. Harii, S. Takahashi, J. Ohe, K. Uchida, M. Mizuguchi, H. Umezawa, H. Kawai, K. Ando, K. Takanashi, S. Maekawa, and E. Saitoh. Transmission of electrical signals by spin-wave interconversion in a magnetic insulator. *Nature*, 464(7286):262–266, March 2010.

[32] A. Hamadeh, O. d'Allivy Kelly, C. Hahn, H. Meley, R. Bernard, A.H. Molpeceres, V.V. Naletov, M. Viret, A. Anane, V. Cros, S.O. Demokritov, J.L. Prieto, M. Muñoz, G. de Loubens, and O. Klein. Full Control of the Spin-Wave Damping in a Magnetic Insulator Using Spin-Orbit

Torque. *Physical Review Letters*, 113(19):197203, November 2014. Publisher: American Physical Society.

[33] S. I. Kiselev, J. C. Sankey, I. N. Krivorotov, N. C. Emley, R. J. Schoelkopf, R. A. Buhrman, and D. C. Ralph. Microwave oscillations of a nanomagnet driven by a spin-polarized current. *Nature*, 425(6956):380–383, September 2003.

[34] A. Slavin and V. Tiberkevich. Nonlinear Auto-Oscillator Theory of Microwave Generation by Spin-Polarized Current. *IEEE Transactions on Magnetics*, 45(4):1875–1918, April 2009.

[35] V. E. Demidov, M. Evelt, V. Bessonov, S. O. Demokritov, J. L. Prieto, M. Muñoz, J. Ben Youssef, V. V. Naletov, G. de Loubens, O. Klein, M. Collet, P. Bortolotti, V. Cros, and A. Anane. Direct observation of dynamic modes excited in a magnetic insulator by pure spin current. *Scientific Reports*, 6(1):32781, September 2016. Bandiera_abtest: a Cc_license_type: cc_by Cg_type: Nature Research Journals Number: 1 Primary_atype: Research Publisher: Nature Publishing Group Subject_term: Magnetic properties and materials;Spintronics Subject_term_id: magnetic-properties-and-materials;spintronics.

[36] N. Bloembergen and S. Wang. Relaxation Effects in *Para* - and Ferromagnetic Resonance. *Physical Review*, 93(1):72–83, January 1954.

[37] Boris Divinskiy, Sergei Urazhdin, Sergej O. Demokritov, and Vladislav E. Demidov. Controlled nonlinear magnetic damping in spin-Hall nanodevices. *Nature Communications*, 10(1):5211, December 2019.

[38] V. V. Naletov, G. de Loubens, G. Albuquerque, S. Borlenghi, V. Cros, G. Faini, J. Grollier, H. Hurdequint, N. Locatelli, B. Pigeau, A. N. Slavin, V. S. Tiberkevich, C. Ulysse, T. Valet, and O. Klein. Identification and selection rules of the spin-wave eigenmodes in a normally magnetized nanopillar. *Physical Review B*, 84(22):224423, December 2011. Publisher: American Physical Society.

[39] V. E. Demidov, S. Urazhdin, E. R. J. Edwards, M. D. Stiles, R. D. McMichael, and S. O. Demokritov. Control of Magnetic Fluctuations by Spin Current. *Physical Review Letters*, 107(10):107204, September 2011.

[40] H. T. Nembach, Justin M. Shaw, T. J. Silva, W. L. Johnson, S. A. Kim, R. D. McMichael, and P. Kabos. Effects of shape distortions and

imperfections on mode frequencies and collective linewidths in nanomagnets. *Physical Review B*, 83(9):094427, March 2011. Publisher: American Physical Society.

[41] J.-M. L. Beaujour, A. D. Kent, D. Ravelosona, I. Tudosa, and E. E. Fullerton. Ferromagnetic resonance study of Co/Pd/Co/Ni multilayers with perpendicular anisotropy irradiated with helium ions. *Journal of Applied Physics*, 109(3):033917, February 2011. Publisher: American Institute of Physics.

[42] Gavin S. Abo, Yang-Ki Hong, Jihoon Park, Jaejin Lee, Woncheol Lee, and Byoung-Chul Choi. Definition of Magnetic Exchange Length. *IEEE Transactions on Magnetics*, 49(8):4937–4939, August 2013. Conference Name: IEEE Transactions on Magnetics.

[43] J. A. Osborn. Demagnetizing Factors of the General Ellipsoid. *Physical Review*, 67(11-12):351–357, June 1945.

[44] Lucile Soumah. *Pulsed Laser Deposition of Substituted thin Garnet Films for Magnonic Applications.* phdthesis, Université Paris Saclay (COmUE), January 2019.

[45] Young-Wan Oh, Kyeong-Dong Lee, Jong-Ryul Jeong, and Byong-Guk Park. Interfacial perpendicular magnetic anisotropy in CoFeB/MgO structure with various underlayers. *Journal of Applied Physics*, 115(17):17C724, May 2014. Publisher: American Institute of Physics.

[46] J.-M.L. Beaujour, W. Chen, K. Krycka, C.-C. Kao, J. Z. Sun, and A. D. Kent. Ferromagnetic resonance study of sputtered Co|Ni multilayers. *The European Physical Journal B*, 59(4):475–483, October 2007.

[47] Haiming Yu, Jiang Xiao, and Helmut Schultheiss. Magnetic texture based magnonics. *Physics Reports*, 905:1–59, April 2021.

[48] L. Landau and E. Lifshitz. 3 - On the theory of the dispersion of magnetic permeability in ferromagnetic bodiesReprinted from Physikalische Zeitschrift der Sowjetunion 8, Part 2, 153, 1935. In L. P. Pitaevski, editor, *Perspectives in Theoretical Physics*, pages 51–65. Pergamon, Amsterdam, January 1992.

[49] Charles Kittel. On the Theory of Ferromagnetic Resonance Absorption. *Physical Review*, 73(2):155–161, January 1948.

[50] Yaroslav Tserkovnyak, Arne Brataas, Gerrit E W Bauer, and Bertrand I Halperin. Nonlocal magnetization dynamics in ferromagnetic heterostructures. *Rev. Mod. Phys.*, 77(4):47, 2005.

[51] Roman Verba, Gennadiy Melkov, Vasil Tiberkevich, and Andrei Slavin. Collective spin-wave excitations in a two-dimensional array of coupled magnetic nanodots. *Physical Review B*, 85(1):014427, January 2012.

[52] Benjamin Pigeau. *Magnetic vortex dynamics nanostructures.* These de doctorat, Paris 11, December 2012.

[53] Abbass Hamadeh. *Synchronization of spin trasnsfer nano-oscillators.* These de doctorat, Paris 11, October 2014.

[54] G. de Loubens, A. Riegler, B. Pigeau, F. Lochner, F. Boust, K. Y. Guslienko, H. Hurdequint, L. W. Molenkamp, G. Schmidt, A. N. Slavin, V. S. Tiberkevich, N. Vukadinovic, and O. Klein. Bistability of Vortex Core Dynamics in a Single Perpendicularly Magnetized Nanodisk. *Physical Review Letters*, 102(17):177602, May 2009.

[55] K. Yu. Guslienko, S. O. Demokritov, B. Hillebrands, and A. N. Slavin. Effective dipolar boundary conditions for dynamic magnetization in thin magnetic stripes. *Physical Review B*, 66(13):132402, October 2002.

[56] O. Klein, G. de Loubens, V. V. Naletov, F. Boust, T. Guillet, H. Hurdequint, A. Leksikov, A. N. Slavin, V. S. Tiberkevich, and N. Vukadinovic. Ferromagnetic resonance force spectroscopy of individual submicron-size samples. *Physical Review B*, 78(14):144410, October 2008.

[57] P. W. Anderson and H. Suhl. Instability in the Motion of Ferromagnets at High Microwave Power Levels. *Physical Review*, 100(6):1788–1789, December 1955.

[58] M. T. Weiss. Microwave and Low-Frequency Oscillation Due to Resonance Instabilities in Ferrites. *Physical Review Letters*, 1(7):239–241, October 1958.

[59] F. H. De Leeuw, R. Van Den Doel, and U. Enz. Dynamic properties of magnetic domain walls and magnetic bubbles. *Reports on Progress in Physics*, 43(6):689–783, June 1980. Publisher: IOP Publishing.

[60] K. Gnatzig, H. Dötsch, M. Ye, and A. Brockmeyer. Ferrimagnetic resonance in garnet films at large precession angles. *Journal of Applied Physics*, 62(12):4839–4843, December 1987.

[61] Giorgio Bertotti, Claudio Serpico, and Isaak D. Mayergoyz. Nonlinear Magnetization Dynamics under Circularly Polarized Field. *Physical Review Letters*, 86(4):724–727, January 2001. Publisher: American Physical Society.

[62] Giorgio Bertotti, Isaak D. Mayergoyz, and Claudio Serpico. Spin-Wave Instabilities in Large-Scale Nonlinear Magnetization Dynamics. *Physical Review Letters*, 87(21):217203, November 2001.

[63] Isaak D. Mayergoyz, Giorgio Bertotti, and Claudio Serpico. *Nonlinear Magnetization Dynamics in Nanosystems*. Elsevier Science, 1er édition edition, April 2009.

[64] https://fr.wikipedia.org/wiki/nutation, October 2021. Page Version ID: 186788721.

[65] G. de Loubens. *Spectroscopie micro-onde d'une nanostructure métallique magnétique hybride*. phdthesis, Université Paris Sud - Paris XI, December 2005.

[66] R. W. Damon. Relaxation Effects in the Ferromagnetic Resonance. *Reviews of Modern Physics*, 25(1):239–245, January 1953.

[67] G. de Loubens, V. V. Naletov, and O. Klein. Reduction of the spin-wave damping induced by nonlinear effects. *Physical Review B*, 71(18):180411, May 2005.

[68] Paul Bryant, Carson Jeffries, and Katsuhiro Nakamura. Spin-wave nonlinear dynamics in an yttrium iron garnet sphere. *Physical Review Letters*, 60(12):1185–1188, March 1988.

[69] V. E. Zakharov, V. S. L'vov, and S. S. Starobinets. Spin-wave turbulence beyond the parametric excitation threshold. *Soviet Physics Uspekhi*, 17(6):896, June 1975. Publisher: IOP Publishing.

[70] R. D. McMichael and P. E. Wigen. High-power ferromagnetic resonance without a degenerate spin-wave manifold. *Physical Review Letters*, 64(1):64–67, January 1990.

[71] George Gibson and Carson Jeffries. Observation of period doubling and chaos in spin-wave instabilities in yttrium iron garnet. *Physical Review A*, 29(2):811–818, February 1984.

[72] S. M. Rezende, O. F. de Alcantara Bonfim, and F. M. de Aguiar. Model for chaotic dynamics of the perpendicular-pumping spin-wave instability. *Physical Review B*, 33(7):5153–5156, April 1986. Publisher: American Physical Society.

[73] S.M. Rezende, F.M. de Aguiar, and O.F. de Alcantara Bonfim. Order and chaos in ferromagnetic spin wave instabilities. *Journal of Magnetism and Magnetic Materials*, 54-57:1127–1131, February 1986.

[74] X. Y. Zhang and H. Suhl. Spin-wave-related period doublings and chaos under transverse pumping. *Physical Review A*, 32(4):2530–2533, October 1985. Publisher: American Physical Society.

[75] F. M. de Aguiar, A. Azevedo, and S. M. Rezende. Characterization of strange attractors in spin-wave chaos. *Physical Review B*, 39(13):9448–9452, May 1989. Publisher: American Physical Society.

[76] G. Wiese and H. Benner. Multistability and chaos by parametric excitation of longwave modes in a YIG sphere. *Zeitschrift für Physik B Condensed Matter*, 79(1):119–131, February 1990.

[77] Jiang Cai, Yoshiyasu Kato, Atsushi Ogawa, Yoshifumi Harada, Meiro Chiba, and Takayuki Hirata. Chaotic Dynamics During Slow Relaxation Process in Magnon Systems. *Journal of the Physical Society of Japan*, 71(12):3087–3091, December 2002. Publisher: The Physical Society of Japan.

[78] F. M. de Aguiar and S. M. Rezende. Observation of Subharmonic Routes to Chaos in Parallel-Pumped Spin Waves in Yttrium Iron Garnet. *Physical Review Letters*, 56(10):1070–1073, March 1986. Publisher: American Physical Society.

[79] Ryan K. Smith, Marek Grabowski, and R. E. Camley. Period doubling toward chaos in a driven magnetic macrospin. *Journal of Magnetism and Magnetic Materials*, 322(15):2127–2134, August 2010.

[80] J. Becker, F. Rödelsperger, Th. Weyrauch, H. Benner, W. Just, and A. Čenys. Intermittency in spin-wave instabilities. *Physical Review E*, 59(2):1622–1632, February 1999. Publisher: American Physical Society.

[81] J. Bragard, H. Pleiner, O. J. Suarez, P. Vargas, J. A. C. Gallas, and D. Laroze. Chaotic dynamics of a magnetic nanoparticle. *Physical Review E*, 84(3):037202, September 2011. Publisher: American Physical Society.

[82] O. R. Sulymenko, O. V. Prokopenko, V. S. Tyberkevych, A. N. Slavin, and A. A. Serga. Bullets and droplets: Two-dimensional spin-wave solitons in modern magnonics (Review Article). *Low Temperature Physics*, 44(7):602–617, July 2018. Publisher: American Institute of Physics.

[83] B. A. Kalinikos, N. G. Kovshikov, and A. N. Slavin. Observation of spin-wave solitons in ferromagnetic films. *Soviet Journal of Experimental and Theoretical Physics Letters*, 38:413, October 1983. ADS Bibcode: 1983JETPL..38..413K.

[84] A. K. Zvezdin and A. F. Popkov. Contribution to the nonlinear theory of magnetostatic spin waves. *Sov. Phys. JETP*, 2(350):150, 1983.

[85] M. Bauer, O. Büttner, S. O. Demokritov, B. Hillebrands, V. Grimalsky, Yu. Rapoport, and A. N. Slavin. Observation of Spatiotemporal Self-Focusing of Spin Waves in Magnetic Films. *Physical Review Letters*, 81(17):3769–3772, October 1998.

[86] Martin V. Goldman, K. Rypdal, and B. Hafizi. Dimensionality and dissipation in Langmuir collapse. *The Physics of Fluids*, 23(5):945–955, May 1980. Publisher: American Institute of Physics.

[87] J.C. Slonczewski. Current-driven excitation of magnetic multilayers. *Journal of Magnetism and Magnetic Materials*, 159(1-2):L1–L7, June 1996.

[88] L. Berger. Emission of spin waves by a magnetic multilayer traversed by a current. *Physical Review B*, 54(13):9353–9358, October 1996.

[89] J. C Slonczewski. Excitation of spin waves by an electric current. *Journal of Magnetism and Magnetic Materials*, 195(2):L261–L268, May 1999.

[90] M. Tsoi, A. G. M. Jansen, J. Bass, W.-C. Chiang, M. Seck, V. Tsoi, and P. Wyder. Excitation of a Magnetic Multilayer by an Electric Current. *Physical Review Letters*, 80(19):4281–4284, May 1998. Publisher: American Physical Society.

[91] M. Tsoi, A. G. M. Jansen, J. Bass, W.-C. Chiang, V. Tsoi, and P. Wyder. Generation and detection of phase-coherent current-driven magnons in magnetic multilayers. *Nature*, 406(6791):46–48, July 2000. Number: 6791 Publisher: Nature Publishing Group.

[92] W. H. Rippard, M. R. Pufall, and T. J. Silva. Quantitative studies of spin-momentum-transfer-induced excitations in Co/Cu multilayer films using point-contact spectroscopy. *Applied Physics Letters*, 82(8):1260–1262, February 2003. Publisher: American Institute of Physics.

[93] Kyung Jin Lee, Alina Deac, Olivier Redon, Jean Pierre Nozières, and Bernard Dieny. Excitations of incoherent spin-waves due to spin-transfer torque. *Nature Materials*, 3(12):877–881, December 2004.

[94] W. H. Rippard, M. R. Pufall, S. Kaka, T. J. Silva, and S. E. Russek. Current-driven microwave dynamics in magnetic point contacts as a function of applied field angle. *Physical Review B*, 70(10):100406, September 2004. Publisher: American Physical Society.

[95] W. H. Rippard, M. R. Pufall, S. Kaka, S. E. Russek, and T. J. Silva. Direct-current induced dynamics in $\mathrm{co}_{90}\mathrm{fe}_{10}/\mathrm{ni}_{80}\mathrm{fe}_{20}$ point contacts. *Physical Review Letters*, 92(2):027201, January 2004. Publisher: American Physical Society.

[96] Stefano Bonetti, Vasil Tiberkevich, Giancarlo Consolo, Giovanni Finocchio, Pranaba Muduli, Fred Mancoff, Andrei Slavin, and Johan Åkerman. Experimental Evidence of Self-Localized and Propagating Spin Wave Modes in Obliquely Magnetized Current-Driven Nanocontacts. *Physical Review Letters*, 105(21):217204, November 2010. Publisher: American Physical Society.

[97] G. Gerhart, E. Bankowski, G. A. Melkov, V. S. Tiberkevich, and A. N. Slavin. Angular dependence of the microwave-generation threshold in a nanoscale spin-torque oscillator. *Physical Review B*, 76(2):024437, July 2007. Publisher: American Physical Society.

[98] Ferran Macià and Andrew D. Kent. Magnetic droplet solitons. *Journal of Applied Physics*, 128(10):100901, September 2020.

[99] B. A. Ivanov and A. M. Kosevich. Bound states of a large number of magnons in a ferromagnet with a single-ion anisotropy. *Soviet Journal of Experimental and Theoretical Physics*, 45:1050, May 1977. ADS Bibcode: 1977JETP...45.1050I.

[100] S. M. Mohseni, S. R. Sani, J. Persson, T. N. Anh Nguyen, S. Chung, Ye. Pogoryelov, P. K. Muduli, E. Iacocca, A. Eklund, R. K. Dumas, S. Bonetti, A. Deac, M. A. Hoefer, and J. Åkerman. Spin Torque–Generated Magnetic Droplet Solitons. *Science*, 339(6125):1295–1298, March 2013.

[101] M. A. Hoefer, T. J. Silva, and Mark W. Keller. Theory for a dissipative droplet soliton excited by a spin torque nanocontact. *Physical Review B*, 82(5):054432, August 2010. Publisher: American Physical Society.

[102] Ferran Macià, Dirk Backes, and Andrew D. Kent. Stable magnetic droplet solitons in spin-transfer nanocontacts. *Nature Nanotechnology*, 9(12):992–996, January 2014.

[103] S. Lendínez, N. Statuto, D. Backes, A. D. Kent, and F. Macià. Observation of droplet soliton drift resonances in a spin-transfer-torque nanocontact to a ferromagnetic thin film. *Physical Review B*, 92(17):174426, November 2015. Publisher: American Physical Society.

[104] D. Xiao, V. Tiberkevich, Y. H. Liu, Y. W. Liu, S. M. Mohseni, S. Chung, M. Ahlberg, A. N. Slavin, J. Åkerman, and Yan Zhou. Parametric autoexcitation of magnetic droplet soliton perimeter modes. *Physical Review B*, 95(2):024106, January 2017. Publisher: American Physical Society.

[105] Sunjae Chung, Q. Tuan Le, Martina Ahlberg, Ahmad A. Awad, Markus Weigand, Iuliia Bykova, Roman Khymyn, Mykola Dvornik, Hamid Mazraati, Afshin Houshang, Sheng Jiang, T.N. Anh Nguyen, Eberhard Goering, Gisela Schütz, Joachim Gräfe, and Johan Åkerman. Direct Observation of Zhang-Li Torque Expansion of Magnetic Droplet Solitons. *Physical Review Letters*, 120(21):217204, May 2018. Publisher: American Physical Society.

[106] Martina Ahlberg, Sunjae Chung, Sheng Jiang, Andreas Frisk, Maha Khademi, Roman Khymyn, Ahmad A. Awad, Q. Tuan Le, Hamid Mazraati, Majid Mohseni, Markus Weigand, Iuliia Bykova, Felix Groß, Eberhard Goering, Gisela Schütz, Joachim Gräfe, and Johan Åkerman. Freezing and thawing magnetic droplet solitons. *Nature Communications*, 13(1):2462, December 2022.

[107] N. Akhmediev and A. Ankiewicz. Three Sources and Three Component Parts of the Concept of Dissipative Solitons. In *Dissipative Solitons: From Optics to Biology and Medicine*, volume 751, pages 1–28. Springer Berlin Heidelberg, Berlin, Heidelberg, 2008. ISSN: 0075-8450, 1616-6361 Series Title: Lecture Notes in Physics.

[108] J. A. Sidles. Noninductive detection of single-proton magnetic resonance. *Applied Physics Letters*, 58(24):2854–2856, June 1991.

[109] D. Rugar, C. S. Yannoni, and J. A. Sidles. Mechanical detection of magnetic resonance. *Nature*, 360(6404):563–566, December 1992.

[110] Z. Zhang, P. C. Hammel, and P. E. Wigen. Observation of ferromagnetic resonance in a microscopic sample using magnetic resonance force microscopy. *Applied Physics Letters*, 68(14):2005–2007, April 1996.

[111] G. de Loubens, V. V. Naletov, M. Viret, O. Klein, H. Hurdequint, J. Ben Youssef, F. Boust, and N. Vukadinovic. Magnetic resonance spectroscopy of perpendicularly magnetized Permalloy multilayer disks. *Journal of Applied Physics*, 101(9):09F514, May 2007.

[112] K. Wago, D. Botkin, C. S. Yannoni, and D. Rugar. Paramagnetic and ferromagnetic resonance imaging with a tip-on-cantilever magnetic resonance force microscope. *Applied Physics Letters*, 72(21):2757–2759, May 1998.

[113] Z. Zhang, P. C. Hammel, M. Midzor, M. L. Roukes, and J. R. Childress. Ferromagnetic resonance force microscopy on microscopic cobalt single layer films. *Applied Physics Letters*, 73(14):2036–2038, October 1998.

[114] Albrecht Jander, John Moreland, and Pavel Kabos. Micromechanical detectors for local field measurements based on ferromagnetic resonance (invited). *Journal of Applied Physics*, 89(11):7086–7090, June 2001.

[115] V. Charbois, V. V. Naletov, J. Ben Youssef, and O. Klein. Mechanical detection of ferromagnetic resonance spectrum in a normally magnetized yttrium–iron–garnet disk. *Journal of Applied Physics*, 91(10):7337, 2002.

[116] V. Charbois, V. V. Naletov, J. Ben Youssef, and O. Klein. Influence of the magnetic tip in ferromagnetic resonance force microscopy. *Applied Physics Letters*, 80(25):4795–4797, June 2002.

[117] Soraya Sangiao, César Magén, Darius Mofakhami, Grégoire de Loubens, and José María De Teresa. Magnetic properties of optimized cobalt nanospheres grown by focused electron beam induced deposition (FEBID) on cantilever tips. *Beilstein Journal of Nanotechnology*, 8:2106–2115, October 2017.

[118] J. A. Sidles, J. L. Garbini, K. J. Bruland, D. Rugar, O. Züger, S. Hoen, and C. S. Yannoni. Magnetic resonance force microscopy. *Reviews of Modern Physics*, 67(1):249–265, January 1995.

[119] Vincent Charbois. *Détection mécanique de la résonance ferromagnétique.* These de doctorat, Paris 7, January 2003.

[120] Hugo Lavenant, Vladimir Naletov, Olivier Klein, Grégoire de Loubens, Laura Casado, and José María De Teresa. Mechanical magnetometry of Cobalt nanospheres deposited by focused electron beam at the tip of ultra-soft cantilevers. *Nanofabrication*, 1(1), January 2014. Publisher: De Gruyter Open Access Section: Nanofabrication.

[121] Marshall Sparks. *Ferromagnetic-relaxation theory.* McGraw-Hill, New York, 1964. OCLC: 859883967.

[122] http://micromagnetics.org/magnum.fd/.

[123] https://github.com/MicroMagnum/MicroMagnum, January 2022.

[124] S. Klingler, A. V. Chumak, T. Mewes, B. Khodadadi, C. Mewes, C. Dubs, O. Surzhenko, B. Hillebrands, and A. Conca. Measurements of the exchange stiffness of YIG films using broadband ferromagnetic resonance techniques. *Journal of Physics D: Applied Physics*, 48(1):015001, December 2014. Publisher: IOP Publishing.

[125] Rohan Adur, Chunhui Du, Hailong Wang, Sergei A. Manuilov, Vidya P. Bhallamudi, Chi Zhang, Denis V. Pelekhov, Fengyuan Yang, and P. Chris Hammel. Damping of Confined Modes in a Ferromagnetic Thin Insulating Film: Angular Momentum Transfer across a Nanoscale Field-Defined Interface. *Physical Review Letters*, 113(17):176601, October 2014. Publisher: American Physical Society.

[126] B. Hoekstra, R. P. van Stapele, and J. M. Robertson. Spin-wave resonance spectra of inhomogeneous bubble garnet films. *Journal of Applied Physics*, 48(1):382–395, January 1977.

[127] Myoung-Woo Yoo, Damien Rontani, Jérémy Létang, Sébastien Petit-Watelot, Thibaut Devolder, Marc Sciamanna, Karim Bouzehouane, Vincent Cros, and Joo-Von Kim. Pattern generation and symbolic dynamics in a nanocontact vortex oscillator. *Nature Communications*, 11(1):601, January 2020. Number: 1 Publisher: Nature Publishing Group.

[128] https://en.wikipedia.org/wiki/fermi-pasta-ulam-tsingou-problem.

[129] https://fr.wikipedia.org/wiki/expérience-de-fermi-pasta-ulam-tsingou.

[130] Jeramy Lewis, Robert E. Camley, and Nicholas R. Anderson. Exploration of Fermi-Pasta-Ulam Behavior in a Magnetic System. *Physical Review Letters*, 120(16):167203, April 2018. Publisher: American Physical Society.

[131] Yu. V. Gulyaev, P. E. Zil'berman, A. G. Temiryazev, and M. P. Tikhomirova. Principal mode of the nonlinear spin-wave resonance in perpendicular magnetized ferrite films. *Physics of the Solid State*, 42(6):1094–1099, June 2000.

[132] Q. Wang, B. Heinz, R. Verba, M. Kewenig, P. Pirro, M. Schneider, T. Meyer, B. Lägel, C. Dubs, T. Brächer, and A.V. Chumak. Spin Pinning and Spin-Wave Dispersion in Nanoscopic Ferromagnetic Waveguides. *Physical Review Letters*, 122(24):247202, June 2019. Publisher: American Physical Society.

[133] Vasyl Tyberkevych, Andrei Slavin, Petro Artemchuk, and Graham Rowlands. Vector Hamiltonian Formalism for Nonlinear Magnetization Dynamics. Technical Report arXiv:2011.13562, arXiv, November 2020. arXiv:2011.13562 [cond-mat] type: article.

[134] S. Perna, F. Bruckner, C. Serpico, D. Suess, and M. d'Aquino. Computational micromagnetics based on normal modes: Bridging the gap between macrospin and full spatial discretization. *Journal of Magnetism and Magnetic Materials*, 546:168683, March 2022.

[135] Saül Vélez, Sandra Ruiz-Gómez, Jakob Schaab, Elzbieta Gradauskaite, Martin S. Wörnle, Pol Welter, Benjamin J. Jacot, Christian L. Degen, Morgan Trassin, Manfred Fiebig, and Pietro Gambardella. Current-driven dynamics and ratchet effect of skyrmion bubbles in a ferrimagnetic insulator. *Nature Nanotechnology*, 17(8):834–841, August 2022. Number: 8 Publisher: Nature Publishing Group.

[136] N. Vukadinovic and F. Boust. Three-dimensional micromagnetic simulations of multidomain bubble-state excitation spectrum in ferromagnetic cylindrical nanodots. *Physical Review B*, 78(18):184411, November 2008. Publisher: American Physical Society.

[137] Joo-Von Kim, Felipe Garcia-Sanchez, João Sampaio, Constance Moreau-Luchaire, Vincent Cros, and Albert Fert. Breathing modes of confined skyrmions in ultrathin magnetic dots. *Physical Review B*, 90(6):064410, August 2014. Publisher: American Physical Society.

[138] Roman Verba, Vasil Tiberkevich, and Andrei Slavin. Hamiltonian formalism for nonlinear spin wave dynamics under antisymmetric interactions: Application to Dzyaloshinskii-Moriya interaction. *Physical Review B*, 99(17):174431, May 2019. Publisher: American Physical Society.

université
PARIS-SACLAY

ÉCOLE DOCTORALE
Physique en
Île-de-France (PIF)

Titre: Dynamique de l'aimantation de nanostructures dans des régimes fortement hors-équilibre

Mots clés: Dynamique de l'aimantation, magnonique, nanomagnétisme, non-linéarité, systèmes dynamiques, YIG

Résumé: Les ondes de spin ou magnons sont les excitations élémentaires de l'ordre ferromagnétique. Leur caractère ondulatoire, leurs propriétés de propagation anisotropes et ajustables, leurs gammes de fréquence (du GHz au THz) et de longueur d'onde (du µm au nm), l'absence de courant de charge associé au transport de spin, sont autant d'atouts pour les nouveaux paradigmes « beyond CMOS » de traitement de l'information et du signal dans le domaine micro-onde qui sont en train d'émerger.

Les propriétés fortement non-linéaires des ondes de spin, qui découlent de l'équation de la dynamique de l'aimantation, conduisent également à de nombreux phénomènes physiques intéressants. Ils se manifestent, entre autres, par l'apparition de dynamique bistable, de solitons, d'instabilités d'ondes de spin, d'auto-oscillations et de chaos. Le type de dynamique non-linéaire dépend d'une part du spectre d'ondes de spin de l'échantillon, que ses propriétés magnétiques, sa géométrie, et le champ appliqué déterminent, et d'autre part de l'excitation. Le développement récent de couches ultra-minces de grenats magnétiques, connus pour leur qualité dynamique inégalée, ouvre des opportunités pour contrôler ces effets non-linéaires. Premièrement, elles peuvent être nanostructurées de façon standard. La nanostructuration induit une quantification du spectre d'excitation, ce qui limite les interactions non-linéaires entre modes. Ensuite, il est possible d'ajuster par dopage leur anisotropie effective, responsable de la dépendance non-linéaire de la fréquence de précession. Enfin, elles peuvent être mises hors équilibre par des courants de spin à leur interface avec un métal à fort couplage spin-orbite.

L'objectif de cette thèse est d'étudier la dynamique fortement hors équilibre induite par un champ magnétique micro-onde dans des nano-disques de grenat d'yttrium fer (YIG) dopé au bismuth (Bi). Le dopage est choisi de façon à ce que l'anisotropie perpendiculaire de la couche magnétique compense quasiment son anisotropie de forme, ce qui annule la dépendance non-linéaire de la fréquence de résonance. Les diamètres des disques étudiés, inférieurs au micron, permettent de confiner fortement les ondes de spin et d'obtenir un spectre discret. Le champ excitateur est appliqué grâce à une antenne micro-onde intégrée, et la dynamique résultante dans les nano-disques de BiYIG est détectée par un microscope de force par résonance magnétique (MRFM). La spectroscopie détaillée du régime linéaire, à faible amplitude d'excitation, met en évidence que le process de nanofabrication réduit l'anisotropie à la périphérie des disques, et que les disques situés directement sous l'antenne micro-onde ont un amortissement accru. Cela n'empêche cependant pas d'atteindre des régimes fortement hors équilibre lorsque l'amplitude de l'excitation est augmentée. En particulier, la raie de résonance du mode principal dans la configuration hors du plan des disques de diamètre supérieur à 500 nm se fractionne et sature rapidement quand l'excitation augmente. Des simulations micromagnétiques reproduisent bien ce comportement inattendu, et permettent de l'attribuer à l'apparition d'une instabilité dynamique. Celle-ci correspond à une auto-modulation du profil de précession qui se localise très fortement et brièvement au centre du disque, de façon quasi-périodique ou chaotique, en fonction du réglage fin des paramètres de contrôle. Afin de sonder expérimentalement cette dynamique complexe, une spectroscopie à deux tons est mise en œuvre. Cette dernière révèle des spectres de modulation en fréquence reflétant la richesse des variations temporelles de la dynamique de l'aimantation au-delà du seuil d'instabilité. Des expériences et simulations complémentaires permettent d'attribuer ce comportement à des effets de taille finie et d'équilibre entre les différents termes d'anisotropie, et d'ébaucher un diagramme de phase sur le type de dynamique attendue en fonction des paramètres pertinents.

Title: Magnetization dynamics of nanostructures in strongly out-of-equilibrium regimes

Keywords: Magnetization dynamics, magnonics, nanomagnetism, non-linearity, dynamical systems, YIG

Abstract: Spin waves or magnons are the elementary excitations of the ferromagnetic order. Their wave character, their tunable and anisotropic propagation properties, their frequency (from GHz to THz) and wavelength (from µm to nm) ranges, the absence of charge current associated with spin transport, are all advantages for the new "beyond CMOS" paradigms of information and signal processing in the microwave domain that are emerging.

The strongly non-linear properties of spin waves, which result from the equation of magnetization dynamics, also lead to many interesting physical phenomena. Among others, they manifest themselves by the appearance of bistable dynamics, solitons, spin wave instabilities, auto-oscillations and chaos. The type of non-linear dynamics depends on one hand on the spin wave spectrum of the sample, which is determined by its magnetic properties, its geometry and the applied field, and on the other hand on the excitation. The recent development of ultra-thin layers of magnetic garnets, known for their unique dynamic quality, opens opportunities to control these non-linear effects. First, they can be nanopatterned in a standard way. The nanopatterning induces a quantization of the excitation spectrum, which limits the nonlinear interactions between modes. Secondly, it is possible by doping to adjust their effective anisotropy, responsible for the nonlinear dependence of the precession frequency. Finally, they can be put out of equilibrium by spin currents at their interface with a metal with strong spin-orbit coupling.

The objective of this thesis is to study the strongly out-of-equilibrium dynamics induced by a microwave magnetic field in bismuth (Bi) doped yttrium iron garnet (YIG) nanodisks. The doping is chosen so that the perpendicular anisotropy of the magnetic layer almost compensates its shape anisotropy, thus canceling the nonlinear dependence of the resonant frequency. The diameters of the studied disks, smaller than one micron, allow to strongly confine the spin waves and to obtain a discrete spectrum. The exciting field is applied through an integrated microwave antenna, and the resulting dynamics in the BiYIG nano-disks are detected by a magnetic resonance force microscope (MRFM). A detailed spectroscopy of the linear regime, at low excitation amplitude, shows that the nanofabrication process reduces the anisotropy at the periphery of the disks, and that the disks located directly under the microwave antenna have an enhanced damping. However, this does not prevent reaching strongly non-equilibrium regimes when the excitation amplitude is increased. In particular, the resonance line of the main mode in the out-of-plane configuration of the disks with diameter larger than 500 nm splits and quickly saturates when the excitation increases. Micromagnetic simulations reproduce well this unexpected behavior, and allow to attribute it to the appearance of a dynamic instability. This instability corresponds to a self-modulation of the precession profile which localizes very strongly and briefly at the center of the disk, in a quasi-periodic or chaotic way, depending on the fine tuning of the control parameters. In order to experimentally probe this complex dynamics, a two-tone spectroscopy is implemented. The latter reveals frequency modulation spectra reflecting the richness of the temporal variations of the magnetization dynamics beyond the instability threshold. Further experiments and simulations allow to attribute this behavior to finite size effects and to the balance between the different anisotropy terms, and to draft a phase diagram on the type of dynamics expected as a function of the relevant parameters.